Mathematical Problems in Engineering

Mathematical Problems of Rock Fracture in Deep Underground Engineering

Lead Guest Editor: Fuqiang Ren
Guest Editors: Chen Cao, Zhihong Lei, and Jinzhou Bai

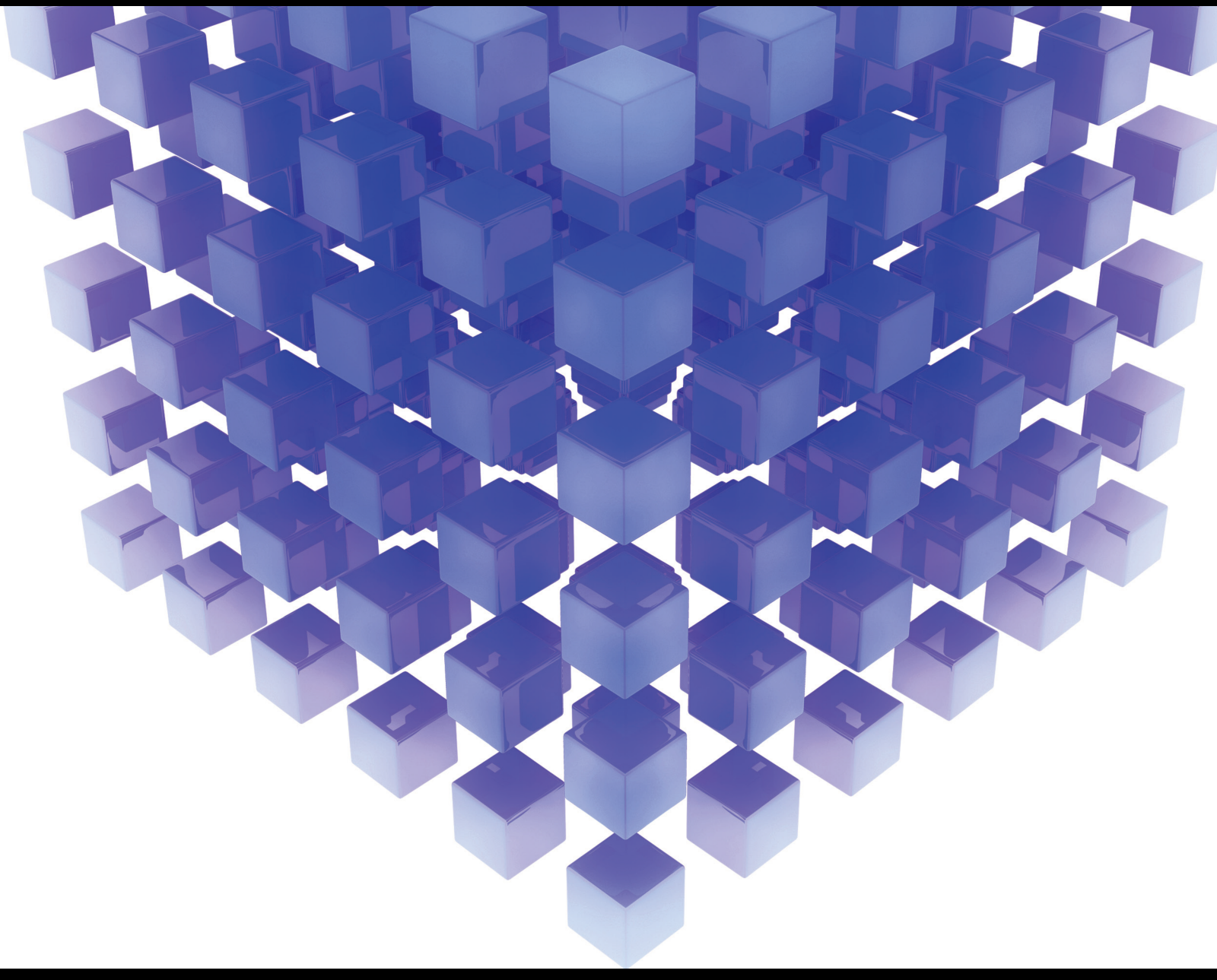

Mathematical Problems of Rock Fracture in Deep Underground Engineering

Mathematical Problems of Rock Fracture in Deep Underground Engineering

Lead Guest Editor: Fuqiang Ren
Guest Editors: Chen Cao, Zhihong Lei, and Jinzhou Bai

Chief Editor

Academic Editors

Contents

Hindawi
Mathematical Problems in Engineering
Volume 2022, Article ID 8260169, 13 pages
https://doi.org/10.1155/2022/8260169

Research Article

Collaborative Control Technology of Crosscut Floor Heave in Soft Rocks under Deep High Horizontal Stress

Hongyang Liu,[1,2] **Chengwei Liu**,[1] **Minghua Zhai**,[2] **Peng Zhang**,[1] **Longjiang Wang**,[3] **Feng Wang**,[2] **and Jiangang Liu**[1]

[1]*School of Mining and Mechanical Engineering, Liupanshui Normal University, Liupanshui 553004, Guizhou, China*
[2]*College of Energy and Mining Engineering, Shandong University of Science and Technology, Qingdao 266590, Shandong, China*
[3]*Planning and Construction Department of Heze High-tech Zone Management Committee, Heze 274047, Shandong, China*

Correspondence should be addressed to Chengwei Liu; liuchengwei12@126.com

Received 29 June 2022; Revised 18 August 2022; Accepted 23 August 2022; Published 13 September 2022

Academic Editor: Fuqiang Ren

The repair rate of deep permanent roadways is about 90%, and most of which are projects treating floor heave. The deformation behaviors of crosscut were analyzed in the work according to a trackage crosscut at the shaft station of Panyidong Coal Mine in Huainan, China. Crosscut has complex characteristics such as globality, difference, and rheology under deep stress because that crosscut passes through multiple strata. The mechanism of crosscut floor heave was studied based on on-site in situ stress tests and surrounding rock composition tests. The floor heave of trackage crosscut is water swelling in the mudstone and sandy-mudstone areas where the mineral components are mainly kaolinite and illite mixed layers. In the areas of fine and medium-fine sandstone, trackage crosscut is in shear dislocation under high horizontal stress. The slip-line field theory was used to study the ultimate load and maximum failure depth of crosscut floor heave. According to the deformation characteristics of crosscut floor heave, a collaborative control technology enhancing the bearing structure of all-sided surrounding rocks was proposed, including filling of the U-shaped steel supports, shallow grouting in the all-sided surrounding rocks and deep grouting in the floor and inverted arches. A support scheme for repairing the floor was designed based on the specific engineering geology of trackage crosscut floor heave at the shaft station of the Panyidong Coal Mine. After repairing, the crosscut floor heave was monitored for 70 d. The results showed the following. (1) After repairing, the maximum cumulative floor heave was 45.3 mm, which was only 8.1% of that before repairing. (2) Crosscut floor heave changed greatly within one week after repair, with a maximum floor heave speed of 4.7 mm/d. The floor heave speed was maintained below 1 mm/d after 40 d, and the floor heave tended to be stable after 60 d. The collaborative control technology enhancing the bearing structure of all-sided surrounding rocks could control the crosscut floor heave in soft rocks under deep high horizontal stress.

1. Introduction

Coal plays a fundamental role in China's energy security strategy [1, 2]. China's total energy consumption reached 5.24 billion tons of standard coal in 2021, an increase of 5.2% over the previous year. The annual coal output of 4.07 billion tons hit a new high, an increase of 4.7% over the previous year. With the increased energy demand and mining intensity, the mining depth of coal resources is increasing at a rate of 10–25 m/*a* [3–5]. The underground rock masses show the characteristic of "three highs and one disturbance" (high in situ stress, high geo-temperature, high karst water pressure, and a strong mining disturbance), and roadways have large deformation, strong rheology, serious damage, and difficulty in supporting [6, 7]. According to statistics, the repair rate of deep permanent roadways is 90%, and most of which are floor heave-treating projects. The floor heave accounts for 2/3 to 3/4 of the roof-to-floor convergence of the roadways, which seriously affects the ventilation, transportation, and personnel passage of the mine [8–10]. Most roadways only support the roof and two sides instead of the floor, which is the most vulnerable part of the

surrounding rock-bearing structure. The floor strata bend and expand under extrusion on both sides, the stress of original rock masses, bearing pressures, and physical and mechanical properties of water and floor, thus, forming a floor heave [9].

The mechanism and deformation characteristics of floor heave are complex due to the complexity of surrounding rock properties, stress environment, and occurrence conditions [11–14]. Scholars have studied the formation, mechanism, and influencing factors of floor heave over the years [15–18]. For example, Ma et al. summarized the mechanism of floor heave under various factors and divided it into types of squeeze flow, flexural fold, shear dislocation, and water swelling. The main factors affecting the floor heave of roadways are floor lithology, surrounding-rock stress, hydraulic effect, and support strength [19]. Malkowski P. *et al.* analyzed the in situ measurement data of floor heave, the results showed that groundwater and fault zones intersecting the excavations were considered as the key factors that affect floor upheavals [20]. Moreover, for rocks containing water-absorbed minerals such as claystones or mudstones, the presence of water is more likely to increase the floor's propensity to the floor heave [21]. Sun et al. analyzed the roadway's deformation and failure mechanism of different layered rock masses employing the Euler formula, theory of pressure bar stability, Mohr–Coulomb criterion, and the deflection failure mechanical model [22]. Based on the analysis of the main floor heave case of Glencore Bulga underground operations, Sungsoon et al. believed that main high horizontal stress with greater covering depths and certain floor-lithology configuration is likely to contribute to the failures of floor strata [23].

The control methods of floor heave in different situations are also different [24, 25]. Zhang et al. proposed the grouting reinforcement method for the large floor heave of the retained goaf-side gate road [26]. Wang et al. analyzed the influencing factors of the floor heave of the roadways in the fault-fractured zone, including the influence of the fault-fractured zone, the poor quality of floor rock masses, the deterioration of soaked floors, and weak floor supports. A comprehensive support scheme is proposed to optimize all-sided supports using the anchor, reinforcing mesh, shotcreting and concrete-filled steel tube support, and floor supports are strengthened by reinforced-concrete floor beams [27]. Zhang et al. proposed the combined bolting-grouting support technology of all-sided anchor cables and precast-block inverted arches to address the serious floor heave problems of roadways in the complex environment of deep high in-situ stress and weak interlayers [28].

To sum up, the two sides and bottom corners are reinforced with bolts to control the floor heave in shallow roadways rather than in deep roadways [29, 30]. At present, there are two types of reinforcement methods for floors in deep roadways. One is to use the all-sided support method of retractable supports of U-shaped steel with floor arches [31–33], and the other is to use the joint reinforcement method of floor bolts and cables and floor grouting [34–36]. The first method has a significant control effect on the floor heave of weak broken roadways; however, it has high costs, complicated processes, and low efficiency of construction. Therefore, most mines adopt the second method, which solves the problem of the floor heave of roadways under different geological conditions.

The above analysis shows that each mechanism and prevention technology of floor heave is proposed for certain geological conditions due to the complex surrounding rock properties and stress environment of roadways. Besides, although scholars have studied the mechanism and control technology of floor heave by theoretical analysis, numerical simulation, and similar material simulation, there are few studies on the deformation characteristics and mechanism of crosscut floor heave at the shaft station. The main crosscut at the shaft station is responsible for important tasks such as transportation, ventilation, and pedestrians. It is an important channel connecting the main roadways and coal seams and often passes through the inclined coal measure strata with multiple lithologies [37–39]. Therefore, the mechanism of crosscut floor heave cannot be explained by a single type, and a single support technology is unavailable for its control.

The deformation characteristics and occurrence mechanism of crosscut floor heave are more complicated, especially in deep mining. The deformation characteristics and mechanism of deep crosscut floor heave in soft rocks were analyzed by taking a trackage crosscut at the shaft station of Panyidong Coal Mine in China as the research object in the work. A collaborative control technology enhancing the bearing structure of full-sided surrounding rocks was proposed to control strong crosscut floor heave in soft rocks under deep high stress.

2. Project Overview

2.1. Location of the Mine and Engineering Geological Conditions of Crosscut. Pan Yidong Coal Mine is located in Panji District, Huainan, Anhui, China, about 22 km away from the urban area (Figure 1). The ground elevation is +20.1 m to +23.8 m, and the elevation of the level 1 is −848 m, so the depth of the shaft station is 868.1 m to 871.8 m. The main trackage crosscut is located on the west side of the shaft station, with a total length of about 300 m. It is an important transport channel connecting the heavy vehicle line of the shaft station and the −848 m trackage roadway (Figure 2).

The excavated section of the trackage crosscut is located in the coal-bearing rock series of the upper shihezi formation in the Permian, passing through the F32 fault (Figure 3). On the hanging wall of the fault, the surrounding rocks' lithology of the roadway is mainly sandy and fine sandstone. On the footwall of the fault, the lithology *o* is mainly mudstone, coal, sandy mudstone, fine sandstone, and medium-fine sandstone, and the average inclination angle of the strata is about 7.5°. The section shape of the roadway is a straight wall with a semicircular arch, and the size is width × middle height = 5,200 × 4,540 mm. The initial support method is the combined support of 36# U-shaped steels, anchor cables, bolts, and shotcreting on the contour of the roadway, with the floor unsupported (Figure 3).

Figure 1: Location of Panyidong coal mine.

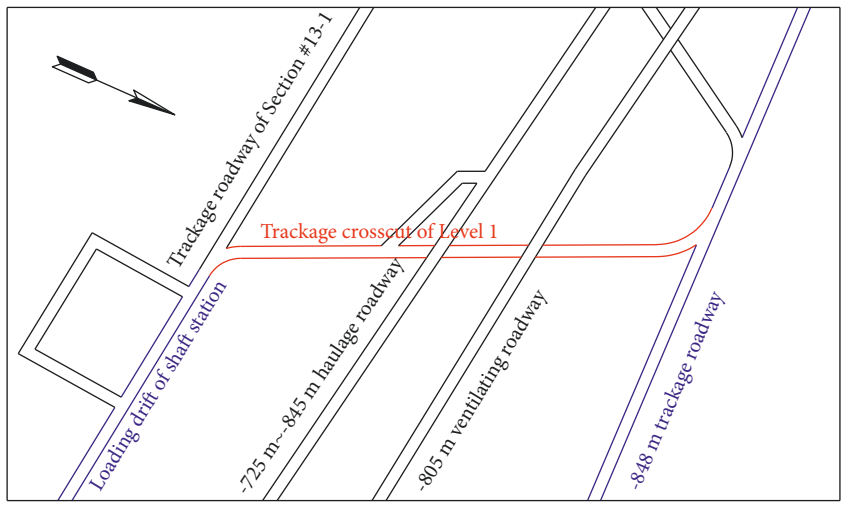

Figure 2: Location of trackage crosscut.

2.2. Characteristics of Crosscut Floor Heave. Obvious floor heave occurred only one month after excavating trackage crosscut. According to the on-site investigation, the deformation of the surrounding rocks of the roadway has the following characteristics.

(1) Globality: all parts of the roadway occurred different degrees of floor heave. The total length of the roadway with floor heave exceeding 100 mm was 210 m, and the maximum uplift reached 280 mm within one month and 560 mm within two months.

(2) Differences: floor heave shows the swelling deformation of mudstone and sandy mudstone (Figure 4(a)); it shows shear-dislocation failure of medium-fine and fine sandstone (Figure 4(b)).

(3) Rheology: the floor heave of the roadway is characterized by the flow deformation over time. As the

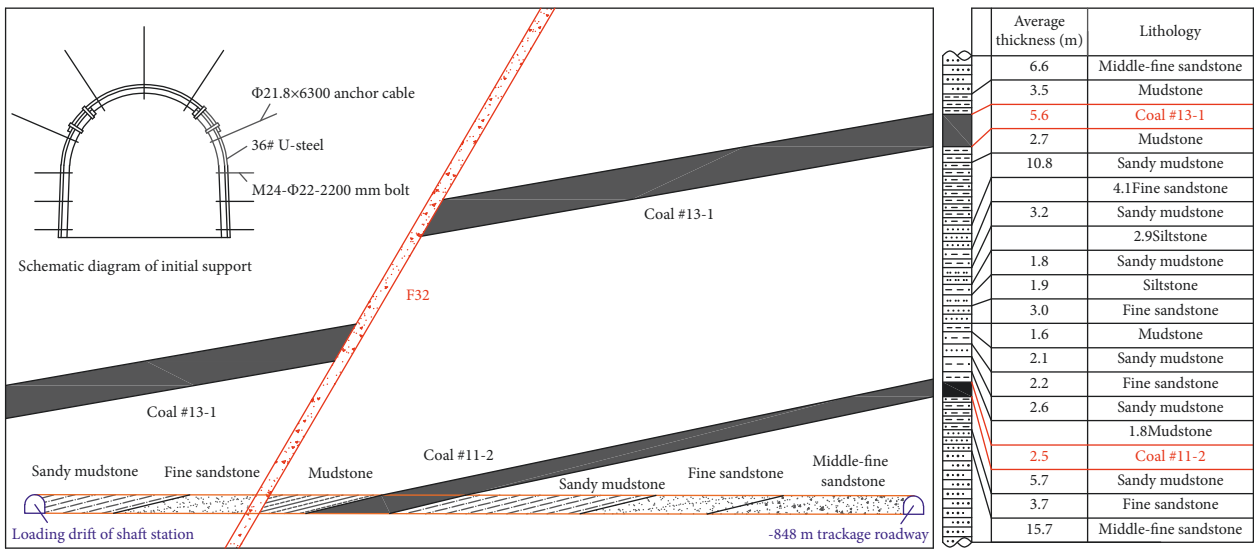

Figure 3: Horizon of trackage crosscut and the comprehensive geological histogram.

(a) (b)

Figure 4: Two types of floor heave. (a) Expansion deformation in the floor. (b) Shear dislocation in the floor.

strata expand and deform to the depth of the floor, the degree of floor heave gradually increases.

3. Mechanism of Crosscut Floor Heave

3.1. Reasons for Crosscut Floor Heave. According to the deformation characteristics of crosscut floor heave, the on-site in-situ stress test, and the laboratory surrounding-rock component test, the reasons for the occurrence of crosscut floor heave are analyzed as follows.

3.1.1. High Horizontal Stress. In situ stress measurements were carried out at three different positions (Measurement station #1~#3 in Figure 5) of trackage crosscut using the stress-relief method. The measuring steps and main devices used by the stress-relief method are shown in Figure 6.

The measurement results (Table 1) show that the maximum principal stress direction is inclined to the horizontal direction. Besides, the overall distribution is east-west and in syncline to the roadway axis. Horizontal stress is greater than the vertical stress, and lateral pressure coefficient λ is about 1.7–1.8. The stability of the surrounding rocks of trackage crosscut is significantly affected by horizontal tectonic stress, and the surrounding rocks of the floor are prone to the floor-heave deformation of shear-slip failure under high horizontal stress. This is the case for the deformation of floor heave in the roadway where surrounding rocks are fine-or medium-fine sandstone.

3.1.2. Mineral Composition of Surrounding Rocks. Four groups of rock samples were selected at the locations with different lithologies in trackage crosscut (Sampling location #1~#4 in Figure 5), and XRD experiments were used to

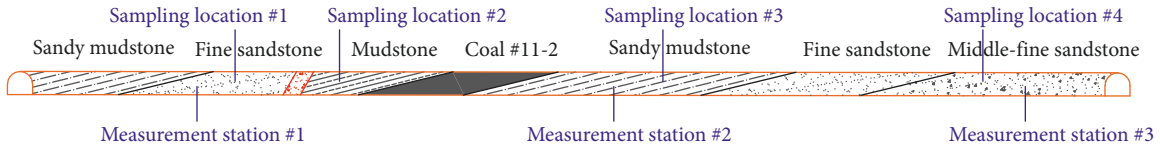

Figure 5: Location of in situ stress measurement and sampled surrounding rocks.

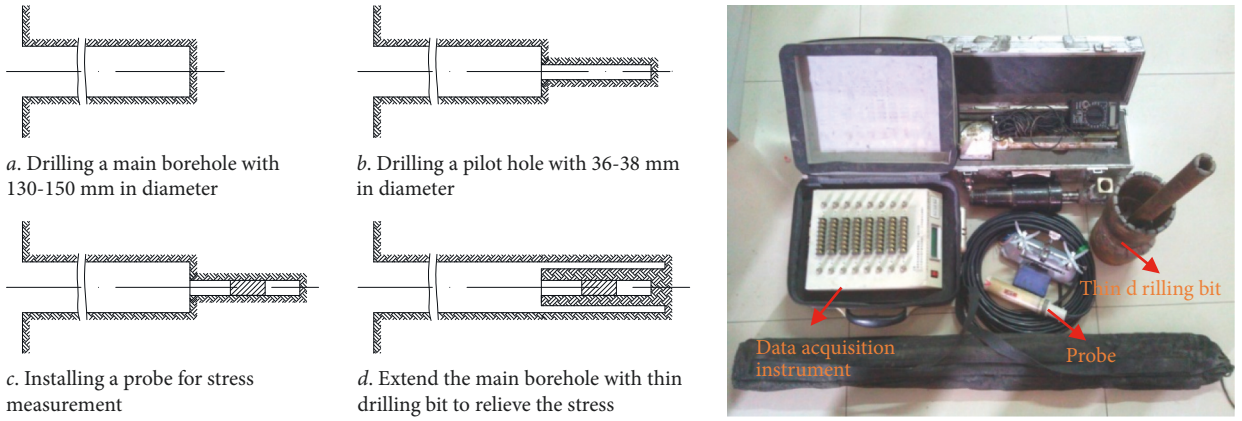

Figure 6: Measuring steps of stress-relief method and the main devices.

Table 1: Measured results of field stress.

Measurement station	Principal stress	Measured results (MPa)	Inclination angle (°)	Azimuth angle (°)
#1	σ_1	33.90	25.3°	183.5°
	σ_2	15.36	64.7°	0.8°
	σ_3	12.73	1.1°	93.0°
	σ_v	18.76		
#2	σ_1	35.82	20.5°	114.3°
	σ_2	20.38	67.5°	320.3°
	σ_3	18.39	9.1°	207.7°
	σ_v	20.99		
#3	σ_1	36.11	11.5°	103.5°
	σ_2	19.13	77.7°	263.4°
	σ_3	18.07	4.1°	12.7°
	σ_v	19.80		

Table 2: Mineral composition contents of rock samples.

Mineral	Rock sample			
	1# fine sandstone (%)	2# mudstone (%)	3# sandy mudstone (%)	4# middle-fine sandstone (%)
Kaolinite	29.5	63.2	43.1	24.7
Quartz	37.6	17.6	25.2	35.2
Illite	7.2	5.6	8.1	6.9
Smectite	2.6	2.4	2.2	2.8
Illite/smectite formation	13.8	7.3	14.7	16.8
Feldspar	1.8	0.4	3.1	2.4
Siderite	4.7		0.3	8.2
Calcite	0.5	0.3	0.3	0.6
Pyrite		0.6	1.1	0.2
Others	Remain	Remain	Remain	Remain

analyze the mineral components of the surrounding rocks. In Table 2, the floor and sandy mudstone are mainly composed of quartz and clay minerals. The kaolinite content reaches 43.1–63.2%, and the total content of illite, montmorillonite, and montmorillonite mixed-layer minerals is about 15.3–25%. In the roadway where the surrounding

rocks of the floor are mudstone and sandy mudstone, the deformation of floor heave occurs with water swelling and becomes more severe under high horizontal stress. It is consistent with the results of field observations.

3.1.3. Low supporting intensity. The surrounding rocks of trackage crosscut are typical soft rocks in deep engineering, but the roadway supports are only supported by U-shaped steels, anchor cables, and bolts. No support measures are taken for the floor, which becomes the outlet for stress release. Therefore, reasonable reinforcement measures need to be taken for the floor.

3.2. Theoretical Calculation of the Ultimate Bearing Capacity and Failure Depth of the Floor. According to the slip-line field theory [40, 41], surrounding-rock stress is redistributed after excavating the underground roadway and the two sides of the roadway form the supporting pressure. If floor rocks are soft, the roadway floor forms a slip-line field under the support pressure of two sides (Figure 7, for the simplified mechanical model).

In Figure 7, areas I, II, and III are called the active stress area, transition area, and passive stress area, respectively; a is the width of the roadway; b the width of the area affected by floor heave; σ_v vertical stress in the area affected by floor heave; $\alpha = \pi/4+\varphi/2$ and $\beta = \pi/4-\varphi/2$; α and β are the angles between the plastic sliding surface and the horizontal plane in areas I and III, respectively, and φ is the internal friction angle of the strata in the floor. It is assumed that the boundaries of the active area and the passive stress area are isosceles triangles to simplify the calculation, and the boundary of the transitioned stress area satisfies the logarithmic-spiral equation. The waist length of the active area is r_0; h is the plastic failure depth at any position of the floor; ω is the included angle between spiral r_0 and r; ξ is the included angle between spiral r and the floor.

It is assumed that the rock masses of the floor are ideal elastic-plastic mediums. When the strata in the floor are unstable and floor heave occurs, the broken rock masses in the floor meet the Hoke–Brown strength criterion [42]:

$$\sigma_1 = \sqrt{m \cdot \sigma_c \cdot \sigma_3 + s \cdot \sigma_c^2} + \sigma_3, \tag{1}$$

where m and s are the parameters related to the rock types and the degrees of crushing of rock masses, respectively, the value range of s is 0~1.0, for intact rocks, $s = 1.0$, σ_c is the uniaxial compressive strength of rocks, and σ_1 and σ_3 are maximum and minimum principal stresses, respectively, when the rock masses are damaged.

Maximum principal stress σ_1^1 in the active stress area is vertical stress transmitted by the coal pillar of the roadway and minimum principal stress is horizontal stress σ_3^1:

$$\sigma_1^1 = \sqrt{m \cdot \sigma_c \cdot \sigma_3^1 + s \cdot \sigma_c^2} + \sigma_3^1. \tag{2}$$

Maximum principal stress σ_1^3 in the passive stress area is the horizontal thrust provided by the active stress area, and

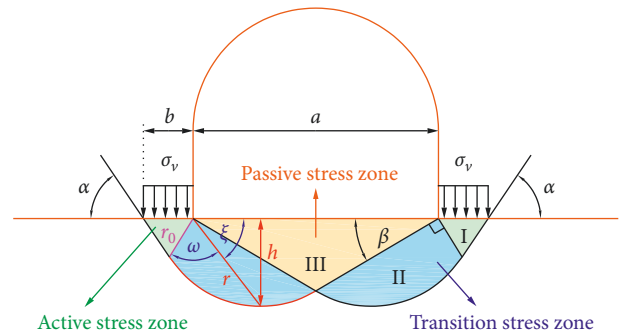

Figure 7: Mechanics model of the floor heave of the roadway.

minimum principal stress σ_3^3 is the free surface stress of the roadway floor, which is equal to 0.

Then,

$$\sigma_1^3 = \sqrt{s} \cdot \sigma_c. \tag{3}$$

When floor heave is about to occur in the roadway, both the active and passive stress areas of the strata on the floor are in the limited equilibrium under vertical stress. At this time, $\sigma_3^1 = \sigma_1^3$. (3) is substituted into (2) to obtain the ultimate load of the rock masses of the floor, denoted as

$$\sigma_1^{\max} = \left(\sqrt{m \cdot \sqrt{s} + s} + \sqrt{s} \right) \sigma_c. \tag{4}$$

When maximum vertical stress σ_v in the area affected by floor heave exceeds the ultimate load of the rock masses in the floor, that is, when $\sigma_v > \sigma_1^{\max}$, the rock masses have floor heave.

The boundary of the transitioned stress area satisfies the logarithmic-spiral equation (26).

Then,

$$r = r_0 \cdot e^{\omega \tan \varphi}. \tag{5}$$

The geometric relationship in Figure 7 shows that failure depth h at any position of the floor is

$$h = r \cdot \sin \xi = r_0 \cdot e^{\omega \tan \varphi} \cdot \sin \xi. \tag{6}$$

From the angle relation in Figure 7,

$$\xi = \frac{\pi}{2} + \beta - \omega = \frac{3\pi}{4} - \frac{\varphi}{2} - \omega. \tag{7}$$

(7) is substituted into (6) to obtain

$$h = r_0 \cdot e^{\omega \tan \varphi} \cdot \sin\left(\frac{3\pi}{4} - \frac{\varphi}{2} - \omega \right). \tag{8}$$

The maximum failure depth $h_{\max}$ of the floor is at $\omega = \pi/4 + \varphi/2$ by taking the derivative of (8) concerning ω:

$$h_{\max} = r_0 \cdot e^{(\pi/4+\varphi/2)\tan \varphi} \cdot \cos \varphi. \tag{9}$$

From the geometric relationship in Figure 7,

$$\cos \alpha = \frac{b}{2r_0}, \quad \cos \beta = \frac{a}{2r}. \tag{10}$$

Since $\alpha = \pi/4 + \varphi/2$ and $\beta = \pi/4 - \varphi/2$, (5), (9), and (10) can be solved simultaneously to obtain

$$h_{\max} = a \cdot e^{(\varphi/2 - \pi/4)\tan\varphi} \cdot \sin\left(\frac{\pi}{4} - \frac{\varphi}{2}\right). \quad (11)$$

The section width of trackage crosscut $a = 5.2$ m; floor frictional angles of the strata in the floor are as follows: $\varphi = 28$, 30, 26, 27, and 23° for mudstone, sandy mudstone, fine sandstone, medium-fine sandstone, and coal, respectively. After substituting into (1), the maximum failure radius of the floor is in the area where the surrounding rocks are coal seams, and $h_{\max} = 2.24$ m.

The height of the heaving area of the floor is measured on-site as $h_0 = 560$ mm, so theoretically, the maximum failure depth of the trackage-crosscut floor is $H = h_{\max} + h_0 = 2.8$ m.

4. Collaborative Control Technology of Crosscut Floor Heave

The above analysis shows that trackage crosscut floor heave belongs to the water swelling-shear dislocation. Control technology of floor heave enhancing the full-section surrounding rock bearing structure is proposed according to its mechanism [18, 32, 33].

4.1. Filling behind U-Shaped Steel Supports. It is inevitable that there are holes in the section formed during entry excavation, which makes the U-steel support and the surrounding rock present random point and line contact, causing the U-steel support to suffer from concentrated load or eccentric load, which reduces the bearing performance of the support. The function of filling behind U-shaped steel supports is that the hole space of the surrounding rock behind the U-steel support is filled with grout to improve the interaction between the surrounding rock and U-shaped steel supports and reduce other inelastic deformations required to achieve the rated resistance of the U-shaped steel supports, conducive to early supporting of U-steels. On the contrary, the injection of grout into the shallow fissures of the surrounding rock can increase the residual strength of the surrounding rock and can effectively prevent the weathering and deliquesce of the argillaceous soft rock.

A pre-embedded T-tube is used for filling (Figure 8). A T-shaped grouting pipe is made of a steel pipe with a wall thickness of 3.25 mm and a diameter of 15 mm, and the grouting section of the T-shaped pipe is buried behind the steel arches. Then, spray 50–80 mm concrete mortars on the roadway surface as a slurry stopper to prevent the outflow of the slurries after filling. Meanwhile, it isolates air and moisture to prevent the corrosion of supporting components such as U-shaped sheds and the water swelling of surrounding rocks rich in clay minerals.

4.2. Shallow Grouting in All-Sided Surrounding Rocks and Deep Grouting in the Floor. Sun et al. proposed a continuous double-shell support of shallow grouting (shallow supporting shell) and deep grouting of anchor cable bundles (deep reinforcing shell) in the floor for the roadways under high horizontal stress [34]. However, the uniformity of the surrounding rock bearing of the roadway is ignored without grouting in all-sided surrounding rocks, which cannot form an effective bearing shell. On this basis, the work proposed the supporting technology of shallow grouting in all-sided surrounding rocks and deep-hole grouting in the floor (Figure 9).

Shallow grouting cements the loose and broken all-sided surrounding rocks into a whole, forming an effective bearing shell, which can resist the deformation and failure of the shallow surrounding rocks in all directions. The deep grouting of the floor has the following advantages, e.g., improving the bearing range of the surrounding rocks, blocking the transfer of deep surrounding rocks' stress to the roadway floor, and protecting the shallow bearing shell.

4.3. Inverted Arch. The inverted arch (Figure 10) can increase the bending resistance of the floor, buffer the long-term damage to the floor caused by high stress, and avoid the plastic flow of the two sides of broken rock masses to the floor [35]. The modifying effect of shallow grouting in all-sided surrounding rocks and deep grouting in the floor on the broken surrounding rocks can control the continuous flow of crosscut floor heave.

5. Engineering Practice and Effect

5.1. Support Scheme of Trackage Crosscut in the Floor. The support scheme for repairing trackage crosscut was designed (Figure 11) according to the maximum failure depth of floor heave calculated in Section 3 and the collaborative control technology in Section 4.

(1) U-shaped steel supports: the 36# U-shaped steel yielding supports were used, and the lap length of each section was 500 mm, with the pre-tightening torque of the clamps not less than 350 N*m*. The distance between the U-shaped steels was 700 mm, and support rods were installed between each row of U-shaped steels. Then, the T-shaped grouting pipes were pre-buried behind the wall for filling.

(2) Bolts: M24-Φ22-2400 mm left-handed high-strength threaded steel bolts without longitudinal bar and grouting bolts were used crosswise. A CK2335 (diameter: 23 mm, length: 35 mm, and gel time: 8~40 s) and a K2360 (diameter: 23 mm, length: 60 mm, and gel time: 41~90 s) anchoring agent were used for each bolt, and the preload was not less than 70 kN.

(3) Anchor cables: Φ21.6 × 6,300 mm anchor cables with the strength of 1864 MPa and grouting anchor cables were used crosswise. A CK2335, a K2360, and a Z2360 (diameter: 23 mm, length: 35 mm, and gel time: 91~180 s) anchoring agent were used for the anchor cable. The design preload was not less than 150 kN.

(4) Inverted arch (Figure 10 for the specific parameters).

(a) (b)

Figure 8: Filling behind the frame with the T-shaped grouting tube. (a) Pre-embedded T-tube. (b) The effect after spraying.

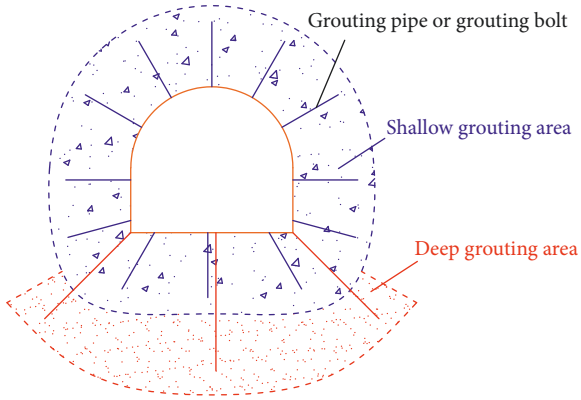

Figure 9: Shallow grouting in all-sided surrounding rocks and deep grouting in the floor.

(5) Spraying layer of concretes: the roof and two sides of C20 concrete layers with a spraying thickness of 150 mm were used to close the surrounding rocks, and the initial spraying thickness was not less than 70 mm. After the bolts and anchor cables were installed, the secondary injection was performed.

(6) Filling: after the roof and the two sides were sprayed with concretes, they could be filled behind the U-shaped steel frames.

(7) Shallow grouting in all-sided surrounding rocks and deep grouting in the floor: after the above procedures were completed, grouting was performed using grouting bolts and grouting anchor cables. The slurries were cement-water glass, and 28.66 L water glass was added to 1 m^3 cement slurry, with the grouting pressure of 3–5 MPa.

5.2. Control Effect of Floor Heave of Trackage Crosscut. After the trackage crosscut was repaired according to the new support scheme, the floor heave mass was monitored at three monitoring stations with different lithologies (Figure 12). There were four monitoring points (A, B, C, and D)

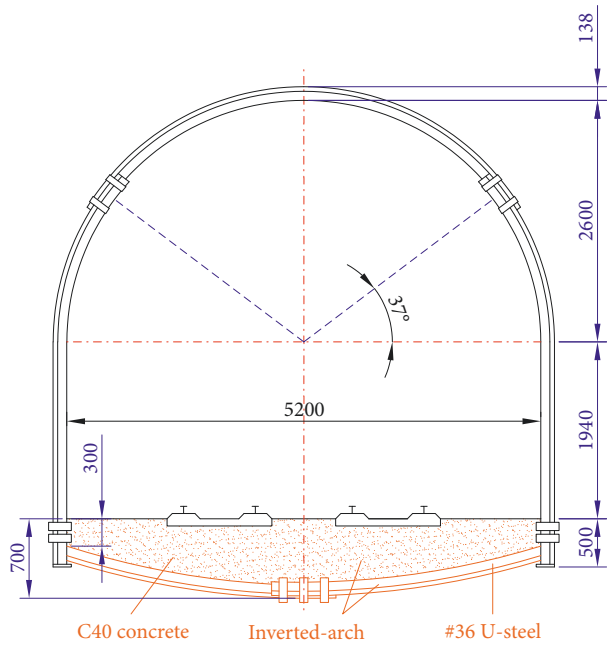

Figure 10: Inverted arch composed of U-shaped steel and concretes.

at each monitoring station, and each monitoring point was a bolt of length of 800 mm, which was fully grouted in the rock mass to avoid movement during the observation period (Figure 13). To determine the convergence, the distance AB, CD, and AD (or BD) was measured with a tape measure or a laser range finder. The floor heave mass variation with time was obtained (Figure 14).

(1) During the monitoring time of 70 days, the cumulative floor heave masses of trackage crosscut of the three stations are 40.2, 45.3, and 35.1 mm, respectively, and the maximum value occurs in the area where the surrounding rocks are coal. During monitoring, the maximum floor heave speeds of the three stations are 4.2, 4.7, and 3.7 mm/d, respectively.

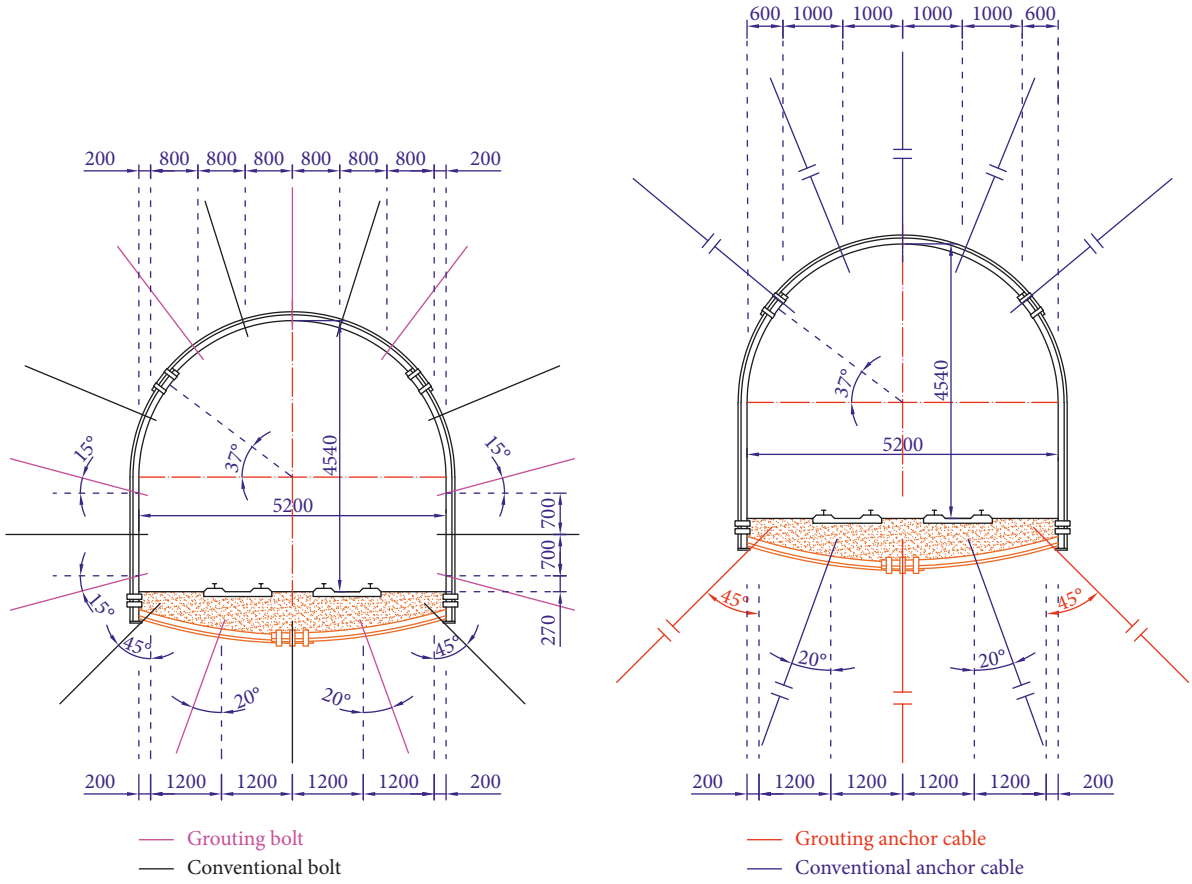

(a)

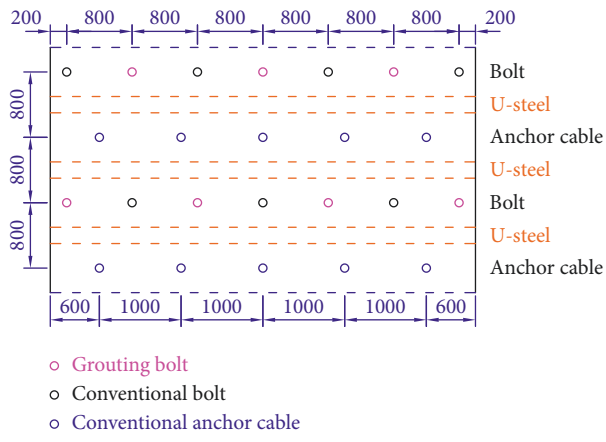

(b)

Figure 11: Continued.

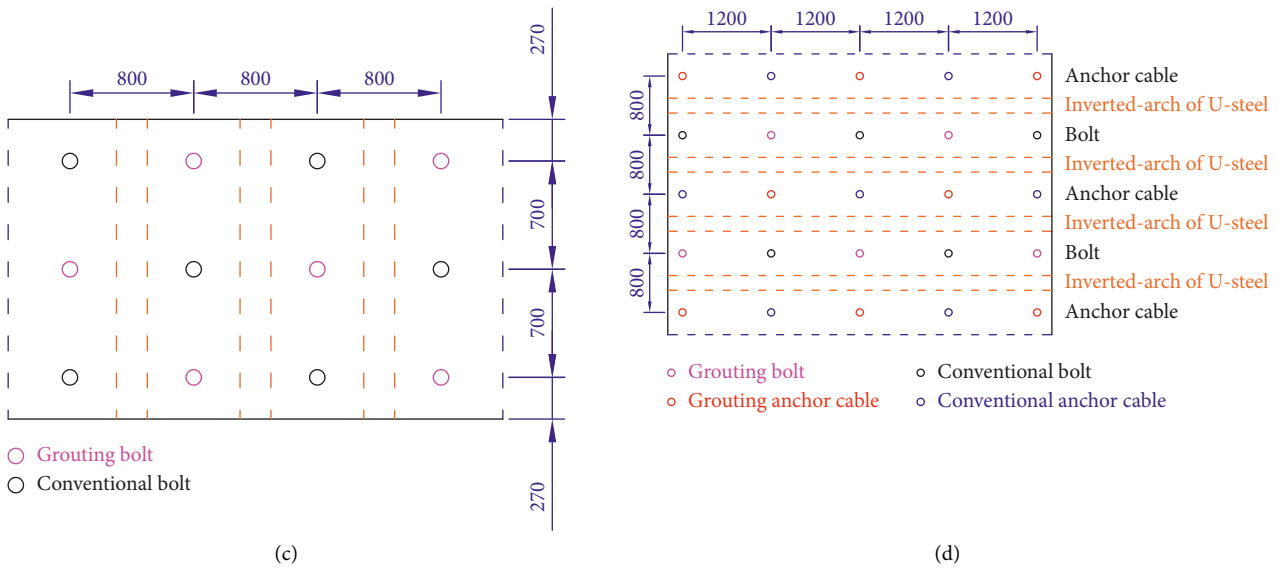

Figure 11: Support scheme of trackage crosscut. (a) Section view of the bolt and anchor cable layouts. (b) Bottom view of the bolt and anchor cable layouts in the roof. (c) Side view of the bolt layout in rib. (d) Top view of the bolt and anchor cable layouts in the floor.

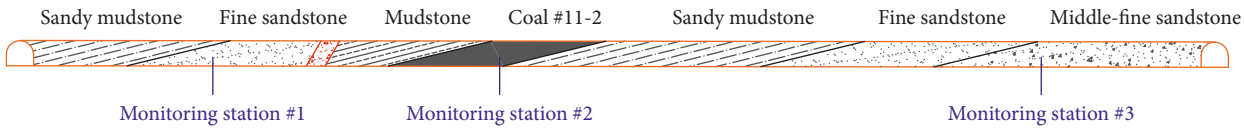

Figure 12: Location of the monitoring station.

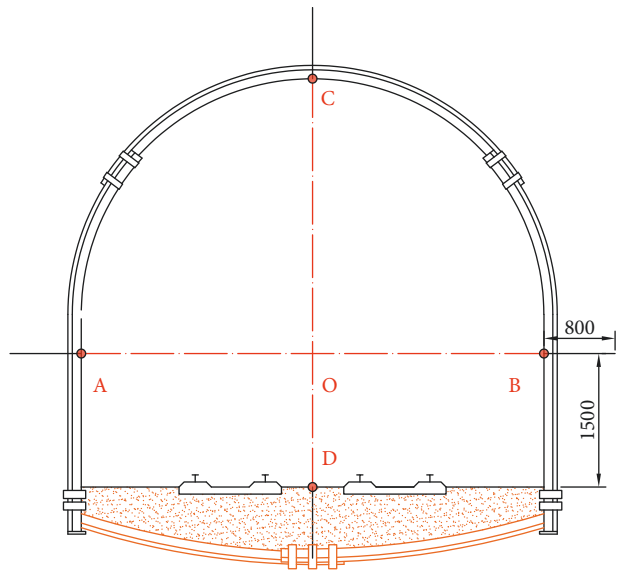

Figure 13: Monitoring station.

The maximum speed also occurs in the areas where the surrounding rocks are coal.

(2) Floor heave changes greatly only within a week after the restoration. After 40 d, the floor heave remained below 1 mm/d. After 60 d, the floor heave speed was close to 0, and the floor heave mass remain unchanged, indicating that the trackage crosscut had become stable at this time.

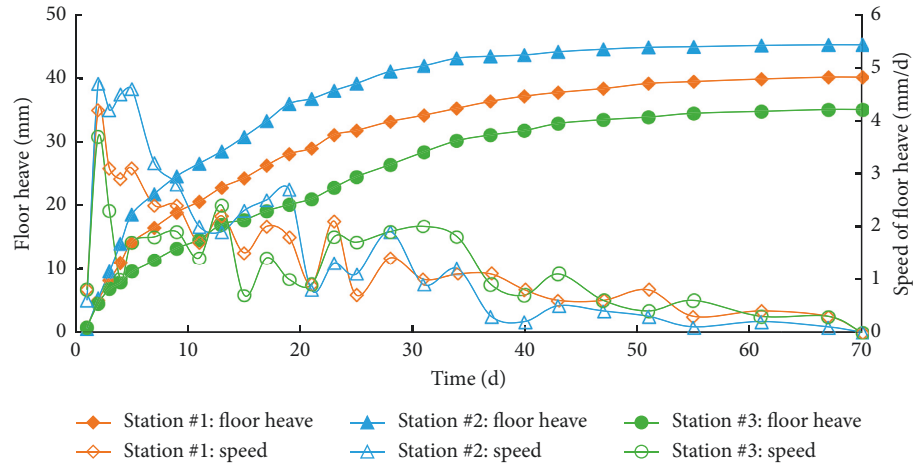

Figure 14: Floor heave curves with time.

After adopting the new support scheme, the maximum floor heave mass is only 8.1% of the maximum mass before restoration. It shows that the control technology enhancing the all-sided surrounding rock bearing structure has a good control effect on crosscut floor heave.

6. Summary and Conclusions

Based on the trackage crosscut at the shaft station of Panyidong Coal Mine, the work studied the control technology of crosscut floor heave under deep high horizontal stress.

(1) Crosscut passed through multiple strata, and the occurrence conditions of surrounding rocks were complicated. Its deformation has complex characteristics such as globality, difference, and rheology under deep high horizontal stress.

(2) Crosscut floor heave showed water swelling in the mudstone and sandy mudstone areas where the mineral components were kaolinite and montmorillonite mixed layers. It presented shear dislocation under high horizontal stress in the areas of fine and medium-fine sandstone.

(3) Based on the slip-line field theory, the ultimate load of crosscut floor heave in the floor strata is $\sigma_1^{\max} = (\sqrt{m \cdot \sqrt{s} + s} + \sqrt{s})\sigma_c$. The maximum failure depth of floor heave without supports is $h_{\max} = a \cdot e^{(\varphi/2 - \pi/4)\tan\varphi} \cdot \sin(\pi/4 - \varphi/2)$. According to the calculation, the maximum failure depth of the unsupported crosscut floor in theory is 2.8 m.

(4) Given the deformation characteristics and mechanism of crosscut floor heave, a collaborative control technology enhancing the all-sided surrounding rock bearing structure was proposed, including the filling of U-shaped steel supports, shallow grouting in all-sided surrounding rocks, and deep grouting in the floor and inverted arches.

(5) According to the trackage crosscut at the shaft station of Panyidong Coal Mine, a support scheme for repairing the floor was designed, and the crosscut floor heave was continuously monitored for 70 d. The results showed the following. (1) After repairing, the maximum cumulative floor heave mass was 45.3 mm, which was only 8.1% of that before repairing. (2) Floor heave changed greatly within one week after repairing, and the maximum floor heave speed was 4.7 mm/d. The floor heave speed was maintained below 1 mm/d after 40 d, and the floor heave mass was stable after 60 d.

Data Availability

All data included in this study can be obtained from the corresponding author upon request.

Conflicts of Interest

The authors declare that there are no conflicts of interest regarding the publication of this paper.

Acknowledgments

This work was supported by the National Natural Science Foundation of China (51778215 and 52174072), the Education Department of Guizhou Province Fund (Qianjiaohe KY Zi [2017] 265, Qianjiaohe KY Zi [2019] 073, Qianjiaohe KY Zi [2020] 050, Qianjiao XKTJ [2020] 23), the Science and Technology Department of Guizhou Province Fund (Qiankehe Platform Talent-YSZ [2021] 001), the Natural Science Foundation of Shandong Province (ZR2021QE170), and the Liupanshui Science and Technology Bureau fund (52020-2018-04–08).

References

[1] X. L. Li, S. J. Chen, Q. M. Zhang, X. Gao, and F. Feng, "Research on theory, simulation and measurement of stress behavior under regenerated roof condition," *Geomechanics and Engineering*, vol. 26, no. 1, pp. 49–61, 2021.

[2] H. Y. Liu, B. Y. Zhang, X. L. Li et al., "Research on roof damage mechanism and control technology of gob-side entry

retaining under close distance gob," *Engineering Failure Analysis*, vol. 138, Article ID 106331, 2022.

[3] H. P. Xie, "Research review of the state key research development program of China: deep rock mechanics and mining theory," *Journal of China Coal Society*, vol. 44, no. 5, pp. 1283–1305, 2019.

[4] X. J. Feng, Z. Ding, Q. J. Hu, X. Zhao, M. Ali, and J. T. Banquando, "Orthogonal numerical analysis of deformation and failure characteristics of deep roadway in coal mines: a case study," *Minerals*, vol. 12, no. 2, p. 185, 2022.

[5] L. Yuan, "Research progress of mining response and disaster prevention and control in deep coal mines," *Journal of China Coal Society*, vol. 46, no. 3, pp. 716–725, 2021.

[6] X. J. Chen, L. Y. Li, L. Wang, and L. L. Qi, "The current situation and prevention and control countermeasures for typical dynamic disasters in kilometer-deep mines in China," *Safety Science*, vol. 115, pp. 229–236, 2019.

[7] P. Wang, N. Zhang, J. G. Kan, B. Wang, and X. L. Xu, "Stabilization of rock roadway under obliquely straddle working face," *Energies*, vol. 14, no. 18, p. 5759, 2021.

[8] P. Gong, Z. G. Ma, X. Y. Ni, and R. R. Zhang, "Floor heave mechanism of gob-side entry retaining with fully-mechanized backfilling mining," *Energies*, vol. 10, no. 12, p. 2085, 2017.

[9] X. P. Lai, H. C. Xu, P. F. Shan, Y. L. Kang, Z. Y. Wang, and X. Wu, "Research on mechanism and control of floor heave of mining-influenced roadway in top coal caving working face," *Energies*, vol. 13, no. 2, p. 381, 2020.

[10] H. S. Jia, L. Y. Wang, K. Fan, B. Peng, and K. Pan, "Control technology of soft rock floor in mining roadway with coal pillar protection: a case study," *Energies*, vol. 12, no. 15, p. 3009, 2019.

[11] Q. Yin, R. C. Liu, H. W. Jing, H. J. Su, L. Y. Yu, and L. X. He, "Experimental study of nonlinear flow behaviors through fractured rock samples after high-temperature exposure," *Rock Mechanics and Rock Engineering*, vol. 52, no. 9, pp. 2963–2983, 2019.

[12] Q. Yin, J. Y. Wu, C. Zhu, M. C. He, Q. X. Meng, and H. W. Jing, "Shear mechanical responses of sandstone exposed to high temperature under constant normal stiffness boundary conditions," *Geomechanics and Geophysics for Geo-Energy and Geo-Resources*, vol. 7, no. 2, p. 35, 2021.

[13] G. Feng, X. C. Wang, M. Wang, and Y. Kang, "Experimental investigation of thermal cycling effect on fracture characteristics of granite in a geothermal-energy reservoir," *Engineering Fracture Mechanics*, vol. 235, Article ID 107180, 2020.

[14] Z. Chun, L. Yun, and F. Gan, "Influence of temperature on quantification of mesocracks: implications for physical properties of fine-grained granite," *Lithosphere*, vol. 2021, Article ID 7824057, 2021.

[15] S. Mo, H. L. Ramandi, J. Oh et al., "A new coal mine floor rating system and its application to assess the potential of floor heave," *International Journal of Rock Mechanics and Mining Sciences*, vol. 128, Article ID 104241, 2020.

[16] X. J. Feng, Z. Ding, Y. Q. Ju, Q. M. Zhang, and M. Ali, "Double peak' of dynamic strengths and acoustic emission responses of coal masses under dynamic loading," *Natural Resources Research*, vol. 31, no. 3, pp. 1705–1720, 2022.

[17] M. Wang, D. J. Zheng, K. W. Wang, and W. F. Li, "Strain energy analysis of floor heave in longwall gateroads," *Royal Society Open Science*, vol. 5, no. 8, Article ID 180691, 2018.

[18] J. G. Kan, G. C. Li, N. Zhang, P. Wang, C. L. Han, and S. Wang, "Changing characteristics of sandstone pore size under cyclic loading," *Geofluids*, vol. 2021, Article ID 6664925, 1–2 pages, 2021.

[19] Z. Q. Ma, Y. D. Jiang, Y. Liu, W. S. Du, and D. Z. Kong, "Investigation on support pattern of a coal mine roadway under dynamic pressure of mining - a case study," *International Journal of Oil, Gas and Coal Technology*, vol. 18, no. 3/4, pp. 402–422, 2018.

[20] P. Malkowski, L. Ostrowski, and L. Bednarek, "The effect of selected factors on floor upheaval in roadways—in situ testing," *Energies*, vol. 13, no. 21, p. 5686, 2020.

[21] P. Malkowski, L. Ostrowski, and J. Stasica, "Modeling of floor heave in underground roadways in dry and waterlogged conditions," *Energies*, vol. 15, no. 12, p. 4340, 2022.

[22] X. M. Sun, P. Y. Miao, F. X. Shen, W. C. Zhao, and M. H. Yang, "Study on floor heave mechanism of horizontal layered soft rock roadway in deep well under different stress states," *Journal of Mining and Safety Engineering*, vol. 35, no. 6, pp. 1099–1106, 2018.

[23] S. Mo, K. Tutuk, and S. Saydam, "Management of floor heave at Bulga Underground Operations-A case study," *International Journal of Mining Science and Technology*, vol. 29, no. 1, pp. 73–78, 2019.

[24] G. Y. Wang and L. Jin, "Study on dynamic responses of roadway controlled by borehole pressure relief and prestressed grouting anchor cable on the floor under dynamic load," *Chinese Journal of Applied Mechanics*, vol. 34, no. 5, pp. 881–886, 2017.

[25] X. Q. Wang, J. G. Kan, and J. K. Jiao, "Mechanism of floor heave in the roadway with high stress and soft rock and its control practice," *Journal of Mining & Safety Engineering*, vol. 34, no. 2, pp. 214–220, 2017.

[26] Z. Y. Zhang and H. Shimada, "Numerical study on the effectiveness of grouting reinforcement on the large heaving floor of the deep retained goaf-side gateroad: a case study in China," *Energies*, vol. 11, no. 4, p. 1001, 2018.

[27] J. Wang, C. C. Hu, and J. P. Zuo, "Mechanism of roadway floor heave and control technology in fault fracture zone," *Journal of China Coal Society*, vol. 44, no. 2, pp. 397–408, 2019.

[28] D. Zhang, J. B. Bai, S. Yan, R. Wang, N. K. Meng, and G. Y. Wang, "Failure mechanism of surrounding rock and control of floor heave in heterogeneous composite rock roadway," *Chinese Journal of Geotechnical Engineering*, vol. 44, no. 9, pp. 1699–1709, 2022.

[29] K. Wang, Y. L. Huang, H. D. Gao et al., "Recovery technology of bottom coal in the gob-side entry of thick coal seam based on floor heave induced by narrow coal pillar," *Energies*, vol. 13, no. 13, p. 3368, 2020.

[30] C. L. Wang, G. Y. Li, A. S. Gao, F. Shi, Z. J. Lu, and H. Lu, "Optimal pre-conditioning and support designs of floor heave in deep roadways," *Geomechanics and Engineering*, vol. 14, no. 5, pp. 429–437, 2018.

[31] J. P. Zuo, Y. J. Sun, and K. Li, "Study of the reinforced supporting length and floor heave control technology of soft rock roadway influenced by collapse column," *Journal of China University of Mining & Technology*, vol. 46, no. 1, pp. 18–26, 2017.

[32] X. Z. Hua and Y. F. Li, "Mechanics analysis on floor deformation of gob-side entry retaining and prevention and control of floor heave," *Journal of China Coal Society*, vol. 41, no. 7, pp. 1624–1631, 2016.

[33] Z. S. Wang, J. Z. Li, J. Lin, L. Yang, and X. Z. Meng, "Mechanism and control technology of floor heave in deep high-stress water-rich clay soft rock roadway," *Coal Science and Technology*, vol. 49, no. 7, pp. 71–78, 2021.

[34] L. H. Sun, B. S. Yang, C. D. Sun, X. Li, and Z. W. Wang, "Experimental research on mechanism and controlling of

floor heave in deep soft rock roadway," *Journal of Mining & Safety Engineering*, vol. 34, no. 2, pp. 235–242, 2017.

[35] X. Z. Hua, M. Yang, Q. J. Liu, and P. Yang, "Model test on evolution mechanism of floor heave in gob-side retaining entry of deep mine," *Journal of Mining & Safety Engineering*, vol. 35, no. 1, pp. 1–9, 2018.

[36] L. H. Sun, B. S. Yang, W. B. Yang, and C. D. Sun, "Reinforcement mechanism and experimental study on continuous double shell of deep roadway," *Journal of Mining & Safety Engineering*, vol. 30, no. 5, pp. 687–691, 2013.

[37] Y. D. Jiang, Y. X. Zhao, W. G. Liu, and Q. Li, "Research on floor heave of roadway in deep mining," *Chinese Journal of Rock Mechanics and Engineering*, vol. 23, no. 14, pp. 2396–2401, 2004.

[38] C. Wang, Y. P. Wu, and X. P. Huang, "Mechanism of floor failure of roadway supported by inverted arch under complicated surrounding rocks and its control," *Journal of Mining & Safety Engineering*, vol. 36, no. 5, pp. 959–976, 2019.

[39] Y. Shuaifeng, M. Haifeng, C. Zhiheng et al., "Permeability enhancement mechanism of sand-carrying hydraulic fracturing in deep mining: a case study of uncovering coal in cross-cut," *Energy Science & Engineering*, vol. 7, no. 5, pp. 1867–1881, 2019.

[40] Z. Z. Zhang, M. Deng, X. Y. Wang, W. J. Yu, F. Zhang, and V. D. Dao, "Field and numerical investigations on the lower coal seam entry failure analysis under the remnant pillar," *Engineering Failure Analysis*, vol. 115, Article ID 104638, 2020.

[41] H. Cheng, H. B. Zhao, J. F. Xu, F. Y. Qin, Y. X. Zhang, and L. F. Hu, "Study on floor heave mechanism and control technology of roadway based on slip line field theory," *Journal of Mining Science and Technology*, vol. 6, no. 3, pp. 314–323, 2021.

[42] H. H. Zhu, Q. Zhang, and L. Y. Zhang, "Review of research progresses and applications of hoek-Brown strength criterion," *Chinese Journal of Rock Mechanics and Engineering*, vol. 32, no. 10, pp. 1945–1963, 2013.

Hindawi
Mathematical Problems in Engineering
Volume 2022, Article ID 1998227, 11 pages
https://doi.org/10.1155/2022/1998227

Research Article

Study on the Influence of Cracks on the Mechanical Performance of Tunnel Lining Structure Based on Fracture Mechanics Theory

Taotao Hu,[1,2] **Xiong Hu**,[1] **Jianxun Chen**,[1] **Chuanwu Wang**,[1] **and Yi Yang**[3]

[1]*School of Highway, Chang'an University, Xi'an 710064, China*
[2]*State Key Laboratory for Strength and Vibration of Mechanical Structures, School of Aerospace Engineering, Xi'an Jiaotong University, Xi'an 710049, China*
[3]*Alxa League Transportation Engineering Quality and Rural Highway Service Center, Alxa League 750306, China*

Correspondence should be addressed to Taotao Hu; tthu@chd.edu.cn and Chuanwu Wang; wangcw17@163.com

Received 9 March 2022; Accepted 9 April 2022; Published 9 May 2022

Academic Editor: Fuqiang Ren

The problem of tunnel lining cracking is becoming more and more common. The existence of cracks changes the stress state of lining structure and has an adverse impact on the safety of lining structure. In this paper, the mechanical properties of tunnel cracked lining structure are studied. Based on the theories of structural mechanics and fracture mechanics, the performance indexes of cracks in the arch waist of tunnel secondary lining are studied with the reference of stress intensity factor. The numerical simulation calculation is carried out. Finally, the XFEM extended finite element method is used, the crack damage of secondary lining under different crack depths is demonstrated and analyzed, and the theoretical value is compared with the numerical value. The results show that, for the cracked model (the crack depth is 12 cm), the stress and displacement at the arch waist increase greatly compared with the uncracked model and are the most significant with the increase of crack depth. In the initial stage of crack development, the growth of stress and displacement of the structure is not obvious, and the small change of crack depth in the later stage can also cause great growth of stress and displacement. Compared with the uncracked model, when the crack depth is 3 cm, the maximum vertical stress increases by 4.3 times and the maximum settlement increases by 1.3 times. When the crack depth is 18 cm, it increases by 21.2 times and 2.94 times, respectively. The research results can provide a theoretical basis for the prevention and treatment of cracks in the arch waist of tunnel secondary lining during tunnel operation.

1. Introduction

The number and scale of tunnels around the world are increasing, but various diseases and problems during tunnel operation also follow, among which the most common problem is the cracking of tunnel secondary lining. It is very important to study tunnel lining cracks. Fracture mechanics is a powerful tool to study cracks. It mainly studies the failure of materials and structures with defects. This paper will study the application of fracture mechanics theory in tunnel lining cracks.

Many scholars [1–5] published various views about the theory of fracture mechanics previously. Based on the development of fracture mechanics theory, some scholars [6–10] obtained the relevant physical and mechanical parameters of rock mass through experimental research, which provided a theoretical basis for the external force factors affecting the stress state of tunnel lining, and more and more scholars [11–15] pay attention to the influence of cracks on the safety of tunnel lining structure through model experiments and gradually improve the research system of the influence of cracks on materials and structures. Huang et al. [16] used extended finite element method to study the distribution law, propagation process, appearance, and occurrence mechanism of cracks in lining under the action of main influencing factors, providing a reference for the analysis of causes of cracks in lining. Li et al. [17] used the elastoplastic damage constitutive model of concrete to study the stress, damage, and bearing capacity of tunnel lining structure through simulation calculation and found that the

crack of the vault is mainly caused by the tension of the lining structure. Wang et al. [18] calculated the stress intensity factor of lining crack tip based on fracture mechanics theory and established a theoretical analysis method for crack stability of plain concrete lining of highway tunnel. Yu [19] discussed the influence of cracks on the safety of lining structures and found that when the structure was fractured in one part and could no longer bear the bending moment, its overall stress distribution would change, and larger bending moments would be generated in other parts, thus inducing new cracking. Yuan [20] adopted the research means of combining model test and numerical simulation, revealing that the existence of cracks would have an impact on the load, lining stress, and crack depth imposed on each part of the lining when cracking.

At the same time, many scholars pay attention to the influence of crack depth on the safety of tunnel lining structure. Xu [21] applied the theory of fracture mechanics to analyze the fracture behavior when longitudinal cracks were located in the tunnel vault and obtained the influence law of crack depth on the stress intensity factor. Liu et al. [22] analyzed the influence of crack location, crack depth, and formation resistance on the bearing capacity of lining structure and found that the safety factor of tunnel vault decreases linearly with the increase of crack depth, and under the condition of the same crack depth, the crack is the most unfavorable in the vault and has little impact on the structural safety factor in the arch waist, side wall, and arch foot. Zhang [23] applied finite element numerical analysis and found that crack depth had a significant impact on the safety of tunnel lining structure. Liu et al. [24] used finite element software to conduct numerical simulation analysis on the stress performance of tunnel lining cracks and found that the greater the crack depth, the greater the displacement and stress of tunnel structure, and the more obvious the stress concentration at the crack tip. Zheng [25] proposed that the crack depth should be used as a reference index for the classification of lining cracking diseases. Wang et al. [26] analyzed the impact of cracks of different lengths and depths on the safety of lining structure and found that the damage degree of arch crack to lining structure is much greater than that of arch waist crack, and crack depth has a more significant impact on the safety of lining structure than crack length. Through numerical simulation software, Liu and Han [27] found that when the lining vault cracks, the crack depth is positively correlated with the stress intensity at the crack tip and negatively correlated with the stability coefficient. Based on fracture mechanics and concrete fracture mechanics theory, Huang [28] obtained the variation rule of stress intensity factor and stability factor at various positions with crack depth and Angle. Yang et al. [29] studied the effects of crack location, crack depth, and crack width on the stress of lining structure. The results show that, with the change of crack depth and width, the position of the most dangerous section of tunnel lining also changes. Xiao et al. [30] used finite element software to establish finite element models of tunnel lining with different crack depths and fracture positions and found that the arch crack is the most harmful to the structure, and the crack depth has a significant impact on the bearing performance of the structure. Zhao et al. [31] calculated the stress intensity factor at the crack tip, indicating that the proportion and influence of longitudinal cracks in lining diseases are the largest, and the stability of lining cracks is closely related to crack location, crack type, and crack angle.

A large number of studies show that the factor of tunnel lining crack depth has a greater impact on structural safety, but there is a lack of clear research on lining crack with crack depth as a parameter. Therefore, based on the theory of linear elastic fracture mechanics, this paper establishes the calculation model of tunnel cracked lining structure with different crack positions and depths, compares it with the noncrack model, arranges and analyzes the calculation results, summarizes the relationship between crack depth and structural safety, and then establishes a research and analysis of tunnel lining cracking with crack depth as variable.

2. Study on Fracture Mechanics Theory of Tunnel Lining Structure

2.1. Numerical Simulation Model of Concrete Cracks. The fracture mechanics model mainly studies the crack propagation and instability of existing structures and considers the effect of crack tip stress concentration on crack propagation. This model can simulate the width, length, and depth of cracks, but only a single crack can be considered. This paper mainly studies the crack propagation of cracked lining structure and the residual bearing capacity after cracking. Therefore, the fracture mechanics model is used to deal with the cracks of the secondary lining structure in this numerical simulation analysis.

There are many types of cracks with combined characteristics in the actual tunnel structure, among which type I-II composite crack is the most common and dangerous crack form. The tunnel problem is simplified as a plane strain problem. It is assumed that the main cracking modes of the tunnel lining cracks are type I cracks and type I-II composite cracks. Therefore, this paper mainly studies the fracture mechanics theory of single open fracture (type I) [32].

2.2. Overview of the Tunnel Lining Structure. The authenticity of the numerical analysis results of tunnel secondary lining depends on whether the corresponding numerical model is reasonable or not. In order to better compare and analyze with the test data, this modeling only considers the secondary lining structure and studies the stress-strain at the crack tip and the bearing capacity of the structure. The thickness of the secondary lining of a tunnel is 40 cm, and an inverted arch is set. The section of the lining structure is shown in Figure 1.

2.3. Structural Mechanics Calculation of the Tunnel Lining Structure. In the tunnel structure, the longitudinal cracks have serious harm to the structure, and the arch waist of the lining structure is stressed greatly and there are many cracks. Therefore, this paper studies and analyzes the arch waist of the secondary lining. The tunnel adopts curved wall lining

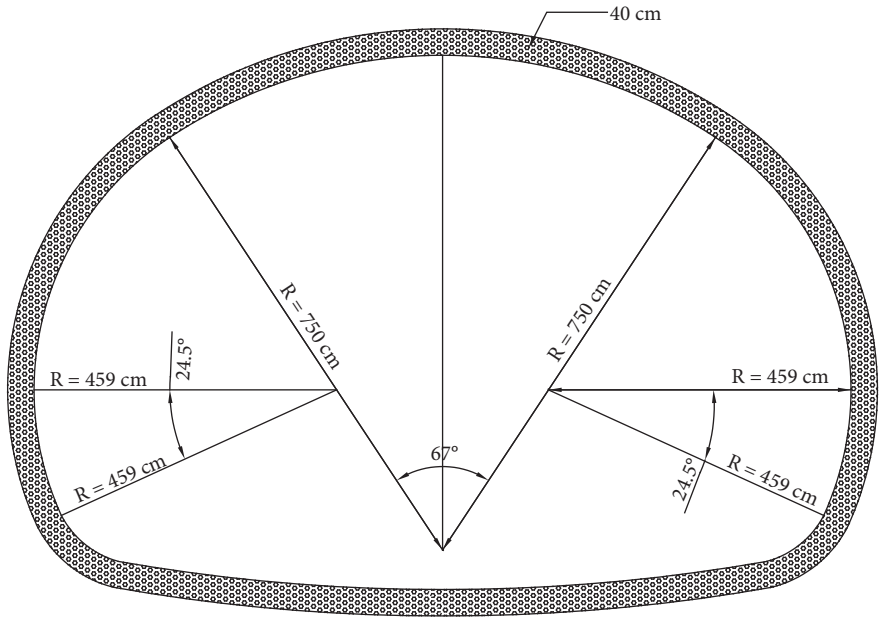

Figure 1: Section of secondary lining.

form, which is composed of arch ring, curved side wall, and bottom plate. When there is upward bottom pressure, inverted arch is set. The arch ring and curved side wall are calculated as a whole without hinged arch, and the influence of inverted arch on lining internal force is generally not considered [33].

2.3.1. Force Method Equation and Lining Internal Force under Active Load. The basic structure is shown in Figure 2. The unknown forces are X_{1p} and X_{2p}. According to the condition that the relative displacement of the arch waist section is zero, the force method equation can be listed:

$$\begin{aligned} X_{1P}\delta_{21} + X_{2P}\delta_{22} + \Delta_{2p} + f\beta_{ap} + u_{ap} = 0, \\ X_{1P}\delta_{11} + X_{2P}\delta_{12} + \Delta_{1p} + \beta_{ap} = 0, \end{aligned} \tag{1}$$

where β_{ap} and u_{ap} are the displacement of wall bottom. Calculate the effects of X1p, X2p, and external load, respectively, and then add them according to the superposition principle to obtain

$$\beta_{ap} = X_{1P}\overline{\beta}_1 + X_{2P}\left(\overline{\beta}_2 + f\overline{\beta}_1\right) + \beta_{ap}^0. \tag{2}$$

Since the horizontal displacement is not considered at the wall bottom, $u_{ap} = 0$, substitute (1) to obtain

$$\begin{aligned} X_{1P}\left(\delta_{21} + f\overline{\beta}_1\right) + X_{2P}\left(\delta_{22} + f^2\overline{\beta}_1\right) + \Delta_{2P} + f\beta_{ap}^0 = 0, \\ X_{1P}\left(\delta_{11} + \overline{\beta}_1\right) + X_{2P}\left(\delta_{12} + \overline{\beta}_2 + f\overline{\beta}_1\right) + \Delta_{1P} + \beta_{ap}^0 = 0, \end{aligned} \tag{3}$$

where δ_{ik} and Δ_{ip} are the element displacement and active load displacement of the basic structure; $\overline{\beta}_1$ is the unit rotation angle of the wall bottom (°); β_{ap}^0 is the load rotation angle of the wall bottom of the basic structure (°); f is the lining rise (m).

After calculating X1p and X2p, under the action of active load, the internal force of lining is

$$\begin{aligned} N_{ip} &= X_{2p} + X_{2p}\cos\varphi_i + N_{ip}^0, \\ M_{ip} &= X_{1p} + X_{2p}y_i + M_{ip}^0. \end{aligned} \tag{4}$$

2.3.2. Calculation of Final Internal Force of Lining. When the $\sigma_h = 1$ elastic resistance diagram is regarded as the external load acting alone, the excess force $X_{1\sigma}, X_{2\sigma}$ can be obtained by referring to the calculation method of X1p and X2p, and the output method equation is listed:

$$\begin{aligned} X_{1\sigma}\left(\delta_{21} + f\overline{\beta}_1\right) + X_{2\sigma}\left(\delta_{22} + f^2\overline{\beta}_1\right) + \Delta_{2\sigma} + f\beta_{a\sigma}^0 = 0, \\ X_{1\sigma}\left(\delta_{11} + \overline{\beta}_1\right) + X_{2\sigma}\left(\delta_{12} + f\overline{\beta}_1\right) + \Delta_{1\sigma} + \beta_{a\sigma}^0 = 0, \end{aligned} \tag{5}$$

where $\Delta_{1\sigma}, \Delta_{2\sigma}$ is the displacement of the basic structure in $X_{1\sigma}, X_{2\sigma}$ direction caused by the load in the unit elastic resistance diagram (m); $\beta_{a\sigma}^0$ is the rotation angle (°) of the wall bottom of the basic structure caused by the load in the unit elastic resistance diagram; $\beta_{a\sigma}^0 = M_{a\sigma}^0\overline{\beta}_1$. The meaning of other symbols is the same as above.

After solving $X_{1\sigma}, X_{2\sigma}$, the internal force of any section of lining under the single action of load in the unit elastic resistance diagram can be calculated:

$$\begin{aligned} N_{i\sigma} &= X_{2\sigma}\cos\varphi_i + N_{i\sigma}^0, \\ M_{i\sigma} &= X_{1\sigma} + X_{2\sigma}y_i + M_{i\sigma}^0. \end{aligned} \tag{6}$$

The final internal force value of any section of lining can be obtained by using the superposition principle:

$$\begin{aligned} N_i &= N_{ip} + \sigma_h N_{i\sigma}, \\ M_i &= M_{ip} + \sigma_i M_{i\sigma}. \end{aligned} \tag{7}$$

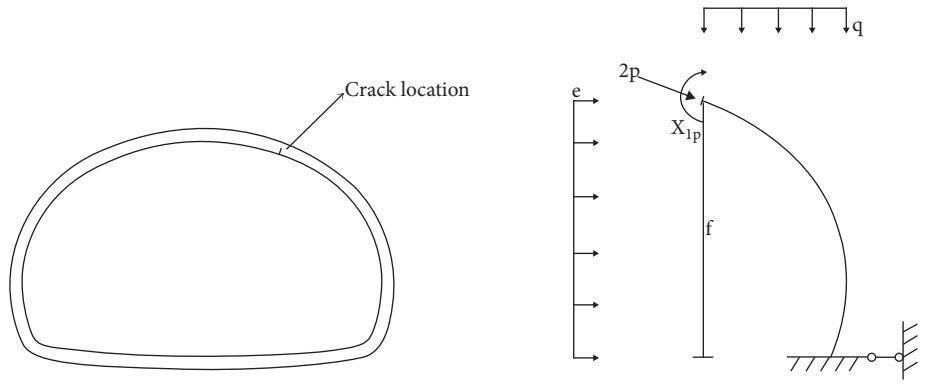

Figure 2: Basic structural stress diagram.

According to the above, the arch waist bending moment M_d and the arch waist axial force N_d can be finally obtained.

2.4. Fracture Mechanics Calculation of Tunnel Lining Structure. Most of the cracks in the tunnel lining structure are longitudinal cracks. The cracks in the arch waist of the longitudinal cracks do great harm to the lining structure. Therefore, this paper only analyzes the longitudinal cracks in the arch waist.

2.4.1. Fracture Mechanics Calculation Model. In this paper, the thickness of the secondary lining of the model is $h = 40$ cm. In order to analyze the crack at the arch waist more conveniently, the arch lining structure is approximately linear on the left and right sides of the center line. At present, the crack is mainly evaluated by the width of the crack. The wider the crack, the greater the harm to the structural safety. In the actual structure, the depth of crack plays an important role in the structure, and the width is considered to be the expression of depth. For the calculation model in this paper, in order to discuss the influence of different crack depths on the structure, the crack depth at the arch waist is determined as $a = 3$~18 cm. The arch waist bending moment M_d and arch crown axial force N_d of the structure can be obtained from Section 2.3. The final calculation model and crack simplified model are shown in Figure 3.

2.4.2. Calculation of Stress Intensity Factor. The calculation of the stress intensity factor of the model is divided into two parts; that is, the results are calculated under the separate action of the arch waist bending moment M_d and the arch waist axial force N_d. Then the stress intensity factor under the load of the model is obtained according to the superposition principle.

(1) Single Side Crack in Pure Bending [34]. The infinite strip with width b has a unilateral crack with depth "a," which acts on the bending moment M per unit thickness, as shown in Figure 4, and its stress intensity factor is

$$K_{IM} = F\sigma\sqrt{\pi a}, \tag{8}$$

where

$$F = \sqrt{\frac{2b}{\pi a} tg \frac{\pi a}{2b}}\ \frac{0.923 + 0.199\,(1 - \sin \pi a/2b)^4}{\cos \pi a/2b},$$
$$\sigma = \frac{6M}{b^2}. \tag{9}$$

Get

$$K_{IM} = S_M \cdot M, \tag{10}$$

where

$$S_M = F\frac{6}{b^2}\sqrt{\pi a}. \tag{11}$$

For the calculation model in this paper, when the secondary lining structure $B = 40$ cm, KIM is directly proportional to the arch waist bending moment M_d, while the bending coefficient SM is only related to the crack depth "a." When $a = 3$~18 cm, the values of F and S_M are obtained, as shown in Table 1.

It can be seen from Table 1 that when the crack depth "a" is small, the stress intensity factor changes slowly. When a is greater than 9 cm, the stress intensity factor increases rapidly, which also shows that when the crack depth reaches a certain value, the stress intensity factor mutates to reach the fracture toughness and fracture.

(2) Unilateral Crack Under Tension [34]. The infinite strip with width B has a unilateral crack with depth "a", which is subjected to unidirectional uniform tension, as shown in Figure 5, and its stress intensity factor is

$$K_{IN} = F\sigma\sqrt{\pi a}, \tag{12}$$

where

$$F = \sqrt{\frac{2b}{\pi a} tg \frac{\pi a}{2b}}\ \frac{0.752 + 2.02\,(a/b) + 0.37\,(1 - \sin \pi a/2b)^3}{\cos \pi a/2b},$$
$$\sigma = \frac{N}{A}. \tag{13}$$

Get

$$K_{IM} = S_N \cdot N, \tag{14}$$

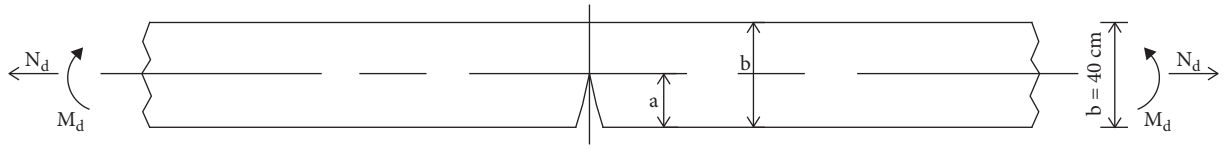

Figure 3: Fracture mechanics calculation model.

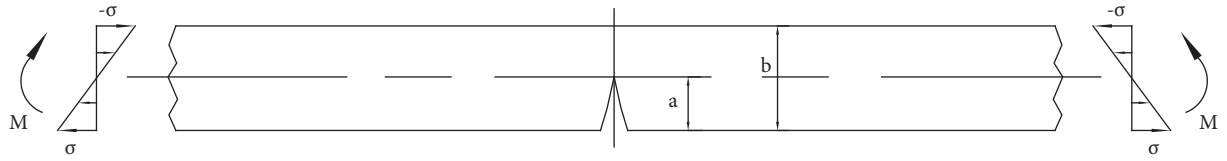

Figure 4: Pure bending calculation model.

Table 1: F and S_M values under pure bending.

Crack depth a (cm)	3	6	9	12	15	18
F	1.42	1.47	1.48	2.37	3.74	4.82
S_M ($m^{-3/2}$)	16.3	23.9	29.5	54.6	96.3	135.9

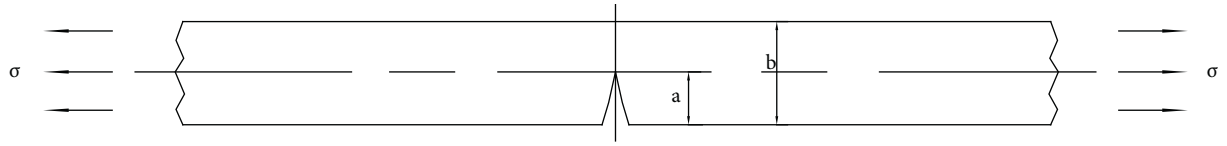

Figure 5: Pure tensile calculation model.

where

$$S_N = F\frac{\sqrt{\pi a}}{A}. \tag{15}$$

For the calculation model in this paper, when the secondary lining structure $B = 40$ cm, KIN is directly proportional to the arch waist bending moment M_d, while the tensile coefficient S_M is only related to the crack depth "a". When $a = 3$~18 cm, F and S_N values are obtained, as shown in Table 2.

It can be seen from Table 2 that when the crack depth "a" is small, the stress intensity factor changes slowly. When a is greater than 9 cm, the stress intensity factor increases rapidly, which also shows that when the crack depth reaches a certain value, the stress intensity factor mutates to reach the fracture toughness and fracture.

(3) Calculation of Stress Intensity Factor in Various Cases. In online elasticity, when several loads act on an elastomer at the same time, the stress and displacement caused by the load group at a certain point are equal to the sum of the stress and displacement components caused by each single load at that point. This is the superposition principle of linear elasticity theory [35]. Using this principle, when calculating K under complex load, it can also be decomposed into the sum of K under several simple load conditions.

According to the above superposition principle, the stress intensity factor under the joint action of arch waist bending moment M_d and arch waist axial force N_d is

Table 2: F and S_M values under pure tension.

Crack depth a (cm)	3	6	9	12	15	18
F	1.55	1.60	2.13	3.96	6.21	9.37
S_N ($m^{-3/2}$)	1.19	1.73	2.83	6.08	10.7	17.6

$$K_I = K_{IM} + K_{IN} = S_M \cdot M_d + S_N \cdot N_d. \tag{16}$$

When the arch waist bending moment M_d and the arch waist axial force N_d are constant, $b = 40$ cm, and "a" takes different values between 3 and 18 cm, the variation range of stress intensity factor K_I calculated from (12) is shown in Table 3.

It can be seen from Table 3 that, in the initial stage of crack development, the growth of stress intensity factor caused by the propagation of crack depth "a" is slow, but in the later stage, a small change in "a" leads to a huge change in stress intensity factor, which eventually leads to crack penetration and fracture.

3. Numerical Simulation of Tunnel Lining Cracks

3.1. Finite Element Model Establishment. The total length of the tunnel is 709 m, the geological condition is complex, the calculated section buried depth is 50 m, and the section surrounding rock is grade III. In the calculation, considering the symmetry of the structure, only the right half is taken to establish the model for analysis. The actual thickness of the

Table 3: Calculation results of stress intensity factor.

Crack depth a (cm)	K_I
$a = 3$	$16.3M_d + 1.19N_d$
$a = 6$	$23.9M_d + 1.73N_d$
$a = 9$	$29.5M_d + 2.83N_d$
$a = 12$	$44.6M_d + 6.08N_d$
$a = 15$	$67.3M_d + 10.7N_d$
$a = 16$	$93.3M_d + 12.8N_d$
$a = 17$	$117.2M_d + 14.7N_d$
$a = 18$	$135.9M_d + 17.6N_d$

Table 4: Physical and mechanical parameters of surrounding rock and support.

Material	Elastic modulus E (MPa)	Poisson's ratio	Bulk density (kN/m^3)	Cohesion (MPa)	Internal friction angle (°)	Dilatancy angle (°)
Surrounding rock (class IV)	2630	0.35	23	0.45	30	30
Shotcrete	21000	0.2	25	2	60	60
Secondary lining concrete	31000	0.2	25	3	60	60
Bolt	200000	0.3	78	—	—	—

soil layer above the top of the tunnel is 50 m, the left and right is 100 m, and below the tunnel is 100 m. The calculation boundary conditions are: horizontal constraint on the right, vertical constraint on the lower, and symmetrical constraint on the left.

According to "the code for design of highway tunnels [36]," the stress analysis of the tunnel should be analyzed according to the grade reduction of surrounding rock. Therefore, the section with a buried depth of 50 m of the tunnel should be calculated and analyzed according to grade IV surrounding rock. The yield condition of surrounding rock and concrete is Drucker–Prager criterion [37], and its physical and mechanical parameters are shown in Table 4.

The calculation model of surrounding rock and lining structure model are shown in Figures 6 and 7, respectively.

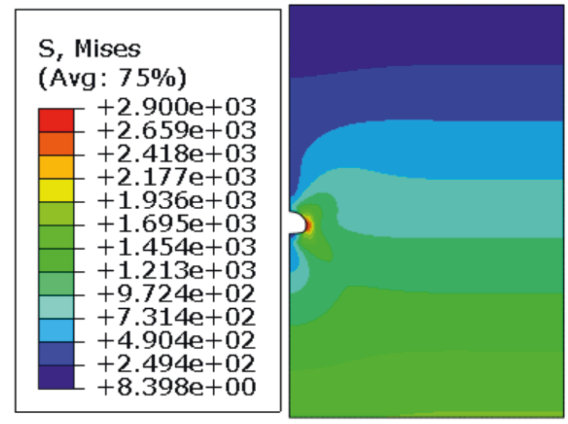

Figure 6: Calculation model of surrounding rock.

3.2. Analysis and Comparison of Cracked and Uncracked Models. In order to better analyze the displacement and stress of the crack model, the finite element calculation results of the lining structure in the uncracked model and the crack model (crack depth 12 cm) are compared in this paper, as shown in Table 5. The displacement diagrams and directional stress diagrams of the two models are shown in Figures 8–11.

It can be seen from the results in Table 5 that, for the cracked model, the displacement and stress at the lining arch waist are much higher than those of the uncracked model. It means that once longitudinal cracks appear in the lining, the safety of the structure will be greatly endangered. The maximum stress at the crack occurs at the crack tip; that is, the crack tip is a dangerous point. The research on crack body under plane stress state shows that [38], for type I crack, when the lining concrete material meets $K_c \geq K_c$ or $\delta \geq \delta_c$, the model will fail and the crack begins to expand.

3.3. Analysis and Comparison between Models with Different Values of Crack Depth. Under the same load conditions, when the size parameters of the model are different, the stress intensity factor KI of the lining structure is also different. The crack depth "a" at the arch waist is 3 cm, 6 cm, 9 cm, and 18 cm, respectively, for calculation. The calculated stress intensity factor KI, vertical maximum stress, and maximum settlement are listed in Table 6.

The stress and displacement nephogram in Y-direction is shown in Figures 12–19.

Through the comparison of data in Table 6 and Figures 12–19, it can be seen that, at the crack tip, the greater the crack depth "a," the greater the stress intensity factor, the increase trend of vertical maximum stress and maximum settlement at the arch waist, the more obvious the stress concentration at the crack tip, and the final stress intensity factor increases to the fracture toughness, resulting in fracture and structural damage.

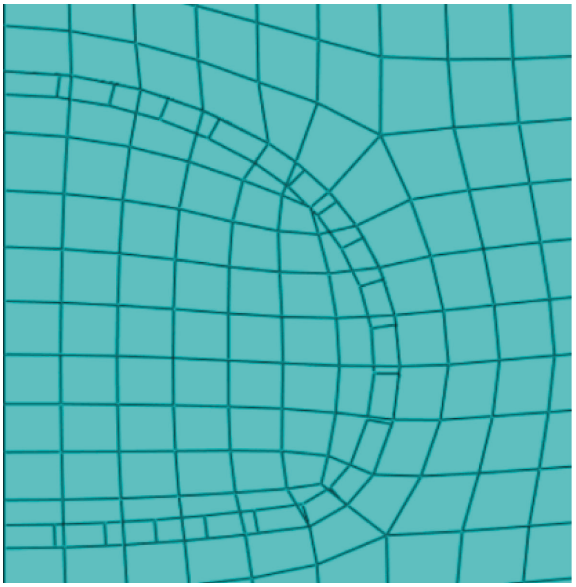

Figure 7: Lining structure model and unit division.

Table 5: Comparison of calculation results of finite element model.

	Uncracked model	Cracking model
Maximum settlement of lining arch waist (mm)	10.96	23.12
Maximum vertical stress of lining arch waist (MPa)	17.04	174.4

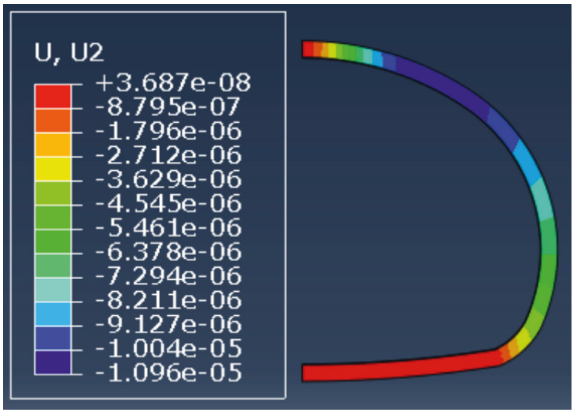

Figure 8: *Y*-direction displacement diagram.

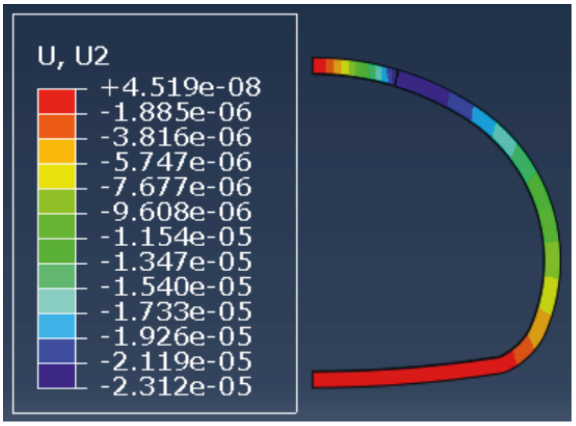

Figure 9: *Y*-direction displacement diagram of uncracked model of cracking model.

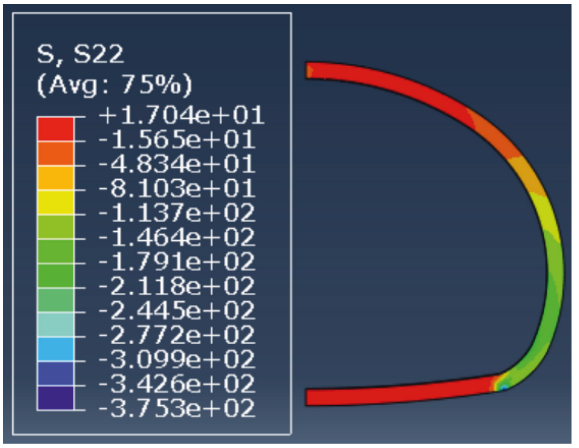

Figure 10: Y-direction stress diagram of uncracked model.

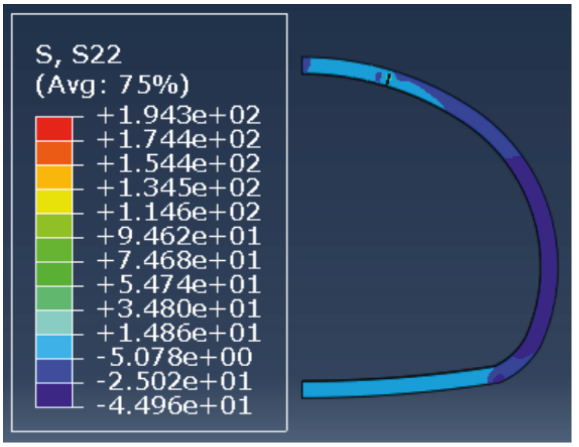

Figure 11: Y-direction stress diagram of cracking model.

Table 6: K_I values under different crack depths.

Crack depth a (cm)	a/h	Stress intensity factor KI	Maximum vertical stress (MPa)	Maximum settlement (mm)
3	0.075	0.35	74.37	14.21
6	0.15	0.77	123.8	18.41
9	0.225	1.14	152.6	20.20
18	0.45	5.35	362.2	32.21

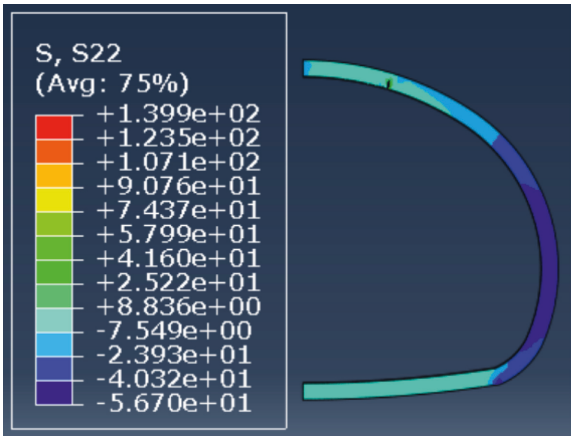

Figure 12: Y-direction stress diagram of $a = 3$ cm model.

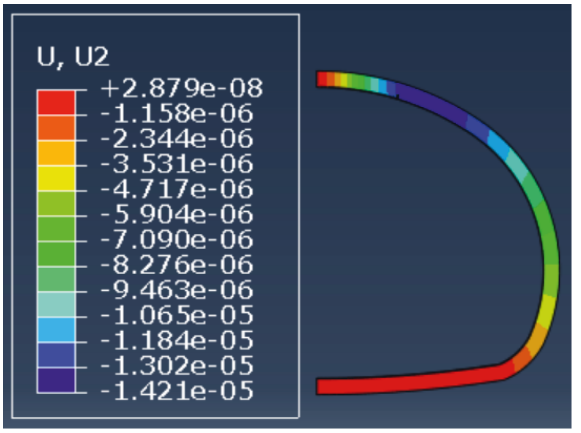

Figure 13: Y-direction displacement diagram of $a = 3$ cm model.

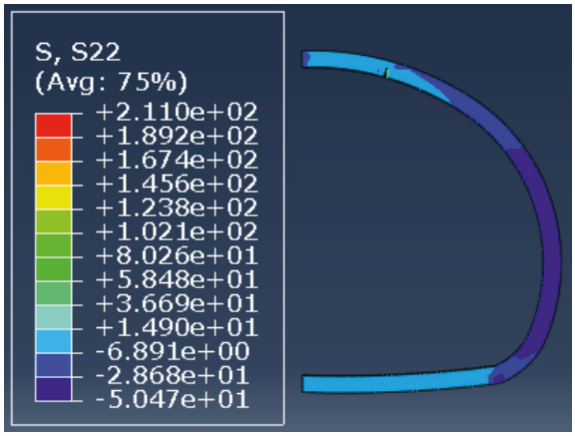

Figure 14: Y-direction stress diagram of $a = 6$ cm model.

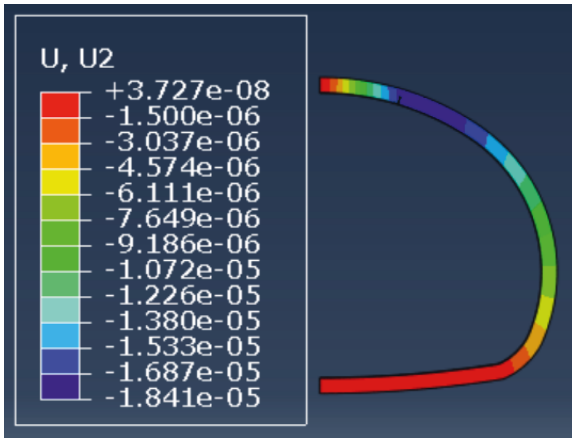

Figure 15: Y-direction displacement diagram of $a = 6$ cm model.

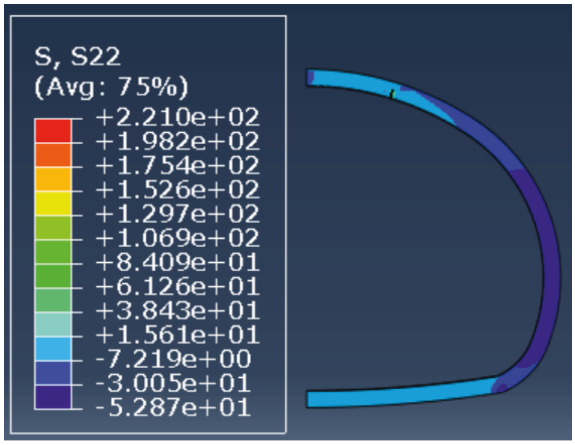

Figure 16: Y-direction stress diagram of $a = 9$ cm model.

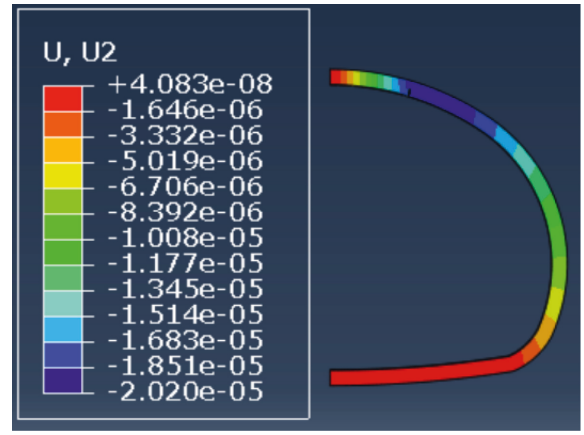

Figure 17: Y-direction displacement diagram of $a = 9$ cm model.

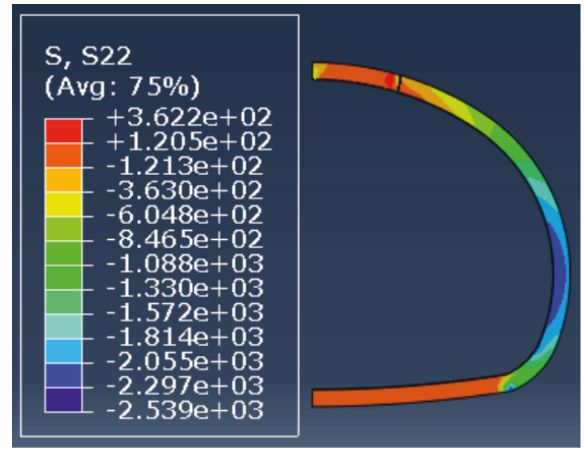

Figure 18: Y-direction stress diagram of $a = 18$ cm model.

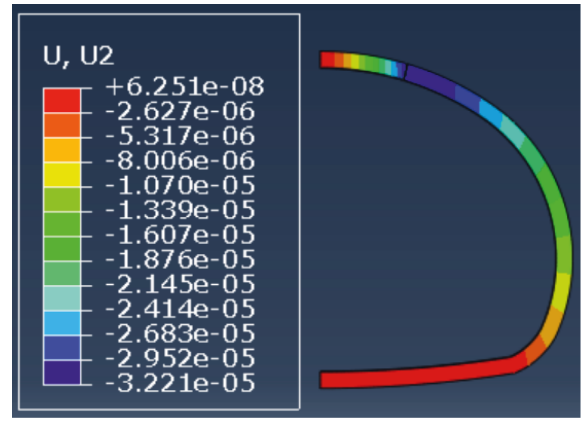

Figure 19: Y-direction displacement diagram of $a = 18$ cm model.

4. Comparison between Theoretical Value and Numerical Value

The stress intensity factor KI of the secondary lining calculation model is calculated according to Table 3, and compared with the numerical value, the detailed results are shown in Table 7, and the comparison curve is shown in Figure 20.

It can be seen from Table 7 and Figure 20 that the difference between the theoretical value and the numerical value is about 10%. Considering the coarse mesh division in the model in this paper, some calculation parameters need to be discussed. In order to make the calculation results more accurate, more mesh seeds can be arranged near the crack position and reduce the mesh size. It is believed that, with the

Table 7: Comparison between K_I theoretical value and numerical calculation results.

Crack depth a (cm)	K_I numerical value (MPa·m$^{1/2}$)	K_I theoretical calculated value (MPa·m$^{1/2}$)	Error (%)
3	0.35	0.31	−11.43
6	0.77	0.85	10.39
9	1.14	1.25	9.65
12	2.13	2.04	−4.23
15	3.51	3.31	−5.70
18	5.35	4.93	−7.85

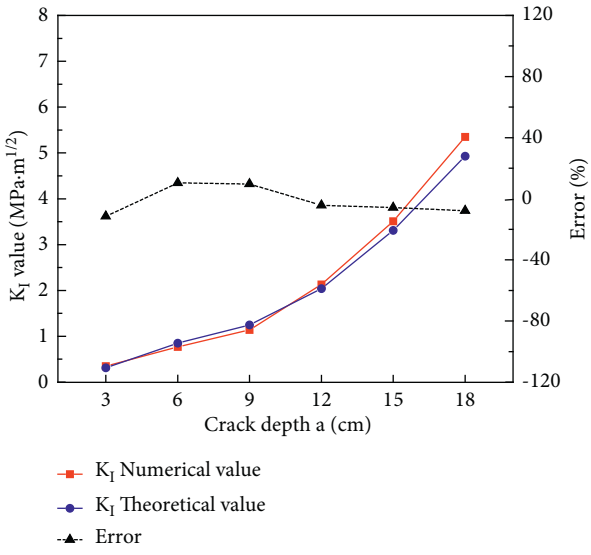

Figure 20: Comparison curve of KI theoretical value and calculated value.

more and more precision of the mesh and the optimization of the finite element model, the numerical calculation results will be closer to the theoretical value.

5. Conclusion

Tunnel lining cracks seriously affect the safe construction and operation of tunnel structure. With the development of fracture mechanics and its wide application in concrete, this paper mainly uses the theory of fracture mechanics to analyze the crack problem of tunnel structure. Through numerical calculation and theoretical analysis, the application of fracture mechanics in tunnel lining cracking is studied, and the following conclusions are obtained.

(1) The fracture mechanics model is used to simulate and analyze the cracking of the secondary lining structure, and the longitudinal cracks in the arch waist of the secondary lining are analyzed by fracture mechanics. The calculation of structural mechanics and fracture mechanics of lining structure shows that, in the early stage of crack development, the propagation of crack depth has little effect on the growth of stress intensity factor, but in the later stage, the small change of crack depth will have a great impact on stress intensity factor and eventually lead to crack penetration and fracture.

(2) The stress and displacement at the arch waist of uncracked model and cracked model are analyzed by ABAQUS finite element analysis software. For the cracked model, the displacement and stress at the arch waist of the lining are much higher than those of the uncracked model. This means that once longitudinal cracks appear in the lining, the safety of the structure will be greatly endangered.

(3) By analyzing and comparing the stress intensity factor, vertical maximum stress and maximum settlement between different crack depth models, it shows that, at the crack tip, the greater the crack depth, the greater the stress intensity factor, the increase trend of vertical maximum stress and maximum settlement at the arch waist, and the more obvious the stress concentration at the crack tip. Finally, the stress intensity factor increases to the fracture toughness, resulting in the failure of the structure.

Data Availability

The data in this paper are obtained according to theoretical derivation and numerical simulation. The subject needs further research and is inconvenient to be disclosed. The data that support the findings of this study are available from the corresponding author upon reasonable request.

Conflicts of Interest

The authors declare that they have no conflicts of interest.

Acknowledgments

This research was supported by National Key R&D Program of China (Grant Number: 2018YFB1600100), National Natural Science Foundation of China (Grant no. 51908052), Natural Science Basic Research Program of Shaanxi (Program nos. 2022JM-203, 2020JQ-371), the Open Fund of State Key Laboratory for Strength and Vibration of Mechanical Structures (Grant No. SV2019-KF-13), and Xi'an Jiaotong University.

References

[1] J. W. Hutchinson, "Singular behaviour at the end of a tensile crack in a hardening material," *Journal of the Mechanics and Physics of Solids*, vol. 16, no. 1, pp. 13–31, 1968.

[2] J. R. Rice and G. F. Rosengren, "Plane strain deformation near a crack tip in a power-law hardening material," *Journal of the Mechanics and Physics of Solids*, vol. 16, no. 1, pp. 1–12, 1968.

[3] J. W. Hutchinson and P. C. Paris, *Stability Analysis of J-Controlled Crack Growth*, pp. 37–61, ASTM STP 668 Philadelphia. Ame. Soc. Testing & . Mater, 1979.

[4] C. Zhu, M. Karakus, M. C. He et al., "Volumetric deformation and damage evolution of Tibet interbedded skarn under multistage constant-amplitude-cyclic loading," *International Journal of Rock Mechanics and Mining Sciences*, vol. 152, 2022.

[5] Y. Wang, H. N. Yang, J. Q. Han, and C. Zhu, "Effect of rock bridge length on fracture and damage modelling in granite containing hole and fissures under cyclic uniaxial increasing-amplitude decreasing-frequency (CUIADF) loads," *International Journal of Fatigue*, vol. 158, 2022.

[6] Z.-j. Wu, Z.-y. Wang, L.-f. Fan, L. Weng, and Q.-s. Liu, "Micro-failure process and failure mechanism of brittle rock under uniaxial compression using continuous real-time wave velocity measurement," *Journal of Central South University*, vol. 28, no. 2, pp. 556–571, 2021.

[7] X. S. Li, Q. H. Li, and Y. J. Hu, "Study on three-dimensional dynamic stability of open-pit high slope under blasting vibration," *Lithosphere*, vol. 2022, Article ID 6426550, 2022.

[8] H. Peijie, *Study on Type I Fracture Characteristics of Granite under Cyclic Loading and Unloading*, Shandong University of architecture, Jinan, China, 2020.

[9] C. Zhu, M. C. He, X. H. Zhang, Z. G. Tao, Q. Yin, and L. F. Li, "Nonlinear mechanical model of constant resistance and large deformation bolt and influence parameters analysis of constant resistance behavior," *Rock and Soil Mechanics*, vol. 42, no. 7, pp. 1911–1924, 2021.

[10] Qi. Wang, S. Xu, M. He, B. Jiang, W. Huayong, and Y. Wang, "Dynamic mechanical characteristics and application of constant resistance energy-absorbing supporting material," *International Journal of Mining Science and Technology*, vol. 19, 2022.

[11] Q. Wang, M. He, S. Li et al., "Comparative study of model tests on automatically formed roadway and gob-side entry driving in deep coal mines," *International Journal of Mining Science and Technology*, vol. 31, no. 4, pp. 591–601, 2021.

[12] Y.-q. Su, F.-q. Gong, S. Luo, and Z.-x. Liu, "Experimental study on energy storage and dissipation characteristics of granite under two-dimensional compression with constant confining pressure," *Journal of Central South University*, vol. 28, no. 3, pp. 848–865, 2021.

[13] Z. Dou, S. X. Tang, X. Y. Zhang et al., "Influence of shear displacement on fluid flow and solute transport in a 3D rough fracture," *Lithosphere*, vol. 4, 2021.

[14] P. Zhang, D. F. Zhang, Y. Yang et al., "A case study on intergrated modeling of spatial information of a complex geological body," *Lithosphere*, vol. s10, 2022.

[15] L. Liu, Z. Li, G. Cai, X. Geng, and B. Dai, "Performance and prediction of long-term settlement in road embankments constructed with recycled construction and demolition waste," *Acta Geotechnica*, vol. 256, 2022.

[16] H. Huang, D. Liu, Y. Xue, P. Wang, and L. Yin, "Numerical analysis of tunnel lining crack cracking based on extended finite element," *Journal of geotechnical engineering*, vol. 35, no. 2, pp. 266–275, 2013.

[17] Y. Li, M. Wang, H. Xu, Y. Zhang, and D. Wang, "Stress analysis of subway tunnel lining structure with crack disease," *China Railway Science*, vol. 35, no. 3, pp. 64–69, 2014.

[18] Y. Wang, Z. Liu, S. Zhang, J. Qiu, and Y. Xie, "Crack stability analysis of plain concrete lining of in-service highway tunnel," *Chinese Journal of highway*, vol. 28, no. 7, pp. 77–85, 2015.

[19] J. Yu, "Study on the influence law of highway tunnel lining cracks on structural stress distribution," *Journal of Civil Engineering*, vol. 50, no. S1, pp. 70–75, 2017.

[20] T. Yuan, *Study on the Influence of Tunnel Lining Cracking on Structural Mechanical Performance*, Beijing Jiaotong University, Beijing, China, 2019.

[21] M. Xu, *Application of Fracture Mechanics Theory in Highway Tunnel Lining Cracking*, Chongqing Jiaotong University, Chongqing, China, 2008.

[22] X. Liu, P. Zhang, and M. Zhou, "Analysis of the influence of longitudinal cracks on the bearing capacity of tunnel lining," *Journal of rock mechanics and engineering*, vol. 31, no. 10, pp. 2096–2102, 2012.

[23] Y. Zhang, *Safety Evaluation of Damaged Tunnel Structure Based on Finite Element Method*, Lanzhou Jiaotong University, Anning, China, 2013.

[24] F. Liu, L. Liu, and B. C. A. I. Wang, "Influence analysis of lining cracks on tunnel stability," *Journal of Shijiazhuang Railway University (NATURAL SCIENCE EDITION)*, vol. 26, no. S2, pp. 180–182+187, 2013.

[25] Y. Zheng, *Study on Lining Crack Mechanism and Structural Safety Evaluation of Highway Tunnel*, Central South University, Hunan, China, 2014.

[26] W. Wang, J. Deng, and J. Yin, "Study on safety of railway tunnel lining structure under space crack disease," *China Science and technology of work safety*, vol. 12, no. 1, pp. 33–37, 2016.

[27] Y. Liu and Y. Han, "Classification of tunnel lining cracking disease based on fracture mechanics theory," *China Railway Science*, vol. 40, no. 3, pp. 72–79, 2019.

[28] R. Huang, *Study on Crack Stability of Highway Tunnel Based on Fracture Mechanics*, Chongqing Jiaotong University, Chongqing, China, 2020.

[29] Z. Yang, Z. Zhou, T. Ling, W. Wu, and J. Chen, "Study on the influence law of tunnel lining cracks on structural stress," *Traffic science and engineering*, vol. 36, no. 4, pp. 43–53, 2020.

[30] S. Xiao, Ke. Li, X. Jiang, S. Wu, and C. Yao, "Study on bearing safety and crack evaluation standard of cracked lining," *Highway traffic technology*, vol. 37, no. S1, pp. 41–47, 2021.

[31] W. Zhao, R. Huang, bin. Zeng, N. Peng, and H. Kou, "Multi factor analysis of lining crack stability of highway tunnel," *Journal of underground space and engineering*, vol. 17, no. S1, pp. 419–425, 2021.

[32] X. Yu, *Fracture Mechanics of Rock and concrete*, Central South University Press, Changsha, China, 1991.

[33] Z. Li and Y. Zhang, "Bearing capacity analysis and treatment technology of cracked tunnel," *Tunnel construction*, vol. 23, no. 4, 2003.

[34] China Academy of Aeronautics, *Manual of Stress Intensity Factors*, pp. 119-120, Science Press, Beijing, China, 2003.

[35] C. Jin and S. Zhao, *Fracture Mechanics*, Science Press, Beijing, China, 2006.

[36] JTG D70-2004, *Code for Design of Highway Tunnel*, 2004.

[37] Z. Xia, *Plastic Mechanics*, Tongji University Press, Shanghai, China, 1991.

[38] A. A. Wells, "Application of fracture mechanics of and beyond general yielding," *British Welding Journal*, vol. 10, pp. 563–570, 1963.

Hindawi
Mathematical Problems in Engineering
Volume 2022, Article ID 2124231, 12 pages
https://doi.org/10.1155/2022/2124231

Research Article

Risk Assessment of Water Inrush from Coal Floor Based on Karst Fractal-Vulnerability Index Method

Rui-Peng Li,[1] **Lulin Zheng**,[1] **Jing Xie**,[2] **Jian-Yun Lin**,[1] **and Qing Qiu**[1]

[1]*College of Mining, Guizhou University, Guiyang, Guizhou 550025, China*
[2]*Guizhou Lindong Mining Group Co., Ltd, Guiyang, Guizhou 550023, China*

Correspondence should be addressed to Lulin Zheng; llzheng@gzu.edu.cn

Received 20 January 2022; Revised 9 February 2022; Accepted 28 February 2022; Published 4 May 2022

Academic Editor: Fuqiang Ren

Hidden karst structures are developed irregularly in the Middle Permian Maokou Formation aquifer from the northern part of the Guizhou coalfield, China. Mining operations associated with the exploitation of coal seams from the lower part of the Upper Permian Longtan Formation are threatened by karst waters from the underlying strata. To improve the accuracy of water inrush risk assessment of the karst aquifer floor in the northern Guizhou coalfield, the karst fractal quantification technique is implemented. In this study, the karst aquifer of the Maokou Formation located under the floor of the No. 15 coal seam from the Honglin Coal Mine is considered as the research object. Based on the karst results predicted by geophysical exploration methods, the fractal theory is used to quantify the degree of karst development, while the risk of water inrush from the floor of the coal seam is evaluated by applying ArcGIS information processing technology combined with the vulnerability index method. The results indicate the following observations: the mean fractal dimension of karst in the study area is 1.53, the karst structures are highly developed, and the overall distribution of karst is characterized by an irregular NW-SE direction; the main controlling factors affecting water inrush from the floor of the No. 15 coal seam are expressed by the water pressure of the aquifer, the abundance of water in the aquifer, the degree of karst development, the thickness of the effective impermeable layer, the mining depth, the coal seam dip angle, and the degree of fault complexity; the areas with the highest risk of floor water inrush are predominantly concentrated in the northwestern and central parts, but there is also a risk of floor water inrush in the first mining area of the No. 15 coal seam. This study takes into consideration complex factors such as the typical karst aquifer and the hydrogeological conditions in the northern part of the Guizhou coalfield, which results in a more realistic interpretation and can provide further guidance for water control activities in the mining area.

1. Introduction

The karst water disaster of the coal seam floor is one of the main hazards threatening the safety of mining operations of coal resources in the northern Guizhou coalfield [1, 2]. In this region, the coal-bearing strata of the Upper Permian Longtan Formation lie on the limestones of the Middle Permian Maokou Formation, which are characterized by strong karst features and different volumes of water. Moreover, the aquifer located between the Maokou Formation aquifer and the bottom mineable coal seam is thin (less than 4 m), which seriously affects the safe and efficient mining of the coal seam deposits. Therefore, the prediction and evaluation of water inrush from the karst floor of the coal seam beds are the major problem influencing the safe production activities in the northern Guizhou coalfield.

In recent years, the methods used to evaluate the risk of floor water inrush mainly include the water inrush coefficient method [3], the five-figure double coefficients method [4], and the vulnerability index method [5, 6]. Among these, the vulnerability index method comprehensively considers multiple essential control factors and their relative weights of floor water inrush, reflecting the nonlinear dynamic process of water inrush. This method has been widely used [7, 8] because it has a better solution for the problem of predicting water inrush from coal floor strata. Floor karst water damage is a typical geological hazard encountered during the production of "karst" coal mines. The factors which led to its

formation are complex and its distribution is extremely irregular. The evaluation of the vulnerability index method in this area considers the floor karst aquifer as a unified aquifer and ignores the degree of karst development. Although it has significance in guiding coal mining operations, the accuracy has a certain deviation from the actual scenario [9–11]. The karst development of the aquifer is an important factor affecting the water inrush from the coal seam floor in the northern part of the Guizhou coalfield. However, karst development can be measured by applying indirect geophysical exploration or drilling techniques, while direct observation or measuring methods are not applicable [12, 13]. Additionally, the obtained data represents the quantitative results of karst development and distribution inferred from inversion, which cannot be combined with the vulnerability index method for qualitative and quantitative evaluation of water inrush from the coal seam floor. Therefore, the scientific and rational quantification of karst development and the integration of the vulnerability index to comprehensively evaluate and predict the risk of water inrush from the coal seam floor in the northern part of the Guizhou coalfield have become an important subject.

To apply the vulnerability index method, domestic and foreign researchers used the fractal theory to quantify the complex structural characteristics of faults, which improved the prediction accuracy of water inrush from coal seam floors. Li et al. [14] substituted the fault fractal dimension with the fault distribution density, size, and nature to improve the accuracy of water inrush prediction by applying the vulnerability index method. Qiao et al. [15] calculated the fractal dimension index of the fault syncline and anticline and combined the vulnerability index method to predict the vulnerability zoning of the study area. The Maokou Formation limestone karst located at the bottom of the No. 15 coal seam in the Honglin Coal Mine is well developed; however, the aquifer is thin, which means that there is a possibility of water inrush from the floor. Therefore, based on the results obtained from geophysical exploration techniques, this study introduces the fractal theory to quantify the degree of karst development, while the comprehensive evaluation of the floor water inrush was analyzed in combination with the vulnerability index method. The karst fractal-vulnerability index method thoroughly analyzes the typical complex karst geology in the northern part of the Guizhou coalfield, making the evaluation results more realistic and providing a theoretical basis for water control measures in this area.

2. Overview and Engineering Background of the Study Area

The Honglin Coal Mine is in the northwestern part of Guizhou Province, to the east of Wumeng Mountain and at the junction of Qianxi and Dafang counties. The boundary of the mining area represents an irregular polygon, with a length of approximately 4 km from east to west and a width of approximately 3.7 km from north to south, covering an area equal to circa 12.55 km^2. The quasi-mining elevation ranges from +1750 m to +1100 m above sea level. The overall topography of the region is high in the northeast and low in the southwest. It is a monoclinal structure that belongs to the Zhongshan landform and develops an erosion-dissolution landform. The existing structural features in the area are mainly shaped by the Yanshan Movement tectonic events. Small- and medium-sized faults are well developed in the region. These are mainly distributed in the northeastern part of the mining area, while the fault strike has a predominantly east-west direction. The encountered strata from bottom to top are represented by the Maokou Formation, Longtan Formation, Changxing Formation, Yelang Formation, and Quaternary sediments. The most important water-bearing aquifers are the medium aquifers from the Changxing Formation, the medium aquifers from the Yulongshan section of the Yelang Formation, the weak aquifers from the Longtan Formation, and the strong aquifers from the Maokou Formation (Figure 1). In the mining area, the Longtan Formation consists of coal-bearing strata. It is rich in water and weak in water capacity, which represents the direct water source of the mine, but it does not pose a threat to mine production after long-term mining dredging. The major coal seams of the entire area are the No. 9 and the No. 15 coal seams. The bottom plate of the No. 15 coal seam is the limestone aquifer of the Maokou Formation, and the average thickness of the impermeable layer (mainly aluminium mudstone) is 4 m. The water-bearing medium primarily consists of pure carbonate rock karst water, with dissolved pores and caves.

According to the hydrogeological drilling survey, the water level of this aquifer has an elevation of 1599.7 m in borehole 505, accompanied by the presence of a local water head. At the same time, there is no water level in borehole 606, which is located not too far from borehole 505. This indicates that the karst development of the Maokou Formation is strong, water-bearing, and irregular, which threatens the safety of mining activities of the No. 15 coal seam. Physical exploration has been performed in the first and the second mining areas by using controllable audio frequency magnetotelluric methods and seismic resonance frequency imaging methods to better understand the karst development of the existing aquifers. The analysis of the development degree of limestones (elevation +1350 m) of the Maokou Formation in the No. 15 coal seam floor was carried out in combination with the hydrogeological conditions. The results indicate that the karst fractures of the Maokou Formation limestones in the floor of the No. 15 coal seam may have various degrees of development in the survey area, and the distribution area is different. A large, banded karst fractured zone is developed in the northwestern, southeastern, and southern parts of the survey area, and several small elliptic karst fracture zones are extended in the middle and western parts of the survey area (Figure 2).

3. Basic Theory

3.1. Fractal Theory. The fractal theory is a nonlinear discipline founded by Mandelbrot. Its principle is to enlarge a part of a complex object, whose type and complexity are like those of the whole object [16–18]. It can be used to quantify

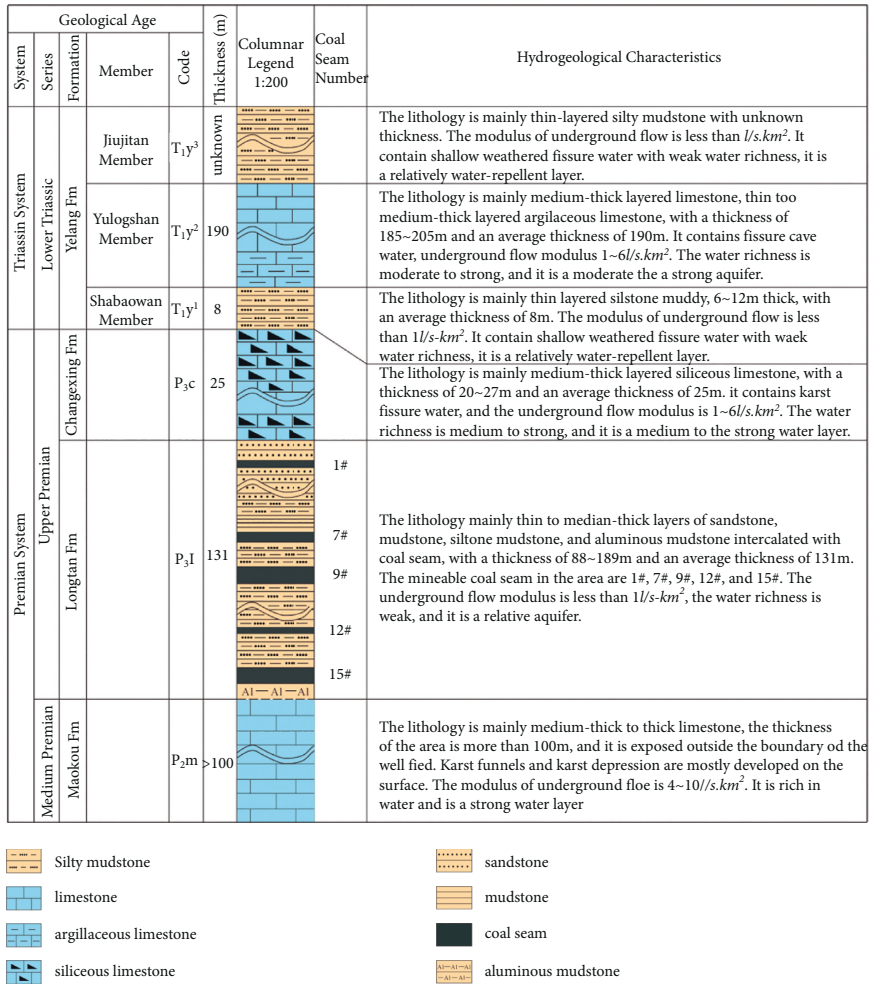

Figure 1: Hydrogeological generalized model of the Honglin Coal Mine.

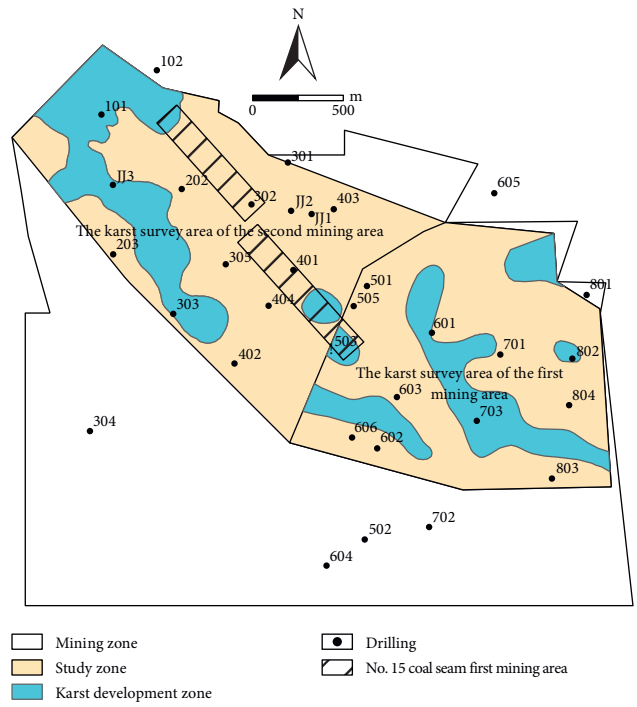

Figure 2: Schematic diagram of the limestone karst development in the Maokou Formation in the Honglin Coal Mine research area.

complex structures and irregular structures and is widely used in geological engineering applications. In recent years, the box dimension method has been the main method used to calculate the fractal dimensions. The process mainly includes the three following steps: (1) Cover the research object with a grid composed of square blocks with the side length equal to r_0, and count the number of grids covered by the research object $N(r)$. (2) Reduce the side length of the grid by applying the method of $r = r_0/2, r_0/4, rr_0/8_0, r_0/16$, respectively, and count the number of grids $N(r)$ covered by the research object under different scale grids. (3) Plot the results to the $\ln r - \ln N(r)$ coordinate system, obtain a straight line through function fitting, and consider the absolute value of its slope as the fractal dimension D_s. The equation is expressed as

$$\ln N(r) = A - D_s \ln r, \tag{1}$$

where r is the side length of the square grid; $N(r)$ is the number of grids covered by the research object; D_s is the fractal dimension; and A is a dimensionless constant.

3.2. Vulnerability Index Method. The application of the vulnerability index method is based on ArcGIS software. It analyzes and determines the main controlling factors of coal seam water inrush, establishes each main controlling factor thematic layer, uses the Analytic Hierarchy Process to determine the weight of each main controlling factor, applies the ArcGIS information fusion technology to establish a comprehensive topic figure, and finally introduces the vulnerability index to establish a regional evaluation model. The formula is expressed as

$$\mathrm{VI} = \sum_{k=1}^{n} W_k \times f_k(x, y), \tag{2}$$

where VI is the vulnerability index; n is the number of main controlling factors; k is the serial number of the factor; W_k is the weight of the kth factor; and $f_k(x, y)$ is the normalized value of the kth element, where (x, y) are geographic coordinates.

3.3. Application of the Karst Fractal Theory. The major particularity of a fractal theory is self-similarity; that is, a certain structure or process has similar characteristics on different spatial scales [19]. In recent years, some researchers consider that several geological phenomena show evident self-similarity and iterative patterns in distribution and geometric forms [20, 21]. Specifically, fault fractal technology has gradually advanced, which combined with the vulnerability index method, has improved the prediction accuracy of the vulnerability index method, and has been widely used in the field of coal seam floor water inrush hazard evaluation [22, 23]. Previous studies have shown that karst development morphology has a wide range of complex structures with iterative patterns, as well as irregular shapes and phenomena, which correspond to the statistical analysis of the fractal theory [24, 25]. At present, the fractal theory of karst development is predominantly used in karst tunnel engineering operations and rarely applied in coal seam floor water inrush evaluation methods [26, 27]. Therefore, this paper aims to include the karst fractal and the fault fractal theories into the vulnerability index method to improve the accuracy of coal floor water inrush predictions.

Based on the map illustrating the karst geophysical prospecting results, this paper divided the study area into two regions, and, for the convenience of performing calculations, as shown in Figure 3, grids i and ii consist of 200m × 200 m square blocks which were assigned distinct numbers. The total number of blocks covering the karst area is equal to 103. According to the previously mentioned steps, the number of 100m × 100 m, 50m × 50 m, 25m × 25 m, and 12.5 m × 12.5 m grids covered by each block in the study area was counted in separate stages; then the linear fitting procedure was performed in accordance with equation (1) to calculate the karst fractal dimension of all the blocks. The results are illustrated in Tables 1 and 2. It is noticeable that in both cases the mean value $R^2 = 0.97$, which indicates that the fitting effect is reasonable.

After assigning the calculated fractal dimension values to the center point of each block, the Surfer software tools were applied to perform kriging interpolation and to draw the contour maps, while the ArcGIS software was used to perform statistical partitioning to obtain the karst thematic map (Figure 4). It is observed that larger karst fractal dimensions generate stronger karst development characteristics; therefore, the risk of water inrush from the floor increases. According to Tables 1 and 2, the average value of the karst fractal dimension in the study area is 1.53, and the overall karst development is relatively strong. Based on the ArcGIS platform software, the fractal dimension of karst in the study area was calculated, while the threshold of karst zoning was determined by applying the natural discontinuity method, specifically: $D_s \geq 1.65$ is a strong karst development area; $1.25 \leq D_s < 1.65$ is a relatively strong karst development area; $0.95 \leq D_s < 1.25$ is a medium karst development area; $0.95 \leq D_s < 1.25$ is a weak karst development area; and $D_s < 0.65$ is an underdeveloped area. The karst terrain of the Maokou Formation aquifer presents an irregular distribution with a northwest-southeast direction (Figure 4).

4. Evaluation of Water Inrush from the Coal Seam Floor

4.1. Calculation and Analysis of the Main Controlling Factors. The rationality of the main controlling factors determines the accuracy of the vulnerability index evaluation method. The floor of the No. 15 coal seam in the Honglin Coal Mine is primarily threatened by the karst aquifer of the Maokou Formation, but the thin impermeable floor and the occasional water heads are also important factors. The evaluation method combines the hydrogeological characteristics with the geophysical prospecting data of the Honglin Coal Mine and considers the four aspects of the Maokou limestone aquifer, the floor impermeable layer, the coal seam mining conditions, and the geological structure. The comprehensive analysis identified seven major controlling factors affecting the water inrush from the floor of the No. 15 coal seam:

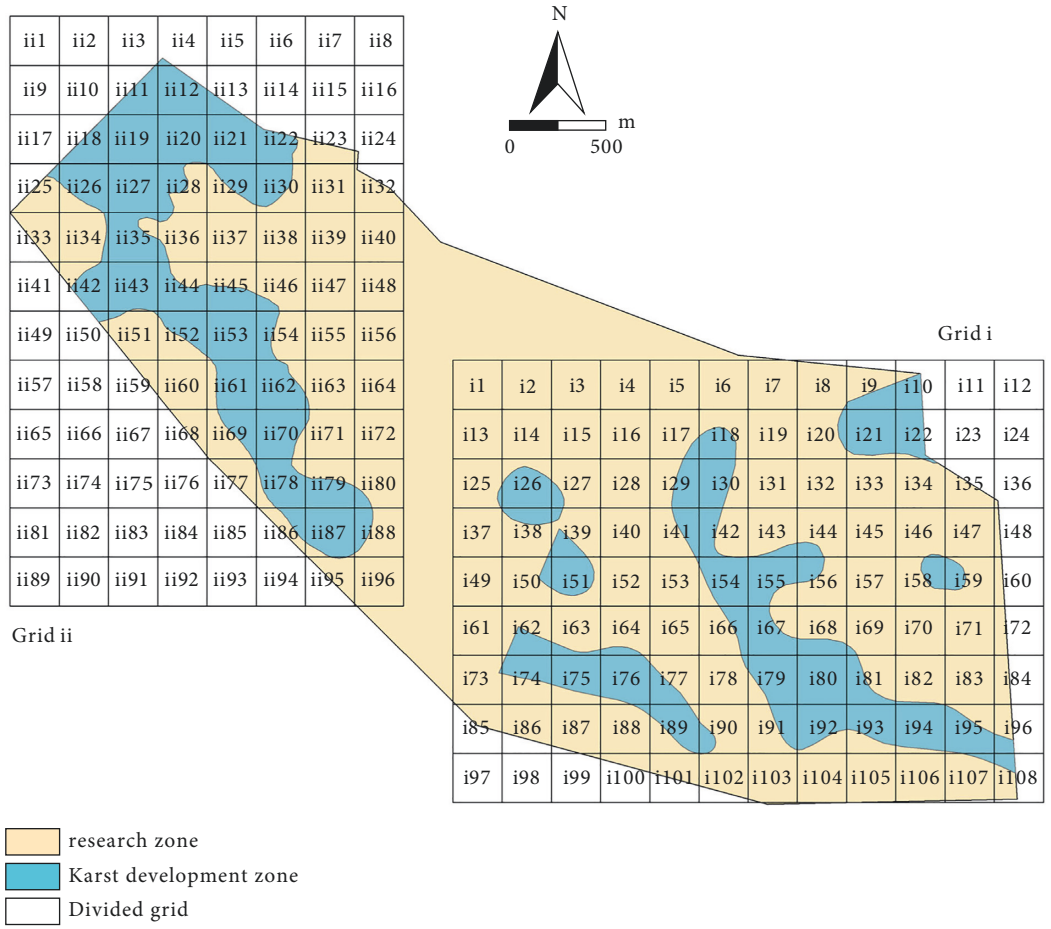

Figure 3: Grid division map of the karst area of the Honglin Coal Mine.

Table 1: Calculation results of the karst fractal dimension of grid i in the research area of the Honglin Coal Mine.

No.	D_s	No.	D_s	No.	D_s	No.	D_s	No.	D_s
i8	0.3170	i30	1.8311	i54	1.9486	i73	0.4170	i90	1.4195
i9	1.6984	i34	0.7585	i55	1.9224	i74	1.7696	i91	1.6618
i10	1.6087	i38	1.5590	i56	1.5066	i75	1.8930	i92	1.8915
i17	1.2510	i39	1.5853	i58	1.6030	i76	1.9874	i93	1.8616
i18	1.6901	i41	1.6481	i59	1.5567	i77	1.6595	i94	1.9791
i20	1.2634	i42	1.6962	i62	1.6723	i78	0.8644	i95	1.8738
i21	1.9802	i43	1.3726	i63	1.3370	i79	1.9473	i96	1.4485
i22	1.7872	i44	1.3229	i64	1.3196	i80	2.0000	i102	0.2000
i25	0.9400	i46	0.7615	i66	1.6163	i81	1.7585	i107	1.1170
i26	1.8987	i50	1.2925	i67	1.8799	i82	0.9814	i108	1.4451
i27	1.2634	i51	1.8325	i68	1.6601	i88	1.0136		
i29	1.7567	i53	0.5000	i69	0.8229	i89	1.8585		

Table 2: Calculation results of the karst fractal dimension of grid ii in the research area of the Honglin Coal Mine.

No.	D_s	No.	D_s	No.	D_s	No.	D_s	No.	D_s
ii4	0.9241	ii25	1.1955	ii42	1.7907	ii54	1.7370	ii79	1.7856
ii11	1.7903	ii26	1.9059	ii43	2.0000	ii61	1.9369	ii80	1.3078
ii12	1.9422	ii27	2.0000	ii44	1.8569	ii62	1.9447	ii86	1.4540
ii13	1.4219	ii28	1.7152	ii45	1.7652	ii63	0.7585	ii87	1.9804
ii18	1.7903	ii29	1.7465	ii46	1.3497	ii69	1.7633	ii88	1.5662
ii19	2.0000	ii30	1.7665	ii50	1.1592	ii70	1.9672	ii95	0.6755
ii20	2.0000	ii34	1.2136	ii51	1.0147	ii71	0.8229		
ii21	1.9966	ii35	1.9672	ii52	1.7926	ii77	0.5000		
ii22	1.7605	ii36	1.3081	ii53	2.0000	ii78	1.9383		

aquifer water pressure, aquifer water richness, degree of karst development, effective impermeable layer thickness, mining depth, coal seam inclination, and fault complexity. The thematic map of each major controlling factor was created (Figure 5) and analyzed based on the mining data combined with the Surfer and the ArcGIS software tools:

(1) *Hydraulic Pressure in the Aquifer*. When the aquifer's water level is higher than the coal seam floor, specific water pressure will exist. If the water pressure increases, the possibility of water inrush from the coal seam floor also increases. The changing trend of the water pressure in the aquifer occurs in the southeast direction, and the water pressure in the northwestern part has the highest values (Figure 5(a)).

(2) *Water Abundance of the Aquifer*. This controlling factor is defined by the unit water influx. The unit water influx in the study area is within the range of 0~0.0039 ($q \leq 0.1$ L/s·m). Therefore, the mining area is characterized by a weak water richness, and the

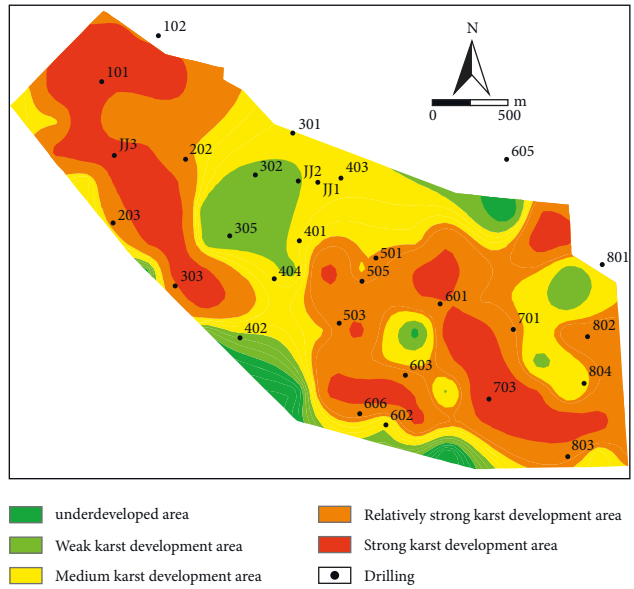

Figure 4: Thematic map of the karst development zoning in the research area of the Honglin Coal Mine.

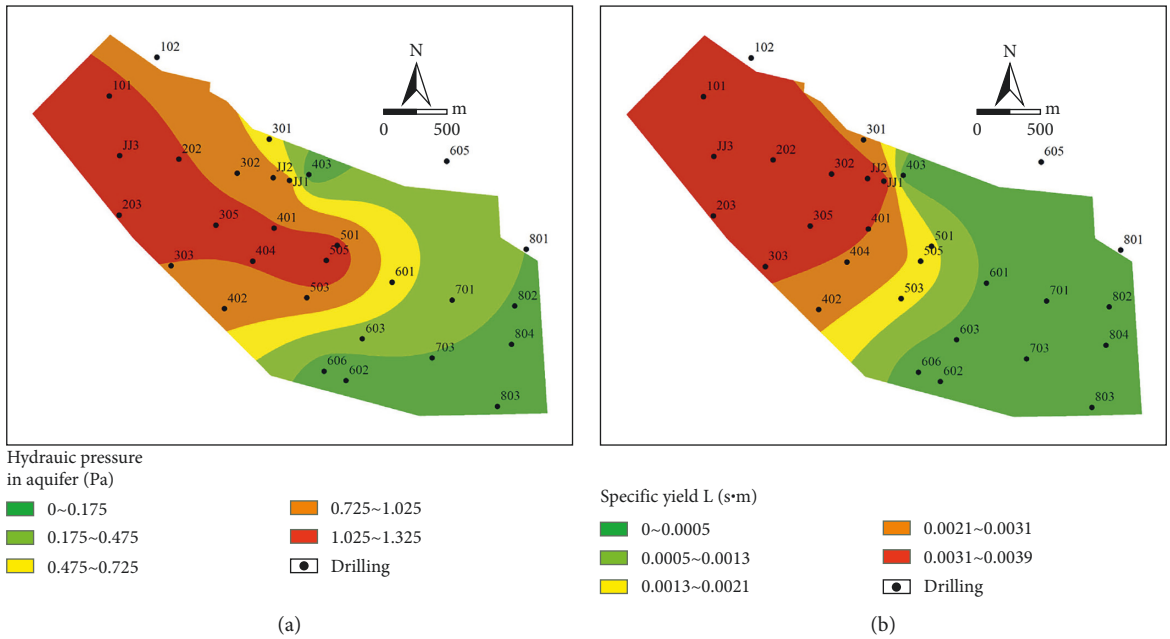

(a) (b)

Figure 5: Continued.

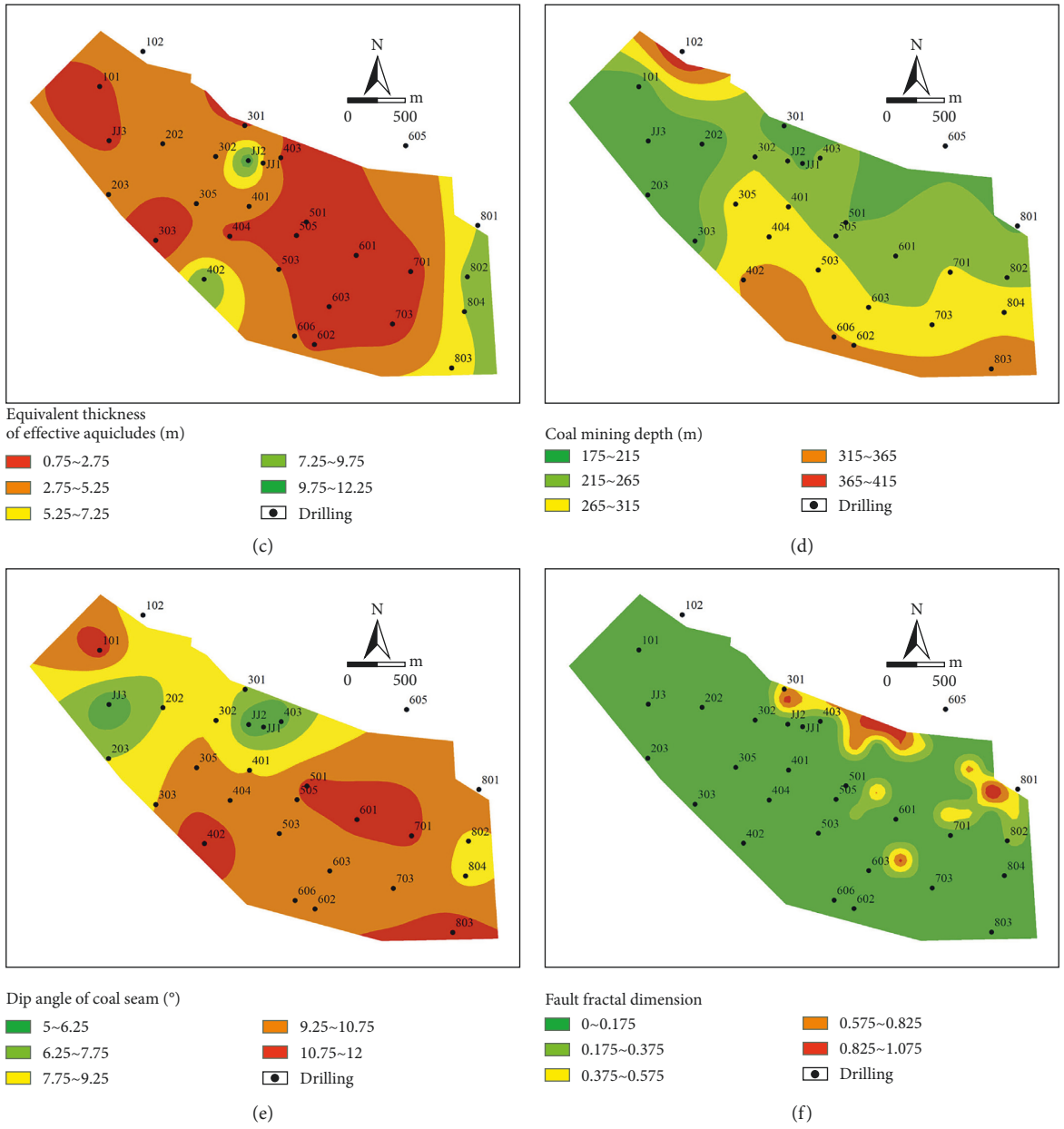

Figure 5: Thematic map of the main controlling factors in the research area of the Honglin Coal Mine. (a) Thematic map of the hydraulic pressure in the aquifer; (b) thematic map of the water abundance of the aquifer; (c) thematic map of the equivalent thickness of the effective aquiclude; (d) thematic map of the coal mining depth; (e) thematic map of the dip angle of the coal seam; (f) thematic map of the fault complexity.

relative water richness increases from east to west. The changing trend is similar to the water pressure trend (Figure 5(b)).

(3) *Degree of Karst Development*. It is characterized by the karst fractal dimension. The aquifers of the Maokou Formation predominantly consist of carbonate rocks and are susceptible to the dissolution of groundwaters. Consequently, karst failure zones and caves of varying sizes and shapes are created, which become water storage facilities of different volumes. During coal mining operations, the water-conducting fissure zones represent accessible paths for the water-bearing karst areas, therefore increasing the possibility of water inrush. The overall karst development of the Maokou Formation aquifer in the study area is extremely irregular, indicating that the strong karst development zones are concentrated in the northwest and southeast (Figure 4).

(4) *Equivalent Thickness of the Effective Aquiclude*. This determines the strength of the water-blocking capacity. If the impermeable layer becomes thinner, then the water-blocking effect is worse, which means

that it is easier to provoke a water inrush. The thickness of the impermeable layer located below the coal seam deposits is relatively thin, with a thickness in the range of 0.75~12.25 m, which has an immense impact on the water inrush from the coal seam floor (Figure 5(c)).

(5) *Coal Mining Depth*. When the mining depth increases, the stress on the two walls of the mining face becomes more concentrated, while the bottom plate is prone to damage and cracks, which increases the number of water channels. Thus, the possibility of water inrush from the bottom layer grows. The overall trend of the mining depth in the study area increases from north to southeast, and the maximum mining depth located in the northernmost part is equal to 415 m (Figure 5(d)).

(6) *Dip Angle of the Coal Seam*. During the mining process, as the inclination angle of the coal seam increases, the mineral pressure formed on the working face becomes more evident. Consequently, the damage done to the coal seam floor is greater, and the risk of water inrush increases. The inclination angle of the No. 15 coal seam is in the range of 5°~12°, which represents a gently inclined sedimentary layer. The coal seam inclination angles are relatively inclined in a sizable area in the southeastern part and a small area in the northwestern part (Figure 5(e)).

(7) *Fault Complexity*. This controlling factor is characterized by the fractal dimension of the fault, which is identical to the method used for describing the complexity of the karst system. The No. 15 coal seam in the study area comprises a small number of small faults and no large faults. Most of the small faults are predominantly distributed in the northern and eastern parts of the study area. Among these, there are several normal faults, with a drop height between 0.5 and 2 m. The fractal dimension values of the faults range between 0 and 1.075. Although the complexity of the faults in the study area is relatively low, it is still an important factor that affects the possibility of water inrush from the floor (Figure 5(f)).

4.2. Calculating Weights by the Analytic Hierarchy Process. Analytic Hierarchy Process (AHP) is a practical subjective decision-making analysis technique, which represents the core method of the vulnerability index method [28]. The method decomposes a complex problem into different factors and forms a multilevel structure model according to the mutual influence relationship and membership relationship between factors. By analyzing and comparing the importance of each factor, the judgment matrix was created, and, finally, the qualitative and quantitative analyses of multiple factors were completed [29–31]. There are generally four steps: (a) establishment of a hierarchical structure model, (b) construction of a comparative judgment matrix, (c) calculation of the largest eigenvalue of the matrix and the corresponding eigenvector, and (d) hierarchical ranking and consistency check.

4.3. Establishment of the Hierarchical Model. By analyzing the main controlling factors affecting the water inrush from the floor of the No. 15 coal seam, the research object is divided into three levels, namely, A (target layer), B (criterion layer), and C (index layer), as illustrated in Figure 6.

4.4. Construction of a Judgment Matrix to Determine the Weight of the Main Controlling Factor. By taking into consideration the index system of the water inrush risk from the floor of the No. 15 coal seam and associating it with the analysis of the previously mentioned main controlling factors, the importance of each factor was evaluated according to the 1~9 scale method. This scaling method was established by T. L. Saaty, by soliciting the experts' opinions and by analyzing data from the available literature. Thus, a judgment matrix was constructed. The judgment matrix of the first-level index is $A_i = \begin{bmatrix} 1 & 5/3 & 5/2 & 3/2 \\ 3/5 & 1 & 3/2 & 4/5 \\ 2/5 & 2/3 & 1 & 3/5 \\ 2/3 & 5/4 & 5/3 & 1 \end{bmatrix}$, where the weight is $w_{A_i} = (0.375, 0.218, 0.15, 0.257)$. The judgment matrix of the secondary index is $B_{1j} = \begin{bmatrix} 1 & 4 & 2 \\ 1/4 & 1 & 1/2 \\ 1/2 & 2 & 1 \end{bmatrix}$, where the weight is $w_{B_{1j}} = (0.513, 0.182, 0.305)$; $B_{2j} = [1]$, where the weight is $w_{B_{2j}} = (1)$; $B_{3j} = \begin{bmatrix} 1 & 4/5 \\ 5/4 & 1 \end{bmatrix}$, where the weight is $w_{B_{2j}} = (0.444, 0.556)$; $B_{4j} = [1]$, where the weight is $w_{B_{2j}} = (1)$. At the same time, all the judgment matrices passed the consistency test. By applying the linear weighting method, the weight value of the first-level index is multiplied with the weight value of the related second-level index, and, finally, the weight value of the influence of each main controlling factor on the risk of water inrush from the floor is obtained; namely, $w = (0.192, 0.068, 0114, 0.218, 0.067, 0.083, 0.257)$. The weight of each main controlling factor is illustrated in Table 3.

4.5. Data Normalization of Each Main Controlling Factor. To eliminate the influence of the data of different main controlling factor dimensions on the evaluation results and to make the factors comparable, the data were normalized. Considering the positive and the negative correlation of the main controlling factors with the evaluation results, the positive correlation factors (water pressure of the aquifer, water aquifer, degree of karst development, mining depth, coal seam inclination, and fault complexity) are unified by applying the maximum value processing equation (3), where the minimum value is 0 and the maximum value is 1. At the same time, the negative correlation factor (effective water barrier thickness) is normalized to the minimum value

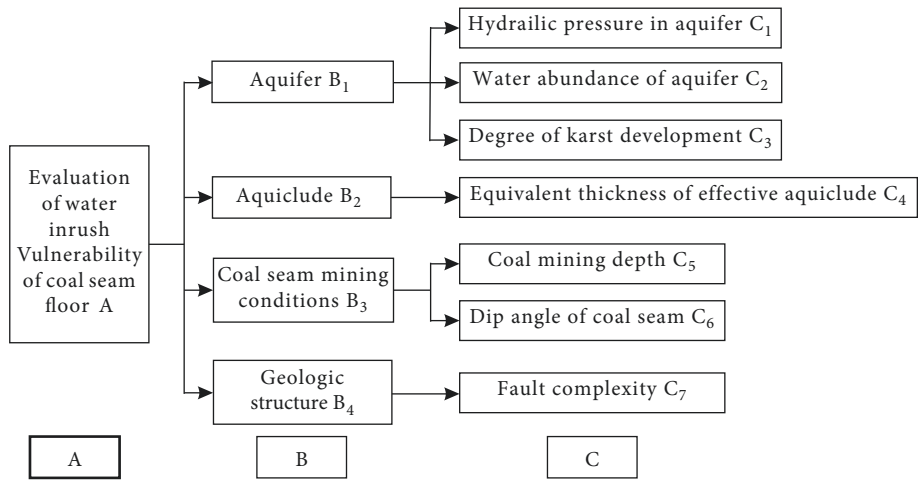

Figure 6: Evaluation index of water inrush from the floor of the No. 15 coal seam in the Honglin Coal Mine.

Table 3: Weights of the main controlling factors for water inrush.

Influential factors	Hydraulic pressure in the aquifer (w_1)	Water abundance of the aquifer (w_2)	Degree of karst development (w_3)	Equivalent thickness of the effective aquiclude (w_4)	Coal mining depth (w_5)	Dip angle of the coal seam (w_6)	Fault complexity (w_7)
Weights (w_i)	0.192	0.068	0.114	0.218	0.067	0.083	0.257

processing equation (4), with the minimum value equal to 1 and the maximum value equal to 0. The formula is expressed as

$$Y_{ij} = \frac{X_{ij} - \min(X_i)}{\max(X_i) - \min(X_i)}, \tag{3}$$

$$Y_{ij} = \frac{\max(X_i) - X_{ij}}{\max(X_i) - \min(X_i)}. \tag{4}$$

4.6. Creation of a Model of the Vulnerability Index of the Floor. The vulnerability assessment model of the karst floor water inrush of the Maokou Formation in the No. 15 coal seam of the Honglin Coal Mine was proposed based on the application of formula (2), on the vulnerability index VI, as well as the weights of the main controlling factors determined by the Analytic Hierarchy Process. The formula is expressed as

$$\begin{aligned} \mathrm{VI} = \sum_{k=1}^{7} W_k \times f_k(x, y) &= 0.192 \times f_1(x, y) + 0.068 \times f_2(x, y) + 0.114 \times f_3(x, y) + 0.218 \times f_4(x, y) \\ &+ 0.067 \times f_5(x, y) + 0.083 \times f_6(x, y) + 0.257 \times f_7(x, y). \end{aligned} \tag{5}$$

4.7. Water Inrush Hazard Zoning of the Coal Seam Floor. The main controlling factors are normalized on the thematic map by using the ArcGIS information fusion and data processing functions. Consequently, a comprehensive evaluation model for water inrush vulnerability of the coal seam floor is proposed. The natural discontinuity method was used to assess the frequency statistics of the vulnerability index of each block in the study area (Figure 7), and the unified partition thresholds for the vulnerability evaluation were determined to be 0.35, 0.41, 0.46, and 0.51. When the vulnerability index has greater values, the possibility of floor water inrush increases. According to the partition threshold, the research area is divided into 5 areas, specifically: $\mathrm{VI} \geq 0.51$ is the dangerous area; $0.46 \leq \mathrm{VI} \leq 0.51$ is the less dangerous area; $0.41 \leq \mathrm{VI} \leq 0.46$ is the transition area; $0.36 \leq \mathrm{VI} \leq 0.41$ is the safer area; and $\mathrm{VI} < 0.35$ is the safe zone. Afterwards, the risk assessment map of the No. 15 coal seam floor is created (see Figure 8).

5. Results

As illustrated in Figure 8, the relative risk of water inrush decreases from northwest to southeast. The floor water inrush risk area is primarily concentrated in the middle, northwestern, and western parts, which indicates a large area of bands and a small area represented by an ellipse. The safe zone is mainly concentrated in the southeastern and north-

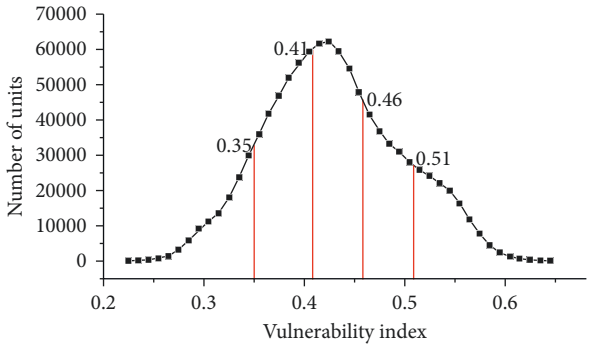

Figure 7: Frequency broken line chart of vulnerability index of coal seam floor in Honglin Coal Mine research area. The broken line represents the frequency distribution of the vulnerability index in the study area. The values at the intersection with the red lines represent the partition threshold calculated by the natural discontinuity method.

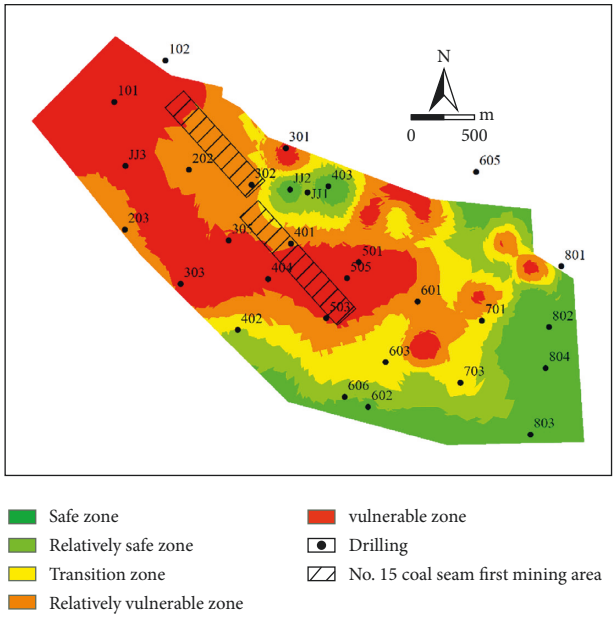

Figure 8: Water inrush risk zoning map of the No. 15 coal seam floor of the Honglin Coal Mine.

central parts. The arguments for such conclusions are as follows:

(1) In the northwestern part, the relative head pressure is high, water is abundant, and the perimeter is characterized by the presence of a karst fracture zone. Therefore, it is easy to produce a water channel.

(2) The water abundance in the central part of the study area shows a weakening trend, while the degree of karst development is low. However, the thickness of the effective impermeable layer becomes thinner, which cannot adequately prevent the water pressure accumulated below this layer.

(3) The aquifer and the water richness in the western part of the study area also indicate a weakening trend, while the thickness of the effective impermeable layer shows a thickening trend. However, this area is characterized by the presence of several complex faults and a karst fracture area, which facilitates the formation of a water channel and, consequently, may lead to water inrush.

(4) The mining depth of the No. 15 coal seam in the north-central part of the study area is shallow. The coal seam inclination angle is slow. The stress and the mine pressure on the floor and the two sides are small. Additionally, the effective impermeable layer is thicker, and the depth of the flood damage is not enough to penetrate the effective impermeable layer. Therefore, this perimeter is considered a safe zone.

(5) Karst fractures exist in the southeastern part of the study area. However, the water pressure and the water richness of the aquifer show a weakening trend, while the thickness of the relative aquifer is increasing. Consequently, the possibility of water inrush from the coal seam floor is negligible.

At present, there are no exploitation activities in the first mining area of the No. 15 coal seam in the Honglin Coal Mine, but the risk of water inrush from the floor in this area is relatively high. The main concerns are related to the high water pressure and the thin thickness of the impermeable layer. Therefore, the exploration operations should be strengthened, while the measures related to water exploration, water release, and thickening of the floor concreting should be adopted to ensure a safe mining environment.

6. Conclusions

(1) Based on the karst fractal-vulnerability index method, the water inrush hazard of the No. 15 coal seam floor of the Honglin Coal Mine is evaluated. Complex factors such as the typical karst aquifer in the northern Guizhou coalfield and the hydrogeological conditions of the study area are fully examined, which makes the evaluation results more reasonable and practical.

(2) To improve the accuracy of the karst geophysical prospecting evaluation results, the karst fractal dimension is used to quantify the degree of karst development of the coal seam floor. The overall fractal dimension value of the research area is equal to 1.53, and the degree of karst development is relatively high. By applying the natural discontinuity method, the karst development is divided into five categories: underdeveloped karst area, weak karst development area, medium karst development area, relatively strong karst development area, and strong karst development area. Furthermore, the karst development area is characterized by an irregular northwest-southeast direction.

(3) The water inrush danger zone of the No. 15 coal seam floor in the study area is primarily concentrated in the middle, northwestern, and western parts, with a large area of bands and a small area represented by

an ellipse. The safety zone is concentrated in the southeastern and north-central parts. There is a risk of water inrush from the floor in the first mining area of the No. 15 coal seam, and water prevention measures should be improved and strengthened.

Data Availability

Some or all data, models, or codes generated or used during the study are available from the corresponding author upon request.

Conflicts of Interest

The authors declare that there are no conflicts of interest regarding the publication of this paper.

Acknowledgments

This work was supported by the National Natural Science Foundation of China (no. 52164006), Science and Technology Support Project of Guizhou Province, China (Project No. [2022] general 248), and the National Natural Science Foundation for Young Teachers of Guizhou University (Guizhou University Cultivation no. [2020] 81).

References

[1] B. Li, X. Wang, Z. Liu, and T. Li, "Study on multi-field catastrophe evolution laws of water inrush from concealed karst cave in roadway excavation: A case of Jiyuan coal mine," *Geomatics, Natural Hazards and Risk*, vol. 12, no. 1, pp. 222–243, 2021.

[2] J. Hao, H. Bian, A. Chen, J. Lin, and D. Xu, "Karst water pressure's varying rule and its response to overlying strata movement in coal mine," *Advances in Civil Engineering*, vol. 2020, Article ID 8848924, 7 pages, 2020.

[3] W. P. Li, W. Qiao, X. Q. Li, and R. H. Sui, "Characteristics of water disaster, evaluation methods and exploration direction for controlling groundwater in deep mining," *Journal of China Coal Society*, vol. 44, no. 8, pp. 2437–2448, 2019.

[4] J. L. Li, G. S. Chen, B. Zhang, and Y. H. Cui, "The evaluation of water inrush risk on coal floor based on five figures and double coefficients method," *Journal of Henan Polytechnic University (Natural Science)*, vol. 36, no. 2, pp. 30–34, 2017.

[5] Q. Wu, Y. Z. Liu, and Y. Liu, "Using the vulnerable index method to assess the likelihood of a water inrush through the floor of a multi-seam coal mine in China," *Mine Water and the Environment*, vol. 30, no. 1, pp. 54–60, 2010.

[6] S. Q. Liu, Q. Wu, and Z. Li, "Vulnerability evaluation and application of water inrush variable weight in mining areas with multiple coal seams and a single aquifer," *Journal of China University of Mining and Technology*, vol. 50, no. 3, pp. 587–597, 2021.

[7] Y. Hu, W. Li, S. Liu, Q. Wang, and Z. Wang, "Risk assessment of water inrush from aquifers underlying the Qiuji coal mine in China," *Arabian Journal of Geosciences*, vol. 12, no. 98, 2019.

[8] G. Dai, X. Xue, Ke Xu, L. Dong, and C. Niu, "A GIS-based method of risk assessment on no. 11 coal-floor water inrush from Ordovician limestone in Hancheng mining area, China," *Arabian Journal of Geosciences*, vol. 11, no. 22, 2018.

[9] C. Li, W. K. Yang, B. Yang, Y. Z. Dong, and L. Yang, "Vulnerability assessment of water inrush from independent karst water system of coal seam floor in Datong Coalfield (north district)," *Coal Engineering*, vol. 53, no. 6, pp. 130–134, 2021.

[10] Y. Zeng, Q. Wu, S. Liu, Y. Zhai, W. Zhang, and Y. Liu, "Vulnerability assessment of water bursting from Ordovician limestone into coal mines of China," *Environmental Earth Sciences*, vol. 75, no. 22, 2016.

[11] X. Shang, Y. Wang, and R. Miao, "Acoustic emission source location from P-wave arrival time corrected data and virtual field optimization method," *Mechanical Systems and Signal Processing*, vol. 163, Article ID 108129, 2022.

[12] J. Yan, "Selection and practice of several main geophysical methods for advanced geological prediction of karst tunnels," *Tunnel Construction (Chinese and English)*, vol. 40, no. S1, pp. 327–336, 2020.

[13] K. Chalikakis, V. Plagnes, R. Guerin, R. Valois, and F. P. Bosch, "Contribution of geophysical methods to karst-system exploration: An overview," *Hydrogeology Journal*, vol. 19, no. 6, pp. 1169–1180, 2011.

[14] J. L. Li, H. Y. Zhang, X. Y. Wang, Y.-L. Feng, Z. Liu, and L. Han, "Application and suggestion of vulnerability index method in prediction of water inrush from coal seam floor," *Journal of Coal Industry*, vol. 39, no. 4, pp. 725–730, 2014.

[15] W. Qiao, W. Li, X. Zhang et al., "Prediction of floor water disasters based on fractal analysis of geologic structure and vulnerability index method for deep coal mining in the Yanzhou mining area," *Geomatics, Natural Hazards and Risk*, vol. 10, no. 1, pp. 1306–1326, 2019.

[16] L. H. Duan and J. L. Zhang, "Comprehensive evaluation of water inrush risk from the second-level coal seam floor of Chengjiao Coal Mine," *Coal Engineering*, vol. 53, no. 1, pp. 128–132, 2021.

[17] B. Yang, W. Sui, and L. Duan, "Risk assessment of water inrush in an underground coal mine based on GIS and fuzzy set theory," *Mine Water and the Environment*, vol. 36, no. 4, pp. 617–627, 2017.

[18] M. Gao, J. Xie, J. Guo, Y. Lu, Z. He, and C. Li, "Fractal evolution and connectivity characteristics of mining-induced crack networks in coal masses at different depths," *Geomechanics and Geophysics for Geo-Energy and Geo-Resources*, vol. 7, no. 1, p. 9, 2021.

[19] R. Li, Q. Wang, X. Wang, X. Liu, J. Li, and Y. Zhang, "Relationship analysis of the degree of fault complexity and the water irruption rate, based on fractal theory," *Mine Water and the Environment*, vol. 36, no. 1, pp. 18–23, 2017.

[20] Y. C. Qiu and K. Liu, "Advances in applied studies of fractal theory in geography in China," *Journal of Geographical Sciences*, vol. 14, no. 1, pp. 62–68, 2004.

[21] F. Shen, L. Yue, Z. Liu et al., "Heterogeneity of tight sandstone reservoirs based on fractal theory: The Xu-6 member of Xujiahe Formation in Guang'an area, central Sichuan Basin," *Arabian Journal of Geosciences*, vol. 14, no. 15, 2021.

[22] L. Q. Shi, L. Liu, J. Zhou, T. J. Xing, C. Niu, and Y. Wang, "Fault Fractal Information Dimension and Its Application in Floor Water Burst," *Journal of Mining And Strata Control*, vol. 19, no. 1, pp. 12–16, 2014.

[23] J.-L. Li, S.-W. Wang, Y. Wang, X.-Y. Wang, and X.-X. Wang, "Water inrush risk assessment of coal floor after CBM development based on the fractal-AHP-vulnerlability index method," *Geotechnical & Geological Engineering*, vol. 39, no. 5, pp. 3487–3497, 2021.

[24] M. Xu, D. Wang, J. H. Qi, and Y. N. Yang, "Study on morphological characteristics of karst landform based on the fractal theory," *Journal of Chengdu University of Technology (Science & Technology Edition)*, vol. 38, no. 3, pp. 328–333, 2011.

[25] X. X. Fu, X. S. Liu, X. Z. Shao, and J. L. Hu, "Fractal characteristics of paleokarst development in ordovician in ordos basin," *Carsologica Sinica*, vol. 36, no. 1, pp. 23–31, 2017.

[26] W. Gao, J. H. Qi, M. Xu, Y. X. Li, and N. F. Wang, "A preliminary study on the effect of fractal features of surface karst landforms on tunnel engineering construction," *Modern Tunnel Technology*, vol. 53, no. 2, pp. 35–43, 2016.

[27] C. S. Li, Y. K. Liao, and J. F. Ding, "Study on hydrochemical dynamics-fractal index evaluation technique of karst development in tunnel," *Modern Tunnelling Technology*, vol. 54, no. 6, pp. 24–31+41, 2017.

[28] Q. Wu, Y. Liu, D. Liu, and W. Zhou, "Prediction of floor water inrush: The application of GIS-based AHP vulnerable index method to donghuantuo coal mine, China," *Rock Mechanics and Rock Engineering*, vol. 44, no. 5, pp. 591–600, 2011.

[29] M. Yan, S. Zhu, and H. Duan, "Risk assessment of water inrush from Ordovician limestone based on analytic hierarchical process modelling and water resistance," *Arabian Journal of Geosciences*, vol. 14, no. 24, p. 2733, 2021.

[30] K. Zhou, "Water richness zoning and evaluation of the coal seam roof aquifer based on AHP and multisource geological information fusion," *Geofluids*, vol. 2021, Article ID 1097600, 16 pages, 2021.

[31] L. Xiao, Q. Wu, C. Niu et al., "Application of a new evaluation method for floor water inrush risk from the Ordovician fissure confined aquifer in Xiayukou coal mine, Shanxi, China," *Carbonates and Evaporites*, vol. 35, no. 3, 2020.

Hindawi
Mathematical Problems in Engineering
Volume 2022, Article ID 7222370, 10 pages
https://doi.org/10.1155/2022/7222370

Research Article

Experimental Study of 3D Micro-CT on Meso-Structure Evolution of Coal Samples with Different Coal Grades under the Action of Temperature

Jianlin Xie,[1] **Dong Zhao**,[2] **and Pengwei Li**[1]

[1]*College of Environment and Safety, Taiyuan University of Science and Technology, Taiyuan, Shanxi 030024, China*
[2]*College of Mining Engineering, Taiyuan University of Technology, Taiyuan, Shanxi 030024, China*

Correspondence should be addressed to Jianlin Xie; tyxiejianlin@163.com

Received 10 February 2022; Accepted 23 March 2022; Published 26 April 2022

Academic Editor: Fuqiang Ren

In the three-dimensional micro-CT experiment system, the room temperature is set to 300°C when different coal samples (lignite, anthracite, lean coal and gas coal) are observed for mesoscopic observation. The evolution regularity of mesoscopic structure is analyzed according to the CT scan of coal samples under different temperatures and three sections of scanning images, and by ImageJ image processing software, image processing, and analysis of the characteristics of the profile, the following conclusions are obtained: (1) Coal specimen will have an overall expansion deformation along with the rise of temperature. The sample expansion can be divided into two types: outward expansion and inward expansion. Outward expansion means that the expansion of the skeleton extends outward from the adjacent pores, while inward expansion means that the solid skeleton intrudes into the adjacent pores. When the temperature rises, the outward expansion and inward expansion occur simultaneously. The dominant expansion mode is influenced by the type of coal sample and the temperature value. (2) With the increase of temperature, coal and anthracite coal specimen pore fissure structure shows an expansion tendency before contraction, while gas coal and lean coal show reverse patterns; in addition to the above the reason of the difference vitrinite differences, one must also consider selected specimen original porosity and mechanical physical properties, such as a combination of other factors. (3) In the temperature range of 100–200°C, when the temperature increases at the same rate, lignite porosity increases the most, followed by gas coal, lean coal, and anthracite. (4) There are certain differences in the variation trends of the pixel proportions of the three sections of the coal specimen, and the temperature values of the three curves at the maximum pixel point are also different, which indicates that the expansion of each point in the coal specimen with the change of temperature is not completely synchronous, and the physical and mechanical properties of the sample are heterogeneous.

1. Introduction

The pore and fissure structure of the coal body plays a vital role in the permeability of the coal body. The fissure is the main channel for seepage and connects countless pores around it. In coal, the fissure degree is several to tens of times smaller than the porosity, while the fissure permeability is several orders of magnitude larger than the pore permeability. Therefore, increasing the coal fissure degree can greatly increase the coal permeability, thereby increasing coal seam gas drainage efficiency [1–6]. Existing studies have shown that temperature has a great influence on the generation, development, and expansion of pores and cracks in coal. The effect of temperature on coal and rock is related to coal type, physical structure of the section, components involved, and heating temperature of coal. Many scholars have carried out a large number of detailed experiments and obtained valuable results from the genesis and classification of coal pores and fissures based on the influence of temperature on the pore structure and permeability of coal and rock masses [7–12].

Gan et al. [8] classifies the pores of coal body by their genesis and divides pores into intermolecular pores, coal plant pores, crack pores, and thermogenic pores. Thermal factors are regarded as a type of pores. Qi [9] divided coal pores into: dissolution pores, mold pores, plant tissue

pores, intergranular pores, and intercrystalline pores. Zhang [10] studied a large number of coal samples by means of scanning electron microscopy and divided the coal pores into primary pores (a few to tens of microns), metamorphic pores, exogenous pores, and mineral pores. Primary pores refer to pores that have been formed when coal is deposited, mainly including cell pores and inter-chip pores. Metamorphic pores are the pores formed by various physical and chemical processes during the metamorphic process of coal. There are mainly interchain pores (the pore diameter is between 0.01 and 0.13 μm) and pores (the pore diameter is between 0.1 and 3 μm). Exogenous pores refer to the pores formed by the influence of external factors after coal is consolidated and formed into rock. It mainly includes horn-grain pores (aperture diameter of 2 ~ 103 μm), granular pores (aperture diameter between 0.5 and 5 μm), and friction pores. Mineral pores refer to the pores created by the existence of minerals. The size of the pores is in the order of micrometers, including dissolution pores, mold pores, and intercrystalline pores. Yan et al. [11] applied the μCT225kVFCB high-precision CT experimental system to study the influence of coal rank, ash content, and coal microscopic components on the pore structure of coal through micro-CT experiments. The relationship between the porosity, permeability, and fractal dimension of the coal sample is obtained. It is pointed out that the coal type minerals will affect the porosity and average particle size of the coal body. Indicators of sexual evaluation. Zhang et al. [12] analyzed the influence of structural deformation on coal pore and fissure structure through CT scanning experiments of four types of coal samples, and pointed out that compared with primary coal samples, a large number of exogenous pores and micro-fractures are easily formed in the fragmentation stage of coal, and the average pore size is. The mixed surface porosity is also the largest; the mylonitic coal is prone to plastic deformation at the stage of mylonitic coal, and the mylonitic material develops and fills the pores, and the average pore size and surface porosity are the smallest. Wang et al. [13] established a computational digital model that simulates the pore structure of coal based on CT three-dimensional reconstruction technology and put forward many intuitive research methods in the use of CT three-dimensional digital technology, which broadened the application of CT technology. Chen Tonggang et al. used X-CT technology to reconstruct the pore and fissure structure of the experimental coal sample, including minerals, and pointed out that the CT number and porosity have a good correlation, which can be used to analyze and evaluate the pores, fissures, and spaces in the coal form. Yuet al. [14, 15] used CT technology to study the law of lean coal pores and fissures with temperature and pointed out that the small pores of lean coal connect and expand into large pore clusters at 300°C, from 180°C ~ . At 600°C, the number of pores decreases first and then increases. Song et al. [16] used micro-CT technology to test the seepage pores of coal samples for mesoscopic characterization and pointed out that the number of coal pores, surface porosity, etc. increase with the increase of structural deformation, and the local powdery mylonite of coal particles will be filled. Part of the coal body's pores causes the average pore size of the coal body to decrease.

To sum up, the evolution characteristics of mesostructure of coal samples of different coal grades under the action of temperature need to be further studied. In this article, the microstructure evolution characteristics of lignite, anthracite, lean coal, and gas coal during real-time heating in the range of room temperature~300°C were studied by micro-CT technique, aiming to reveal the microstructure evolution law of different coal grade samples under the effect of temperature.

2. Experimental System and Process

2.1. Experimental Method. CT scanning can effectively distinguish pores and solid skeleton. Even after the CT image of the specimen is processed by gray level, it can be further quantitatively analyzed with gray level 0–255 to quantitatively express the ratio of pores and solid skeleton on the corresponding point of the specimen represented by a single pixel point. That is, for the heating of the specimen, the change of the shape of the internal pores and skeleton of the tested object can be studied by the change of the sum of pixels in different color scales of the image, and the change of permeability can be studied indirectly.

The amount of data scanned by CT are relatively large. Three fixed sections of the specimen are selected for analysis, namely the section 5 mm from both ends of the specimen in the radial direction and the midpoint section. The experiments are carried out at room temperature, 100°C, 200°C, and 300°C. The scanned pattern is grayed, and the influence process of temperature change on the formation, connection, and expansion of pores and cracks of the specimen is analyzed.

2.2. Experimental System. The test system adopts μCT225kVFCB high-precision micro-CT system of Institute of Mining Technology, Taiyuan University of Technology. As shown in Figure 1, the scanning magnification of the system is 1~400 times, the maximum sample size is 50 mm and the spatial resolution is 0.5 μm. In addition, a self-made atmosphere furnace is used to heat the sample slowly, and the furnace is heated by 300 W furnace wire with temperature control accuracy of ±1°C.

2.3. Sample Preparation. Among the experimental samples, lignite coal samples are selected from Ulanqab mining area in Inner Mongolia, and gas coal, lean coal, and anthracite are selected from Shanxi Coking Coal Zhengli, Ximing, and Lutaishan mines, respectively. After the sample is sent to the laboratory, it is processed into a cylindrical specimen with a bottom diameter of 7 mm and a height of 20 mm by rough specimen and manual fine grinding.

2.4. Experimentation. In the experiment, the specimen was first placed on the micro-CT turntable for CT scanning observation at room temperature. Then the sample was

(a) (b)

Figure 1: μCT225kVFCB high-accuracy micro-CT system. (a) Three-dimensional micro-CT experiment system. (b) Data acquisition and analysis system.

placed in an atmosphere furnace and heated. When the heating temperature was shown to a predetermined temperature, the sample was kept at constant temperature for 30 min, and then cooled to room temperature. The atmosphere furnace was removed to carry out the scanning experiment of the sample at this experimental temperature. During heating, constant temperature, and cooling process, the sample was always under the protection of argon environment. The first temperature point of heating was set as 100°C, then 200°C, and finally 300°C. The change of mesostructure of specimen with the increase of temperature was observed by CT pattern. This experiment focuses on the analysis of three specific faults scanned and studies the changes of pores and fissures of the section under the condition of temperature rise. By combining the changes of its characteristic pores and fissures, the law of permeability changing with temperature is reflected.

3. Meso-Statistical Analysis of Each Section of Coal Sample under Temperature

3.1. Statistical Analysis Principle. For the analysis of CT images, the image of the specimen is theoretically regarded as composed of many very small square grids (pixels). In this way, the different color order of each small grid can reflect the characteristics and differences of solid particles and pore distribution of coal and rock samples. By counting the number of pixels of all color orders in the circle of the specimen image and analyzing the percentage of pixels under the fixed color order, the change of pore cracks in the specimen can be reflected.

With the color level as abscissa and the percentage of pixel number of different color levels as ordinate, it can be obtained from the graph analysis that all pores and the critical part of pores and skeleton can be summarized by describing a pixel point with 0–50 color level value. That is, pixels with a color level value of 0 represent pores, pixels with a color level value of 255 represent solid skeleton, and pixels with a color level value of 0–50 represent areas where porosity and skeleton change critically, and pores are in the majority in this area. The above experimental principles are the basis of statistical calculations.

3.2. Statistical Analysis of Lignite Samples. The three sections of the sample were selected for postprocessing of CT scanning images, and the images of the three sections varying with temperature (room temperature, 100°C, 200°C, and 300°C) are shown in Figure 2.

It can be seen from Figure 2 that the formation, development, and expansion of pores and fractures of lignite coal samples are very obvious in the range of room temperature~300°C, and some fractures even cross the coal samples between 200 and 300°C.

Before 100°C, the coal sample is mainly formed by cracks, and the shape of coal sample hardly changes; After 100°C, the pores and fractures are further expanded and connected, and the expansion develops towards bedding, forming many large channels. These large channels increase the permeability of the coal body. The continuous expansion of the large fractures drives the surrounding pores to further aggravate the intensity of deformation, so that the small fractures directly become pure pores from the transition area between the pores and the coal skeleton. No solid particles will be mixed during this period.

In addition, in the temperature range from room temperature to 100°C, the shape of the coal sample has hardly changed. After 100°C, the shape change of the sample intensifies, but the deformation of the sample is still dominated by internal pore expansion. Figure 2 qualitatively discusses the pore fracture evolution process of lignite samples at room temperature~300°C and carries out color scale quantitative statistics and analysis on the above three sections. The results are shown in Figures 3–5.

Figures 3–5 show the proportion of pixels of each color scale in the three sections of lignite sample at different temperatures. Figure 4(a) shows the cumulative percentage of 0~255 color scale pixels in each section image at room temperature~300°C, and Figure 4(b) shows the percentage of pixels at room temperature~300°C when the color scale values are 20, 30, 40, and 50. It should be noted that when the color scale is 0, it means that the study area is all pores or fractures; when the color scale is 255, it reflects that the research object is coal skeleton (continuum); if the color scale is between 0 and 255, the analysis scope covers both pore and skeleton structures. For the same specimen, the

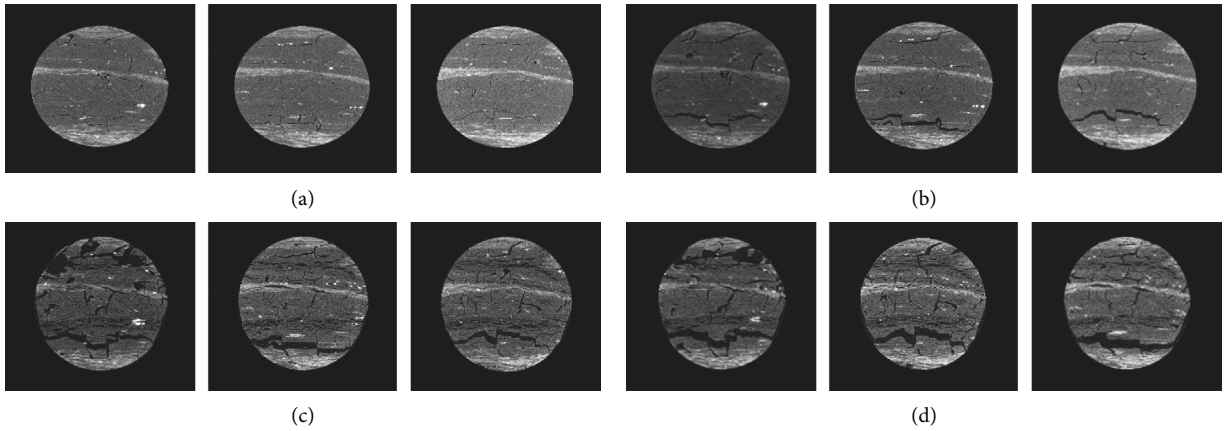

Figure 2: The CT scanned images of lignite test piece. (a) Room temperature section (sections 1, 2, and 3 from left to right). (b) 100°C section (sections 1, 2, and 3 from left to right). (c) 200°C section (sections 1, 2, and 3 from left to right). (d) 300°C section (sections 1, 2, and 3 from left to right).

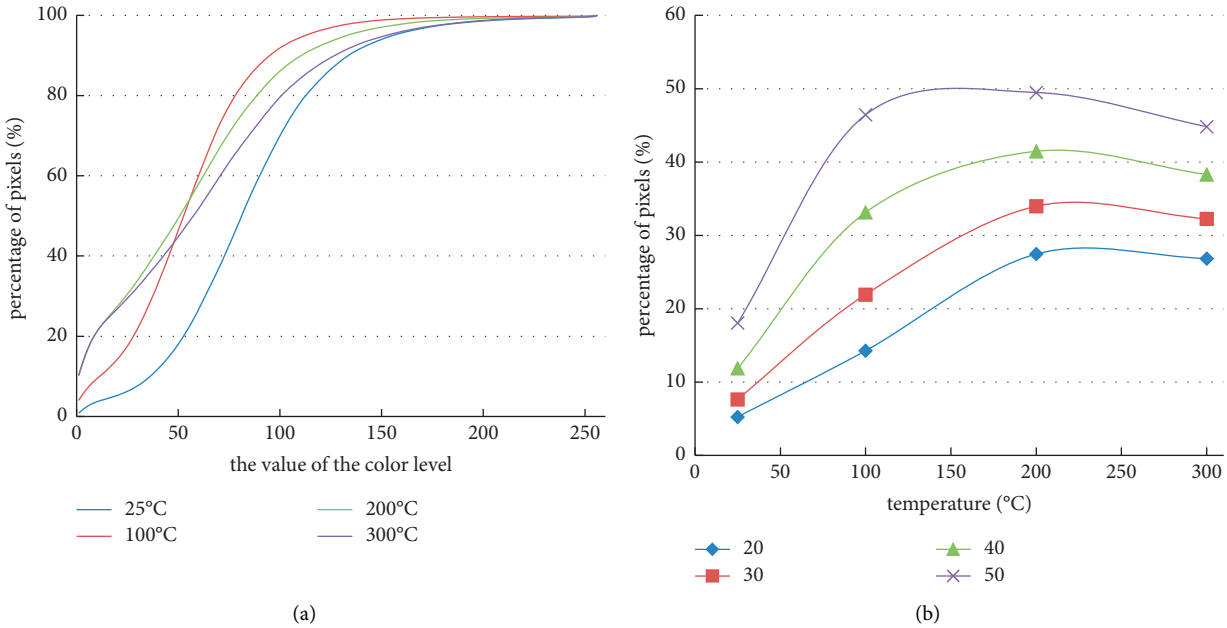

Figure 3: The statistical figure for the section 1 of the lignite sample. (a) Cumulative proportion of pixels with 0 ~ 255 color levels at different temperatures. (b) Pixel ratio graph under specific color gradation with temperature change.

smaller the color order in the regional image range, the larger the proportion of pore structure, and the more serious the coal damage. On the contrary, the better the continuity of the specimen.

According to the above analysis, it can be seen that in Figures 3(a)~5(a), although the CT scanning sections of the test piece are different, the cumulative proportion of pixels in each color scale is generally the same, that is, for normal temperature, the percentage change of pixel value in the range of 0~50 and 200~255 color scale is not large, which means that the color scale values below 50 and above 150 are relatively constant at this time. Correspondingly, when the color scale is between 50 and 200, the pixel cumulative curve rises faster and the percentage ratio changes greatly. The reason is that when the color scale is above 50, the research scope is dominated by pore and fracture structure, while when the color scale is 200, the coal skeleton structure (continuum) has a great advantage, which makes it possible to take the color scale below 50 and above 200 as the measurement standard of pore (fracture) structure and skeleton (continuum) structure at room temperature. In addition, by comparing the cumulative distribution curves of pixels with different temperature scales, it can be found that when the temperature is higher, the proportion of pixels with color scales below 50 also increases It reflects that choosing 50 as the critical level value is appropriate. Based on the above analysis, it can be concluded that the proportion of pore and fracture structures in the sample area below 50 color level is relatively large, and the pore structure of the sample changes rapidly with the increase of temperature in this area. This phenomenon corresponds to the drastic change of

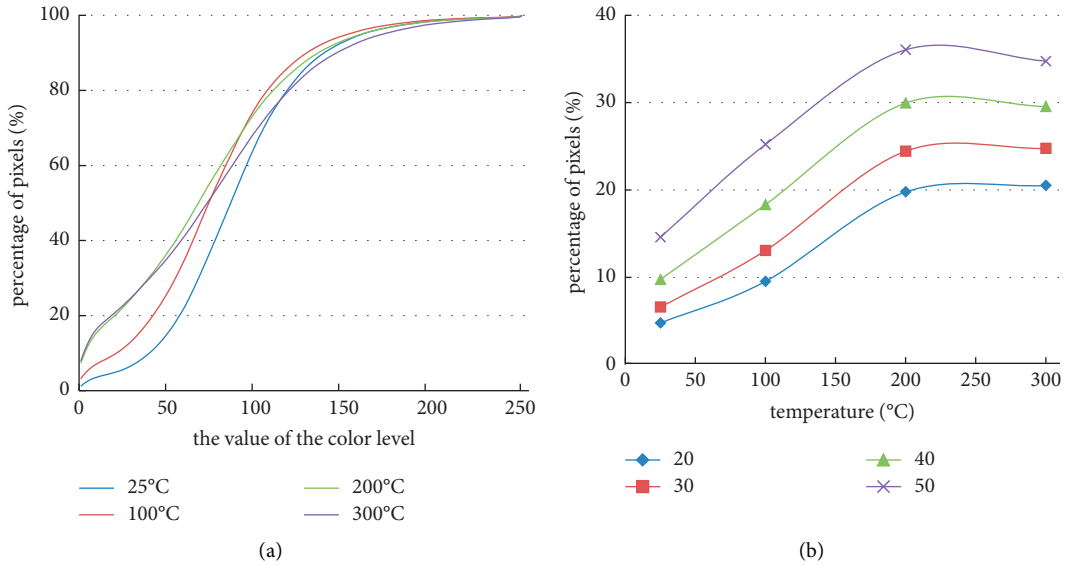

Figure 4: The statistical figure for the section 2 of the lignite sample. (a) Cumulative proportion of pixels with 0 ~ 255 color levels at different temperatures. (b) Pixel ratio graph under specific color gradation with temperature change.

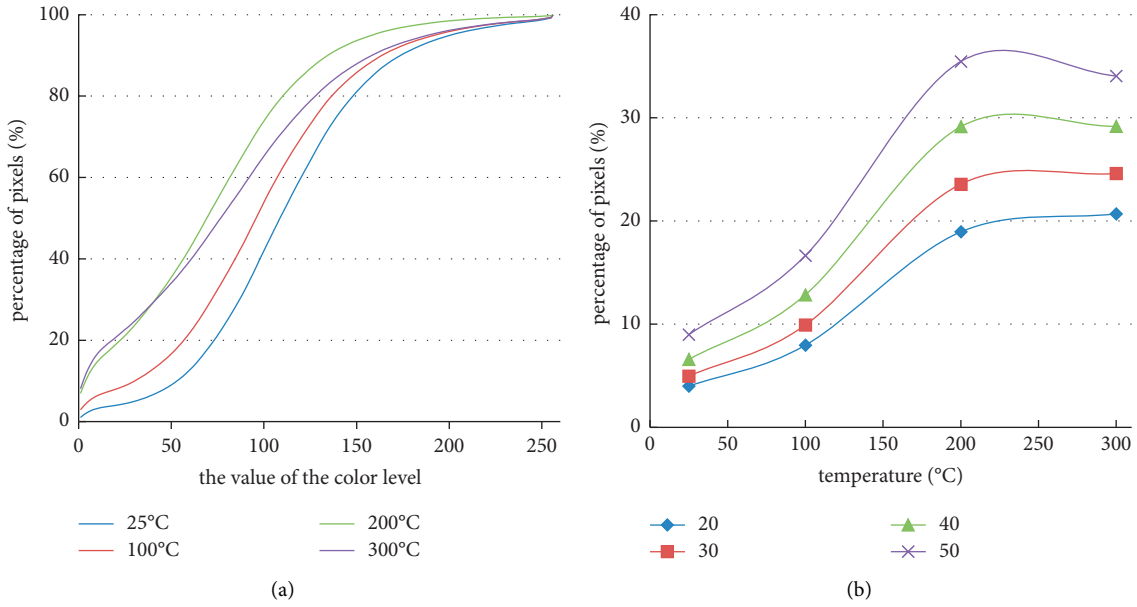

Figure 5: The statistical figure for the section 2 of the lignite sample. (a) Cumulative proportion of pixels with 0 ~ 255 color levels at different temperatures. (b) Pixel ratio graph under specific color gradation with temperature change.

permeability of coal samples in macroscopic state. Obviously, this phenomenon corresponds to the drastic change of coal sample permeability in the macro state.

Next, the change trend of 50 and its nearby color order under different temperature conditions is taken as an example to illustrate the evolution law of pore and fracture structure (Figures 3(b)~5(b)). Similarly, the proportion of color scales in different CT scanning sections is basically the same. Even in the same section, the change trend of each color scale below 50 is almost the same. Before 200°C, the percentage of pixels within the color scale increases gradually with the increase of temperature, and when the temperature exceeds 200°C, the percentage of pixels with color scales of 50 and below shows a negative correlation with the temperature. The reason is that the lignite specimen expands and deforms with the increase of temperature, resulting in the change of proportion. The sample expansion involved here includes the increase of the overall porosity of the specimen with the increase of the pores between some skeletons with the increase of temperature, and the decrease of the overall porosity of the specimen due to the decrease of the pore area due to the intrusion of the solid skeleton into the adjacent pores. With the increase of temperature, these two phenomena occur at the same time. The dominant mode

is affected by coal type, physical structure of section, and temperature factors. Between normal temperature and 200°C, the accumulation of temperature makes the pore and fracture structure of lignite specimen produce, expand, and connect, and the permeability of lignite specimen also increases. When the temperature exceeds 200°C, the lignite specimen skeleton invades the adjacent pores, the expanded pores and fracture structures are squeezed, and the permeability of the sample decreases gradually with the increase of temperature.

In the above analysis process, the cumulative proportion of color scale pixels and temperature change trend of the three sections are basically the same. It should be noted that there are still some differences in the sum of pixels of each section. According to the statistics of the total pixel size of the three sections, as shown in Figure 6, it can be seen that the overall pixel values of the three sections show a trend of increasing first and then decreasing, which verifies the inference that the porosity change is caused by the interaction between the framework and pores of lignite specimen. In addition, the temperature values of the three curves are different when they are located at the pixel maximum point, which reflects that the expansion of temperature changes at each point in the lignite specimen used in the test is not completely synchronous, which is caused by the nonuniformity of physical and mechanical properties of coal.

3.3. Statistical Analysis of Anthracite, Lean Coal, and Gas Coal Samples. Due to the limitation of space, only the change of the sum of pixels in different sections of the coal samples with three coal grades with the increase of temperature is analyzed. As shown in Figure 7, in the range of room temperature to 300°C of anthracite, the total pixels of the three sections are decreasing, indicating that the three sections have a tendency to shrink with the increase of temperature. In the temperature range of 100~200°C, the section pixels have a slight rise, that is, the section area has a slight increase in this temperature range. These phenomena also reflect the law of sample deformation with temperature. Obviously, this phenomenon is obviously different from that of lignite specimens. In addition to the vitrinite difference, the influence of other factors such as the original porosity and mechanical physical properties of the selected specimens should be considered.

As shown in Figure 8, in the range of room temperature~200°C of lean coal, the total pixels of the three sections almost have no change, indicating that with the increase of temperature profile almost has no deformation, at 200°C to 300°C, the total number of pixels decreased sharply, indicating that at this temperature range, the three sections of the coal sample had a shrinkage effect, and the contour shape changed greatly. That is to say, the three sections have a tendency to shrink with the increase of temperature, and the situation of the solid framework in the specimen invading the pores is dominant.

As shown in Figure 9. In the range of room temperature to 100°C, the total pixels of the three sections almost have no change, indicating that the section almost has no deformation with the increase of temperature. In the range of

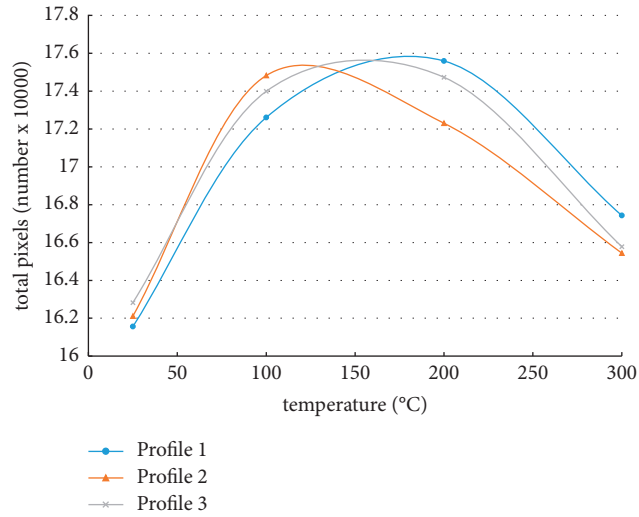

Figure 6: The diagram of pixel variation with the increasing temperature of lignite.

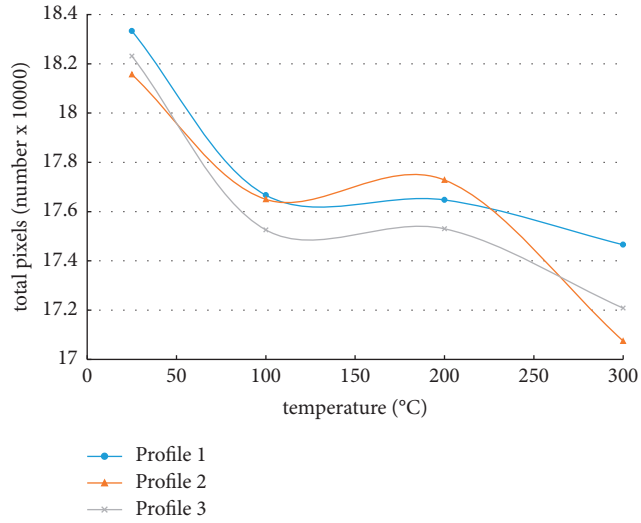

Figure 7: The diagram of pixel variation with the increasing temperature of anthracite.

100°C to 300°C, the sum of pixels decreases sharply, indicating that the three sections of the coal sample have a shrinkage effect in this temperature range. The evolution curves of the gas coal specimen and the lean coal specimen are similar.

4. Variation Patterns of Pore Clusters of Coal Samples of Different Coal Ranks under Temperature

4.1. Analysis Principle. After the CT image is grayed, the image within the range of 0 color order is extracted by the graphics processing software. The analysis of the pixel change can directly reflect the change of the area size. The 0 color order in the sample image is the extraction index, and

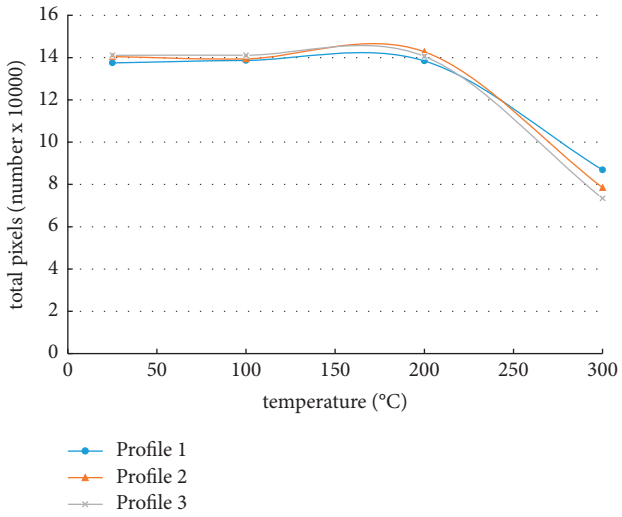

Figure 8: The diagram of pixel variation with the increasing temperature of lean coal.

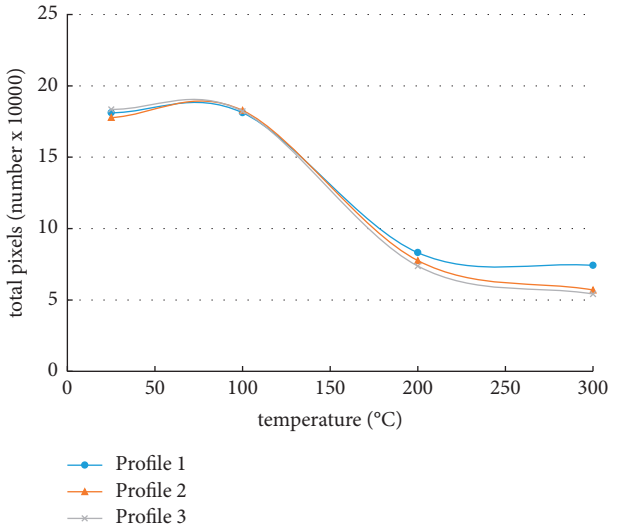

Figure 9: The diagram of pixel variation with the increasing temperature of gas coal.

the score of the 0 color order is the background. All of them are set to 255 color order, so the counting of the 0 color order pixels can reflect the scale change of the pores. The images of lignite, anthracite, lean coal, and gas coal samples were processed according to the standard, and the variation law with temperature was analyzed.

4.2. Change Rule of Lignite Porosity. The change of 0 color pixel of lignite with temperature is shown in Figure 10. From the figure, it can be seen that the number of original and new cracks in sections 1, 2, 3 increased from 7154, 4160, and 7492 at room temperature to 242561, 213543, and 228129 at 300°C, respectively, which increased by 30 times. It can be seen that the temperature has an impact on it. The change of fractures is positively correlated with the change of permeability. The formation, expansion, and connection of

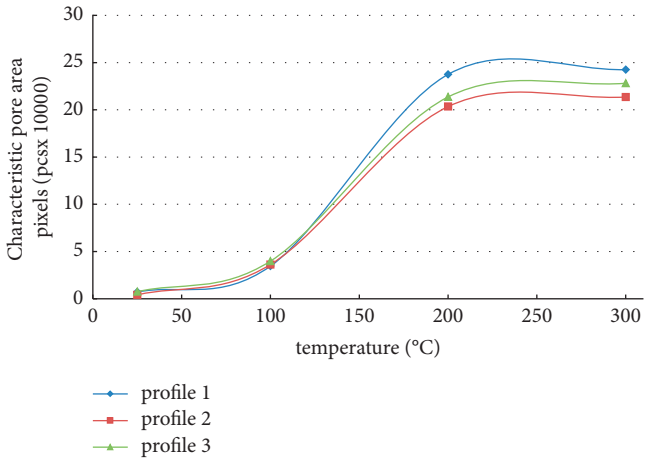

Figure 10: Characteristic pore region pixel number of lignite with the increasing temperature.

fractures merge into large fractures, which will inevitably lead to the increase of coal permeability. From the figure, this situation is very obvious at 200–300°C, so the increase of coal permeability should be tens to millions of times between 200 and 300°C. The change law of pore fracture under the 0 color order of lignite is consistent with that obtained by statistical method in Section 2.2 above.

4.3. Variation of Pore Mass of Anthracite, Lean Coal, and Gas Coal. As shown in Figure 11, there is a change of 0 color pixels of low-value anthracite with temperature. From the experimental data, the number of original and new fracture pixels of sections 1, 2, 3 increases from 134, 606, and 254 at room temperature to 12438, 16842, and 12135 at 300°C, respectively. The pixel increases by 95%~98%, resulting in great changes in macroscopic permeability. Analysis of the reasons, coal samples at room temperature~100°C coal solid particles due to the original cementation, pore fissure change is not obvious, after 100°C, the temperature destroyed its internal cementation structure, resulting in the generation, development, and expansion of cracks, study the law of temperature change is the key to study the anthracite permeability change with temperature.

As shown in Figure 12, the number of original and new fracture pixels in sections 1, 2, 3 increased from 534, 245, and 968 at room temperature to 14783, 30182, and 72731 at 300°C, which increased by 50 times. On the one hand, with the increase of temperature, a large number of micro cracks are generated, developed, and connected, which leads to the increase of the number of fracture pixels. On the other hand, coal pores expand and increase in situ. The increase of permeability at room temperature and 100°C is dominated by the development and expansion of primary fractures. Many new pore cracks were added to the specimens at 200–300°C, and the number of pore pixels was further increased.

As shown in Figure 13, the number of 0 color pixels of gas coal varies with temperature. From the experimental data, it can be seen that coal pixels are large at room temperature~100°C.

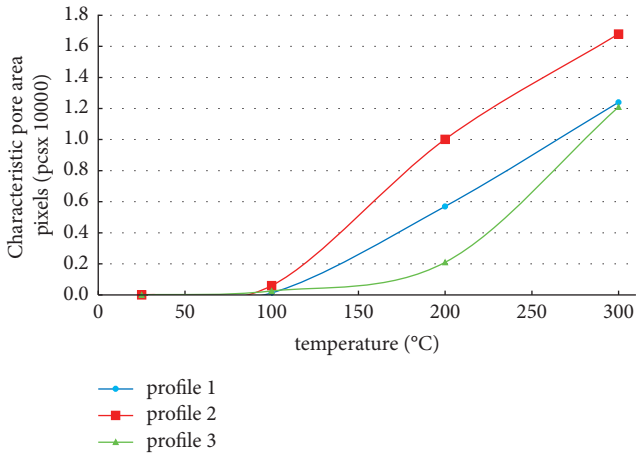

Figure 11: Characteristic pore region pixel number of anthracite with the increasing temperature.

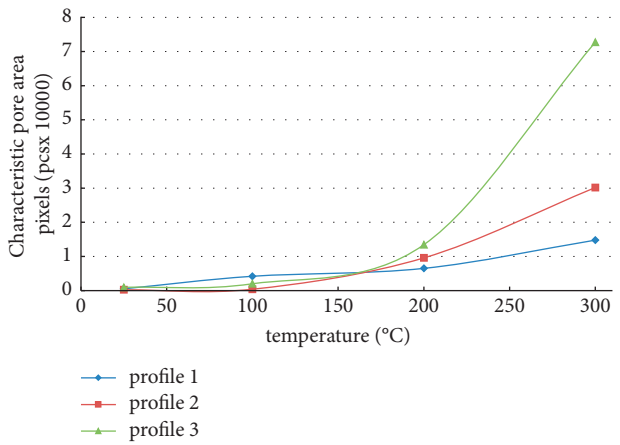

Figure 12: Characteristic pore region pixel number of lean coal with the increasing temperature.

5. Discussion on the Evolution of Coal Pore Structure under Temperature

The coal matrix has thermal expansion characteristics. If the initial porosity of the coal is large under the effect of temperature, the thermal expansion of the coal skeleton will increase the porosity, which further increase the pore pixels of the coal in the CT image. If the initial porosity is small, then too many solid particles per unit volume will be heated and expanded, and will quickly invade and squeeze the adjacent pores, resulting in the decrease in porosity of the specimen. With the increase of temperature, the pore and fissure structure of lignite specimens and anthracite specimens showed a trend of expansion first and then compression, while gas coal and lean coal showed the opposite law. The reason for the above differences except the difference of vitrinite. It is also necessary to consider the combined effect of other factors, such as the original porosity and mechanical and physical properties of the selected sample, that means the change of the pore structure of the coal sample under the action of temperature is related to the coal rank.

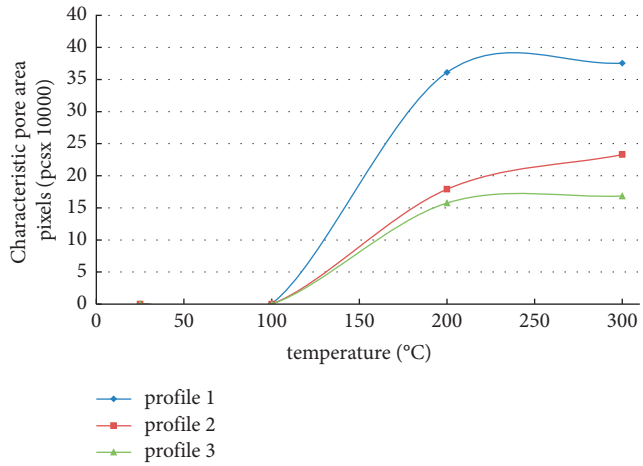

Figure 13: Characteristic pore region pixel number of gas coal with the increasing temperature.

Jianlin and Yangsheng [17]used polarized light microscope to observe the evolution of coal and rock mass pore structure under the action of temperature and found that the pore structure changes obviously under the coexistence of solid matrix and pores, which is consistent with the conclusions of this article. Yaoqinget al. [18] adopted the experimental study of the influence of temperature on the permeability characteristics of lignite and found that before 50°C, when the volumetric stress and pore pressure remain unchanged, the permeability of coal samples will decreases with the increase of temperature. The opposite pattern will appear after 50°C. In addition, it is also found that the permeability fluctuates at very low and very high points with the increase of temperature. It is believed that this fluctuation of permeability is the result of the comparison between the thermal stress and the effective stress of the coal.

Liet al. [19] adopted the permeability of the coal body changes with temperature and stress in the experimental study, found that the permeability changes with the temperature fluctuation, and explained the effect of internal and external expansion caused by the heating of the coal body. The conclusion is consistent with this article.

6. Conclusion

In micro-CT scanning, the three sections of coal samples were scanned at three different temperatures, and then images were processed and analyzed with the help of image processing software. From the experimental results, it is feasible to characterize the development and change of pores and cracks by different color levels of pixel values, and the change of pixels in pores and cracks can also reflect the change of coal permeability. Experimental results show:

The solid skeleton of the coal sample will undergo expansion and deformation with the increase in temperature. On the one hand, this inflated deformation will increase the pores between some skeletons, which further increase the overall porosity of the sample. On the other hand, the pore area will reduce when the solid framework invades into the adjacent pores, leading to the decrease in the overall porosity

of the specimen. These two phenomena occur at the same time as the temperature rises. Which method is dominant depends on the combined effect of coal type, physical structure of the section, and temperature. Ct scanning and image analysis is an effective method to quantitatively describe these phenomena, which can quantitatively analyze the law of porosity change caused by the expansion of solid particles or the change of solid skeleton shape.

As the temperature rises, the pore and fissure structure of the lignite and anthracite specimens appear expands first and then shrinks, while gas coal and lean coal show the opposite pattern. The reason for the above difference except the difference in vitrinite group. The combined effect of the original porosity, mechanical and physical properties, and other factors of the selected specimen should be considered.

In the temperature range of 100–200°C, when the same temperature is increased, the porosity of lignite increases the most in four specimens, followed by gas coal, lean coal, and anthracite.

There is a certain difference in the color-level pixel ratio of the three sections of the coal sample. The temperature values are different when the three curves are located at the pixel maximum point, which explains that the various inside points of coal sample expanded with temperature changes are not completely synchronized, and the physical and mechanical properties of the samples are heterogeneous.

Data Availability

The raw/processed data required to reproduce these findings cannot be shared at this time as the data also form part of an ongoing study.

Conflicts of Interest

The authors declare that they have no conflicts of interest to this work.

Authors' Contributions

Dong Zhao was involved in data curation. Pengwei Li performed investigation. Jianlin Xie reviewed and edited the original draft.

Acknowledgments

The authors greatly acknowledge the financial support from the Key Research and Development Project of Shanxi Province (201603D121031) and Fundamental Research Program of Shanxi Province (201801D121278).

References

[1] G. Wang, D. Han, C. Jiang, and Z. Zhang, "Seepage characteristics of fracture and dead-end pore structure in coal at micro- and meso-scales," *Fuel*, vol. 266, p. 117058, 2020.

[2] J. Pan, Z. Zhang, M. Li, Y. Wu, and K. Wang, "Characteristics of multi-scale pore structure of coal and its influence on permeability," *Natural Gas Industry B*, vol. 6, no. 4, pp. 357–365, 2019.

[3] F. Xin, H. Xu, D. Tang et al., "Pore structure evolution of low-rank coal in China," *International Journal of Coal Geology*, vol. 205, pp. 126–139, 2019.

[4] A. Gerami, P. Mostaghimi, R. T. Armstrong, A. Zamani, and M. E. Warkiani, "A microfluidic framework for studying relative permeability in coal," *International Journal of Coal Geology*, vol. 159, pp. 183–193, 2016.

[5] G. Zou, J. She, S. Peng, Q. Yin, H. Liu, and Y. Che, "Two-dimensional SEM image-based analysis of coal porosity and its pore structure," *International Journal of Coal Science & Technology*, vol. 7, no. 2, pp. 350–361, 2020.

[6] K. Wang, G. Zhang, Y. Wang et al., "A numerical investigation of hydraulic fracturing on coal seam permeability based on PFC-COMSOL coupling method," *International Journal of Coal Science & Technology*, vol. 9, no. 1, pp. 1–17, 2022.

[7] Q. Gan, J. Xu, S. Peng, F. Yan, R. Wang, and G. Cai, "Effects of heating temperature on pore structure evolution of briquette coals," *Fuel*, vol. 296, p. 120651, 2021.

[8] M. Li, D. Wang, and Z. Shao, "Experimental study on changes of pore structure and mechanical properties of sandstone after high-temperature treatment using nuclear magnetic resonance," *Engineering Geology*, vol. 275, p. 105739, 2020.

[9] D. Wang, P. Zhang, and S. Liu, "Experimental study on evolutionary characteristics of pore-fissure structure in coal seam under temperature impact," *Journal of China Coal Society*, vol. 43, no. 12, pp. 3395–3403, 2018.

[10] G. Zou, Q. Zhang, S. Peng et al., "Influence of geological factors on coal permeability in the Sihe coal mine," *International Journal of Coal Science & Technology*, vol. 9, no. 1, pp. 1–13, 2022.

[11] T. Liu, B. Lin, X. Fu, and A. Liu, "Mechanical criterion for coal and gas outburst: a perspective from multiphysics coupling," *International Journal of Coal Science & Technology*, vol. 8, no. 6, pp. 1423–1435, 2021.

[12] H. Yu, H. Jia, S. Liu, Z. Liu, and B. Li, "Macro and micro grouting process and the influence mechanism of cracks in soft coal seam," *International Journal of Coal Science & Technology*, vol. 8, no. 5, pp. 969–982, 2021.

[13] H. Gan, S. P. Nandi, and P. Lwalker, "Nature of the porosity in American coals," *Fuel*, vol. 51, no. 6, pp. 272–277, 1972.

[14] H. A. O. Qi, "On morphological character and origin of micropores in coal," *Journal of China Coal Society*, vol. 12, no. 4, pp. 51–57, 1987.

[15] H. Zhang, "Genetic types of coal pores and their applications," *Journal of China Coal Society*, vol. 26, no. 1, pp. 40–44, 2001.

[16] J.-w. Yan, H.-f. Yao, W. Li, Z.-q. Kang, and Z.-c. Feng, "Pore structure and fractal characteristics of coals by μCT technology," *China MINING Magazine*, vol. 24, no. 6, pp. 151–156, 2015.

[17] X. Zhang, Z. Kang, and H. Yao, "Pore structure analysis of coal with different coal structure based on CT technology," *Coal Mine Safety*, vol. 45, no. 8, pp. 203–206, 2014.

[18] G. Wang, X. Yang, and X. Zhang, "Establishment of digital coal model using computed tomography based on reverse engineering technology and three-dimensional reconstruction," *Rock and Soil Mechanics*, vol. 36, no. 11, pp. 3322–3328+3344, 2015.

[19] Y. Yu, Y. Hu, and W. Liang, "Study on pore characteristics of lean coal at different temperature by CT technology," *Chinese Journal of Geophysics*, vol. 55, no. 2, pp. 637–644, 2012.

[20] Y. Yu, Y. Hu, and W. Liang, "Micro-CT experiment on the thermal cracking law of lean coal," *Journal of China Coal Society*, vol. 35, no. 10, pp. 1696–1700, 2010.

[21] X. Song, Y. Tang, and L. I. Wei, "Advanced characterization of seepage pores in deformed coals based on micro-CT," *Journal of China Coal Society*, vol. 38, no. 03, pp. 435–440, 2013.

[22] X. I. E. jianlin and Z. H. A. O. Yangsheng, "Meso-mechanism of permeability decrease or fluctuation of coal and rock with the temperature increase," *Chinese Journal of Rock Mechanics and Engineering*, vol. 36, no. 3, pp. 543–551, 2017.

[23] H. U. Yaoqing, Z. H. A. O. Yangsheng, and Y. A. N. G. Dong, "Experimental study of effect of temperature on permeability characteristics of lignite," *Chinese Journal of Rock Mechanics and Engineering*, vol. 29, no. 8, pp. 1585–1590, 2010.

[24] Z. Li, X. Xian, and Q. Long, "Experiment study of coal permeability under different temperature and stress," *Journal of China University of Mining and Technology*, vol. 38, no. 4, pp. 523–527, 2009.

Hindawi
Mathematical Problems in Engineering
Volume 2022, Article ID 7528535, 14 pages
https://doi.org/10.1155/2022/7528535

Research Article

Fractal Analysis of Failure Process and Damage Evolution of Jointed Sandstone Based on DIP Technique

ZiQi Liu,[1] **LuLin Zheng**,[1] **Hao Liu**,[2,3] **Chun Zhu**,[4] **WenJiBin Sun**,[1] **XiaoRong Liu**,[1] **Qing Qiu**,[1] **and ZhiBin Hao**[1]

[1]*Mining College, Guizhou University, Guiyang, Guizhou 550025, China*
[2]*Resources and Environment College, Guizhou University, Guiyang, Guizhou, 550025, China*
[3]*Department of Civil and Environmental Engineering, Technical University of Catalonia (UPC), Barcelona 08034, Spain*
[4]*School of Earth Sciences and Engineering, Hohai University, Nanjing 210098, China*

Correspondence should be addressed to LuLin Zheng; llzheng@gzu.edu.cn

Received 14 March 2022; Accepted 7 April 2022; Published 20 April 2022

Academic Editor: Fuqiang Ren

The Lannigou gold mine deposit is mainly composed of calcium-bearing sandstone and siltstone, and there are a lot of microdefects such as joints and cracks in the sandstone. The mesostructure of jointed sandstone makes a difference to the fracture process and mechanical properties. The RFPA^{2D} software and Digital Image Processing Technology (DIP) were used to create a real microscopic structural numerical model of jointed sandstone with varied dip angle prefabricated cracks. A digital image-based rock microscopic scale fracture box dimension algorithm was established with MATLAB software. It is used to analyze the fractal characteristics of the acoustic emission field of unique prefabricated fractured sandstone. This study demonstrates that the mechanical parameter of jointed sandstone with different prefabricated cracks have manifest anisotropy, which includes elastic modulus and compressive strength. When the leaning angle of the cracks increases, they all increase linearly. There are three modes of starting-crack under uniaxial compression: from the peak of the prefabricated crack; from the middle of the prefabricated crack; and from the joint. Damage degree and rupture model are quantitatively represented by the fractal dimension. The more fractal dimensions there are, the more serious the damage, and the more complicated the rupture mode becomes. This research offers a novel method for investigating the evolution of rock microscopic scale fractures. This has to have engineering practical value for in-depth studies of rock fracture, instability, and failure, as well as the mechanisms that cause rock engineering disasters.

1. Introduction

The "Golden Triangle" of Dian, Qian, and Gui is one of China's Carlin-type gold deposit regions, with over 800 tons of gold resources [1]. Lannigou Gold Mine is the largest deposit in the region [2]. The ore types are mainly calcium-bearing sandstone and siltstone, which has good exploration and exploitation potential. Due to the long-term influence of various geological processes, there are an abundance of joints, fissures, and other microdefects in the sandstone in the mining area. The crack initiation, propagation, and run through in the rock are all part of a dynamic evolutionary process. This process affects the strength and stability of the rock under the engineering or the environment. It also results in the formation of complex mesostructured sandstone, complicating its mechanical behavior and damage evolution [3, 4]. The rock mass is distributed with fissures of different dips direction and dips, which will have a significantly affected on the fracture damage mechanism of the rock mass [5]. The mesostructure and internal defects of rock are closely related to the macroscopic deformation of the rock mass during the rock failure process. As a result, studying rock deformation and damage evolution from the standpoint of micromechanics is an important and hot topic in the field of rock mechanics today. This has significant scientific significance and engineering practical significance

for in-depth study of rock fracture, instability, and failure and the occurrence mechanism of rock engineering disasters [6].

Many scholars have been making the study of the initiation and propagation of cracks in rocks and have received a lot of research results. Griffith proposed that the stress concentration near the crack tip of a rock mass with an opening type crack was the lead cause of rock mass rupture [7]. Nemat-Nasse et al. used the method of linear elastic fracture mechanics to study the initiation, propagation, and penetration mechanisms of varying amounts and different spatial arrangements of pretensioned cracks. It also reveals the stress concentration phenomenon caused by the interaction between multiple cracks and free surfaces. A related theoretical model was created. The strength of its interaction factors was analyzed [8]. Liu et al. used the Geo-CAAS system to study the deformation and strength characteristics of rocks with single and multiple random defects under uniaxial compression, and the influence of the position and volume content of the defects on the strength of the rock was analyzed [9]. Wong et al. carried out split failure test on a rock sample containing a precrack. He combined numerical simulation to examine the influence of factors such as sample width, preset crack length, and inclination on the crack initiation, propagation, and failure mode [10]. Liu et al. used real-time laser holographic interferometry and other methods to continuously and dynamically observe the crack propagation and failure process of rock samples, and the changes in the mechanical properties of rock cracks are analyzed [11]. Zhao et al. performed uniaxial compression tests on brittle rock-like specimens with precrack. The global strain field evolution process diagram of the sample is obtained by using digital technology [12–14]. In addition, the crack propagation path and stress field distribution characteristics at different stages of the loading process are analyzed. Under uniaxial compression, Li et al. investigated the acoustic emission characteristics and mechanical behavior of fractured coal samples with various dip angles [15].

Above research results have significant reference value for understanding the failure and damage evolution of fractured rock mass in macroscale. However, it rarely involves the uneven distribution of stress and local failure caused by rock microheterogeneity. Because the microscopic heterogeneity of rock determines its macroscopic fracture process, taking into account, the heterogeneity caused by the material's internal structure in the numerical model will help to reveal the rock's fracture mechanism more deeply.

The study used DIP technique to describe the microscopic inhomogeneity of joint sandstone, which is then combined with the RFPA^{2D} software to create a real microscopic numerical model that took into account different inclination fractured sandstone. The impact of sandstone mesostructure on the macromechanical properties and mesoscale fracture process of fractured sandstones with different dip angles was investigated. The fractal characteristics of sandstone mesoscale fracture acoustic emission distribution and damage evolution process in numerical experiments are discussed in depth. The research results can not just merely enhance the understanding of mechanism of single crack propagation in rock but also provide references for the related research of rock damage and fracture.

2. Finite Element Method for Crack Growth Simulation

2.1. Characterization of the Real Mesostructure. Digital image processing is a new technology of image processing. It entails converting study objects into digital photographs, then analyzing and processing the image information by computer to obtain the required research results. A rectangular matrix of image elements (pixels) constitutes a digital image. Each pixel is an area at which transverse and longitudinal scan lines cross. Each scan line is of equal width, and the brightness, also known as the grayness, of each pixel is represented by an integer. Red (R), green (G), and blue (B), the three basic colors, are comprised in each pixel. Each pixel is made up of R, G, and B functions. As a result, three discrete functions are necessary to mathematically characterize image information in color space. Because it is closely comparable to how humans see color, Hue, Saturation, and Intensity ((brightness) HSI) space is also employed as a substitute for true color space. The predominate wavelength of the color, which is the major color property observed by humans, is represented by the hue component H (with values ranging from 0 to 360). The color purity is represented by the saturation component S (which ranges from 0 to 1). Only the brightness or color brightness is represented by luminance component I (from 0 to 1). This is a more humane way of describing color.

The geometric shape and spatial distribution of the material's mesocomponent are differentiated by digital image processing technologies using gray and color differences. The difference in brightness and color of distinct media in the rock is thresholded using this approach. It can divide each medium's distribution to provide the material's nonuniformity characterization image [16, 17]. Figure 1(a) shows a two-dimensional CT slice acquired from Tianjin Sanying Company's high-resolution CT scanning of a sandstone sample. Found by CT scanning experiment that sandstone mainly contains two kinds of mineral media, named the sandstone matrix and calcite, and the image pixels are 200 pixels × 500 pixels and the actual size is 40 mm × 100 mm, and it is a 24 bit color image in BMP format. The color change of the image is not obvious. Thus, image processing to stretch contrast in order to increase the tonal differentiation between the features was conducted using multithreshold segmentation by assessing the fluctuation in values of Intensity (I) in the HIS color space. Figure 1(a) shows the AA′ scan line passing through the mineral medium, and Figure 1(b) shows the sandstone surface scan curve. The I value of sandstone is below 150, and the I value of calcite fluctuates is above 150. After a series of observations and experiments, the study settles on I = 150 as the image splitting threshold. Figure 1(c) is the result of performing threshold segmentation on the image of Figure 1(a), where green represents joints (calcite) and dark blue represents sandstone. The spatial distribution and shape of calcite in the sandstone can be seen more precisely using

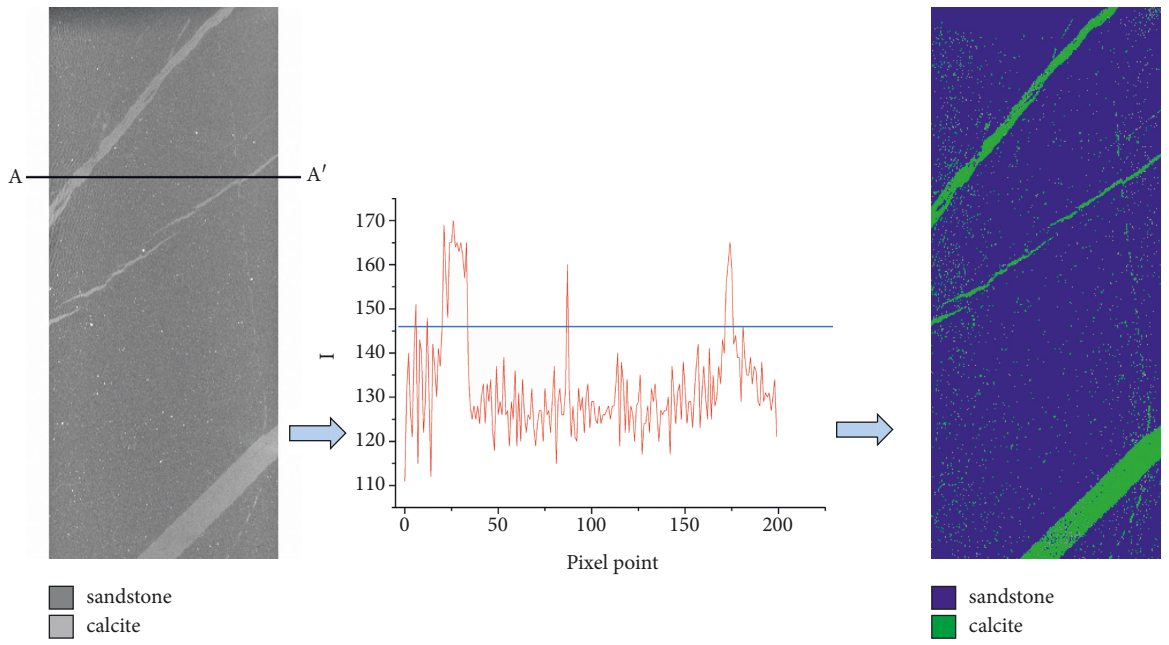

FIGURE 1: Digital image characterization of jointed sandstone. (a) Two-dimensional CT slice. (b) Variation in the I value along scan line AA′. (c) Threshold-segmentation characterization image of sandstone.

the characterization imagery derived through threshold segmentation.

2.2. The Damage Constitutive Relation on the Mesoscale. The change of elastic modulus of strain equivalence hypothesis defines the damage variable in RFPA^{2D}. When a material is damaged by an external force, the damage constitutive relationship can be described as [18, 19]

$$E = (1 - \omega)E0, \tag{1}$$

where E_0 is the undamaged material's elastic modulus, E is the damaged material's elastic modulus, and ω is the damage variable.

Because the sandstone's tensile strength is much lower than its compressive strength, we used the maximum tensile stress and Mohr–Coulomb failure/shear strength as element failure criteria, and Figure 2 shows the mesodamage constitutive relationship. There is no damage at first because the stress-strain curve is linearly elastic. Brittle damage occurs when the maximum tensile strain is attained in the meso-element. The principal failure mode of brittle rocks is tensile-induced failure. When the tensile stress reaches the element's tensile strength (ft), damage occurs according to the main damage criteria. The tensile damage function is written as follows [20]:

$$F^{-}(\sigma) = \sigma_3 + f_t = 0, \tag{2}$$

where the primary stress vector is σ. Under uniaxial tension, the mesoscopic element's constitutive relationship is illustrated in the third quadrant of Figure 2, and can be expressed as follows [21]:

$$\omega = \begin{cases} 0, & \varepsilon_{t0} \le \varepsilon < 0, \\ 1 - \dfrac{\lambda \varepsilon t0}{\varepsilon}, & \varepsilon_{tl} \le \varepsilon < 0, \\ 1, & \varepsilon \le \varepsilon_{tl}, \end{cases} \tag{3}$$

where λ denotes the element's residual intensity coefficient, which is defined as $f_{tr} = \lambda f_t$ (where f_t is the mesoscopic element's tensile strength and f_{tr} is the residual strength at the element's initial tensile failure), and εtl is the element's ultimate tensile strain. The element approaches the state of tensile fracture when its uniaxial tensile strain reaches the ultimate tensile strain, and η is the ultimate strain coefficient, which is formally specified as $\varepsilon tl = \eta \varepsilon t0$. $\varepsilon t0$ is the tensile strain associated with the elastic limit, also known as the tensile failure strain threshold, and it is calculated as follows [22]:

$$\varepsilon_{t0} = \frac{-f_t}{E_0}. \tag{4}$$

The Mohr–Coulomb criterion is employed as the second failure criterion for mesoscopic elements under uniaxial compression conditions, as seen in the first quadrant of Figure 2, depicting damage to elements under compression or shear stress [23]:

$$F^{+}(\sigma) = \sigma 1 - \sigma 3 \frac{1 + \sin \phi}{1 - \sin \phi} - f_c = 0, \tag{5}$$

where φ represents the friction angle, σ_1 and σ_3 represent the primary stresses, and fc represents the uniaxial compressive

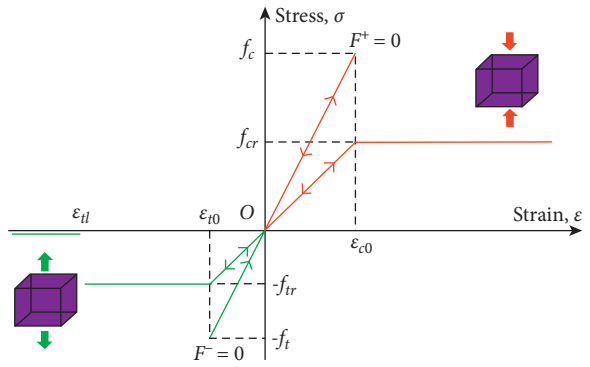

Figure 2: Constitutive Relation for mesoelement damage.

strength. Under uniaxial compression, the damage variable ε of element can be represented as follows [24, 25]:

$$\omega = \begin{cases} 0, & \varepsilon < \varepsilon_{c0}, \\ 1 - \dfrac{\lambda \varepsilon_{c0}}{\varepsilon}, & \varepsilon \geq \varepsilon_{c0}, \end{cases} \tag{6}$$

where λ represents the residual strength coefficient, defined as $ftr/ft = fcr/fc = \lambda$, and $\varepsilon t0$ represents the compressive strain at the elastic limit, which can be calculated as [24, 25]:

$$\varepsilon_{c0} = \frac{f_c}{E_0}. \tag{7}$$

2.3. Establishment of Numerical Simulation. The mesoscopic fracture process of jointed sandstone was simulated using RFPA2D software and digital image processing technology (see Section 2.1 of this article) in this work. Through two-dimensional FEM, RFPA^{2D} can model the mesoscopic failure mechanism of rock [16, 17, 22–25], and Section 2.2 shows the constitutive model of damage to the element. The actual size of this experimental model is 40 mm × 100 mm. The image is divided into 200 × 500 and 100,000 pixels, and the whole characterization image is transformed into 100,000 finite element meshes. Each finite element grid can characterize different mesoscopic materials in the sandstone sample (see Figure 3). The higher the brightness, the greater the elastic modulus. According to the characterized color and brightness, each material component is assigned a parameter value and the material parameters of each microscopic medium are shown in Table 1 [26]. This model analyses the inhomogeneity of sandstone and calcite, while the mechanical parameters of the mesoelements are assigned using the Monte-Carlo technique [27, 28].

To investigate the differences in mechanical characteristics of jointed sandstones with varying inclination angles cracks, as well as the impact of sandstone mesoscopic heterogeneity on the evolution of macrofracture damage. To ensure that the image's underlying medium remains unchanged, this experiment created seven groups of cracks with varying dip angles ($\alpha = 0^\circ, 15^\circ, 30^\circ, 45^\circ, 60^\circ, 75^\circ, 90^\circ$). α is the angle formed by the horizontal direction and the fissure

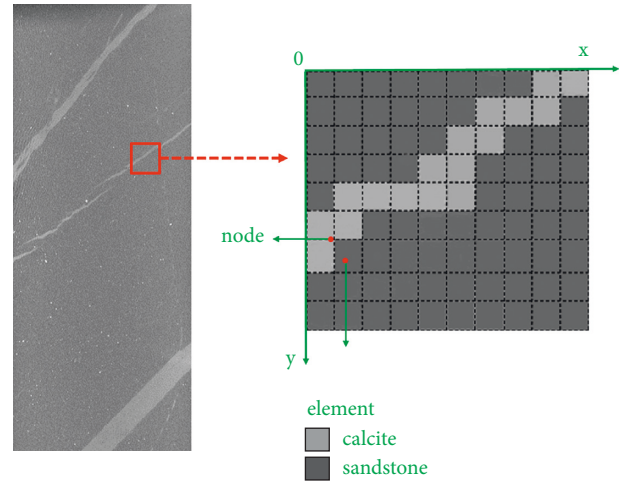

Figure 3: Mesh of finite element microscopic of rock samples.

that has been prefabricated (Figure 4). The prefabricated crack is 14 mm long and 1 mm wide, which is contained in the middle of the jointed sandstone (Figure 4). Figure 5 is a simplified diagram of the numerical model loading. The plane strain analysis is used to simulate. The numerical model utilizes axial displacement loading, with the initial displacement set to 0.001 mm, the single-step displacement increment set to 0.0005 mm, and the loading stopping when the specimen is failure. It is presumed that the elastic modulus and strength of sandstone and calcite mesoscale elements obey the Weibull random distribution [29]:

$$f(u) = \frac{m}{u_0}\left(\frac{u}{u_0}\right)^{m-1} \exp\left(-\frac{u}{u_0}\right)^m, \tag{8}$$

where u_0 denotes the average of the mesoelement parameters; u represents the properties of the mesoelements, such as elastic modulus or strength; m represents the homogeneity of material, the greater the homogeneity m, the more uniform the material.

3. Results and Discussion

3.1. Sandstone Mechanical under Uniaxial Compression. The distribution of primary stress and elastic modulus during the initial stage of loading when $\alpha = 45^\circ$ is shown in Figure 6. The brighter the figure, the greater the stress. Through comparison, it is found that the stress distribution in the microstructure of sandstone is uneven. At the tip of the prefabricated fracture and the crucial surface (relatively low mechanical surface) of the calcite vein and sandstone, the stress concentration distribution is more visible. This demonstrates that the presence of internal cracks in sandstone, as well as the heterogeneity of the mesostructure, has a significant impact on stress distribution.

The elastic modulus and compressive strength simulation results of seven sets of fractures with varied dip angles in jointed sandstone are shown in Table 2. The elastic modulus and compressive strength of numerical samples varied significantly, as demonstrated in Figure 7, with increasing crack inclination, the specimen's compressive strength

Table 1: Material mechanical parameters of jointed sandstone.

Material	Elastic modulus (GPa)	Compressive strength (MPa)	Poisson ratio	Compression-tension ratio	Internal friction angle (C°)
Sandstone	108.2	118	0.16	14	35
Calcite	80.5	101	0.303	11	30

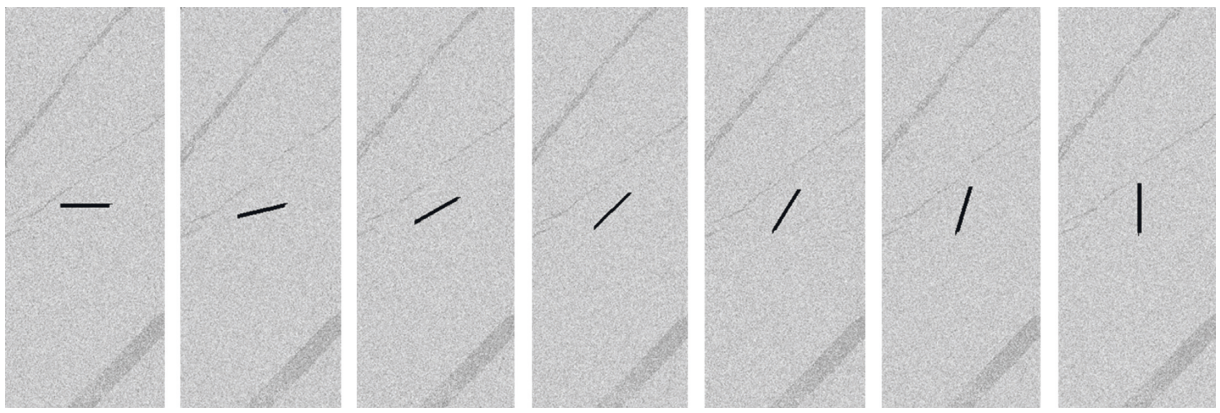

Figure 4: Internal fissures in jointed sandstone with various dip angles.

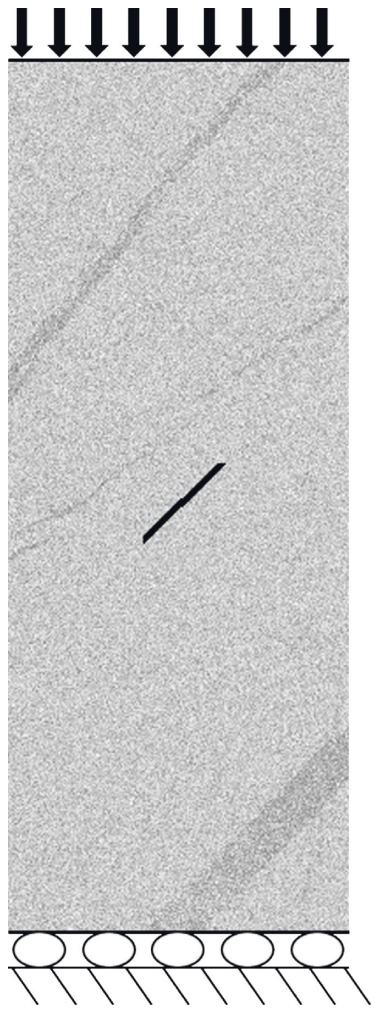

Figure 5: A schematic illustration of the numerical model's mechanical loading model.

increases linearly. This is owing to the sandstone's weak calcite cementation, which generates significant anisotropy in its compressive strength. The numerical simulation results are consistent with the research conclusions of Li et al. [15], indicating that the numerical simulation results obtained in this study are reliable. Sandstone's compressive strength peaks at 64.32 MPa when the angle is 90°; it reaches the minimum when the angle is 0°, which is 32.27 MPa, and the difference between the minimum and maximum is 32.05 MPa. The specimen's elastic modulus grows linearly as the crack inclination angle increases. The elastic modulus reaches the maximum value at $\alpha = 90°$, which is 107.74 GPa; it reaches the minimum value at $\alpha = 0°$, which is 82.49 GPa, with a difference of 25.25 GPA between the minimum and maximum value.

3.2. Fracture Evolution Process Analysis. Figure 8 depicts the progression of the numerical sample's acoustic emission and elastic modulus during the fracture process. The color green denotes a compression-shear failure in the present loading step element. The red indicates the tensile failure, and the black indicates the complete failure. When $\alpha = 0°$, the cracks began to sprout, extended perpendicular to the center of the prefabricated fractures, and eventually penetrated, as seen in Figure 8. Tensile stress causes wing cracks to form and spread, as seen in the AE diagram, and ultimately resulted in axial splitting failure. When $\alpha = 15°$, the wing crack is located about $^1/_4$ of the distance from the tip of the prefabricated crack. And the secondary wing cracks that have formed around the lower-end wing crack are all propagating along the weak surface. Tensile stress initiates and propagates wing cracks, which dominate the macroscopic secondary wing cracks on the specimen's weak surface at the right lower corner. As the load increases, upper secondary wing cracks

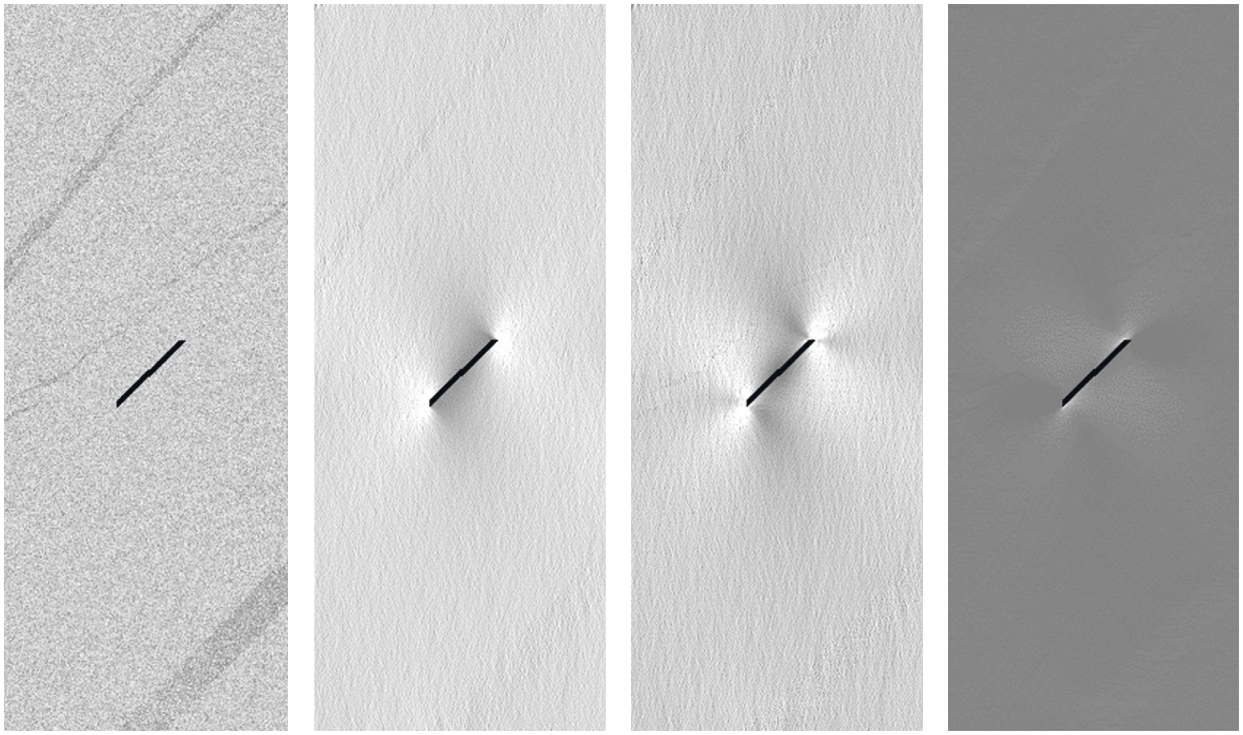

Figure 6: Elastic modulus and internal principal stress distribution in sandstone during the initial loading stage. (a) Elastic modulus; (b) max principal; (c) maximum shear stress; (d) minimum principal stress.

Table 2: Results of numerical sample simulations for compressive strength and elastic modulus.

Crack dip angle (°)	Compressive strength (MPa)	Elastic modulus (GPa)
$\alpha = 0^\circ$	32.27	82.49
$\alpha = 15^\circ$	35.01	87.20
$\alpha = 30^\circ$	40.33	93.54
$\alpha = 45^\circ$	42.71	98.62
$\alpha = 60^\circ$	49.75	101.34
$\alpha = 75^\circ$	56.30	103.23
$\alpha = 90^\circ$	64.32	107.74

begin to crack, and the wing cracks near the tips of the prefabricated cracks eventually spread the joints in a straight line. Moreover, the upper end near the wing cracks and the cementation point (weak surface) of the sandstone produce shear failure and cause funnel-shaped damage between joints and cracks. The generation of macroscopic shear zones in sandstone was associated with the accumulation of tensile failure elements, as seen in Figure 8(b), and the fractures finally penetrated. When $\alpha = 30^\circ$ and $\alpha = 45^\circ$, the wing crack starts at the tip of the prefabricated crack and propagates along the direction perpendicular to the tip of the prefabricated crack. The crack development trend of the two models in the early stage was similar. However, with the increase of load, a wing crack was initiated near the weak surface of the lower right part of the prefabricated crack at $\alpha = 45^\circ$. Due to the hindrance action of the internal sandstone matrix, the crack did not continue to expand. Instead, the macro secondary wing crack was suddenly initiated at the upper left part of the crack tip. Because tensile stress is constantly acting at the tip of the wing crack, the final specimens will undergo shear failure along the wing cracks and joint ends. In the later stage, the secondary wing cracks will penetrate the specimen, causing it to split axially. When $\alpha = 60^\circ$, the wing cracks begin to fracture along the prefabricated crack's tip and expand in the direction of the maximum primary stress. With the increase of load, multiple intermittent secondary cracks are initiated in the opposite direction of the wing crack that has already expanded in the lower part of the prefabricated crack. Furthermore, a macroscopic shear zone is also generated, causing the crack to penetrate. When $\alpha = 75^\circ$, the propagation path of the wing crack at both ends of the fracture is similar, but the crack propagation at the lower part is faster. With the increase of load, the lower left part begins to rupture in patches, meantime the upper part breaks in shear. When $\alpha = 90^\circ$, cracks initiated at the upper and lower joints of the specimen, and the prefabricated crack tip did not produce a significant mechanical response, which is different from the research of Li et al. [15]. In the study by Li et al. [15], the crack started along the tip of the prefabricated crack and caused the final penetration to produce axial splitting failure. Because this study considered the microscopic uniformity of the rock, the crack along the weak surface initiation and expansion occurs at the place, which eventually leads to splitting and failure of the sample.

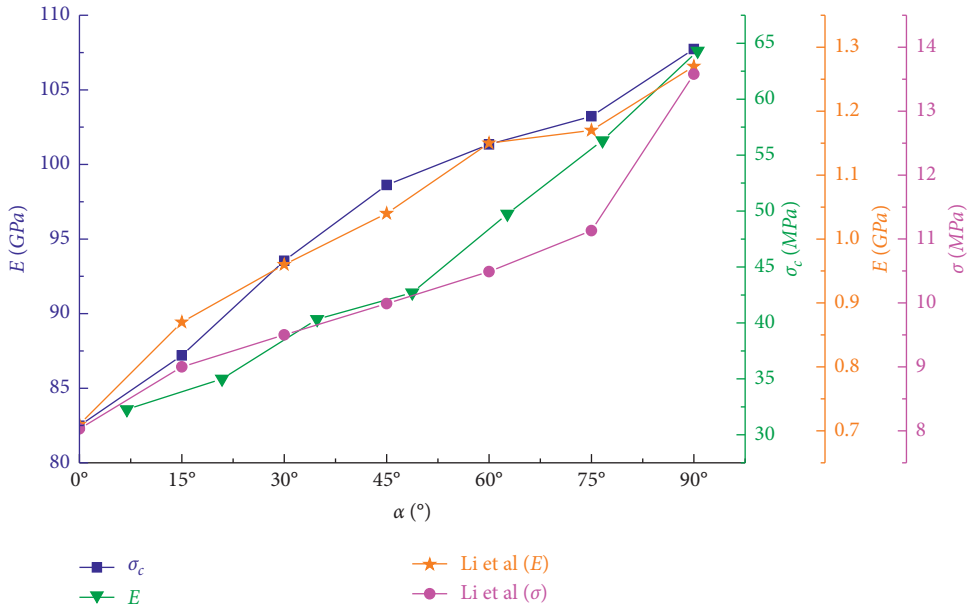

Figure 7: Numerical model compressive strength and elastic modulus.

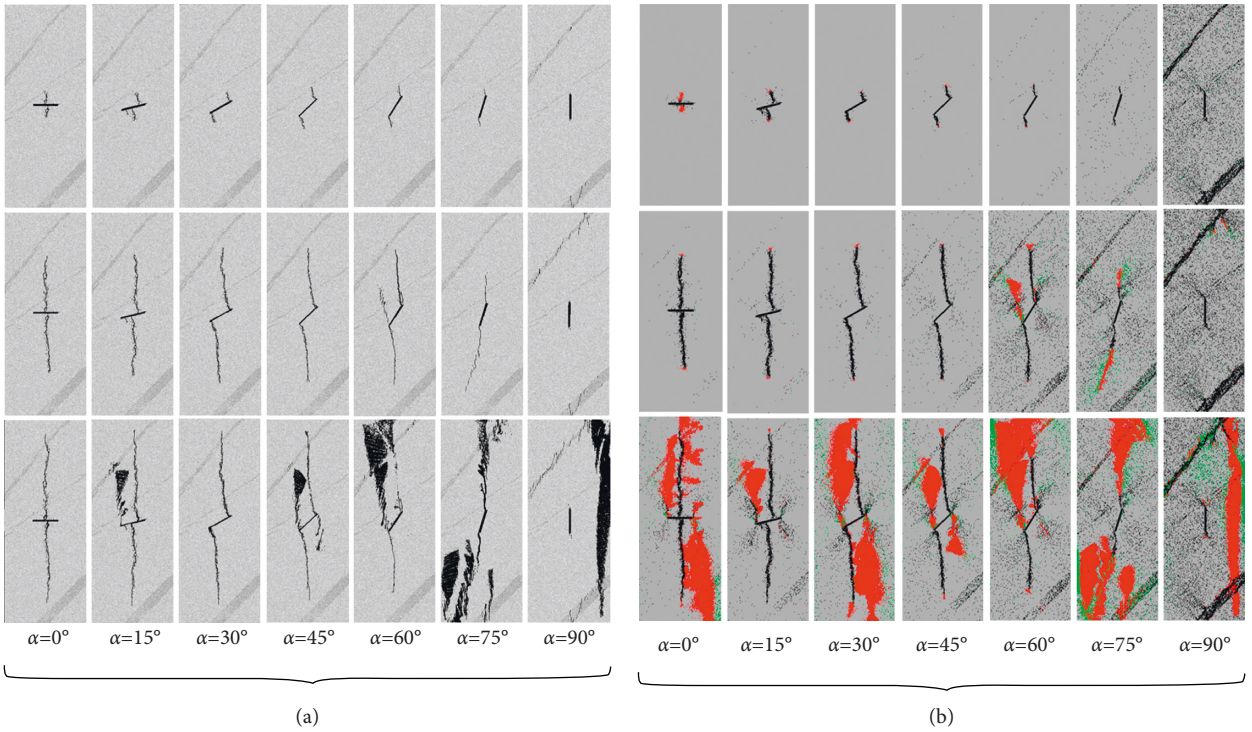

Figure 8: The fracture process' acoustic emission development and elastic modulus diagram. (a) Elastic modulus evolution diagram of sandstone fracture process; (b) AE evolution diagram of sandstone fracture process.

3.3. Analysis on the Evolution Characteristics of Acoustic Emission Distribution. Acoustic emission (AE) is a transient elastic wave caused by the quick release of sound source energy as microcracks in the rock form and expand. Every microscopic fracture will produce acoustic emission phenomenon, and it is a measurable response of rock deformation under load, as a result, it is a useful tool for studying how rock's interior damage develops [30]. The failure of each element is regarded to be the source of an acoustic event in RFPA^{2D}. RFPA^{2D} can be utilized to model acoustic emission activities because the rock discharges its stored elastic energy all through the fracture process [16–18]. As the rock fracture process can be characterized by the acoustic emission evolution, the damage progression characteristics of the rock can be investigated in depth by measuring the number of damaged elements and the released energy. The relationship

among the AE energy, stress, and accumulated AE energy of the specimen under different loading conditions with the loading step is shown in Figure 9.

The load-step number and acoustic emission-step number curve of the specimen is related to its failure mode. At the initial stage of loading, since there is no element damage, the accumulated AE energy and the AE count are both 0. The stress increases linearly when the loading step is increased. There is a visible stress reduction after peak strength, yet there is still residual strength.

There are two situations in which the process takes place: The rupture modes of $\alpha = 0^{\circ}$ and $\alpha = 30^{\circ}$ are roughly the same. When the load is located in the elastic stage, the AE signal has appeared. At the same time, element damage occurs inside the sample, and a small sharp increase in AE occurs successively. As the load increases, dense microcracks and acoustic emission signals appear in the sample. When the load reaches the peak stress, the microcracks extend and expand, and the cumulative AE increases roughly exponentially. After the peak stress, stress enters the falling stage, and the microcracks in the sample rapidly expand until they penetrate. There are still many acoustic emission events, and the sample is not completely destroyed. There was no acoustic emission signal in the other samples at the beginning of loading. With the load is continuously applied, when the stress approaches its maximal value, the AE count rises sharply and reaches its maximum. At this time, the crack extends rapidly, the internal crack of the sample penetrates, and the sample is completely destroyed. After the peak, there is still a slight surge in acoustic emission. When $\alpha = 90^{\circ}$, the sample penetrates instantaneously at the peak stress, and the internal damage is the most severe (Figure 9(g)).

3.4. Fractal Characteristics. Fractal damage theory is proposed by [31]. Fractal theory can assist and explain the failure mechanism of rock masses by quantitatively describing complex objects in nature [31–35]. Xie and Sun study shows that the whole process of rock from crack initiation to final failure has fractal characteristics [36]. Because the box dimension with self-similarity is simple to compute, we used it to characterize the failure evolution of rocks in the study, which is described as [31, 37]

$$\mathrm{Ds} = \lim_{k \longrightarrow \infty} \frac{\lg N r_k(A)}{\lg 1/r_k}, \tag{9}$$

where Ds is the rock damage area's fractal dimension, r_k is the generated shrinking sequence with the square box size of the element, and the number of grids required to cover the target set A with a square box of size r_k with the minimum number of grids is $Nr_k(A)$.

This study is based on the MATLAB platform, using the self-developed digital image and data analysis system of pores and fractures [17] to analyze the acoustic emission graphs at various dip angles and stress levels (as shown in Figure 10). The fractal dimension fitting curve of the rock damage area is shown in Figure 11, the correlation coefficient $R^2 = 0.9730$, and the fractal dimension Ds = 1.153. This demonstrates that the microscopic scale fracture distribution of sandstone has good self-similarity, and the fractal dimension is very convincing. Table 3 shows the calculation results of fractal dimension and acoustic emission energy of numerical samples under different stress levels.

Figure 12 depicts the link between AE energy and various levels of stress. Furthermore, if the stress level is less than 60%, the AE energy curve's amplitude in each set of azimuth angles is quite gentle, and change tends to follow a consistent pattern. When the stress level is greater than 70%, the sample's AE energy curve rapidly rises and maxima at $\alpha = 90^{\circ}$, followed by the sample, when $\alpha = 75^{\circ}$ and $\alpha = 60^{\circ}$. As a result, when $\alpha = 90^{\circ}$, the energy produced by the sandstone sample's fracture is the highest, internal damage is the most severe, and ultimate damage is the most serious.

As seen in Figures 13 and 14, with increasing stress levels at all azimuth angles, the fractal dimension continues to increase. The fractal dimension and the load of the rock damage zone have a positive association. In addition, the rise in fractal dimension is timed to coincide with the change in damage. Figure 14 describes and confirms the influence of the prefabricated crack inclination on damage degree of jointed sandstone from a fractal perspective. When the stress level is 10%, Ds = 0, and the sandstone sample is in the linear elastic stage, indicating that the sample has not been damaged. When the stress level is less than 20%, the Ds of the samples will rapidly increase. As the stress increases and the Ds of each sample increases linearly when the stress level is above 30%. Finally, the Ds value of $\alpha = 90^{\circ}$ is 1.86 when the stress level is 100%, which is the crest value. The Ds value of $\alpha = 0^{\circ}$ is 1.41, which is the least value. Analyzing Figures 9 and 12, it concludes that the final rupture mode of the sample is the most complicated when $\alpha = 90^{\circ}$. Besides, it releases the most energy (Figure 12), the internal damage is the most severe, and the ultimate damage is the most serious, so the Ds is the largest. At $\alpha = 0^{\circ}$, the crack is perpendicular to the middle part of the prefabricated crack and starts to crack and transfixion, the final fracture mode is the simplest with the least energy released (as shown in Figure 12) and the least damage, so the fractal dimension is the smallest. For other samples with prefabricated cracks, the fractal dimension is between $\alpha = 90^{\circ}$ and $\alpha = 0^{\circ}$. As a result, the bigger the Ds, the more severe, the sample damage is, and the more complex, the eventual failure mode is.

In summary, the fractal research results show rock mesoscale failure evolution process is fractal, and the damage degree of rock failure can be characterized by fractal dimension. Thus, using the box dimension to the rock fracture process analysis based on the acoustic emission field is very effective, the presented method does not take into account a large number of rock mechanics parameters, making it a simple and effective new method for evaluating mesoscale rock damage evolution. Therefore, we may use the method presented in the study to calculate the fractal dimension and evaluate the damage characteristics of rock mesoscale failure, so as to reveal the understanding of the mechanism of rock crack propagation.

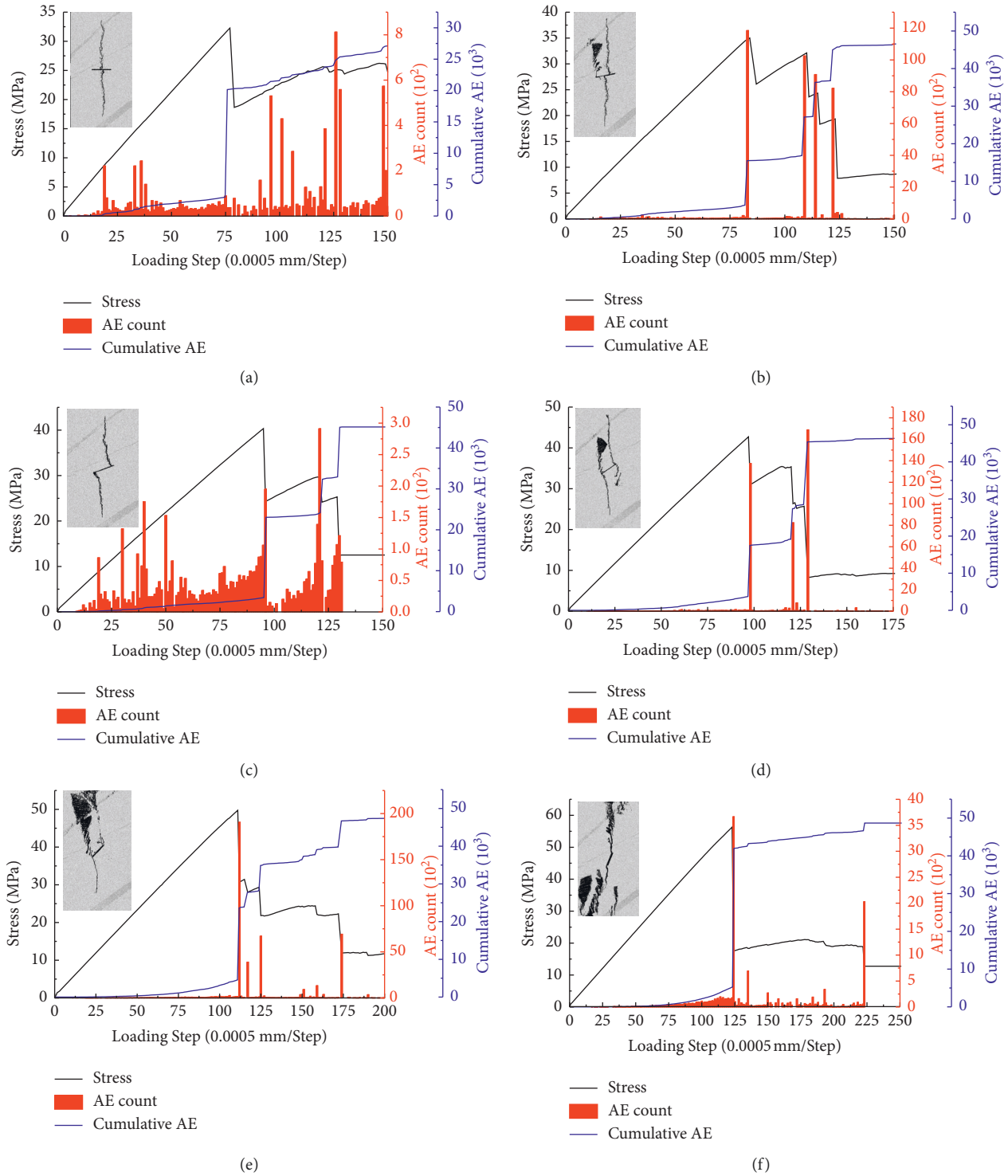

Figure 9: Continued.

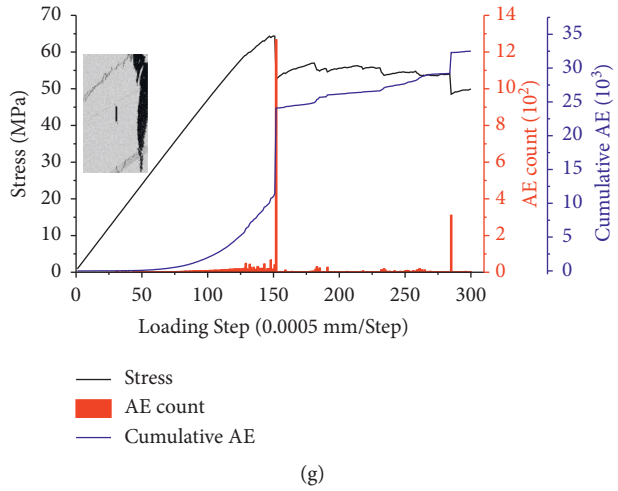

(g)

Figure 9: The relationship between the AE energy, stress, and accumulated AE energy of the specimen. (a–g) Specimens 0°, 15°, 30°, 45°, 60°, 75°, 90°, respectively.

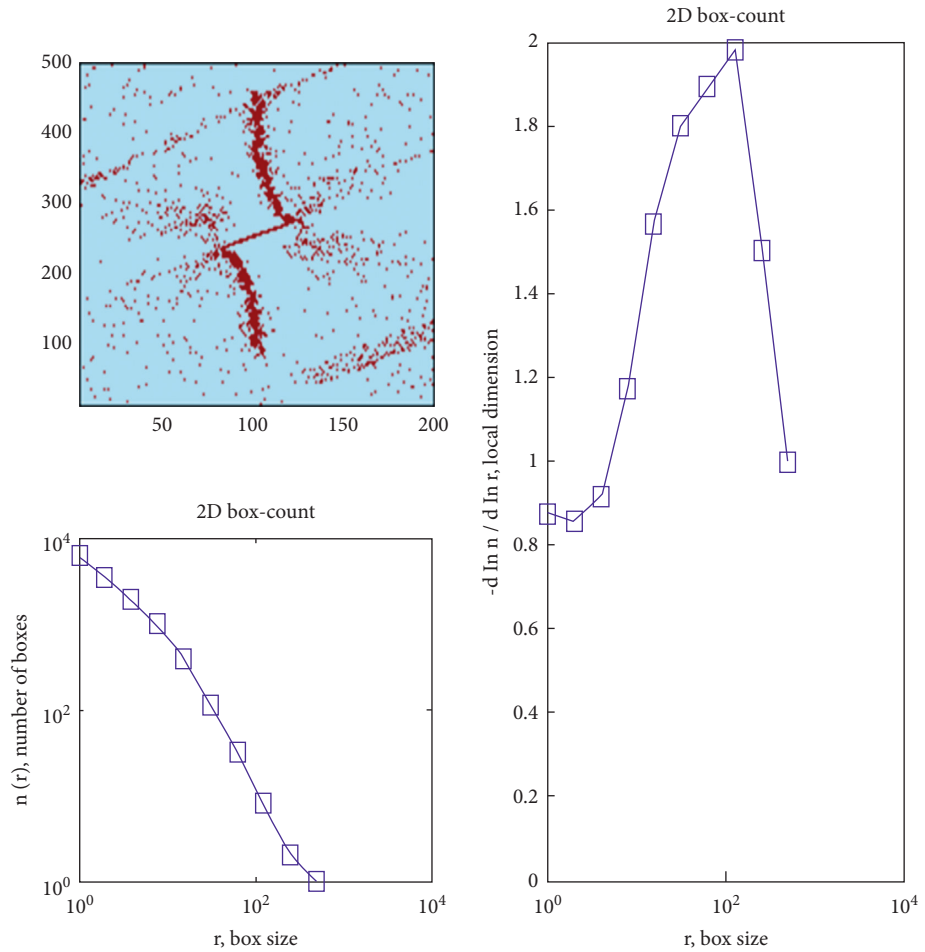

Figure 10: Fractal dimension calculation process based on MATLAB ($\alpha = 45°$, and stress level is 60%).

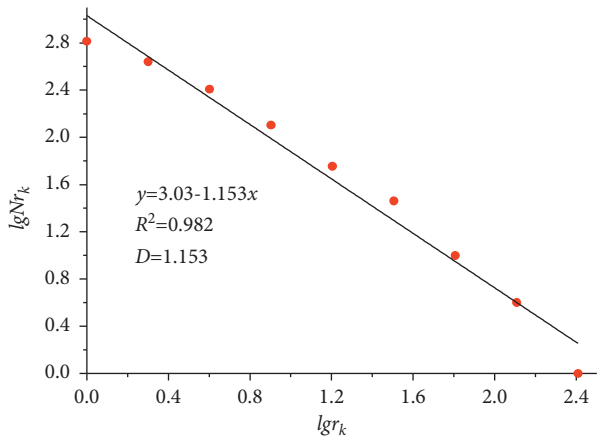

Figure 11: Fractal Dimension fitting curve ($\alpha = 45^\circ$, and stress level is 60%).

Table 3: Calculation results of AE energy and fractal dimension of specimens under different stress levels.

Numerical sample		Stress level 10%	20%	30%	40%	50%	60%	70%	80%	90%	100%
$\alpha = 0^\circ$	AE	0	1	18	22	33	65	73	78	82	102
	Ds	0.92	0.88	1.05	1.10	1.20	1.26	1.29	1.36	1.37	1.41
$\alpha = 15^\circ$	AE	0	7	28	42	63	71	86	91	98	116
	Ds	0.84	0.88	1.02	1.09	1.19	1.27	1.31	1.35	1.39	1.47
$\alpha = 30^\circ$	AE	0	18	19	24	38	55	67	88	92	106
	Ds	0.83	0.90	1.04	1.12	1.18	1.24	1.28	1.34	1.39	1.45
$\alpha = 45^\circ$	AE	0	7	18	34	49	66	71	80	95	102
	Ds	0.83	0.86	0.92	0.96	1.06	1.153	1.27	1.35	1.42	1.48
$\alpha = 60^\circ$	AE	0	5	9	11	14	30	32	72	96	149
	Ds	0	0.54	0.95	1.14	1.24	1.31	1.40	1.64	1.76	1.70
$\alpha = 75^\circ$	AE	0	5	7	12	16	33	51	92	112	177
	Ds	0.85	0.82	0.86	0.93	1.05	1.20	1.34	1.41	1.50	1.59
$\alpha = 90^\circ$	AE	0	2	5	10	24	44	58	114	154	193
	Ds	0.87	0.84	0.89	0.99	1.13	1.27	1.40	1.50	1.60	1.86

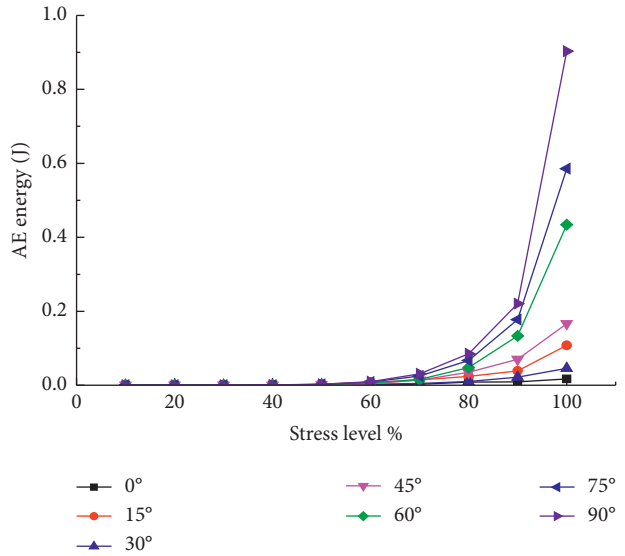

Figure 12: Relationship between stress level and AE energy at various azimuths.

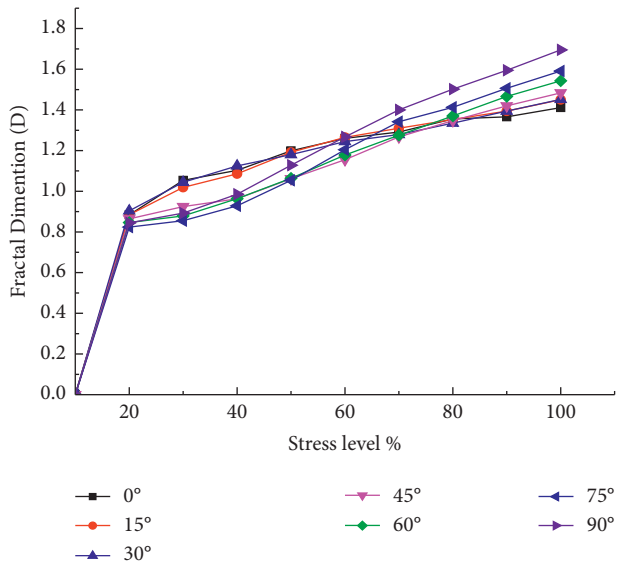

Figure 13: Relationship between stress level and fractal dimension at various azimuths.

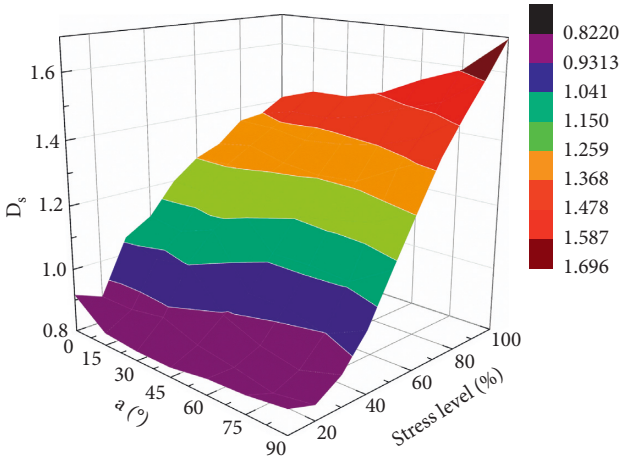

Figure 14: Relationship between azimuth, stress level, and fractal dimension.

4. Conclusion

To systematically explore the mesoscopic damage evolution mechanism of jointed sandstone, DIP, micro-CT scanning, and numerical simulation experiments were used. Using DIP and RFPA^{2D} software, a numerical model based on real mesostructure is created to investigate the fractal behavior of mesoscale failure in sandstone, and the model is applied to characterize the damage evolution, crack propagation, and failure mode of rock fracture. The following are the primary conclusions:

(1) Anisotropy is seen in the elastic modulus and compressive strength of jointed sandstone with varied prefabricated cracks. As the inclination of the crack increases, they all change linearly. There are three types of final cracking modes of the sample under uniaxial compression: from the tip of the prefabricated crack ($\alpha = 15^{\circ}$, $\alpha = 30^{\circ}$, $\alpha = 45^{\circ}$, $\alpha = 60^{\circ}$, $\alpha = 75^{\circ}$); from the middle of the prefabricated crack initiation of cracks ($\alpha = 0^{\circ}$); cracks from the joints ($\alpha = 90^{\circ}$).

(2) A digital image-based rock microscopic scale fracture box dimension algorithm was written with MATLAB software. It can quantitatively evaluate the damage evolution process of jointed sandstone with different prefabricated fractures. The conclusion is that as the fractal dimension gets larger, the crack propagation gets more fully, and the rock damage degree gets higher.

(3) In this study, the *Ds* value of $\alpha = 90^{\circ}$ is 1.86, and the failure mode is the most complicated. The *Ds* value of $\alpha = 0^{\circ}$ is 1.41, and the fracture mode is the simplest. Fractal dimension of other prefabricated fracture angle specimens is between these two values. The fractal dimension can be efficiently used to characterize the samples' final failure mode. The bigger the Ds, the more severe the sample damage is, and the more complex the eventual failure mode is.

(4) In a further stage of the research, a three-dimensional numerical model of the true microstructure of sandstone with various prefabricated cracks will be created, and its macroscopic failure and mesoscopic evolution mechanisms will be thoroughly investigated.

Data Availability

Research data may be obtained by appropriate request.

Conflicts of Interest

The authors declare that they have no conflicts of interest.

Acknowledgments

This study was funded by the Guizhou Province Science and Technology Support Program Project (no. QIANKEHE Support [2021] General 516) and National Natural Science Foundation of China (nos. 51574093, 41962008, and 51774101).

References

[1] M. H. Chen, J. W. Mao, F. P. Bierlein, T. Norman, and P. J. Uttley, "Structural features and metallogenesis of the carlin-type Lannigou gold deposit, Guizhou province, China," *Ore Geology Reviews*, vol. 43, no. 1, pp. 217–234, 2011.

[2] M. H. Chen, L. L. Wu, P. J. Uttley, T. Norman, Z. Jianmin, and Q. Yunzhong, "REE features of arseuian pyrite and vein quartz and their fluid inclusions in the Jinfeng (Lannigou) gold deposit, Guizhou province, China," *Acta Petrologica Sinica*, vol. 23, no. 10, pp. 2423–2433, 2007.

[3] M. L. Huang, "Research on fracture mechanism by interaction of multi-crack in brittle rock," *Chinese Journal of Rock Mechanics and Engineering*, vol. 20, no. 3, p. 423, 2001.

[4] C. Zhu, M. Karakus, M. C. He et al., "Volumetric deformation and damage evolution of Tibet interbedded skarn under multistage constant-amplitude-cyclic loading," *International*

Journal of Rock Mechanics and Mining Sciences, vol. 152, Article ID 105066, 2022.

[5] Y. T. Du, Y. C. Li, S. L. Zhang, and L. X. Lü, "Propagation mechanism of 3D through fracture with different dip angles under uniaxial compression load," *Journal of Shandong University of Science and Technology*, vol. 35, no. 3, pp. 53–60, 2016.

[6] Y. S. Pan, *Study on Rock Burst Initiation and Failure Propagation," PhD Thesis*Tsinghua University, Beijing, China, 1999.

[7] A. Griffith, "The phenomena of rupture and flow in solids," *Philosophical Transactions of the Royal Society of London - Series A: Containing Papers of a Mathematical or Physical Character*, vol. 221, no. 582-593, pp. 163–198, 1921.

[8] S. Nemat-Nasser and M. Obata, "A microcrack model of dilatancy in brittle materials," *Journal of Applied Mechanics*, vol. 55, no. 1, pp. 24–35, 1988.

[9] X. L. Liu, S. J. Wang, E. Z. Wang, J. Wang, and B. Hu, "Evolutionary rules of flaws in rock subjected to uniaxial compression and rock strength," *Chinese Journal of Rock Mechanics and Engineering*, vol. 27, no. 6, pp. 1195–1201, 2008.

[10] R. H. C. Wong, P. Lin, and C. A. Tang, "Experimental and numerical study on splitting failure of brittle solids containing single pore under uniaxial compression," *Mechanics of Materials*, vol. 38, no. 1, pp. 142–159, 2006.

[11] D. M. Liu, M. F. Cai, Y. B. Zhou, and Z. Y. Chen, "Dynamic monitoring on developing process of rock cracks," *Chinese Journal of Rock Mechanics and Engineering*, vol. 25, no. 3, pp. 467–472, 2006.

[12] C. Zhao, C. Bao, H. Matsuda, C. F. Zhao, and J. S. Tian, "Application of digital image correlation method in experimental research on crack propagation of brittle rock," *Chinese Journal of Geotechnical Engineering*, vol. 37, no. 5, pp. 944–951, 2015.

[13] C. Zhao, C. Bao, J. S. Tian, H. Matsuda, and C. Morita, "Experimental study of coalescence mode of cracks and strength of rock with double flaws based on strain localization," *Chinese Journal of Rock Mechanics and Engineering*, vol. 34, no. 11, pp. 2309–2318, 2015.

[14] C. Zhao, J. S. Tian, and H. Matsuda, "Study on the crack propagation and damage evolution characteristics of rock based on the global strain field under uniaxial compression," *Chinese Journal of Rock Mechanics and Engineering*, vol. 34, no. 4, pp. 763–769, 2015.

[15] D. Li, E. Wang, X. Kong, M. Ali, and D. Wang, "Mechanical behaviors and acoustic emission fractal characteristics of coal specimens with a pre-existing flaw of various inclinations under uniaxial compression," *International Journal of Rock Mechanics and Mining Sciences*, vol. 116, pp. 38–51, 2019.

[16] Z. Li, L. Li, B. Huang et al., "Numerical investigation on the propagation behavior of hydraulic fractures in shale reservoir based on the DIP technique," *Journal of Petroleum Science and Engineering*, vol. 154, pp. 302–314, 2017.

[17] H. Liu, Y. Zuo, Z. Wu, and W. Sun, "Fractal analysis of mesoscale failure evolution and microstructure characterization for sandstone using DIP, SEM-EDS, and micro-CT," *International Journal of Geomechanics*, vol. 21, no. 9, Article ID 04021153, 2021.

[18] C. A. Tang, L. G. Tham, S. H. Wang, H. Liu, and W. H. Li, "A numerical study of the influence of heterogeneity on the strength characterization of rock under uniaxial tension," *Mechanics of Materials*, vol. 39, no. 4, pp. 326–339, 2006.

[19] Y.-J. Zuo, Q. Zhang, T. Xu, Z.-H. Liu, Y.-Q. Qiu, and W.-C. Zhu, "Numerical tests on failure process of rock particle under impact loading," *Shock and Vibration*, vol. 2015, Article ID 678573, 12 pages, 2015.

[20] G. Li and C.-A. Tang, "A statistical meso-damage mechanical method for modeling trans-scale progressive failure process of rock," *International Journal of Rock Mechanics and Mining Sciences*, vol. 74, pp. 133–150, 2015.

[21] W. C. Zhu, J. Liu, C. A. Tang, X. D. Zhao, and B. H. Brady, "Simulation of progressive fracturing processes around underground excavations under biaxial compression," *Tunnelling and Underground Space Technology*, vol. 20, no. 3, pp. 231–247, 2004.

[22] C. Tang, "Numerical simulation of progressive rock failure and associated seismicity," *International Journal of Rock Mechanics and Mining Sciences*, vol. 34, no. 2, pp. 249–261, 1997.

[23] S. Y. Wang, S. W. Sloan, D. Sheng, and C. Tang, "Numerical analysis of the failure process around a circular opening in rock," *Computers and Geotechnics*, vol. 39, pp. 8–16, 2011.

[24] S. Y. Wang, S. W. Sloan, C. A. Tang, and W. C. Zhu, "Numerical simulation of the failure mechanism of circular tunnels in transversely isotropic rock masses," *Tunnelling and Underground Space Technology*, vol. 32, pp. 231–244, 2012.

[25] L. Zheng, H. Liu, Y. Zuo et al., "Fractal study on the failure evolution of concrete material with single flaw based on DIP technique," *Advances in Materials Science and Engineering*, vol. 2022, Article ID 6077187, 15 pages, 2022.

[26] H. Diao, "Rock mechanical properties and brittleness evaluation of shale reservoir," *Acta Petrologica Sinica*, vol. 29, pp. 3300–3306, 2013.

[27] R. Y. Rubinstein and D. P. Kroese, *Simulation and the Monte Carlo Method*, John Wiley & Sons, Hoboken, NY, United States of America, 2011.

[28] F. Rossi, A. Di Carlo, and P. Lugli, "Microscopic theory of quantum-transport phenomena in mesoscopic systems: a Monte Carlo approach," *Physical Review Letters*, vol. 80, no. 15, pp. 3348–3351, 1998.

[29] W. Weibull, "A statistical distribution function of wide applicability," *Journal of Applied Mechanics*, vol. 18, no. 3, pp. 293–297, 1951.

[30] Z.-j. Wu, Z.-y. Wang, L.-f. Fan, L. Weng, and Q.-s. Liu, "Micro-failure process and failure mechanism of brittle rock under uniaxial compression using continuous real-time wave velocity measurement," *Journal of Central South University*, vol. 28, no. 2, pp. 556–571, 2021.

[31] B. B. Mandelbrot, *The Fractal Geometry of Nature*, W. H. Freman, New York, 1982.

[32] P. Bouboulis, L. Dalla, and V. Drakopoulos, "Construction of recurrent bivariate fractal interpolation surfaces and computation of their box-counting dimension," *Journal of Approximation Theory*, vol. 141, no. 2, pp. 99–117, 2006.

[33] H. Liu, L. Zheng, Y. Zuo et al., "Study on mesoscopic damage evolution characteristics of single joint sandstone based on micro-CT image and fractal theory," *Shock and Vibration*, vol. 2021, Article ID 6547028, 18 pages, 2021.

[34] B. Liu and Y. Ning, "Application of fractal theory to geotechnical engineering," *Applied Mechanics and Materials*, vol. 52-54, pp. 1291–1295, 2011.

[35] Q. Wang, M. He, S. Li et al., "Comparative study of model tests on automatically formed roadway and gob-side entry driving in deep coal mines," *International Journal of Mining Science and Technology*, vol. 31, no. 4, pp. 591–601, 2021.

[36] H. P. Xie and H. Q. Sun, "The foundation of fractal mathematics and the application of fractal in rock mechanics," *Mining World*, vol. 0, no. 4, pp. 1–6, 1996.

[37] J. Li, Q. Du, and C. Sun, "An improved box-counting method for image fractal dimension estimation," *Pattern Recognition*, vol. 42, no. 11, pp. 2460–2469, 2009.

Hindawi
Mathematical Problems in Engineering
Volume 2022, Article ID 6888916, 12 pages
https://doi.org/10.1155/2022/6888916

Research Article

Long-Term Bearing Deformation Characteristics of Caved Gangue in Gob under Different Moisture Conditions

Zhen Wang,[1] Shanming Wei,[2] Zhenhua Zhao,[2,3] Liting Xing,[4] Changsuo Li,[2,3] and Hailong Wang[2,3,5]

[1]*Lixia Holding Group Co. LTD, Jinan 250000, China*
[2]*No. 801 Hydrogeology and Engineering Geological Brigade of Shandong Provincial Bureau of Geology and Mineral Resources, Jinan 250014, China*
[3]*Shandong Provincial Bureau of Geology and Mineral Resources, Jinan 250013, China*
[4]*School of Water Conservancy and Environment, University of Jinan, Jinan 250022, China*
[5]*School of Civil Engineering and Architecture, Linyi University, Linyi 276000, China*

Correspondence should be addressed to Shanming Wei; 95526734@qq.com and Hailong Wang; whlmlp@163.com

Received 4 March 2022; Accepted 26 March 2022; Published 15 April 2022

Academic Editor: Fuqiang Ren

In gob, the caved gangue is in a state of long-term bearing deformation with obvious time-dependent effect, even though the coal seam has been mined for a long time. As time goes on, because of the excessive deformation of caved gangue, the gob surrounding rock will easily aggravate the structural instability and cause dynamic disasters, such as mine water inrush and surface collapse. If the gob is filled with water, the bearing capacity of the caved gangue in waterlogged environment will be worse than that in dry environment, which will greatly increase the possibility of disasters. In order to study the bearing deformation characteristics of caved gangue under different moisture conditions, a testing system used for bearing deformation testing of caved gangue is developed. The typical caved gangue is chosen for samples. In view of the particle size distribution characteristics and stress state of caved gangue, the size distribution of caved gangue obeys the law of normal distribution and the load pattern is designed to step load. With the increase of axial load, the axial deformation of caved gangue increases gradually, the residual bulking coefficient decreases gradually, which are more obvious in load stage than in constant load stage. In the early constant load stage, the axial deformation of caved gangue grows rapidly, then tends to be slow and steady gradually; the relationship between strain and time meets the logarithmic relationship. In load stage, the D-value of axial strain decreases gradually along with the increase of axial load, whereas in constant load stage, it is opposite; the bearing deformation of caved gangue is consisted of two parts: instantaneous compression deformation and long-term deformation. For instantaneous compression deformation, the water acting as the lubricant promotes the compressive strain of caved gangue specimen and is conducive to rotation and slipping between each rock block. For long-term deformation, meanwhile, the water acting as the softening agent reduces the strength of the rock block and is conducive to the crushing of the rock block. The newborn rock blocks may slip and fill the gap between rock blocks, which also promotes the compressive strain of caved gangue specimen. The research results have important significance for forecasting and controlling the movement and deformation of overlying strata caused by mining.

1. Introduction

There are three distinct zones (caved zone, fracture zone, and continuous deformation zone) of disturbance in overlying strata when the coal seam roof is controlled by caving method, based on the deformation and failure characteristics of overlying strata [1–7]. The caved zone is filled by the caved gangue composed of an immediate roof and part overlying strata [8, 9], as shown in Figure 1. The vertical height of the caved zone with a highly irregular shape and different granular caved gangue can reach 4–11 times the mining height [10, 11]. The caved gangue is gradually compressed by the overburden load resulting from mining disturbance, which supports the deformable upper rock strata [12, 13].

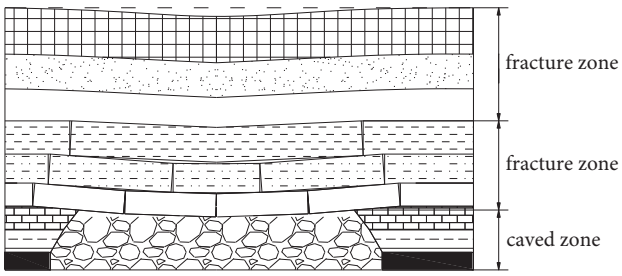

Figure 1: Overlying strata failure mode after mining.

Therefore, the variable load compaction of caved gangue in gob directly determines the movement of the upper strata.

The caved gangue in gob can be treated as a porous medium consisting of caved gangue blocks generated by caving, pilling, and recompressing [14]. Due to the nonuniform stress distribution in a gob, the degree of compaction of caved gangue mass varies with location and time, resulting in a variable load compaction. It is well known that the mining-induced gob stress profile near the working face region varies with the mining direction [15–17], as shown in Figure 2. Apparently, the gob close to the working face has a relatively low-stress situation due to the existence of hydraulic supports and the overburden hinge structure. Moving away from the working face towards the gob, the load carried by the caved gangue gradually increases, which results in a progressive compaction of the loosely packed rocks. The stress level of the caved zone far away from the working face almost recovers back to the original in-situ value and the gob was fully compacted. The caved gangue is in a state of long-term bearing deformation with obvious time-dependent effect, even though the coal seam has been mined for a long time. As time goes on, because of the excessive deformation of caved gangue in gob, the gob surrounding rock will easily aggravate the structural instability and cause dynamic disasters, such as mine water inrush and surface collapse [18–20]. If the gob is filled with water, the bearing capacity of the caved gangue in waterlogged environment will be worse than that in dry environment, which will greatly increase the possibility of disasters. Thus, it is essential to study the bearing deformation characteristics of caved gangue in gob under load, especially with different moisture contents. The results are difficult to obtain by field observation. Because of the concealment of underground excavation engineering, laboratory testing becomes an effective way to solve this problem [21–33].

In the process of laboratory testing, the bearing deformation characteristics of caved gangue are mainly influenced by the own characteristics of specimens and the properties of experimental device. The own characteristics of specimen include compressive strength, particle size, particle size distribution, and moisture content. The properties of experimental device include the size of test vessel, load method, and measuring accuracy. Based on partial influencing factor, some scholars have carried out a series of studies on the caved gangue [34–39]. These studies significantly contribute to the understanding of bearing deformation characteristics of caved gangue. However, the small effective volume of the existing experimental devices is the common defect. With the increase of particle size of caved gangue, the problem of boundary effect will become more and more prominent. Moreover, the patterns of particle size distribution of caved gangue are varied, and the existing studies are mainly focused on single particle size distribution, uniform particle size distribution, and continuous particle size distribution. In this study, in order to study the bearing deformation characteristics of large-size caved gangue, a testing system used for bearing deformation testing of large-size caved gangue was developed. The typical sandstone from the roof was chosen for specimens. In view of the particle size distribution characteristics and stress state of caved gangue in caved zone, the size distribution of caved gangue obeyed the law of normal distribution, and the load method was designed to step load. The research results have important significance for forecasting and controlling the movement and deformation of overlying strata caused by mining.

2. Testing System and Scheme

2.1. Testing System. The testing system used for bearing deformation testing of large-size caved gangue is consisted of load support bracket, load head, testing chamber, servo control system of displacement and load, servo control system of water pressure and water yield, and operating deck, as shown in Figure 3. (1) Load support bracket is consisted of base, frame, supporting structure of hydraulic cylinder, reaction frame, which plays the role of fixed, and supporting action. (2) Load head is connected to hydrocylinder by connecting rod. (3) Testing chamber is cylindric, the effective size are 400 mm diameter and 680 mm high. In order to facilitate the filling of caved gangue specimens, the testing chamber is composed of two compartments. (4) Servo control system of displacement and stress can control the load head by setting displacement or load. The meter full scale of displacement is 400 mm, and the accuracy is 0.01 mm. The maximum load is 600 KN, and the accuracy is 0.01 KN. (5) Servo control system of water pressure and water yield can fill the testing chamber with water by setting water pressure or water yield. The maximum water pressure is 2 MPa, the maximum water supply is 150 L/h, and the accuracy is 0.01 MPa. (6) Operating deck is fully automated, five basic parameters can be collected into a database in real time, such as time, displacement, load, water pressure, and water yield. The maximum sampling frequency is 10HZ.

2.2. Testing Scheme

2.2.1. Particle Size Distribution. The rock specimens are sandstone from the gob of Daizhuang coal mine, which is located near Jining city, Shandong Province, China. Some basic parameters are shown in Table 1. Considering the scale effect, the ratio between the diameter of caved gangue specimen and the maximum particle size of caved gangue should be greater than or equal to 5 [40–42]. Because the internal diameter of testing chamber is 400 mm, the

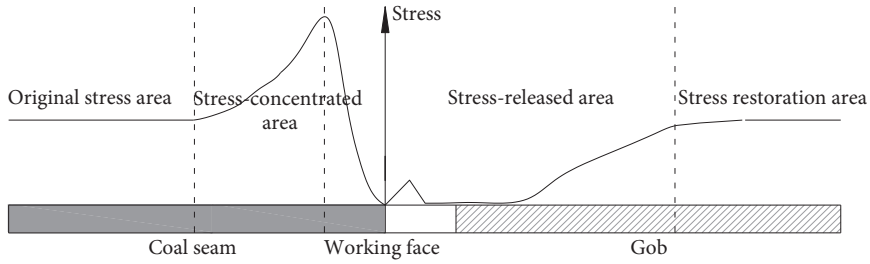

Figure 2: Stress distribution around gob.

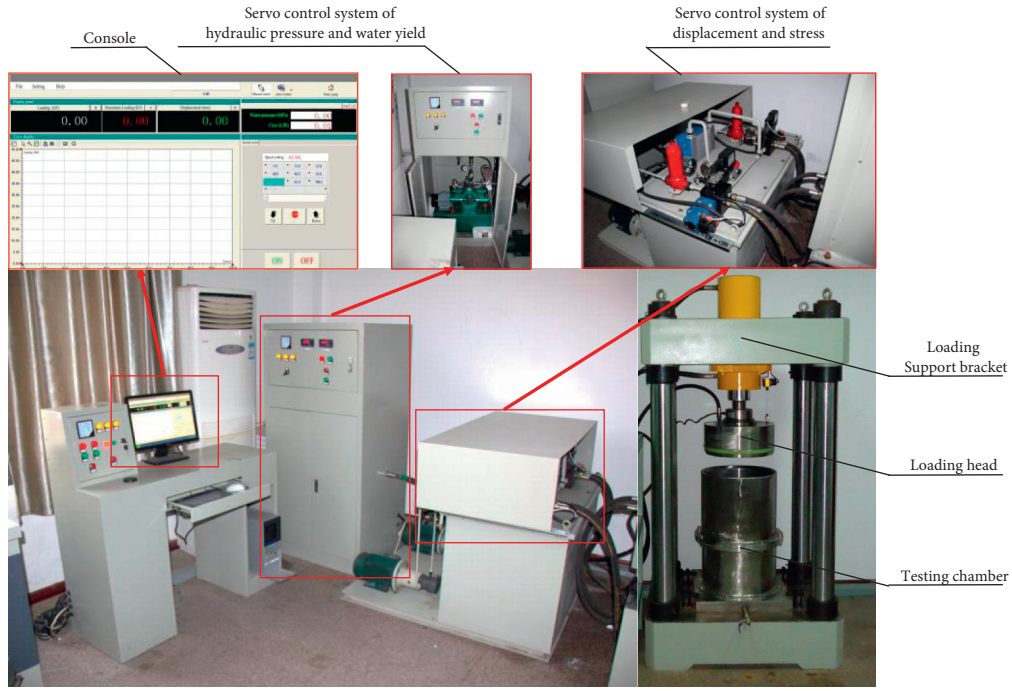

Figure 3: Testing system used for bearing deformation testing of large-size caved gangue.

Table 1: Basic parameters of sandstone.

Moisture condition	Uniaxial compressive strength (MPa)	Tensile strength (MPa)	Modulus of elasticity (GPa)	Poisson's ratio	Density (kg/m^3)	Moisture content (%)
Dry	96.78	7.5	16.1	0.199	2565.6	0
Water saturated	87.21	7.2	15.2	0.209	2578.8	0.516

maximum particle size of caved gangue could be tested is 80 mm. In order to minimize the influence of size effect on the testing results, the maximum particle size of the caved gangue selected in the test is determined to be 40 mm. The caved gangue is divided into 7 categories by the particle size, which are 5–10 mm, 10–15 mm, 15–20 mm, 20–25 mm, 25–30 mm, 30–35 mm, and 35~40 mm, as shown in Figure 4. In this article, the size distribution of caved gangue specimens for testing obeys the law of normal distribution. In a complete caved gangue specimen, according to the particle size of caved gangue from small to large, the mass fraction of 7 categories is 5%, 10%, 20%, 30%, 20%, 10%, and 5%, respectively, as shown in Figure 5. For the caved gangue with a certain particle size, the relation between the mass fraction and particle size is as follows:

$$A = 4.885 + \frac{329.279}{10.761\sqrt{\pi/2}} e^{-2(D-2)^2/10.761^2}, \quad (1)$$

where A is the mass fraction of the caved gangue with a certain particle size (%) and D is the minimum of the caved gangue in a certain particle size (mm).

The actual height of caved gangue specimen is 655 mm, and the total mass is 110 kg. The initial bulking factor of caved gangue specimen is 1.901, and the voidage is 0.901. The assembled caved gangue specimen is shown in Figure 6.

The initial bulking factor of caved gangue (K) is given by

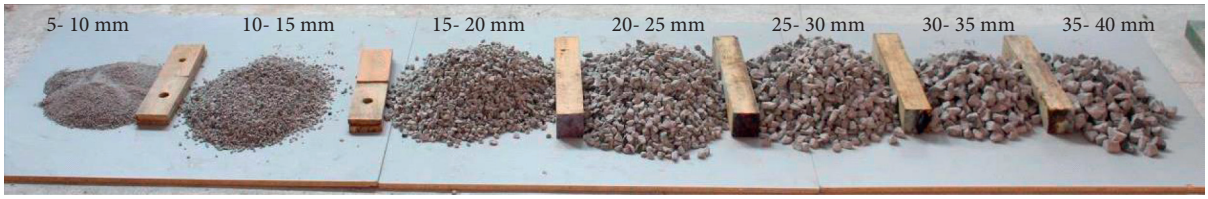

Figure 4: Caved gangue with different particle sizes.

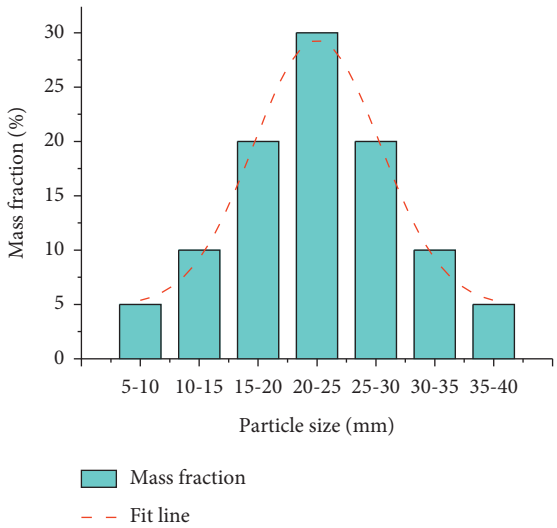

Figure 5: Mass fraction of 7 categories of caved gangue.

$$K = \frac{V_1}{V_0}, \tag{2}$$

where K is the initial bulking factor of caved gangue, V_0 is the volume of complete rock, and V_1 is the volume of caved gangue produced by complete rock in the state of natural accumulation.

The initial voidage of caved gangue (P) is given by

$$P = \frac{V_1 - V_0}{V_0} = K - 1, \tag{3}$$

where P is the initial voidage of caved gangue.

The residual height of caved gangue specimen after the bearing deformation testing (h_1) is given by

$$h_1 = h_0 - u, \tag{4}$$

where h_1 is the residual height of caved gangue specimen after the bearing deformation testing (mm), h_0 is the initial height of caved gangue specimen (mm), and u is the deformation of caved gangue specimen (mm).

The residual bulking factor of caved gangue specimen after the bearing deformation testing (K_1) is given by

$$K_1 = \frac{h_1 \cdot S}{V_0}, \tag{5}$$

where K_1 is the residual bulking factor of caved gangue specimen after the bearing deformation testing and S is the area of testing chamber, 125600 mm^2.

Figure 6: Assembled caved gangue.

2.2.2. Load Method. The pressure acting on the caved gangue in gob is mainly from overlying strata. The pressure value is directly related to the height of the fractured overlying strata and increases with the increase in the height of the fractured overlying strata. In the time interval of two adjacent roof weightings, the pressure acting on the caved gangue in gob is basically unchanged, which is equal to the self-weight stress of total fractured overlying strata. During the roof weighting, the pressure acting on the caved gangue in gob will increase rapidly, and the increment is equal to the self-weight stress of generated fractured overlying strata. So the pressure acting on the caved gangue in gob is stair stepping, which provides evidence for designing the load method in the bearing deformation testing of caved gangue in gob. The load method is divided into 2 stages, namely, load stage and constant load stage. In load stage, the load speed is 0.5 kN/s. In constant load stage, the constant load is 100 kN, 200 kN, 300 kN, and 400 kN, respectively; the duration of each constant load is 4 hours. Before the formal testing, a preload of 20 kN is applied to the caved gangue in gob specimen until the deformation is constant, which needs about 15 minutes. The load method of a complete testing is shown as Figure 7.

3. Testing Results and Analysis

3.1. Bulking and Deformation Characteristics. The parameters of caved gangue specimens during different testing stage are shown in Table 2. With the increase of axial load, the axial deformation of caved gangue specimen increases gradually, as shown in Figure 8(a). The final deformation of caved gangue specimen under dry condition and water-saturated condition is 74.07 mm and 91.00 mm, respectively, and the corresponding strain value is 113.1×10–3 and 138.9×10–3, respectively. The residual bulking factor of

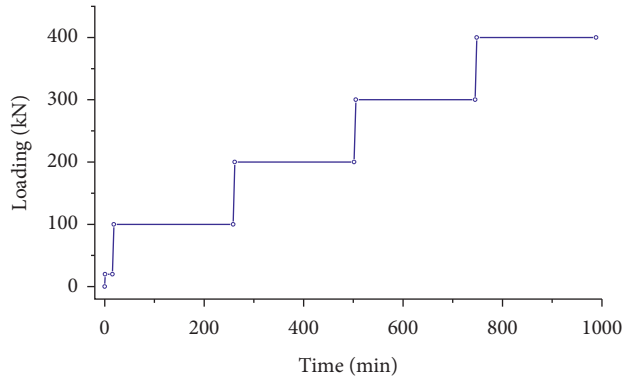

Figure 7: Load method of a complete testing.

Table 2: Parameters of caved gangue specimens during different testing stage.

Moisture condition	Testing stage	Deformation			Strain			Residual bulking factor	
		Initial value (mm)	Final value (mm)	D-value (mm)	Accumulated strain/10^{-3}	Fitting formula of strain-time	R-square	Initial value	Final value
Dry	20–100 kN load	0	20.82	20.82	31.8	—	—	1.901	1.840
	100 kN constant load	20.82	23.01	2.19	35.1	$\varepsilon = 33.77 + 0.25 \ln t$	0.982	1.840	1.834
	100–200 kN load	23.01	38.38	15.37	58.6	—	—	1.834	1.789
	200 kN constant load	38.38	42.23	3.85	64.5	$\varepsilon = 59.72 + 0.85 \ln t$	0.970	1.789	1.778
	200–300 kN load	42.23	54.47	12.24	83.2	—	—	1.778	1.743
	300 kN constant load	54.47	59.67	5.20	91.1	$\varepsilon = 86.37 + 0.91 \ln t$	0.973	1.743	1.727
	300–400 kN load	59.67	68.88	9.21	105.2	—	—	1.727	1.701
	400 kN constant load	68.88	74.07	5.19	113.1	$\varepsilon = 109.90 + 0.59 \ln t$	0.941	1.701	1.686
Water Saturated	20–100 kN load	0	21.27	21.27	32.5	—	—	1.901	1.839
	100 kN constant load	21.27	25.30	4.03	38.6	$\varepsilon = 34.24 + 0.80 \ln t$	0.996	1.839	1.827
	100–200 kN load	25.30	45.10	19.80	68.9	—	—	1.827	1.770
	200 kN constant load	45.10	53.19	8.09	81.2	$\varepsilon = 71.64 + 1.75 \ln t$	0.995	1.770	1.746
	200–300 kN load	53.19	64.26	11.07	98.1	—	—	1.746	1.714
	300 kN constant load	64.26	72.61	8.35	110.9	$\varepsilon = 101.66 + 1.69 \ln t$	0.995	1.714	1.690
	300–400 kN load	72.61	81.75	9.14	124.8	—	—	1.690	1.663
	400 kN constant load	81.75	91.00	9.25	138.9	$\varepsilon = 128.63 + 1.92 \ln t$	0.994	1.663	1.637

Notes: ε is the accumulated strain of caved gangue specimen, $\times 10^{-3}$, t is the hold time in each constant load stage, min.

caved gangue specimen under dry condition and water-saturated condition decreases gradually, which changes from 1.901 to 1.686 and from 1.901 to 1.637, respectively, as shown in Figure 8(b). The axial deformation in load stage is more obvious than that in constant load stage, which accounts for 77.8% of total deformation under dry condition and 67.6% of total deformation under water-saturated condition. The testing results indicate that the water promotes the compressive strain of caved gangue specimen obviously.

In order to show the change of the axial deformation of the caved gangue specimens in constant load stage intuitively, the axial strain-time curves are made, as shown in Figure 9. The fitting formulas of strain-time curves in different constant load stages are shown in Table 2. The

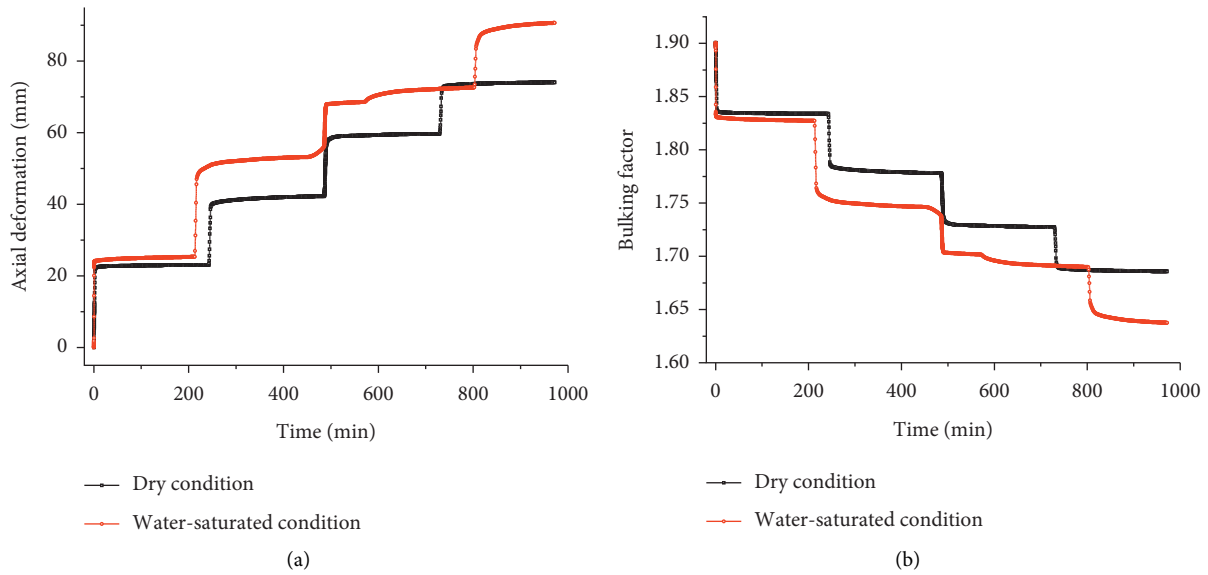

Figure 8: Axial deformation-time curve and bulking factor-time curve of caved gangue specimens. (a) Axial deformation-time curve. (b) Bulking factor-time curve.

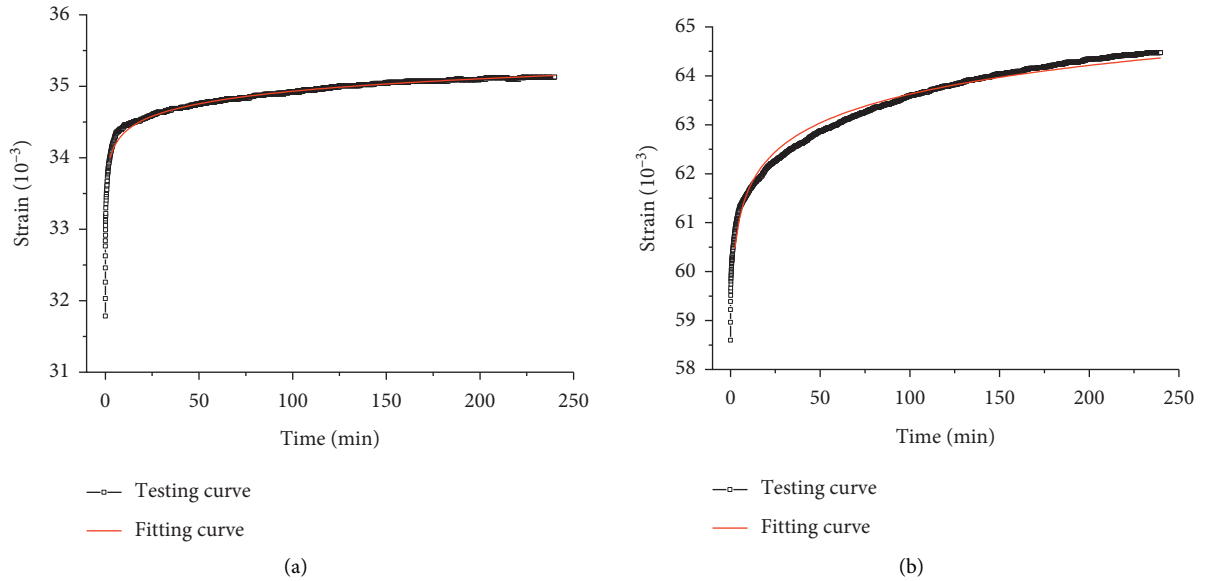

Figure 9: Continued.

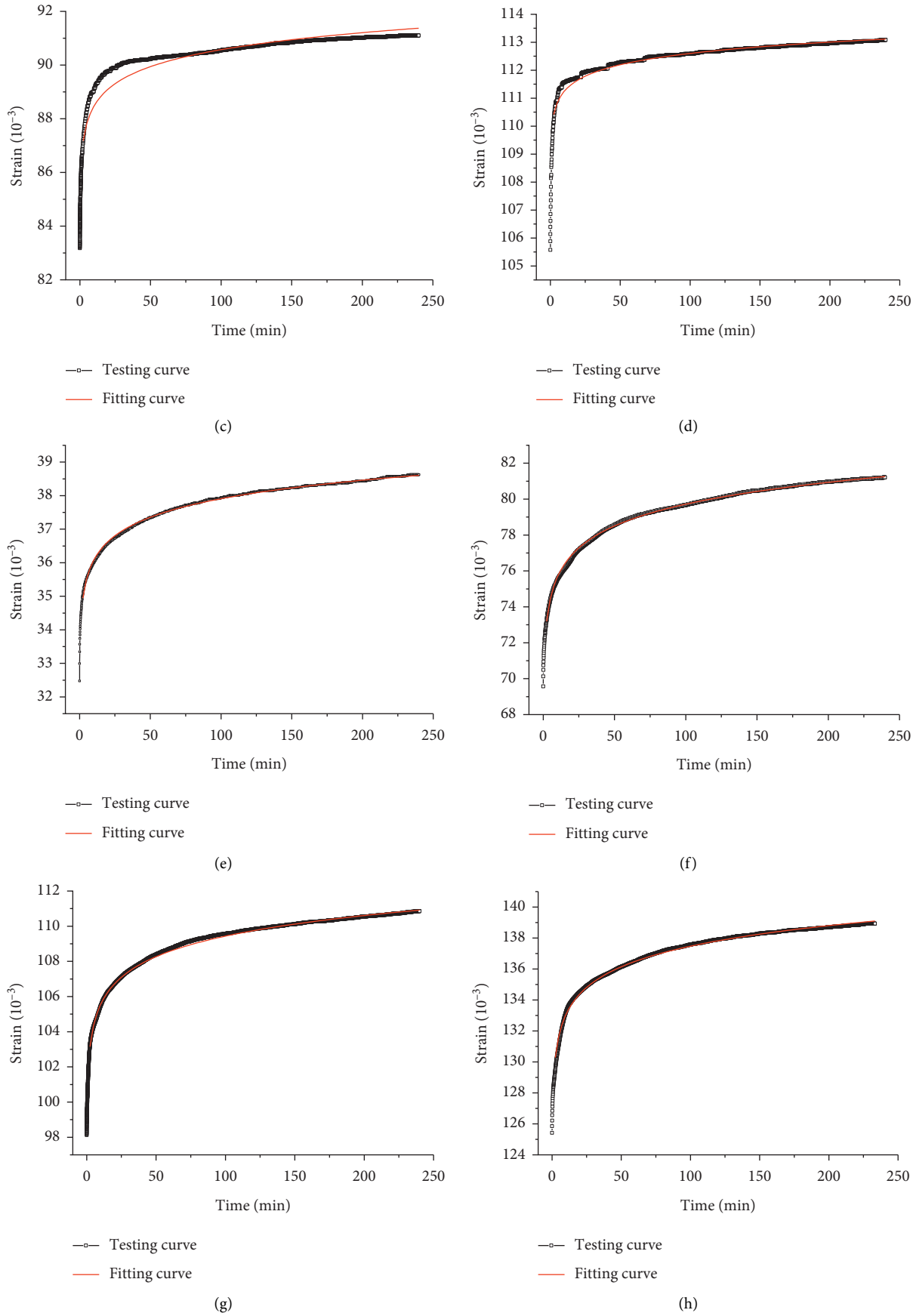

Figure 9: Strain-time curve of caved gangue specimens in constant load stage. (a) 100kN constant load (dry). (b) 200kN constant load (dry). (c) 300kN constant load (dry). (d) 400kN constant load (dry). (e) 100kN constant load (water saturated). (f) 200kN constant load (water -saturated). (g) 300kN constant load (water saturated). (h) 400kN constant load (water saturated).

relationship between strain and time meets the logarithmic relationship. The R-square of each fitting formula is greater than 0.94. In the early stage, the axial strain increases rapidly, then becomes gently. In the late stage, the axial strain is unchanged basically.

The strain D-values of the caved gangue specimens in different stages are shown in Figure 10.

(1) In load stage: From 20 kN to 100 kN, the axial strain D-value is $31.8\times10^{-3}$and 32.5×10^{-3}, respectively, under dry condition and water-saturated condition, which are equal basically and indicate that the water has no effect on the compressive strain of caved gangue specimen. From 100 kN to 200 kN, the axial strain D-value under water-saturated condition is 6.7×10^{-3} greater than that in dry condition, which indicates that the water acting as the lubricant promotes the compressive strain of caved gangue specimen and is conducive to rotation and slipping between each rock block. From 200 kN to 300 kN, the axial strain D-value under dry condition and water-saturated condition is 18.7×10^{-3} and 16.9×10^{-3}, respectively; the latter is less than the former, which is because the previous accumulated strain under water-saturated condition is greater than that under dry condition, and is 81.2×10^{-3} and 64.5×10^{-3}, respectively. From 300 kN to 400 kN, the axial strain D-value is $14.1\times10^{-3}$and 14.0×10^{-3}, respectively, under dry condition and water-saturated condition, which are equal basically.

(2) In constant load stage: In 4 constant load stages, the axial strain D-values under water-saturated condition are all greater than these under dry condition. According to the load from small to large, the increment of the axial strain D-values is 2.8×10^{-3}, 6.5×10^{-3}, 4.8×10^{-3} and 6.2×10^{-3}, which indicates that the water acting as the lubricant promotes the compressive strain of caved gangue specimen and is conducive to rotation and slipping between each rock block. Meanwhile, the water acting as the softening agent reduces the strength of the rock block and is conducive to the crushing of the rock block. The newborn rock blocks may slip and fill the gap between rock blocks, which also promotes the compressive strain of caved gangue specimen. It is worth noting that the crushing of the rock blocks will appear only when the crushing stress is greater than the strength.

3.2. Particle Size Distribution Characteristics. After the testing, the caved gangue specimens under dry condition and water-saturated condition are screened and weighed again. The changes of mass fraction of caved gangue with different particle sizes are shown in Table 3 and Figure 11. Under dry condition and water-saturated condition, the mass fraction of caved gangue with the particle size of 0-5 mm increases by 5.25% and 5.85%, respectively, while the particle size of 5–10 mm increases by 2.46% and 3.09%, respectively. The mass fraction of caved gangue blocks with the particle size of 10–20 mm is basically unchanged, so the particle size of 10–20 mm can be defined as the stable particle size. It does not mean that the load has no effect on the caved gangue blocks with the particle size of 10–20 mm because some caved gangue blocks have obvious new fracture marks after rescreening, which indicates that the mass fraction of caved gangue blocks with the particle size of 10–20 mm is dynamically stabilized, that is, the weight of newborn caved gangue blocks is basically equal to the weight of diminished caved gangue blocks. Under dry condition and water-saturated condition, the mass fraction of caved gangue with the particle size of 20–25 mm decreases by 3.19% and 3.32%, respectively, while the particle size of 25–30 mm decreases by 3.65% and 4.95%, respectively, and the particle size of 30–35 mm decreases by 0.98% and 1.14%, respectively. The mass fraction of caved gangue with the particle size of 35–40 mm is unchanged basically. The particle size distribution of caved gangue specimen provide a strong evidence that many rock blocks are broken into smaller blocks during testing.

3.3. Bearing Deformation Mechanism. During the bearing deformation testing of the caved gangue specimen, there will be a greater frictional force between the inner wall of testing chamber and the caved gangue specimen, which weakens the transfer of axial stress, so the pressure acting on these caved gangue blocks near the bottom of testing chamber is less than that near the top of testing chamber [43]. Because the diameter and height of the caved gangue specimen are 400 mm and 655 mm, respectively, the specimen is narrow and high. The distribution of compressive stress is shown in Figure 12.

The compressive stress of side wall of caved gangue specimen (σ_b) is given by

$$\sigma_b = \frac{\rho g A}{\mu L}\left(1 - \frac{1}{e^{\mu L n' h/A}}\right), \tag{6}$$

where σ_b is the compressive stress of side wall of caved gangue specimen, ρ is the density of caved gangue, g is the gravitational acceleration, μ is the frictional factor between the inner wall of testing chamber and the caved gangue specimen, n' is the specific value of lateral compressive stress and average vertical compressive stress, $n' = \sigma_b/\sigma_{cp}$, σ_{cp} is the average vertical compressive stress, A is the bottom area of caved gangue specimen, L is the perimeter of caved gangue specimen, and h is the height of caved gangue specimen.

The vertical compressive stress of caved gangue specimen (σ) is given by

$$\sigma = \sigma_b\left[1 + 2\mu_0^2 + 2\sqrt{\left(1+\mu_0^2\right)}\left(\mu_0^2 - \mu^2\frac{4x^2}{b^2}\right)\right], \tag{7}$$

where μ_0 is the internal friction coefficient of caved gangue specimen $\mu_0 = \tan\varphi$, φ is the deflection angle of principal

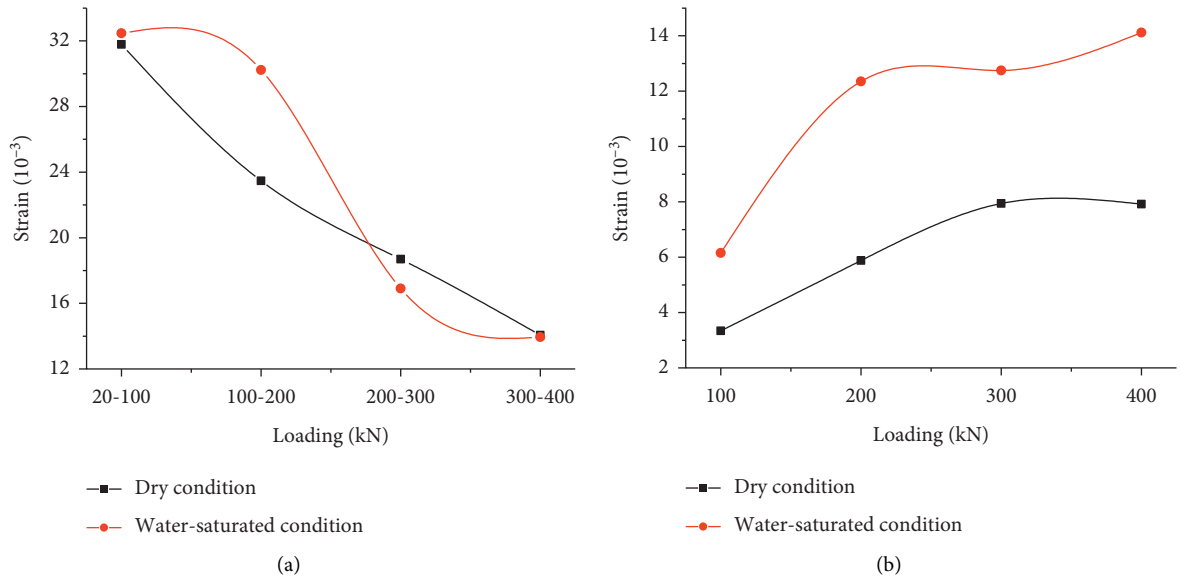

Figure 10: Strain D-values of the caved gangue specimens in different stages. (a) Different load stages. (b) Different constant load stages.

Table 3: Changes of mass fraction of caved gangue with different particle sizes before and after the testing.

Particle size	Mass fraction (%)					
	Dry			Water-saturated		
	Before testing	After testing	D-value	Before testing	After testing	D-value
0–5	0	5.25	5.25	0	5.85	5.85
5–10	5	7.46	2.46	5	8.09	3.09
10–15	10	10.21	0.21	10	10.43	0.43
15–20	20	20.08	0.08	20	20.25	0.25
20–25	30	26.81	-3.19	30	26.68	-3.32
25–30	20	16.35	-3.65	20	15.05	-4.95
30–35	10	9.02	-0.98	10	8.86	-1.14
35–40	5	4.82	-0.18	5	4.78	-0.22

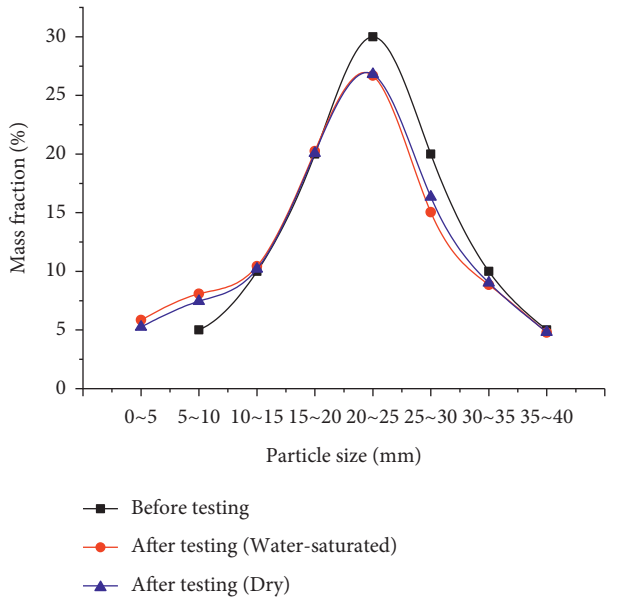

Figure 11: Curves of mass fraction of caved gangue with different particle sizes before and after the testing.

axis in the polar stress diagram near the side surface of caved gangue specimen, b is the diameter of caved gangue specimen, and x is the distance between the calculation point of vertical compressive stress value and the center of caved gangue specimen.

Caved gangue in gob is noncohesive materials and their particles are generally of convex polyhedron shape. The contact between particles can be categorized as angle to face contact and angle to angle contact [44, 45]. A single rock block represented by letter "j" is taken as the object of study, assuming that there are n contacts between rock block "j" and other rock blocks in the caved gangue specimen. Under load, the force and contact area of the ith contact are P_i and δ_i, respectively ($i = 1, 2, \ldots, n$). If there are m contacts on one contact surface labeled "A" of rock block "j", then $m \le n$, as shown in Figure 13.

The normal stress (σ_A) and shear stress (τ_A) acting on the contact surface labeled "A" are given by

$$\sigma_A = \sum_{i=1}^{m} \sigma_i == \sum_{i=1}^{m} \frac{P_i}{\delta_i} \cos\ \alpha_i \tau_A = \sum_{i=1}^{m} \tau_i = \sum_{i=1}^{m} \frac{P_i}{\delta_i} \sin\ \alpha_i, \quad (8)$$

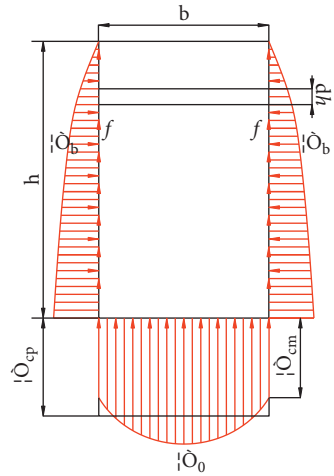

Figure 12: Compressive stress distribution of side wall and bottom of caved gangue specimen.

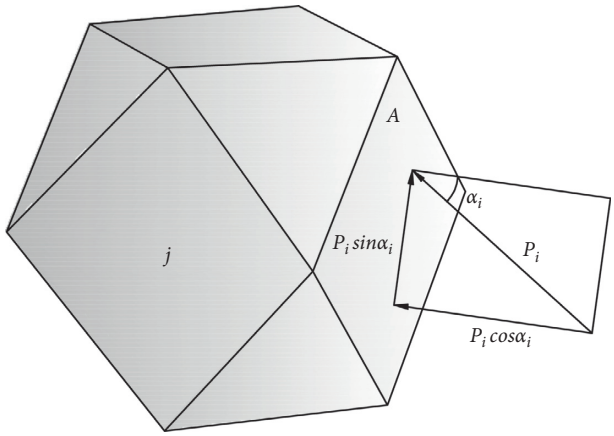

Figure 13: Acting force on the certain contact surface A of rock block j.

where α_i is the angle of intersection of normal of contact surface and acting force.

As a whole, the total normal stress acting on the rock block manifests as compressive stress, which is less than the crushing strength (σ_s) of rock block in the general case; therefore, there will be no crushing between rock blocks. But for some weakness planes, the crushing strength (σ_{sm}) is less than the bearing stress (σ_{im}). Assuming that a total of K weakness planes will be crushed into smaller blocks.

$$\sigma_{im}^k \geq \sigma_{sm}^k \, (k = 1, 2 \ldots K). \tag{9}$$

The total of strain (ε_1) caused by crushing of weakness planes is given by

$$\varepsilon_1 = \sum_{k=1}^{K} \int \left(\sigma_{im}^k - \sigma_{sm}^k\right) \mathrm{d}\zeta_k, \tag{10}$$

where ζ_k is equal to the ratio of strain to crushing stress.

In addition, the shear stress will form the tangential stress (τ_k) on the surface of rock block "j". But because the contact area is very small, the tangential stress is approximated as a uniform distribution. On the kth contact surface, the moment (T_k) about the barycenter of rock block "j" produced by tangential stress is given by

$$T_k = \tau_k \cdot r_k \cdot \delta_k, \tag{11}$$

where r_k is the distance between the kth contact surface and the barycenter of rock block "j".

Around the barycenter of rock block "j", a local coordinate (ξ-η plane) is created, the sum of tangential stress moment vector is given by

$$\begin{aligned} T_{\mathrm{m}\xi} &= \sum_{k=1}^{K} T_k \xi_k = \sum_{k=1}^{K} P_k \sin\, \alpha_k r_k \xi_k \\ T_{\mathrm{m}\eta} &= \sum_{k=1}^{K} T_k \eta_k = \sum_{k=1}^{K} P_k \sin\, \alpha_k r_k \eta_k, \end{aligned} \tag{12}$$

where ξ_k and η_k are the projection coefficients of the local coordinate, which are equal to the ratio of projection value to original value of all shear stress, respectively.

Under the action of moments, the newborn small rock blocks will slide and fill the gap between rock blocks, and the resulting strain (ε_2) is given by

$$\varepsilon_2 = \sum_{k=1}^{K} \int T_k \left(\xi_k \mathrm{d}\theta_\xi^{(k)} + \eta_k \mathrm{d}\theta_\eta^{(k)}\right), \tag{13}$$

where θ_ξ and θ_η are the compliance in shear, which are equal to the ratio of strain to shear stress.

So, during the bearing deformation testing of the caved gangue specimen, the plastic deformation ($_\varepsilon$) is given by

$$\varepsilon = \varepsilon_1 + \varepsilon_2 = \sum_{k=1}^{K} \int \left(\sigma_{im}^k - \sigma_{sm}^k\right) \mathrm{d}\zeta_k + \sum_{k=1}^{K} \int T_k \left(\xi_k \mathrm{d}\theta_\xi^{(k)} + \eta_k \mathrm{d}\theta_\eta^{(k)}\right). \tag{14}$$

It can be seen from the order of magnitude of the strain that ε_2 is greater than ε_1, so the deformation caused by slipping and filling the gap between rock blocks is greater than that caused by the crushing of weakness planes of rock blocks. That is, the major cause of bearing deformation of the caved gangue specimen is that the newborn small rock blocks slip and fill the gap between rock blocks.

The bearing deformation of the caved gangue specimen can be divided into two stages: instantaneous compression deformation and long-term deformation. (1) Instantaneous compression deformation: As the increase of load, the caved gangue specimen becomes compacted gradually. The axial deformation in load stage is more obvious than that in constant load stage, which accounts for 77.8% of total deformation under dry condition, and 67.6% of total deformation under water-saturated condition, the time of load stage is short, the axial deformation will stop basically with the stop of load, but it is inadequate and only relatively stable. The contact between caved gangue blocks is brittle-elastic, the changes of caved gangue blocks mainly include crushing, slipping, and filling, which is more and more prominent with the increase of load. (2) Long-term

deformation: In constant load stage, the impacted crushing of caved gangue is over, but the redistribution of stress between rock blocks will also lead to the crushing of weakness planes of rock blocks, causing the slipping and filling. Under dry condition, the axial deformation in constant load stage accounts for 22.2% of total deformation, and under water-saturated condition, the axial deformation in constant load stage accounts for 32.4% of total deformation. By comparison, the water promotes the compressive strain of caved gangue specimen obviously, especially in constant load stage. The bulk strain of the caved gangue mass is controlled by the rock particle rearrangement, including rotation and slipping between each rock block, and the bulk deformation of a single caved gangue block.

4. Conclusion

(1) The testing system used for bearing deformation testing of caved gangue is developed, which is consisted of load support bracket, load head, testing chamber, servo control system of displacement and load, servo control system of water pressure and water yield, and operating deck. In view of the particle size distribution characteristics and stress state of caved gangue, the size distribution of caved gangue obeys the law of normal distribution, and the load pattern is designed to step load.

(2) With the increase of axial load, the axial deformation of caved gangue increases gradually, the residual bulking coefficient decreases gradually, which are more obvious in load stage than in constant load stage. In the early constant load stage, the axial deformation of caved gangue grows rapidly, then tends to be slow and steady gradually; the relationship between strain and time meets the logarithmic relationship. In load stage, the D-value of axial strain decreases gradually along with the increase of axial load, and in constant load stage, which is opposite.

(3) The bearing deformation of caved gangue is consisted of two parts: instantaneous compression deformation and long-term deformation. For instantaneous compression deformation, the water acting as the lubricant promotes the compressive strain of caved gangue specimen and is conducive to rotation and slipping between each rock block. For long-term deformation, meanwhile, the water acting as the softening agent reduces the strength of the rock block and is conducive to the crushing of the rock block. The newborn rock blocks may slip and fill the gap between rock blocks, which also promotes the compressive strain of caved gangue specimen. The research results have important significance for forecasting and controlling the movement and deformation of overlying strata caused by mining.

Data Availability

The data used to support the findings of this study are included within the article.

Conflicts of Interest

The authors declare that there are no conflicts of interest regarding the publication of this article.

Acknowledgments

This work was supported by the National Science Foundation of China (51704152) and the Natural Science Foundation of Shandong Province (ZR2017BEE001).

References

[1] V. Palchik, "Influence of physical characteristics of weak rock mass on height of caved zone over abandoned subsurface coal mines," *Environmental Geology*, vol. 42, no. 1, pp. 92–101, 2002.

[2] V. Palchik, "Formation of fractured zones in overburden due to longwall mining," *Environmental Geology*, vol. 44, no. 1, pp. 28–38, 2003.

[3] V. Palchik, "Experimental investigation of apertures of mining-induced horizontal fractures," *International Journal of Rock Mechanics and Mining Sciences*, vol. 47, no. 3, pp. 502–508, 2010.

[4] G. Cheng, T. Ma, C. Tang, H. Liu, and S. Wang, "A zoning model for coal mining - induced strata movement based on microseismic monitoring," *International Journal of Rock Mechanics and Mining Sciences*, vol. 94, pp. 123–138, 2017.

[5] D. P. Adhikary and H. Guo, "Modelling of longwall mining-induced strata permeability change," *Rock Mechanics and Rock Engineering*, vol. 48, no. 1, pp. 345–359, 2015.

[6] H. Basarir, I. Ferid Oge, and O. Aydin, "Prediction of the stresses around main and tail gates during top coal caving by 3D numerical analysis," *International Journal of Rock Mechanics and Mining Sciences*, vol. 76, pp. 88–97, 2015.

[7] Q. Wu, J. Shen, W. Liu, and Y. Wang, "A RBFNN-based method for the prediction of the developed height of a water-conductive fractured zone for fully mechanized mining with sublevel caving," *Arabian Journal of Geosciences*, vol. 10, no. 7, pp. 172–180, 2017.

[8] C. Zhang, S. Tu, and Y. Zhao, "Compaction characteristics of the caving zone in a longwall goaf: a review," *Environmental Earth Sciences*, vol. 78, no. 1, pp. 27–42, 2019.

[9] S. Y. Hu, D. D. Han, G. R. Feng et al., "Influence of stress on void ratios of compacted crushed rock masses in coal mine gobs," *Natural Resources Research*, vol. 29, pp. 1362–1373, 2020.

[10] C. Ö. Karacan, "Prediction of porosity and permeability of caved zone in longwall gobs," *Transport in Porous Media*, vol. 82, no. 2, pp. 413–439, 2010.

[11] C. Ö. Karacan and K. Luxbacher, "Stochastic modeling of gob gas venthole production performances in active and completed longwall panels of coal mines," *International Journal of Coal Geology*, vol. 84, no. 2, pp. 125–140, 2010.

[12] M. Li, J. Zhang, N. Zhou, and Y. Huang, "Effect of particle size on the energy evolution of crushed waste rock in coal mines," *Rock Mechanics and Rock Engineering*, vol. 50, no. 5, pp. 1347–1354, 2017.

[13] W. Q. Ma and T. X. Wang, "Experimental study of shear strength features of regenerated rock mass compacted and consolidated by broken soft rocks," *KSCE Journal of Civil Engineering*, vol. 23, pp. 1839–1848, 2019.

[14] J. Chao, M. Yu, T. Chu, X. Han, F. Teng, and P. Li, "Evolution of broken coal permeability under the condition of stress,

temperature, moisture content, and pore pressure," *Rock Mechanics and Rock Engineering*, vol. 52, no. 8, pp. 2803–2814, 2019.

[15] Z. Q. Xiong, X. L. Wang, C. W. Liu, and H. G. Li, "Dynamic development characteristics of caving zone overburden strata in fully-mechanized mining stope under one-pass mining," *Chinese Journal of Rock Mechanics and Engineering*, vol. 33, no. 2, pp. 3692–3698, 2014.

[16] H. P. Xie, H. W. Zhou, J. F. Liu et al., "Mining-induced mechanical behavior in coal seams under different mining layouts," *Journal of China Coal Society*, vol. 36, no. 7, pp. 1067–1074, 2011.

[17] F. Long and S. M. Liu, "A conceptual model to characterize and model compaction behavior and permeability evolution of broken rock mass in coal mine gobs," *International Journal of Coal Geology*, vol. 172, pp. 60–70, 2017.

[18] J. W. Zhang, H. L. Wang, S. J. Chen, and Y. L. Li, "Bearing deformation characteristic of large-size broken rock," *Journal of China Coal Society*, vol. 43, no. 4, pp. 1000–1007, 2018.

[19] H. L. Wang, W. J. Guo, X. Z. Sun, C. Y. Jia, X. Y. Song, and G. B. Zhang, *Disaster Mechanism and Prevention of Water and Sand Inrush across Mining-Induced Roof Fractures*, China Science Publishing and Media Ltd., Beijing, China, 2020.

[20] T. J. Zhang, Y. Guo, M. K. Pang, W. Q. Peng, Y. Li, and S. Zhang, "Creep fractal characteristics of compressed and broken coal rock under different environmental humidity," *Journal of Mining and Safety Engineering*, vol. 37, no. 5, pp. 1037–1044, 2020.

[21] K. Zhang, B. Y. Zhang, J. F. Liu, D. Ma, and H. B. Bai, "Experiment on seepage property and sand inrush criterion for granular rock mass," *Geofluids*, vol. 2017, Article ID 9352618, 10 pages, 2017.

[22] G. B. Zhang, H. L. Wang, S. L. Yan, C. Y. Jia, and X. Y. Song, "Simulated experiment of water-sand inrush across overlying strata fissures caused by mining," *Geofluids*, vol. 2020, Article ID 6614213, 11 pages, 2020.

[23] H. L. Wang, S. J. Chen, and W. J. Guo, "Development and application of test system for water-sand inrush," *Journal of Mining and Safety Engineering*, vol. 36, no. 1, pp. 72–79, 2019.

[24] X. Yang, Y. J. Liu, M. Xue, T. H. Yang, and B. Yang, "Experimental investigation of water-sand mixed fluid initiation and migration in porous skeleton during water and sand inrush," *Geofluids*, vol. 2020, Article ID 8679861, 18 pages, 2020.

[25] B. Yang, T. H. Yang, Z. H. Xu, and X. Yang, "Critical velocity of sand inrush and flow characteristics of water-sand in thick unconsolidated formations of mine in western China," *Journal of Northeastern University*, vol. 39, no. 11, pp. 1648–1652, 2018.

[26] G. Li, Y. Hu, S.-m. Tian, M. weibin, and H.-l. Huang, "Analysis of deformation control mechanism of prestressed anchor on jointed soft rock in large cross-section tunnel," *Bulletin of Engineering Geology and the Environment*, vol. 80, no. 12, pp. 9089–9103, 2021.

[27] M. Gao, J. Xie, Y. Gao et al., "Mechanical behavior of coal under different mining rates: a case study from laboratory experiments to field testing," *International Journal of Mining Science and Technology*, vol. 31, no. 5, pp. 825–841, 2021.

[28] M. Z. Gao, H. C. Hao, S. N. Xue et al., "Discing behavior and mechanism of cores extracted from Songke-2 well at depths below 4,500 m," *International Journal of Rock Mechanics and Mining Sciences*, vol. 149, Article ID 104976, 2022.

[29] C. Zhu, M. Karakus, M. He et al., "Volumetric deformation and damage evolution of Tibet interbedded skarn under multistage constant-amplitude-cyclic loading," *International Journal of Rock Mechanics and Mining Sciences*, vol. 152, Article ID 105066, 2022.

[30] Y.-q. Su, F.-q. Gong, S. Luo, and Z.-x. Liu, "Experimental study on energy storage and dissipation characteristics of granite under two-dimensional compression with constant confining pressure," *Journal of Central South University*, vol. 28, no. 3, pp. 848–865, 2021.

[31] Z.-j. Wu, L.-f. Fan, L. Weng, Q.-s. Liu, and Q. S. Liu, "Micro-failure process and failure mechanism of brittle rock under uniaxial compression using continuous real-time wave velocity measurement," *Journal of Central South University*, vol. 28, no. 2, pp. 556–571, 2021.

[32] Z. Dou, S. X. Tang, X. Y. Zhang et al., "Influence of shear displacement on fluid flow and solute transport in a 3D rough fracture," *Lithosphere*, vol. 2021, Article ID 1569736, 2021.

[33] Z. Dou, Y. M. Liu, X. Y. Zhang et al., "Influence of layer transition zone on rainfall-induced instability of multilayered slope," *Lithosphere*, vol. 2021, Article ID 2277284, 2021.

[34] C. Zhang and L. Zhang, "Permeability characteristics of broken coal and rock under cyclic loading and unloading," *Natural Resources Research*, vol. 28, no. 3, 2019.

[35] Q. Wang, Z. B. Guo, Z. H. Ouyang, S. Y. Yin, and R. Peng, "The influence of crushed rock size on bearing-deformation performance of gangue rib of gob-side entry retaining formed by roof fracturing," *Journal of China University of Mining and Technology*, vol. 51, no. 1, 2022.

[36] B. Y. Yu, S. C. Pan, J. J. Wei, L. Yue, and J. N. Guo, "Particle crushing and permeability evolution of saturated broken rock under compaction," *Journal of Mining and Safety Engineering*, vol. 37, no. 3, pp. 632–638, 2020.

[37] J. Jiang, D. W. Yin, Y. J. Yang, J. B. Ma, and Y. Ge, "Experimental study on long-term load-bearing deformation and fractal characteristics of crushed gangue under dry-wet cycles," *Journal of Mining and Safety Engineering*, vol. 37, no. 1, pp. 176–182, 2020.

[38] Y. J. Xin, H. C. Hao, X. Lü, H. Y. Ji, and D. C. An, "Compaction characteristics test of broken rock in initial lateral pressure," *Journal of China Coal Society*, vol. 43, no. 2, pp. 457–465, 2018.

[39] M. M. Feng, J. Y. Wu, Z. Q. Chen, X. B. Mao, and B. Y. Yu, "Experimental study on the compaction of saturated caved gangue of continuous gradation," *Journal of China Coal Society*, vol. 41, no. 9, pp. 2195–2202, 2016.

[40] C. Zhang, X. C. Zhan, and C. H. Yang, "Mesoscopic simulation of strength and deformation characteristics of coarse grained materials," *Rock and Soil Mechanics*, vol. 34, no. 7, pp. 2077–2083, 2013.

[41] Ministry of Water Resources of the People's Republic of China, *Soecification of Soil Test*, Water Resources and Hydropower Press, Beijing, China, 1999.

[42] W. A. Bishop and D. J. Henkel, *The Measurement of Soils Properties in Triaxial Test*, Edward Arnold, London, UK, 1962.

[43] S. Y. Huang, *Mechanics of Granular Media*, China Machine Press, Beijing, China, 2020.

[44] L. Shao, S. C. Chi, Y. Zhang, and J. Y. Tao, "Study of triaxial shear tests for rockfill based on particle flow code," *Rock and Soil Mechanics*, vol. 34, no. 3, pp. 711–720, 2013.

[45] Y. Huang, J. Li, Y. Teng et al., "Numerical simulation study on macroscopic mechanical behaviors and micro-motion characteristics of gangues under triaxial compression," *Powder Technology*, vol. 320, pp. 668–684, 2017.

Hindawi
Mathematical Problems in Engineering
Volume 2022, Article ID 4289057, 11 pages
https://doi.org/10.1155/2022/4289057

Research Article

A Study of Blast Vibration Propagation Law under Negative Altitude Terrains

Jing Gao,[1] **Cong Huang**,[2] **Xiaomin Huang**,[3] **Jian-Jun Ren**,[4] **and Na Wang**[2]

[1]*Yan'an Xing'an Blasting Engineering Service Co., Ltd, Yan'an, Shanxi 716000, China*
[2]*Mining College of Guizhou University, Guiyang, Guizhou 550025, China*
[3]*School of Mathematics and Statistics, Guizhou University of Finance and Economics, Guiyang, Guizhou 550025, China*
[4]*College of Physics and Engineering, Xingyi Normal University for Nationalities, Xingyi, Guizhou 562400, China*

Correspondence should be addressed to Jing Gao; gaojing0408@163.com

Received 5 January 2022; Accepted 1 February 2022; Published 10 March 2022

Academic Editor: Fuqiang Ren

The propagation characteristics of blast waves and the prediction accuracy of blast vibration velocities along negative slopes are important because those can be used to guide engineering application and theoretical research. In this paper, the wave theory was applied to better understand the propagation mechanism of blast waves along negative slopes. Regression analysis was used for the Sadovsky and the CRSRI blast vibration velocity prediction models during on-site operations. The magnification of peak blast vibration velocity along a negative slope was introduced to determine the threshold altitude difference for the magnification effect to occur. Based on this parameter, the relative errors between the two prediction models were compared. The obtained results indicate that the superposition of incident and reflected blast waves on a negative slope creates the "slope effect" which locally amplifies the blast vibration velocity. The relative error of the CRSRI prediction model was as small as 17.53%, demonstrating a greater accuracy than Sadovsky's prediction model. The magnification effect of a negative slope was observed at specific altitude differences and was more noticeable in the perpendicular direction. This paper creates a theoretical basis for studying the propagation mechanisms of blast vibration waves along negative slopes as well as predicting the blast vibration velocities.

1. Introduction

Blasting operations usually induce a topographic change within the investigated area. These modifications decrease the accuracy of the Sadovsky formula which is commonly used for predicting the blast vibration velocity. The slope magnification effect caused by the propagation of blast waves over undulating terrain has become an essential part of studying the propagation of blast vibrations during rock slope excavations [1].

Previous studies focused on the propagation mechanism of blast waves in rock slopes have laid the foundation for an accurate prediction of the blast vibration velocity. Chen et al. [2] suggested that the altitude magnification effect is caused by the "whipping effect," as the main frequency of the blast wave load is equal to the natural vibration frequency of the bench. Guo et al. [3], Soltys et al. [4], and Man et al. [5] combined theoretical analyses with field tests and confirmed the "slope effect" for both negative and positive slopes, leading to an increase in the slope blast vibration velocity. Qiu [6] considered the rock slope as a multilayered environment and suggested that the blast waves would be superimposed by refraction and reflection after propagating to the interfaces of different layers. In consequence, this would create the "interface group effect" and lead to the altitude magnification effect.

Several studies have been carried out to accurately predict the blast vibration velocity in terrains of varying altitudes. Liu et al. [7], Roy et al. [8], Elevli and Arpaz [9], and Torres et al. [10] applied Sadovsky's formula with modifications in the altitude difference to predict the blast vibration velocity based on a large volume of field data. The conclusions showed that the modified formulas generated safer prediction results, but their solutions were not good

supported by theoretical analysis since no normalization was implemented. Zhu et al. [11], Faradonbeh et al. [12], and Himanshu et al. [13] proposed a modified formula for predicting the blast vibration velocities for sloped terrains based on field data analysis and comparison experiment. They performed dimensional analyses on the altitude difference and obtained acceptable results when they applied the modified formula to practical situations. Tang [14] and Ainalis et al. [15] used dimensional analysis and deduced a formula for predicting blast vibration velocity based on the altitude difference. After applying the results to real-life scenarios, they concluded that the prediction error of the formula was as little as 10%. Li et al. [16] and Kumar et al. [17] studied the blast vibration of a shaft. Their results indicate that the altitude magnification effect had an elevation threshold above which the blast vibration velocity would be attenuated. Wu et al. [18] and Kim and Lee [19] implemented the linear regression approach to generate a predictive model for the blast vibration velocity in benched terrains based on numerical simulations and field tests. The results suggest that the correlation coefficient of the obtained formula was higher compared to the other formulas and could better reflect the influence of altitude difference on the blast vibration velocity. Liu et al. [20] used field tests as well as theoretical analyses and concluded that their modified prediction formula performed better than Sadovsky's formula for terrains with a negative slope when the altitude difference was taken into consideration. Lei et al. [21] and Roy et al. [22] applied an already known altitude difference correction formula and regression fitting analysis approach and concluded that the slope coefficient (β) decreased during the initial stage but afterwards rapidly increased. Lu and Huetrulid [23], Agrawal and Mishra [24], and Hudaverdi [25] analyzed the issue from different theoretical angles and proposed a modified formula that was better theoretically adjusted and more comprehensive in predicting blast vibration velocity. Zhang [26] obtained a high-precision prediction formula for bench blast vibrations by analyzing the propagation mechanism of blast waves and by associating it with the elastic wave mechanics. Yang et al. [27] and Avellan et al. [28] studied the seismic topographic effect of blasting on the follow-wave slope and derived a model for predicting the blast vibration velocity of a follow-wave slope with higher differential elevations.

The previously mentioned studies focused on the efficiency of the blast waves and the prediction of blast vibration velocities, but only some of them considered the negative slopes. Therefore, there is a need for further research. In this study, we investigated the propagation mechanism of blast waves along negative slopes using the elastic wave theory. Afterwards, we applied the regression analysis approach to two prediction models based on the altitude difference, and it was concluded that the prediction results of the CRSRI model were more accurate than those of the Sadovsky model. Finally, we introduced the magnification of peak vibration, so that the threshold altitude difference of the magnification effect of a negative slope could be quantified.

2. Analysis of the Mechanism of the Negative Slope Effect

2.1. Generation Mechanism of Seismic Waves. When explosives are detonated in rocks, a large amount of energy is instantaneously released. The generated energy is dissipated by shock wave overpressure, compressive stress waves, as well as seismic waves. This causes the formation of a crushing zone, fracture zone, and vibration zone spreading outward from the explosion center (Figure 1). Within the vibration zone, seismic waves will cause elastic vibrations of the rock matrix, resulting in damage or even destruction of the matrix structure. Therefore, it is important to investigate the propagation mechanisms of blast waves in the vibration zone [29].

2.2. Basic Classification of Seismic Waves. The propagation of seismic waves in various media is affected by many factors, and the variety of seismic waves is extremely complex. Seismic waves propagating within a medium are called body waves, while those propagating near the surface are known as surface waves. The body waves can either be longitudinal or transverse. The longitudinal waves, whose propagation direction is aligned with the vibration direction of the medium, cause tensile and compressive damage to the medium, while the transverse waves, which propagate perpendicularly to the medium vibration direction, cause shear damage. Surface waves, on the other hand, are generally considered secondary waves which are generated by multiple reflections of the body waves from stratigraphic interfaces. The surface waves include Love waves and Rayleigh waves [30] (Figure 2).

2.3. Propagation Mechanism of Seismic Waves along a Negative Slope. According to the Fermat principle, the blast-generated seismic waves propagating in the negative slope direction will travel along the shortest path between the blast center and a measurement point, instead of a straight line [31] (Figure 3).

When the seismic wave propagates along a negative slope, the incident wave will be completely reflected from the slope, thus forming a reflective stretching area. Assuming that the slope is made of a homogeneous matrix, the propagation velocity of the incident wave can be expressed accordingly [32] as follows:

$$v_i(t) = A_1 f(t). \tag{1}$$

The propagation velocity of the reflected wave can be expressed as follows:

$$v_r(t) = A_1 f(t). \tag{2}$$

By integrating the vector sum of the propagation velocities of the incident and the reflected wave, the displacement of slope particles can be calculated as follows:

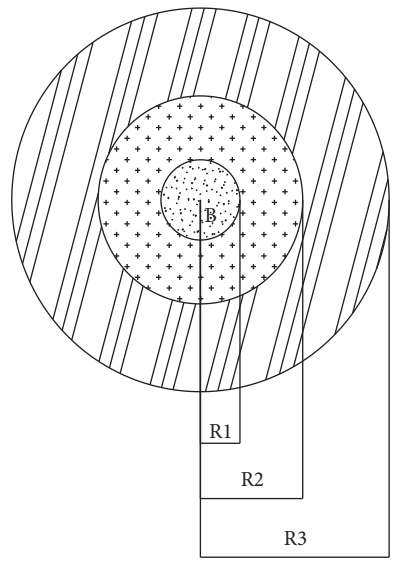

Figure 1: Damaged zones caused by the explosion B-charge; R_1-charging radius; R_2-crushing zone; R_3-fracture zone.

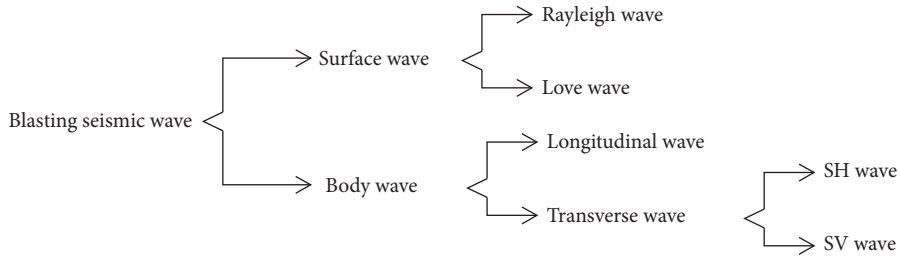

Figure 2: Classification of blast seismic waves.

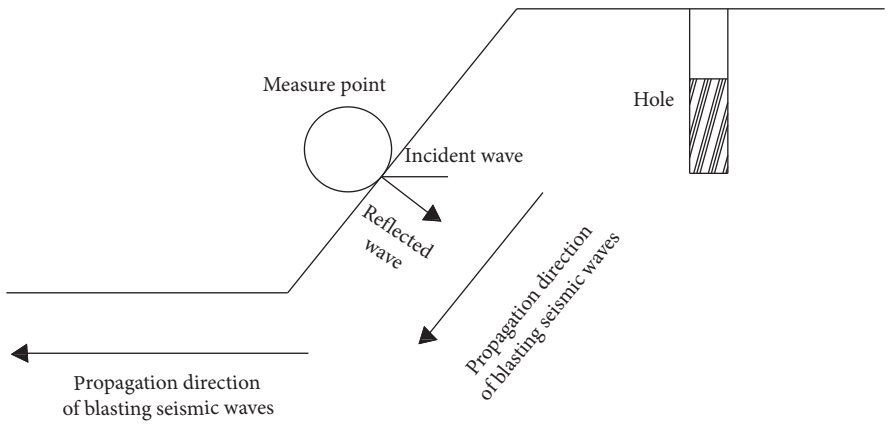

Figure 3: Propagation mechanism of seismic waves along a negative slope.

$$U(t) = \int_0^t \left[v_i(t) - v_r(t)\right] \mathrm{d}x, \\ = 2\int_0^t A_1 f(x) \mathrm{d}x. \tag{3}$$

In equations (1)–(3), A_1 is the amplitude of the incident wave vibration velocity, $v_r(t)$ is the propagation velocity of the incident wave, and $v_r(t)$ is the propagation velocity of the reflected wave. It can be observed from equation (3) that a superposition of the incident and the reflected wave occurs

when they travel along the negative slope direction, resulting in a local increase in vibration intensity.

3. Predictive Models for Negative Slopes and Their Coefficients

Sadovsky's and CRSRI formulas are widely used in practical activities to predict blast vibration velocities. In this study, regression analysis is applied to these two common models to obtain the relative errors between the two prediction models.

3.1. Sadovsky's Predictive Model Coefficients

$$v = \mathrm{K}\left(\frac{\sqrt[3]{Q}}{R}\right)^{\alpha}, \tag{4}$$

where v is the particle peak vibration velocity, m/s; Q represents the amount of explosive, kg; R is the distance from the observation point to the explosion center, m; K is a coefficient related to topographic and geological conditions; α is the attenuation coefficient.

By applying the logarithm for both sides of equation (4), the following formula is obtained:

$$\lg v = \lg K + \alpha \lg\left(\frac{\sqrt[3]{Q}}{R}\right). \tag{5}$$

If we consider that $y = \lg v$, $a = \lg K$, $b = \alpha$, and $x = \lg(\sqrt[3]{Q}/R)$, (5) can be transformed into a single-variable linear function as follows:

$$y = a + bx. \tag{6}$$

The least squares method can be used to calculate the coefficients a and b as follows:

$$\begin{aligned} a &= \frac{n\sum_{i=1}^{n}(x_i y_i) - \sum_{i=1}^{n} y_i \sum_{i=1}^{n} x_i}{n\sum_{i=1}^{n} x_i^2 - \left(\sum_{i=1}^{n} x_i\right)^2}, \\ b &= \frac{\sum_{i=1}^{n}(x_i y_i)\sum_{i=1}^{n} x_i - \sum_{i=1}^{n} y_i \sum_{i=1}^{n} x_i^2}{\left(\sum_{i=1}^{n} x_i\right)^2 - n\sum_{i=1}^{n} x_i^2}. \end{aligned} \tag{7}$$

3.2. CRSRI Predictive Model Coefficients

$$v = \mathrm{K}\left(\frac{\sqrt[3]{Q}}{R}\right)^{\alpha}\left(\frac{\sqrt[3]{Q}}{H}\right)^{\beta}, \tag{8}$$

where H is the bench height; β is the influence coefficient of elevation difference; the other parameters have the same definition as in the previous equations.

By applying the logarithm on both sides of equation (8), the following formula is obtained:

$$\lg v = \lg K + \alpha \lg\left(\frac{\sqrt[3]{Q}}{R}\right) + \beta \lg\left(\frac{\sqrt[3]{Q}}{H}\right). \tag{9}$$

If we consider that $z = \lg v$, $a = \lg K$, $b = \alpha$, $x = \lg(\sqrt[3]{Q}/R)$, $c = \beta$, and $y = \lg(\sqrt[3]{Q}/H)$, equation (9) can be transformed into a two-variable linear function as follows:

$$z = a + bx + cy. \tag{10}$$

The least squares method can then be used to obtain the following equations:

$$\begin{aligned} \left(\sum_{i=1}^{n} x_i^2\right)b + \left(\sum_{i=1}^{n} x_i y_i\right)c + \left(\sum_{i=1}^{n} x_i\right)a &= \sum_{i=1}^{n} x_i z_i, \\ \left(\sum_{i=1}^{n} x_i y_i\right)b + \left(\sum_{i=1}^{n} y_i^2\right)c + \left(\sum_{i=1}^{n} y_i\right)a &= \sum_{i=1}^{n} y_i z_i, \\ \left(\sum_{i=1}^{n} x_i\right)b + \left(\sum_{i=1}^{n} y_i\right)c + na &= \sum_{i=1}^{n} z_i, \end{aligned}$$

$$A = \begin{vmatrix} \sum_{i=1}^{n} x_i^2 & \sum_{i=1}^{n} x_i y_i & \sum_{i=1}^{n} x_i \\ \sum_{i=1}^{n} x_i y_i & \sum_{i=1}^{n} y_i^2 & \sum_{i=1}^{n} y_i \\ \sum_{i=1}^{n} x_i & \sum_{i=1}^{n} y_i & n \end{vmatrix}, \tag{11}$$

$$B = \left(\sum_{i=1}^{n} x_i z_i \quad \sum_{i=1}^{n} y_i z_i \quad \sum_{i=1}^{n} z_i\right)^{\mathrm{T}},$$

$$M = (b \quad c \quad a)^{T}.$$

When $A \neq 0$, the only valid solution for M can be obtained by solving the system of linear equations as follows:

$$M = A^{-1}B. \tag{12}$$

4. Case Study

4.1. Geographical Location. The test site is in Guiyang City, Guizhou Province, China. The surroundings are complex, mainly comprising the low Zhongshan erosion residual hills and depressions. Overall, the terrain is relatively flat, and the ground elevation varies between 1330 m and 1350 m, that is, the maximum height difference is 20 m.

Based on information from drilling logs and field observations, the site profile consists of soil, red clay, and plain fill. The thickness of the upper layer is 0.5–2 m, with an average thickness of 1.0 m. The bedrock is the first and the second section of *Tsz*1 + 2. The layers are consisted of argillaceous dolomite, claystones, tuffaceous claystones. The rocks are usually fractured. The site is located 60 m away from the Guizhou e-commerce industrial park to the east, 65 m away from a small-sized pig shed to the south, 72 m away from a single residential house, and 113 m away from the Binyang Road to the southeast, in proximity to residential areas to the west, and 331 m away from residential houses to the northwest. There are industrial parks, roads, high-intensity residential housing areas, and other similar elements located around the blasting area (Figure 4) [33].

4.2. Blasting Procedures. According to the on-site geological conditions and blasting requirements, this test adopts a multirow deep-hole blasting method, a hole-by-hole initiation technology, and the relevant [34, 35]. Rock powdery emulsion explosives and bulk ammonium nitrate explosives are used in the field, and the specific blasting parameters are shown in Tables 1 and 2.

This design points out that it is allowed to use the above parameters in the indicated area only if the maximum single dose of explosives is less than 21 kg. The specific delay design is shown in Table 3.

In multirow deep-hole blasting, the triangle hole arrangement is selected on the step flat plate, as shown in Figure 5.

The initiation sequence is illustrated in Figure 5. The numbers in the figure represent the delay time. Based on the delay network, the movement and the throwing direction of the explosive pile are indicated in Figure 6.

The network has a parallel connection. It registers the electronic detonator, as well as the number of the main line of the network. The electronic detonator clip of each hole is connected to the main line and is firmly attached to it. After the registration is completed, the detonation network extension is pressed. The time difference can be set manually, and a special detonator is used for charging and detonation. The schematic diagram of the connection between the electronic detonators is illustrated in Figure 7.

4.3. Field Monitoring. TC-4850 and NUBOX-8016 blast vibration meters were used during on-site operations. Both instruments can collect data from tangential, vertical, and radial channels (Figure 8).

Two rounds of data collection were carried out when the test was performed. Five measurement points were selected for each round, and ten field data records were obtained, as shown in Table 4.

4.4. Analysis of Blast Vibration Monitoring Results. Group 1 experimental data were selected from Table 4 to plot the vertical, tangential, and radial peak velocities according to the distance from the blast center (Figure 9).

It can be observed from Figure 9 that for the studied terrain with a negative slope, the peak velocities of blast vibrations in each of the three directions generally decreased with the increase in the distance from the blast center. However, when the distance from the blast center was equal to 150 m and 80 m, the peak velocities of blast vibration showed local magnification in the vertical and tangential direction, respectively. The magnification effect in the vertical direction was bigger than that in the tangential direction.

5. Analysis of the Negative Slope Effect on Blast Vibrations

The negative slope magnification effect on blast vibration velocity was analyzed in detail by considering that the magnification effect in the vertical direction was more pronounced. The first mid-vertical monitoring data were selected for the linear regression analysis of the Sadovsky and the CRSRI formulas.

5.1. Regression Analysis of Sadovsky's Predictive Model. The results of the linear regression approach for Sadovsky's formula are illustrated in Figure 10.

By including the regression parameters into equations (5) and (6), equation (4) can be expressed as

$$v = 15.994\,5\left(\frac{\sqrt[3]{Q}}{H}\right)^{1.05598}. \tag{13}$$

5.2. Regression Analysis of the CRSRI Predictive Model. To obtain a more accurate blast vibration prediction model, the linear regression approach was applied to the CRSRI formula, and the resulting model coefficients are illustrated in Table 5.

By including the parameters from Table 4 into equations (9) and (10), equation (8) can be expressed as

$$v = 0.547\,6 \times \left(\frac{\sqrt[3]{Q}}{H}\right)^{-0.3571}\left(\frac{\sqrt[3]{Q}}{H}\right)^{1.645\,8}. \tag{14}$$

The experimental data from Table 4 are included in equations (13) and (16) to obtain predicted values by using

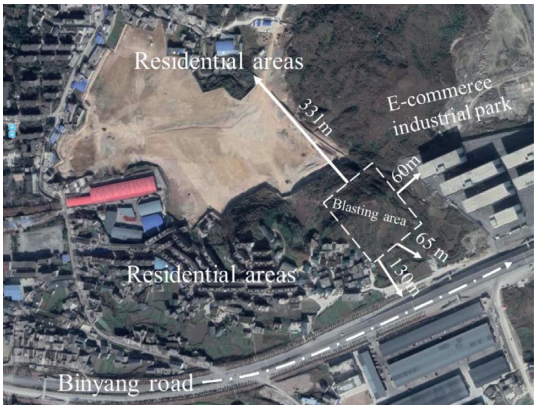

Figure 4: Blasting area surroundings.

Table 1: Layout parameters of the deep-hole blasting.

Rock type	Density (t/m^3)	Aperture mm	Hole arrangement	Piercing mode	Bench height H (m)
Dolomite	2.8	90	Triangle	Vertical	6~8

Table 2: Parameters used for the deep-hole bench blasting procedure.

Bench height H (m)	Resistance line w_1 (m)	Depth Δh (m)	Pitch row a (m)	Array pitch b (m)	Loaded length L_1 (m)	Unit consumption (kg/m^3)	Packing height (m)	One charge of explosives Q (kg)
6	2.5	0.5	2.5	2	2.23			10.5
7	2.8	0.5	2.8	2.5	3.41	0.35	≥3.0	17.2
8	3.0	0.5	3.0	2.5	4.37			21

Table 3: Delay combination scheme of hole-by-hole initiation technology.

Bench height H (m)	Pitch row a (m)	Delay in the hole (ms)	Array pitch b (m)	Delay between the rows (ms)	Rock properties
6	2.5	20	2	30	The argillaceous dolomite has developed joints and cracks; the rock mass is brittle; it is primarily weathered when crushed.
7	2.8	25	2.5	40	
8	3.0	25	2.5	45	

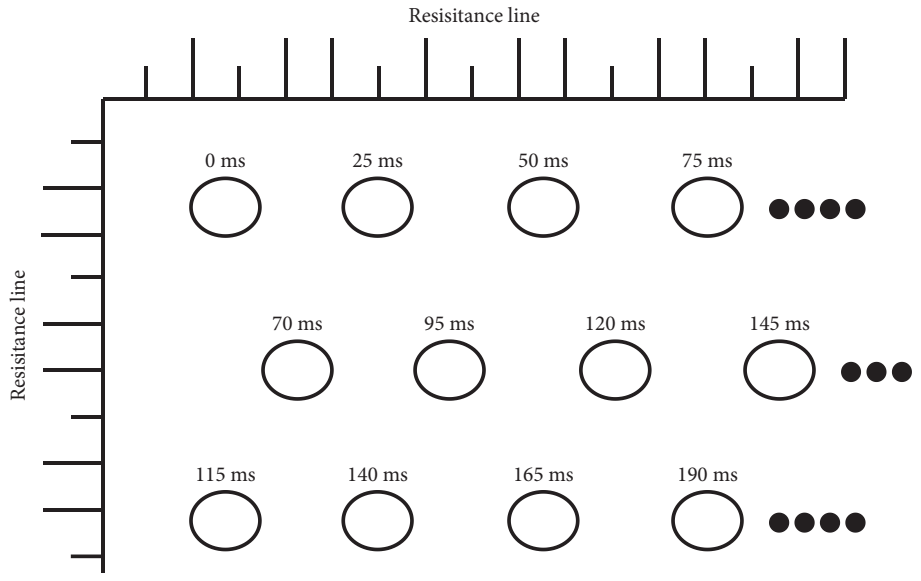

Figure 5: Schematic diagram of the shot hole layout and the delay settings.

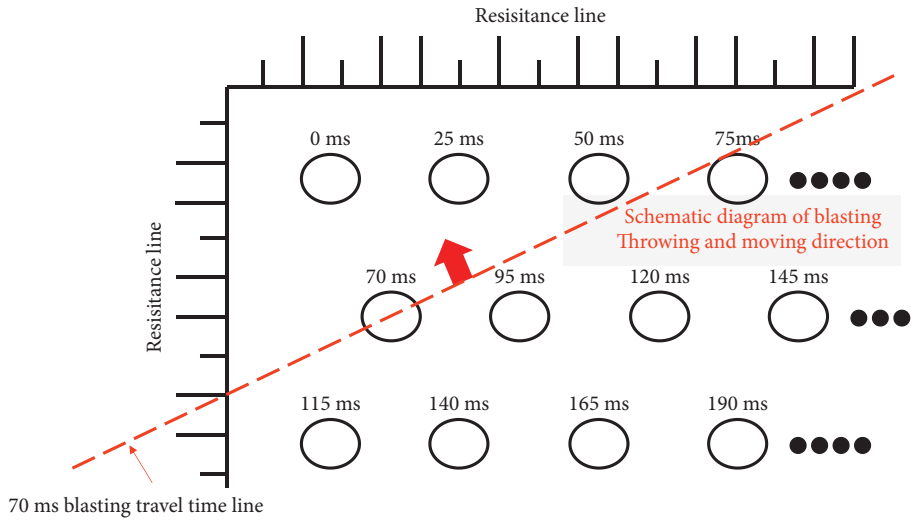

Figure 6: Schematic diagram of the throwing and the moving direction of the explosion.

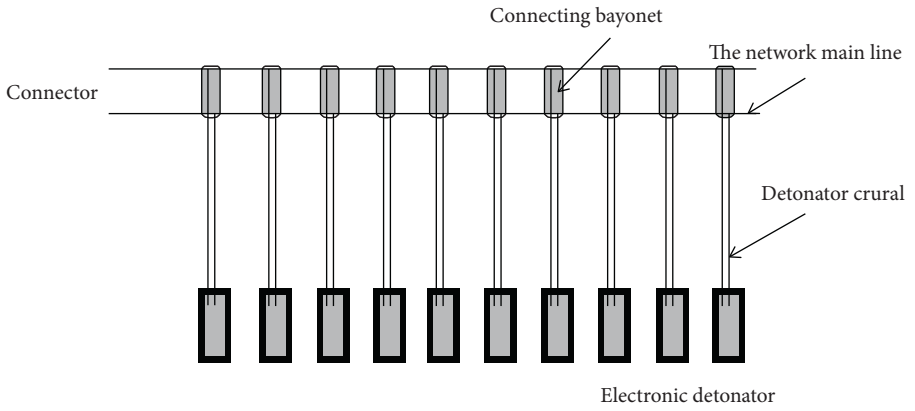

Figure 7: Schematic diagram of the electronic detonator connection.

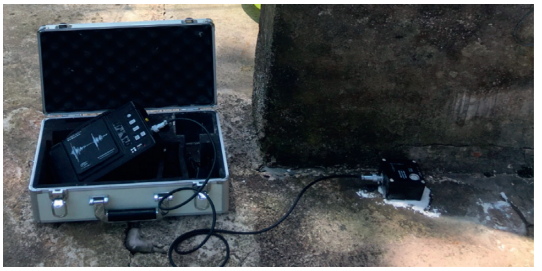

Figure 8: Field monitoring system.

the Sadovsky and the CRSRI formulas. The relative errors of the two formulas were calculated as

$$\text{Relative error} = \left|\frac{\text{Predicted value} - \text{Measured value}}{\text{Measured value}}\right| \times 100\% \quad (15)$$

and are illustrated in Table 6.

According to Figure 10 and Table 6, the R^2 value for Sadovsky's prediction model is 0.526, with the average relative error of the predicted velocity equal to 28.47%. This indicates a poor correlation and large errors for this prediction model. In contrast, according to Tables 3 and 4, the R^2 value for the CRSRI prediction model is 0.918, and the average relative error is equal to 17.53%, which means that

Table 4: Blasting parameters and monitoring data.

Data collection	Measurement point	Distance		Max. charge weight per delay, Q (kg)	PPV, v (cm·s^{-1})		
		Horizontal distance from blasting center, R (m)	Vertical distance from blasting center, H (m)		v_v	v_t	v_r
Group 1	1	60	−4	14	0.689	0.394	0.543
	2	70	−6	12	0.383	0.233	0.260
	3	80	−8	10	0.256	0.237	0.252
	4	150	−8.5	12	0.321	0.200	0.207
	5	155	−12	10	0.127	0.095	0.092
Group 2	1	60	−4	14	0.636	0.391	0.435
	2	70	−6	12	0.373	0.249	0.245
	3	80	−8	10	0.315	0.224	0.213
	4	150	−8.5	12	0.407	0.248	0.217
	5	155	−12	10	0.287	0.126	0.127

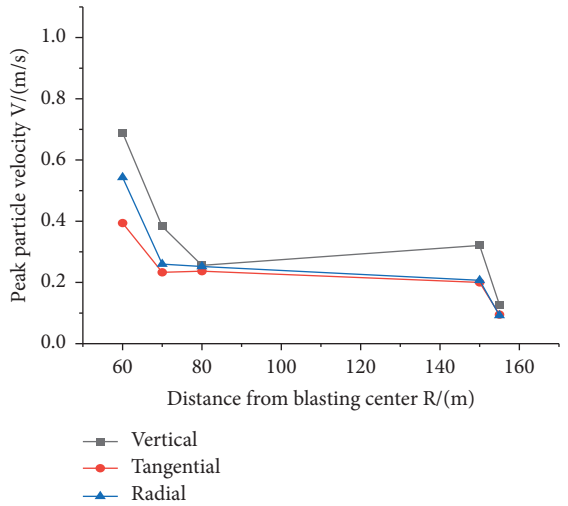

Figure 9: Peak vibration velocity vs. distance from the blast center.

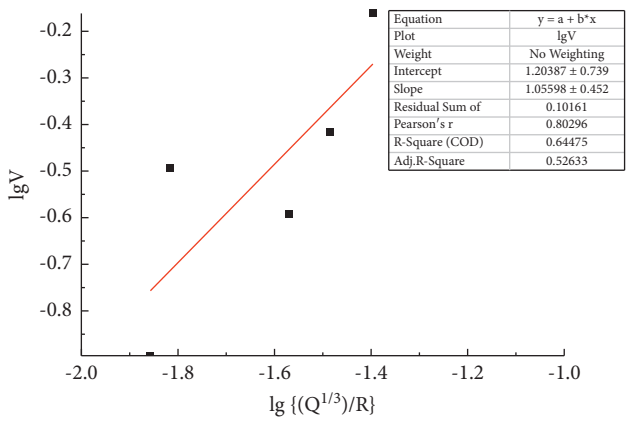

Figure 10: Regression analysis based on Sadovsky's predictive model.

Table 5: Multiple regression parameters for the CRSRI predictive model.

	Intercept		lg{{$Q^{1/3}$}/R}		lg{{$Q^{1/3}$}/H}		Analysis
	Value	Standard error	Value	Standard error	Value	Standard error	Adjusted R^2
lg v_v	−0.261 5	0.4851	−0.357 1	0.407 4	1.6458	0.420 8	0.9179

Table 6: Relative errors of the predicted velocities.

Data collection	Measurement point	PPV, v (cm·s^{-1})			Predicted velocity from Sadovsky's formula, (cm/s)	Predicted velocity from the CRSRI formula, (cm/s)	Relative error of Sadovsky's formula, (%)	Relative error of the CRSRI formula, (%)
		v_v	v_t	v_r				
Group1	1	0.689 0	0.394 0	0.543 0	0.536 7	0.749 7	22.11	8.81
	2	0.383 0	0.233 0	0.260 0	0.432 0	0.380 4	12.78	0.68
	3	0.256 0	0.237 0	0.252 0	0.351 8	0.229 8	37.44	10.24
	4	0.321 0	0.200 0	0.207 0	0.193 2	0.281 5	39.82	12.31
	5	0.127 0	0.095 0	0.092 0	0.175 0	0.149 3	37.79	17.56
Group 2	1	0.636 0	0.391 0	0.435 0	0.536 7	0.749 7	15.62	17.88
	2	0.373 0	0.249 0	0.245 0	0.432 0	0.380 4	15.81	1.98
	3	0.314 7	0.224 0	0.213 0	0.351 8	0.229 8	11.80	26.98
	4	0.407 0	0.248 0	0.217 0	0.193 2	0.281 5	52.54	30.84
	5	0.287 0	0.126 0	0.127 0	0.175 0	0.149 3	39.03	47.98
		Average error					28.47	17.53

Table 7: Peak vertical vibration velocity magnification.

Measurement point	Altitude difference, (m)	v_d	v_m	ε
1	−4	0.749 7	0.536 7	0.396 97
2	−6	0.380 4	0.432 0	−0.119 38
3	−8	0.229 8	0.351 8	−0.346 91
4	−8.5	0.281 5	0.193 2	0.457 30
5	−12	0.149 3	0.175 0	−0.146 79

the CRSRI prediction model of blast vibration is more accurate for negative slopes.

5.3. Analysis of Peak Velocity Magnification for the Negative Slope. The peak velocity magnification parameter (ε) was used to calculate the threshold slope difference for the negative slope magnification effect. Since the values of v_m and v_d are always positive, it is observed from equation (16) that when $v_m > v_d$, then values where $\varepsilon > 0$ result in the slope magnification effect. The formula for ε is expressed as [36]

$$\varepsilon = \frac{v_m - v_d}{v_d} \times 100\%, \tag{16}$$

where v_m is the peak velocity calculated by the CRSRI prediction model, and v_d is the peak velocity calculated by the Sadovsky's prediction model. The peak blast vibration velocities predicted using the Sadovsky and the CRSRI models listed in Table 4 were introduced into equation (16) to calculate the peak velocity magnification at the measurement points (Table 7). This allowed establishing the relationship between the peak vertical velocity magnification and the altitude difference (Figure 11). For visualization purposes, all negative altitude differences were plotted as absolute values.

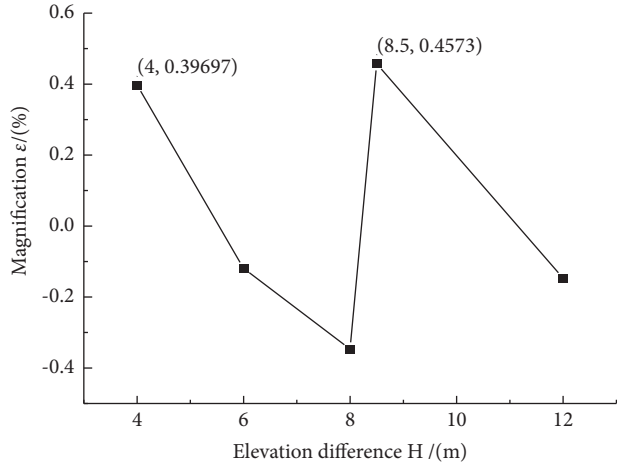

Figure 11: Variation in peak velocity magnification with the altitude difference.

As seen in Figure 11, except for the edge point (where the altitude difference was −4 m, and the peak velocity magnification was 0.3970 > 0), only when the altitude difference was −8.5 m, the peak velocity magnification was 0.4573 > 0, and the peak velocity magnification corresponding to the other altitude differences was smaller than 0 in all cases. This means that the altitude magnification in the vertical direction occurred solely when the altitude difference reached

−8.5 m, that is, the altitude threshold for the altitude magnification effect was equal to −8.5 m. According to Figure 9, the magnification effect of the negative slope was produced only for certain altitude differences, and it was more pronounced in the vertical direction.

6. Conclusions

This study applied the wave theory to analyze the propagation mechanism of blast waves along negative slopes. The linear regression approach was used for on-site data for the Sadovsky and the CRSRI blast vibration velocity prediction models. To compare their relative errors, the magnification of peak blast vibration velocity along a negative slope was introduced to determine the threshold altitude difference for the magnification effect to occur. The conclusions are as follows:

(1) In terrains with a negative slope, the superposition of incident and reflected blast vibration waves on the slope results in the local amplification of blast vibration velocity.

(2) The influence of the negative slope on the peak blast vibration velocity should be acknowledged. The predictions of the peak blast vibration velocity using the CRSRI formula are more accurate when compared to the other formulas.

(3) The magnification effect of the negative slope appears only for certain altitude differences above a threshold and is more obvious for the vertical vibration velocity.

Data Availability

The data used to support the findings of the study are available within the article.

Conflicts of Interest

The authors declare that they have no conflicts of interest.

Acknowledgments

This work was financially supported by the Youth Science and Technology Talent Growth Project of Guizhou Provincial Department of Education (Grant No. ky[2018]414) and Chinese National Natural Science Foundation (51664007). The authors would like to express their gratitude to EditSprings (https://www.editsprings.cn/) for the expert linguistic services provided.

References

[1] G. Q. Hu, S. J. Qu, and X. M. Liang, "Research on the influence of elevation amplification effect on open-pit blasting vibration attenuation," *Gold*, vol. 36, no. 7, pp. 28–32, 2015.

[2] M. Chen, W. B. Lu, P. Li, and M. Liu, "Elevation amplification effect of blasting vibration velocity in rock slope," *Chinese Journal of Rock Mechanics and Engineering*, vol. 30, no. 11, pp. 2189–2195, 2011.

[3] X. B. Guo, Z. X. Xiao, and Z. C. Zhang, "Slope effect of blasting vibration," *Chinese Journal of Rock Mechanics and Engineering*, vol. 20, no. 1, pp. 83–87, 2001.

[4] J. Pyra, A. Sołtys, and J. Winzer, "Analysis of the blast-induced vibration structure in open-cast mines," *Journal of Vibroengineering*, vol. 19, no. 1, pp. 409–418, 2017.

[5] K. Man, X. Liu, and Z. Song, "Frequency Spectrum and Wavelet Packet Analyses of Blasting Vibration Signals for Different Charge Structures in Blasting Peripheral Holes," *Advances in Civil Engineering*, vol. 2020, Article ID 8897441, 11 pages, 2020.

[6] J. M. Qiu, *Study on Elevation Amplification Effect of Open-Pit Bench Blasting*, Jiangxi University of Science and Technology, Ganzhou, China, 2015.

[7] M. Chen, W. B. Lu, and L. Wu, "Safety threshold of blasting vibration velocity to high rock slope of Xiaowan hydropower station," *Chinese Journal of Rock Mechanics and Engineering*, vol. 26, no. 1, pp. 51–56, 2007.

[8] M. P. Roy, P. K. Singh, M. Sarim, and L. S. Shekhawat, "Blast design and vibration control at an underground metal mine for the safety of surface structures," *International Journal of Rock Mechanics and Mining Sciences*, vol. 83, no. 83, pp. 107–115, 2016.

[9] B. Elevli and E. Arpaz, "Evaluation of parameters affected on the blast induced ground vibration (BIGV) by using relation diagram me(RDM)," *Acta Montanistica Slovaca*, vol. 15, no. 4, pp. 261–268, 2010.

[10] V. F. Navarro Torres, L. G. C. Silveira, P. F. T. Lopes, and H. M. de Lima, "Assessing and controlling of bench blasting-induced vibrations to minimize impacts to a neighboring community," *Journal of Cleaner Production*, vol. 187, pp. 514–524, 2018.

[11] C. T. Zhu, H. G. Liu, and J. Y. Mei, "Selection of formula on propagation of the parameters of explosive seismic wave along a slope gradient," *Blasting*, vol. 5, no. 2, pp. 30-31, 1988.

[12] R. Shirani Faradonbeh, D. Jahed Armaghani, M. Z. Abd Majid et al., "Prediction of ground vibration due to quarry blasting based on gene expression programming: a new model for peak particle velocity prediction," *International journal of Environmental Science and Technology*, vol. 13, no. 6, pp. 1453–1464, 2016.

[13] V. K. Himanshu, M. P. Roy, A. K. Mishra, R. K. Paswan, D. Panda, and P. K. Singh, "Multivariate statistical analysis approach for prediction of blast-induced ground vibration," *Arabian Journal of Geosciences*, vol. 11, no. 16, 2018.

[14] H. Tang, *Field Experimental and Theoretical Study on Blasting Wave Propagation Characteristics under Different Terrains*, Graduate University of Chinese Academy of Sciences (Institute of Rock and Soil Mechanics), Wuhan, China, 2007.

[15] D. Ainalis, O. Kaufmann, J.-P. Tshibangu, O. Verlinden, and G. Kouroussis, "Modelling the Source of Blasting for the Numerical Simulation of Blast-Induced Ground Vibrations: A Review," *Rock Mechanics and Rock Engineering*, vol. 50, no. 1, pp. 171–193, 2017.

[16] X. P. Li, J. Meng, and P. C. Xu, "A study on blasting seismic effects of cable shaft in Xiluodu hydropower station," *Rock and Soil Mechanics*, vol. 32, no. 2, pp. 474–480, 2011.

[17] S. Kumar, A. K. Mishra, B. S. Choudhary, R. K. Sinha, D. Deepak, and H. Agrawal, "Prediction of Ground Vibration Induced Due to Single Hole Blast Using Explicit Dynamics," *Mining, Metallurgy & Exploration*, vol. 37, no. 2, pp. 733–741, 2020.

[18] W. Xu, Z. Yunpeng, and G. Qifeng, "Amplification and attenuation effect of blasting vibration on step topography," *Blast and Shock*, vol. 37, no. 6, pp. 1017–1022, 2017.
[19] M. S. Kim and S. S. Lee, "The efficiency of large Hole boring (MSP) method in the reduction of blast-induced vibration," *Applied Sciences-Basel*, vol. 11, no. 4, Article ID 1814, 2021.
[20] C. J. Liu, W. H. Wang, and Q. Y. Li, "An analysis of blasting vibration attenuation effect of negative elevation difference," *Engineering Blasting*, vol. 26, no. 6, pp. 100–106, 2020.
[21] Z. Lei, L. He, and G. Y. Wu, "Vibration propagation law of high-rise buildings under blasting seismic waves," *Engineering Blasting*, vol. 26, no. 3, pp. 16–22, 2020.
[22] M. P. Roy, A. K. Mishra, H. Agrawal, and P. K. Singh, "Blast vibration dependence on total explosives weight in open-pit blasting," *Arabian Journal of Geosciences*, vol. 13, no. 13, 2020.
[23] W. B. Lu and W. Huetrulid, "An improvement to the equation for the attenuation of the peak particle velocity," *Engineering Blasting*, vol. 3, pp. 1–4, 2002.
[24] H. Agrawal and A. K. Mishra, "An innovative technique of simplified signature hole analysis for prediction of blast-induced ground vibration of multi-hole/production blast: an empirical analysis," *Natural Hazards*, vol. 100, no. 1, pp. 111–132, 2020.
[25] T. Hudaverdi, "Development of alternative predictor equations for blast-induced ground vibrations considering stiffness ratio, blast dimension and free face conditions," *International Journal of Mining, Reclamation and Environment*, vol. 35, no. 8, pp. 541–563, 2021.
[26] X. J. Zhang, *Theoretical Study and Application of Elevation Effect of Bench Blasting Vibration*, University of Science and Technology of Beijing, Beijing, China, 2021.
[27] S. Q. Yang, J. H. Zhang, and Z. Y. Lv, "Blasting seismic topographic effects of follow-wave slope with higher differential elevation," *Engineering Blasting*, vol. 27, no. 1, pp. 22–28, 2021.
[28] K. Avellan, E. Belopotocanova, and M. Puurunen, "Measuring, Monitoring and Prediction of Vibration Effects in Rock Masses in Near-Structure Blasting," *Procedia Engineering*, vol. 191, no. 8, pp. 504–511, 2017.
[29] X. Q. Zhang, *Research on the Deep Hole Bench Blasting Vibration Effect on Rock Slope Stability*, Xi'an University of Science and Technology, Xi'an, China, 2013.
[30] Y. B. Yuan, *Study on Vibration Propagation Law of High-Rise Building under Blasting Vibration*, Guiyang:Guizhou University, Guizhou, China, 2020.
[31] Q. M. Yi, S. J. Qu, and W. Y. Xu, "Research on the seismic wave amplification effect on the top of open pit bench," *Modern mining*, vol. 31, no. 1, pp. 40-41 + 65, 2015.
[32] X. Tian, Z. Song, and J. Wang, "Study on the propagation law of tunnel blasting vibration in stratum and blasting vibration reduction technology," *Soil Dynamics and Earthquake Engineering*, vol. 126, Article ID 105813, 2019.
[33] C. Huang, Z. Lei, and S. Y. Wei, "Evaluation and prediction of elevation blasting vibration based on AHP and normal distribution," *Engineering Blasting*, vol. 1–8, 2021.
[34] Z. X. Dong, *Blasting Engineering*, China Architecture & Building Press, Beijing, China, 2015.
[35] F. N. Wang, Z. B. Guo, and X. B. Qiao, "Large deformation mechanism of thin-layered carbonaceous slate and energy coupling support technology of NPR anchor cable in Minxian Tunnel: a case study," *Tunnelling and Underground Space Technology*, vol. 117, Article ID 104151, 2021.
[36] Y. T. Wang, C. S. Zhang, and S. L. Zang, "Slope altitude effect of blasting vibration in open-pit mine," *Journal of Mining Research and Development*, vol. 35, no. 4, pp. 56–59, 2015.

Hindawi
Mathematical Problems in Engineering
Volume 2022, Article ID 7100444, 10 pages
https://doi.org/10.1155/2022/7100444

Research Article

Investigation on the Deformation and Failure Characteristics of Shale Samples Containing Circular Hole considering the Bedding Angle Effect under Uniaxial Compression

Qinyuan Liang,[1] Cheng Zhao,[2] Yu Zhou ,[1] Bo Li,[1,2] and Ruyi Bao[1]

[1]*Key Laboratory of Rock Mechanics and Geohazards of Zhejiang Province, Shaoxing University, Shaoxing, Zhejiang 312000, China*
[2]*Department of Geotechnical Engineering College of Civil Engineering, Tongji University, Shanghai 200092, China*

Correspondence should be addressed to Yu Zhou; zhouyu@usx.edu.cn

Received 7 January 2022; Accepted 7 February 2022; Published 7 March 2022

Academic Editor: Fuqiang Ren

The drilling and blasting method (DBM) is widely used in the excavation of tunnel engineering, and it is essential to first drill circular holes. This paper experimentally explored the influence of bedding angles on crack propagation of shale containing a circular hole. Specifically, the uniaxial compression tests were carried out on shale samples with a single prefabricated hole combined with digital image correlation technology (DIC) to obtain the real-time deformation process near the macro damage. The results show that the peak strength, global shear strain field, failure mode around the circular hole and macro crack failure mode of shale with prefabricated circular hole are closely related to the bedding dip angle. The strength generally increases with the decrease of the bedding angle. Two transitions of failure mode were observed at the point of 45° and 75°: tensile shear mixed failure around the circular hole (less than 45°) first transits into no damage around the circular hole (60° and 70°), and then, tensile failure occurs around the circular hole (90°). In addition, for the cases of 60° and 75°, tensile failure away from the circular hole occurs along the weak surface of bedding, while for the other cases, the tensile failure through the circular hole mainly occurs. These findings have implied that the bedding angle is one essential parameter that needs to be considered for the stability of tunnel surrounding rock.

1. Introduction

Compared with traditional rock crushing mechanical methods (tunnel boring machines, rock breakers), the drilling and blasting method (DBM) has the advantage of low initial investment and cheap explosive energy and the possibility to construct openings with different shapes and sizes, so it is widely used in tunnel excavation [1–4]. To bury explosives, the DBM method usually needs to drill round holes, then clean the holes, and bury explosives for initiation excavation [5, 6]. However, on the one hand, the manually drilled holes can change the mechanical properties of the rock. On the other hand, due to unavoidable factors, the site selection of the tunnel must cross the active fault zone, where the geological structure is strong, and the manually drilled holes are easy to induce engineering geological disasters. Therefore, it is of great significance to study the deformation and crack propagation law of hole rock for the stability of tunnel surrounding rock [7–17].

At present, the researches on the mechanical response of rock materials with prefabricated voids mainly focus on exploring the crack initiation, propagation, and penetrating. Wong et al. [18] have carried out a series of experimental and numerical uniaxial compression tests on granite samples containing a single hole with different sizes of hole and granite samples to study the influence of hole on the failure modes and strength characterizations. It was found that cracks generated near the holes do not seem to tend to extend towards the free boundary, while first propagating outward from the free boundary and then parallel to the free

boundary, resulting in buckling failure. Li et al. [19] studied the influence of preformed holes with different geometries (i.e., size, shape, and angles) on the strength and fracture behaviour of marble using digital image correlation (DIC). It was found that the propagation of tensile cracks around the holes was mainly affected by the nucleation and propagation of cracks in the strain localization zone. Fan et al. [20] carried out a uniaxial compression test of sandstone with a single hole. The results showed that the hole significantly disturbed the internal stress distribution of the hole wall and internal stress was always intensively distributed at both sidewalls of the hole, especially at the midpoint of sidewalls; therefore, the spalling of rock cuttings on the sidewall can be first observed. Wang et al. [21–23] carried out experimental and numerical simulation studies under multiaxial stress conditions with the help of transparent resin materials containing spherical voids. It was found that the main feature of three-dimensional crack propagation under uniaxial compression is the formation of wing cracks wrapped around the initial circular hole. In biaxial compression, the shape of three-dimensional crack propagation is qualitatively affected by the intermediate principal stress. When the intermediate principal stress is relatively low, a large wing crack will also be formed, and its propagation degree is enough to split the sample. Based on DIC and wave velocity tests, Han et al. [24] studied the effect of hole size on the deformation and failure of 90° shale. The results found that large hole diameter (10 mm) and medium hole diameter (6 mm) were dominated by tensile failure, while a small hole diameter (2 mm) exhibited mixed tension and shear failure.

Many scholars have selected granite, marble, sandstone, and rock-like materials as their research objects to study the influence of prefabricated cavities on the deformation and crack propagation laws of rock materials, but few works have considered the influence of cavities on shale with different bedding angles. However, in tunnel engineering, shale is one common surrounding rock material [25, 26]. Because of its obvious layered structure, it shows significant anisotropy, which seriously affects the safety and stability of the tunnel [27–29]. Given this, domestic and foreign scholars have developed the law of the influence of bedding dip on the mechanical behaviour of intact shale. Niandou et al. [30] summarized the failure modes of shale under compressive load into three categories, namely, bedding plane sliding failure mode, sliding failure mode, and shear zone failure mode. Zhang et al. [31] conducted uniaxial compression tests on shales in Western Hubei and Eastern Chongqing with different bedding plane angles and found that the failure mode varies with bedding plane angles: the tensile failure dominates at 0° and 90°, while the failure mode is mainly shear failure when the loading direction is at a certain angle with the bedding plane, that is, 22.5°, 45°, and 67.5°. Hou et al. [29] conducted SEM and uniaxial compression test on shale with different bedding angles and found that the uniaxial compressive strength curve was approximately in the shape of "U": the maximum values occur with the shale bedding angles of 0° and 90°, and the minimal value is 30°. Yin et al. [32] summarized eight factors affecting UCS of shale and concluded that the bedding plane has a significant impact. Zhang et al. [33] studied the anisotropic characteristics of mechanical parameters of shale through uniaxial compression of shale with different bedding angles. It was found that with the gradual increase of bedding angle, the uniaxial compression strength curve exhibits a common "U" shape.

To date, the existing research systematically analyzes the influence law of bedding dip angle on the mechanical behaviour of intact shale, but less work considers the influence caused by the existence of holes. This paper took shale with different bedding angles as the research object and conducted uniaxial compression tests on shale samples with a prefabricated circular hole. With the help of digital image correlation (DIC), the changes in the global strain field during sample loading were monitored. The influence of bedding dip angle on the crack propagation law of shale with a circular hole was discussed, to further provide some technical support for the safety and stability of surrounding rock in tunnel engineering.

2. Test Preparation

2.1. Sample Preparation. The rock samples used in the test were collected from Changning County, Yibin City, Sichuan Province. The rocks in this section belong to the shale of the long-1 submember of the formation of the Lower Silurian system. To explore the influence of bedding dip angle on the crack propagation law of shale with a single circular hole, the rectangular plate samples ($150 \times 75 \times 20$ mm) with the included angles between bedding plane and horizontal lines of 0°, 15°, 30°, 45°, 60°, 75°, and 90° were prepared (as shown in Figure 1). To simulate the blast hole in DBM, the prefabricated single circular hole with a diameter of 6 mm is drilled in the geometric centre of the samples using a glass bit. To reduce individual differences, the above samples are prepared and processed from the same rock block. Before the DIC test begins, considering the natural black appearance of the shale, white paint of the Tamiya brand was sprayed on the surface to form random black and white speckles.

2.2. Introduction to DIC and Test

2.2.1. Introduction to DIC. The basic idea of the digital image correlation method is to quantify the specific subdomains before and after the deformation of the sample, to obtain the full-field deformation and strain of the sample. Assuming that the image grayscale eigenvalue functions before and after deformation of the sample are $f_1(x, y)$ and $f_2(x', y')$, respectively, and the object displacement field functions are $u(x, y)$ and $v(x, y)$. Then, the coordinates before and after image deformation are (x, y) and (x, y), and the relationship is

$$\begin{aligned} x' &= x + u(x, y), \\ y' &= y + v(x, y). \end{aligned} \tag{1}$$

To evaluate the similarity between the reference image and the current image, it is necessary to compare the grey

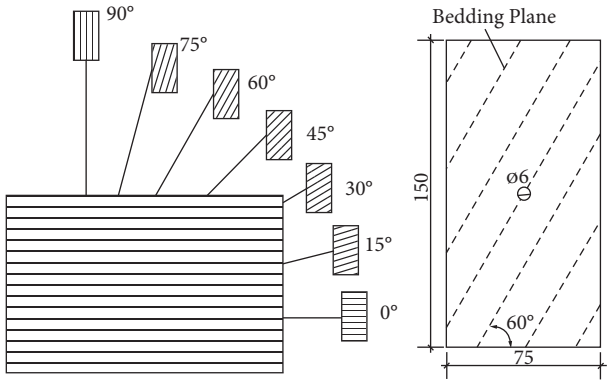

Figure 1: Schematic diagram of bedding angle of samples.

values between the two images and introduce the correlation coefficient C to represent the similarity between the current image after deformation and the reference image without deformation.

$$C = \frac{\sum[f_1(x,y) - f_{1m}] \times [f_2(x',y') - f_{2m}]}{\sqrt{\sum[f_1(x,y) - f_{1m}]^2}\sqrt{\sum[f_2(x',y') - f_{2m}]^2}}, \quad (2)$$

where $f_1(x,y)$ and $f_2(x',y')$ are the grey eigenvalue functions of the image before and after the deformation, and f_{1m} and f_{2m} are the grey mean values of the subregions of the image before and after the deformation. The range of correlation coefficient C is in the range of 0–1. The smaller the correlation coefficient C is, the more irrelevant the two subdomains are; the larger the correlation coefficient C is, the more relevant the two subdomains are. In general, when correlation coefficient C is at its maximum value, the operator region is the target subregion. The global displacement field can be obtained by calculating different subdomains. According to the global displacement field, the global strain field can be calculated by the Cauchy equation. This is the basic principle of digital image technology to obtain object displacement and strain fields [34].

2.2.2. DIC Test. The test equipment (Figure 2) consists of a loading system, observation system, and analysis system. The loading system adopts servo-hydraulic control, and its maximum loading force is 600 kN. To weaken the end effect, the vaseline was smeared on the upper and lower ends of the sample before loading. The displacement control mode is adopted in the test with a loading velocity of 0.2 mm/min. The observation system consists of halogen lamps arranged on both sides of the sample and a set of the high-speed camera system to capture the real-time image of crack incubation and evolution during loading. 300 original images shall be taken before loading, and the post-trigger mode shall be opened during loading at 600 frames per second. Finally, the global strain field can be measured based on the open-access Ncorr software [35]. Unless otherwise stated, the calculation parameters used herein are shown in Table 1.

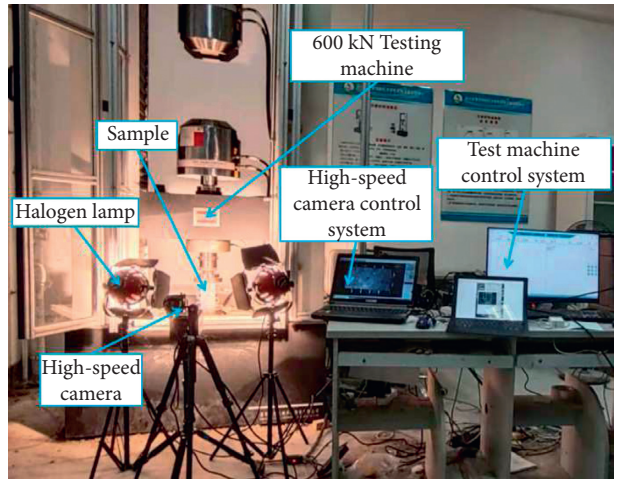

Figure 2: Test equipment.

Table 1: Main calculation parameters used in Ncorr.

Subset radius	Subset spacing	Difference vector cutoff	Strain radius
20 pixels	0	1.00E-08	5 pixels

3. Test Results and Discussion

3.1. Uniaxial Compressive Strength. Figure 3 shows the relationship between uniaxial compressive strength and bedding angle of shale with prefabricated circular holes. It can be seen that the uniaxial compressive strength generally shows a downward trend with the increase of bedding angle. The compressive strength of the 15° sample is the largest, and the uniaxial compressive strength is 147.12 MPa. The uniaxial compressive strength of 30°, 45°, 60°, and 75° specimens decreases gradually with the increase of bedding dip angle. Among them, the uniaxial compressive strength of the 75° specimen is the smallest, and the test value is 40.78 MPa. The peak strength of 90° bedding is 3.37 MPa higher than that of 75° bedding. This is different from the results of Zhang et al. [31], He et al. [36], and Xie et al. [37] (the uniaxial compressive strength is the smallest when the bedding angle is 50°, 60°, and 45°, respectively). The mechanisms behind this phenomenon are as follows: on the one hand, the mechanical properties of shales in different regions are different [33]; on the other hand, it is significantly affected by the prefabricated circular hole set in the geometric centre of shale, which will be discussed in the following section.

According to the test, the variation trend of uniaxial compressive strength of shale with prefabricated circular holes with bedding dip angle is obtained, and the fitting curve is as follows:

$$\sigma_c = 0.00035\theta^3 - 0.03562\theta^2 - 0.7469\theta + 149.31139, \quad (3)$$

where σ_c is uniaxial compressive strength; θ is the angle between bedding and horizontal plane.

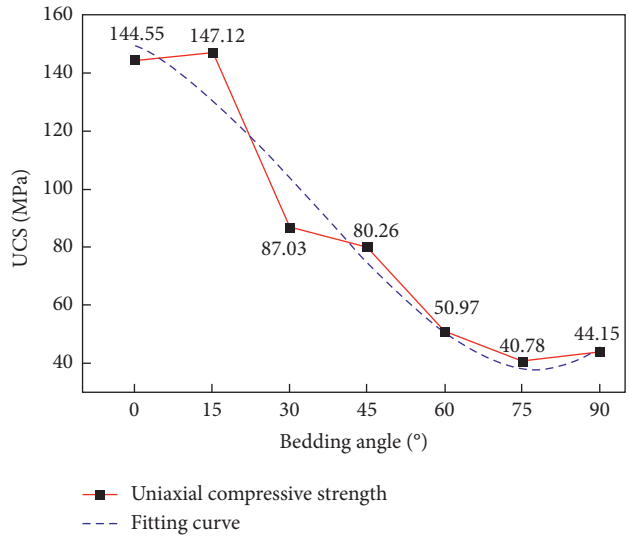

Figure 3: Relationship between uniaxial compressive strength and bedding angle.

3.2. Deformation and Failure Characteristics. To explore the influence of bedding dip angle on crack propagation of shale with a circular hole, the global strain field evolution at the moment of shale failure is quantitatively analyzed by using the digital image correlation method. What should be noted is that, for the case of 75°, a large area of the spalling area appears along the weak bedding surface at the upper right of the test surface, resulting in the lack of speckle data; thus, the global strain field cannot be captured and has not been listed. Given this, this paper only analyzes the strain of shale samples with prefabricated circular holes at 0°, 15°, 30°, 45°, 60°, and 90° and obtains the cloud charts of tensile strain field evolution and shear strain field evolution (as shown in Figures 4–15). The t value represents the time before fracturing.

As can be seen from Figures 4 and 5, for the specimen with a bedding angle of 0°, a tensile concentrated strain region appears at the upper left, and the value of the shear strain field corresponding to this region is large. Therefore, it can be judged that the macro crack at the upper left is a tensile shear failure. A tensile strain concentration area passes through the circular hole and gradually expands along the compressive stress direction. When it tends to fail, the shear strain concentration appears near the circular hole. Therefore, it can be judged that the macro crack passing through the circular hole is dominated by tensile failure, while the mixed failure is dominated around the circular hole.

By observing the tensile strain field in Figures 6 and 7, it can be seen that for the sample with an angle of 15°, at 5000 ms, the crack initiates at the upper part of the circular hole. At 3000 ms, the tensile strain concentration area also occurs at the upper right of the circular hole. As loading time increases, the tensile strain concentration area gradually extends along the loading direction. Two independent cracks finally merge on the right side of the circular hole, and then, instability failure occurs. By observing the shear strain field, it can be found that the global shear strain of the sample is large, and there is a shear strain concentration area around the circular hole. Therefore, it can be judged that the macro crack through the circular hole is dominated by tensile failure, and the failure around the circular hole is dominated by tensile shear mixed failure. Combined with the peak strength date, when the bedding dip angle is 0° and 15°, that is, the loading direction and bedding dip angle are large, the mixed failure of bedding plane and shale matrix occurs. At this time, the peak strength largely depends on the shale matrix itself, reflecting the compressive capacity of the shale matrix.

It can be found that when the bedding angle reaches 30° (shown in Figures 8 and 9), the macro crack penetrating the circular hole is mainly dominated by tensile failure, and the global shear strain of the sample is large. With the bedding angle further increasing to 45° (Figures 10 and 11), the spalling failure occurs at the upper right end of the sample, the macro crack through the circular hole is dominated by tensile failure, and the global shear strain of the sample is large. By comprehensively comparing the 30° and 45° strain fields, the cementation of bedding planes with weak strength begins to significantly affect the deformation process of rock. In particular, when the bedding dip angle is 45°, a local concentration area of tensile strain is generated along the bedding angle, and as loading time increases, the local area of tensile strain slides along the bedding angle and finally runs through the weak bedding plane, resulting in rock instability and failure. Therefore, the uniaxial compressive strength decreased significantly.

Figures 12 and 13 show the cloud charts of tensile strain field and shear strain field evolution of the sample with a bedding angle of 60°, respectively. A tensile concentrated strain zone is generated at the upper right side of the sample and extends to the outside of the sample in the direction of approximately 60°, while the shear one is relatively homogeneous. Therefore, it can be judged that the macro crack is tensile (the failure mode of the sample with a bedding angle of 75° is similar to that of 60°).

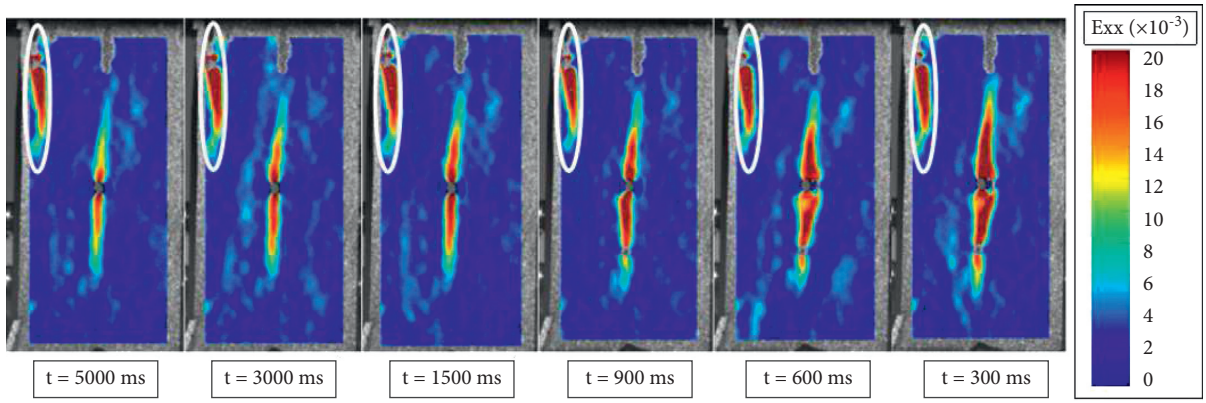

Figure 4: Cloud charts of tensile strain field evolution of shale sample with bedding angle of 0° (where red represents tensile strain, blue represents compressive strain).

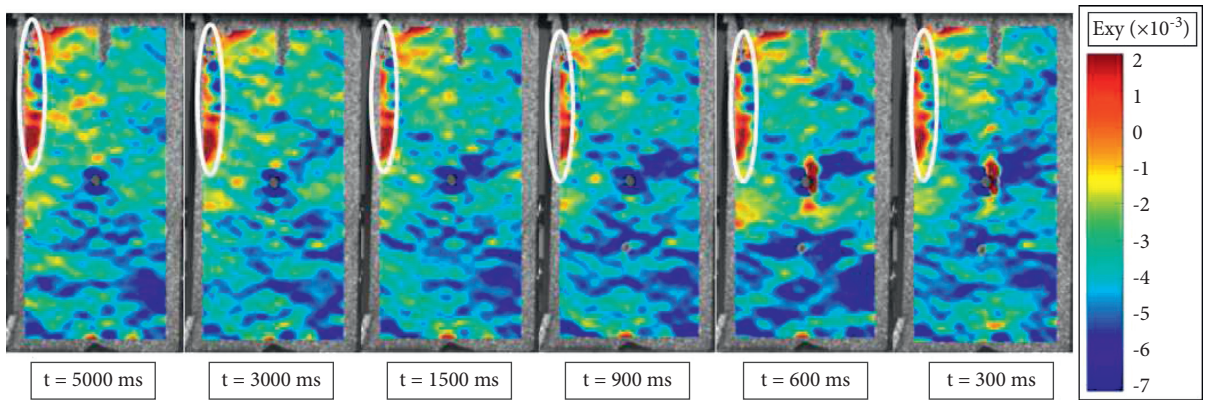

Figure 5: Cloud charts of shear strain field evolution of shale sample with hole bedding angle of 0° (where the t value represents the time before fracturing, red represents positive shear strain and blue represents negative shear strain).

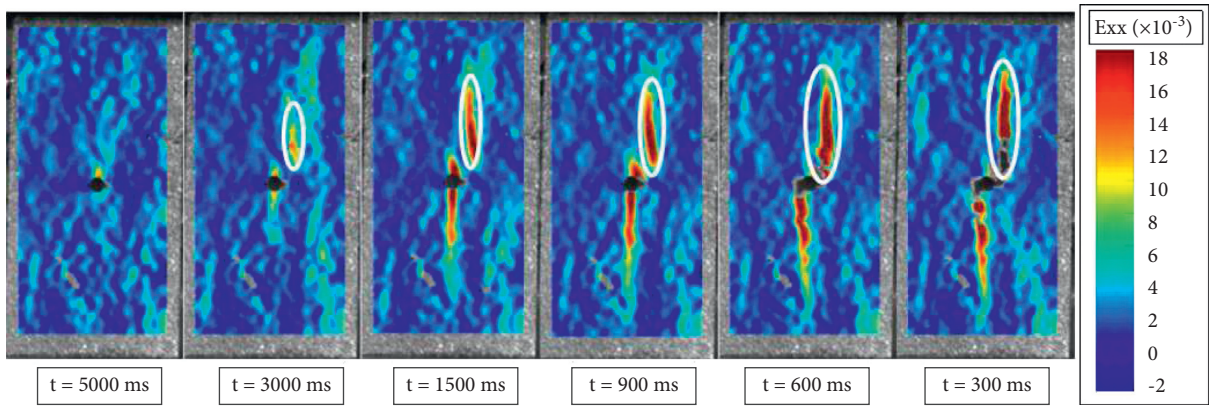

Figure 6: Cloud charts of tensile strain field evolution of shale sample with bedding angle of 15° (where the *t* value represents the time before fracturing, red represents tensile strain and blue represents compressive strain).

Observing the strain field of the 90° specimens shown in Figures 14 and 15, it can be found that a vertical tensile strain concentration zone penetrating a circular hole is first generated in the centre of the shale, and then, a short vertical tensile strain concentration zone appears on the upper right side of the specimens, both of which are parallel to the shale bedding angle. Since the loading direction is parallel to the bedding plane and the bedding plane is in a tension state, a vertical tension strain concentration zone is generated. Therefore, the peak strength largely depends on the strength of the bedding plane, reflecting the compressive capacity of the bedding plane. In summary, it can be inferred that when the bedding dip angle is greater than 45°, the specimen will slip along the weak plane of bedding, and the peak strength is small.

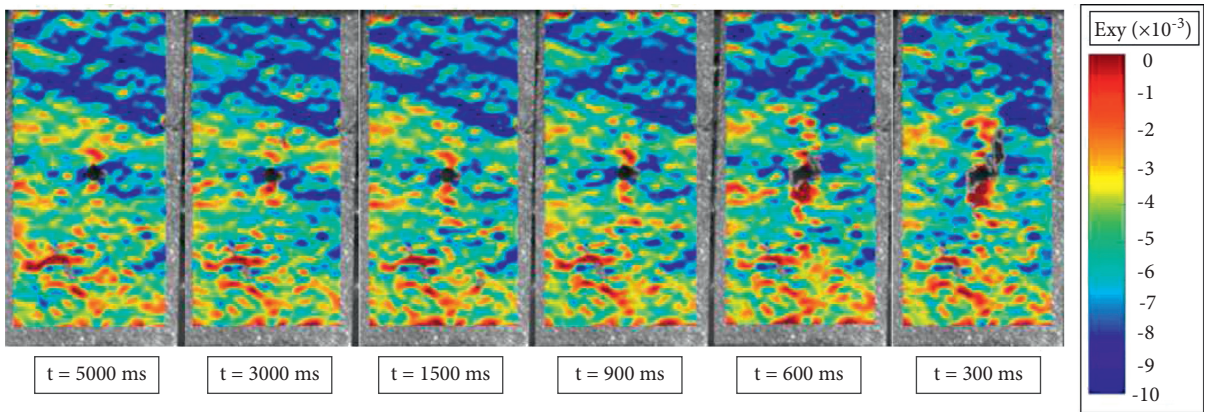

Figure 7: Cloud charts of shear strain field evolution of shale sample with hole bedding angle of 15° (where the *t* value represents the time before fracturing, red represents positive shear strain and blue represents negative shear strain).

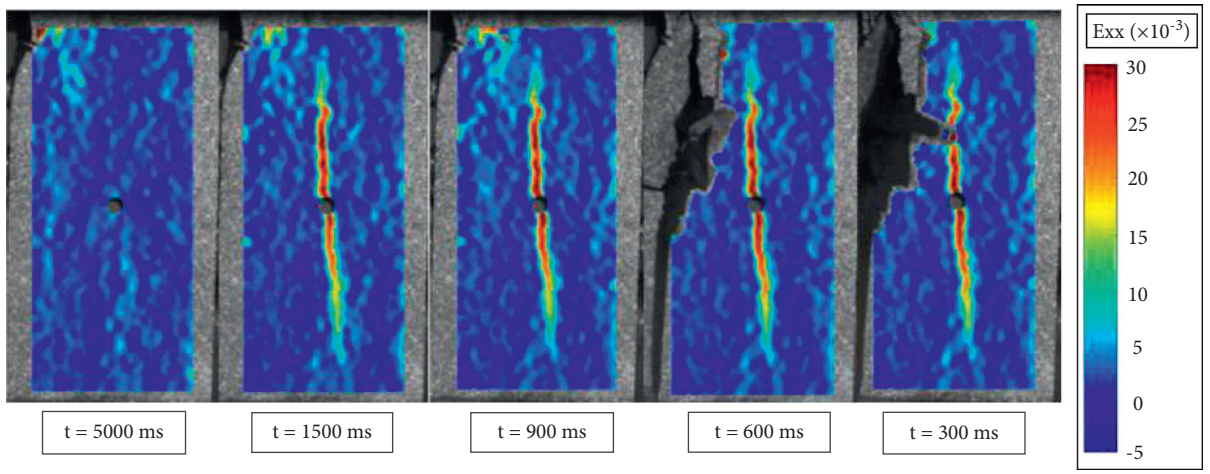

Figure 8: Cloud charts of tensile strain field evolution of shale sample with bedding angle of 30° (where the *t* value represents the time before fracturing, red represents tensile strain and blue represents compressive strain).

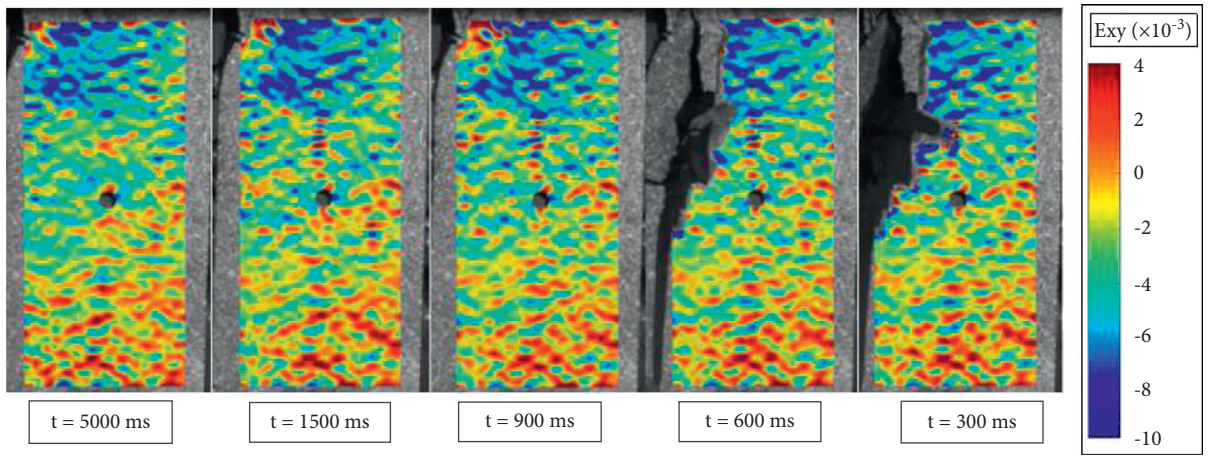

Figure 9: Cloud charts of shear strain field evolution of shale sample with hole bedding angle of 30° (where the *t* value represents the time before fracturing, red represents positive shear strain and blue represents negative shear strain).

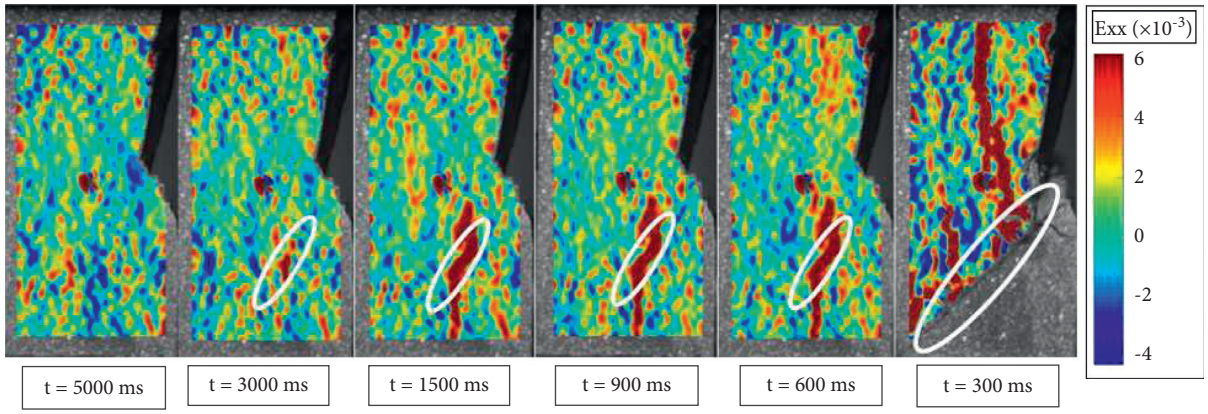

Figure 10: Cloud charts of tensile strain field evolution of shale sample with bedding angle of 45° (where the *t* value represents the time before fracturing, red represents tensile strain and blue represents compressive strain).

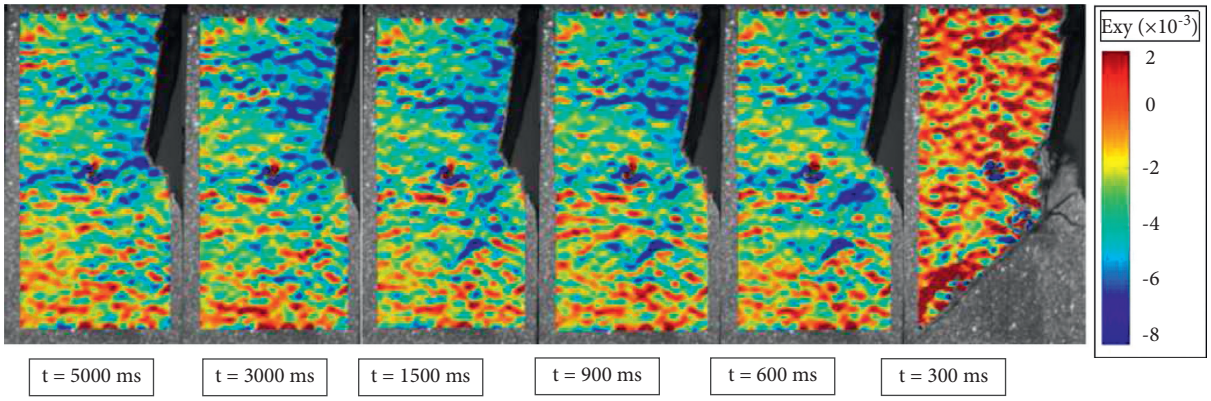

Figure 11: Cloud charts of shear strain field evolution of shale sample with hole bedding angle of 45° (where the *t* value represents the time before fracturing, red represents positive shear strain and blue represents negative shear strain).

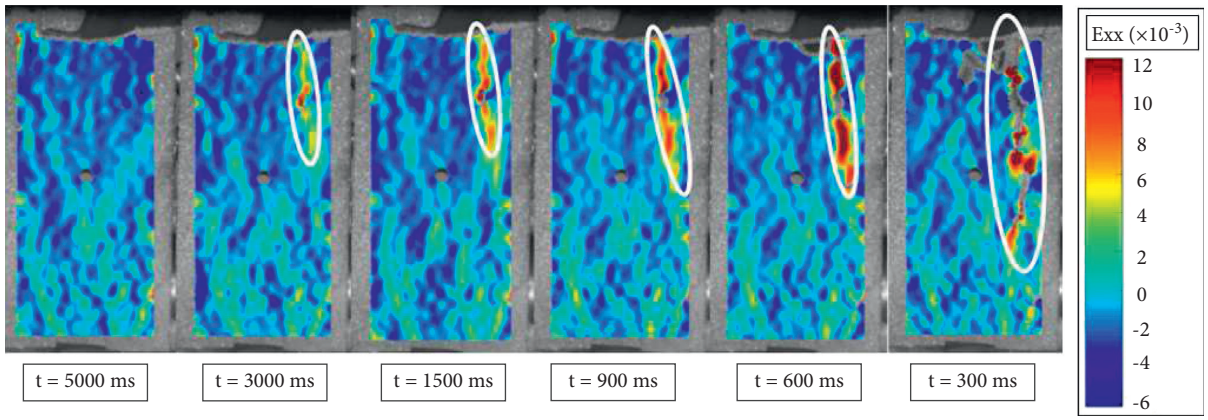

Figure 12: Cloud charts of tensile strain field evolution of shale sample with bedding angle of 60° (where the *t* value represents the time before fracturing, red represents tensile strain and blue represents compressive strain).

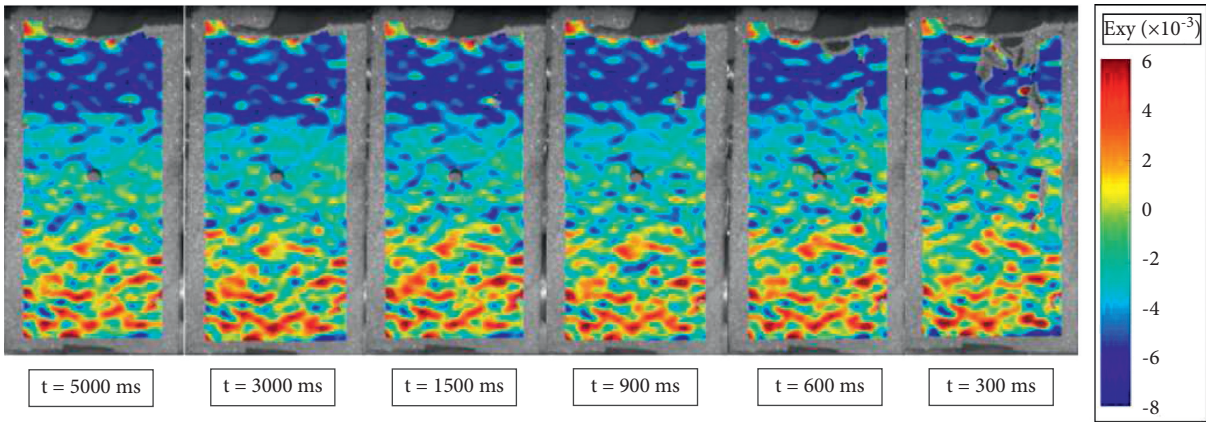

Figure 13: Cloud charts of shear strain field evolution of shale sample with hole bedding angle of 60° (where the *t* value represents the time before fracturing, red represents positive shear strain and blue represents negative shear strain).

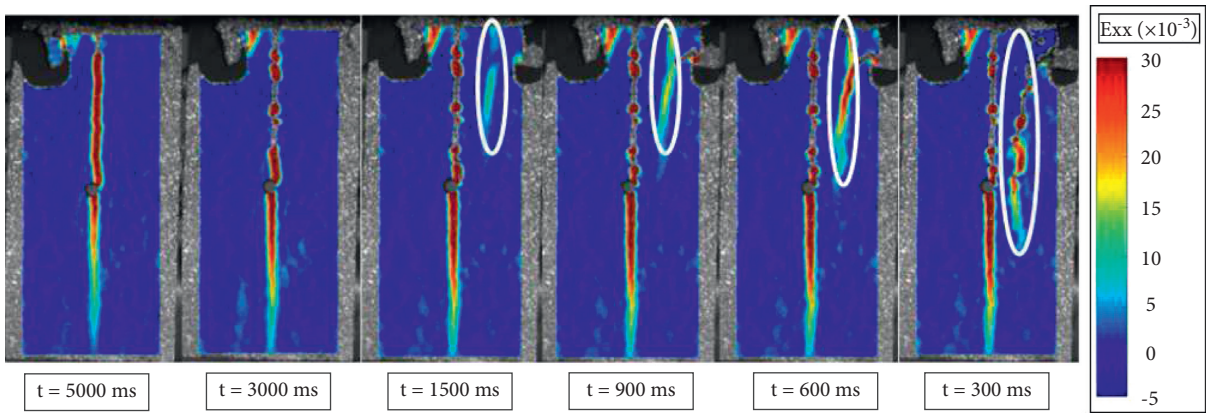

Figure 14: Cloud charts of tensile strain field evolution of shale sample with bedding angle of 90° (where the t value represents the time before fracturing, red represents tensile strain and blue represents compressive strain).

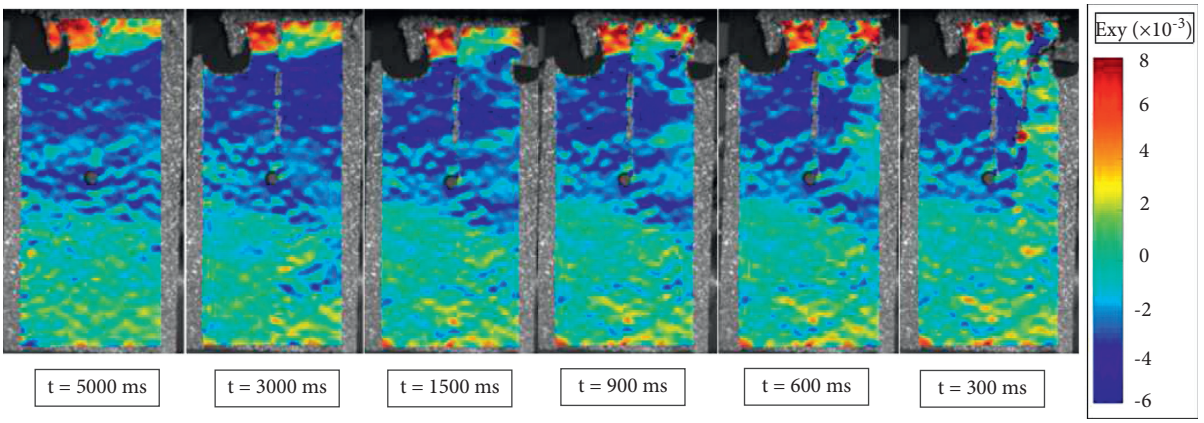

Figure 15: Cloud charts of shear strain field evolution of shale sample with hole bedding angle of 90° (where the t value represents the time before fracturing, red represents positive shear strain and blue represents negative shear strain).

4. Conclusion

In this paper, the influence of bedding angle on the strength characteristics and failure deformation of shale was explored through the uniaxial compression tests combined with DIC. The results provide theoretical support for the stability of tunnel surrounding rock. The main conclusions are as follows:

(1) The peak strength of shale with prefabricated circular holes is closely related to bedding dip angle. With the increase of bedding angle, the peak strength first

increases, then dramatically decreases, and finally slightly increases. When the bedding angle is small (0° and 15°), the peak strength of the shale mainly depends on the strength of the shale matrix. When the bedding angle is large (60°, 75°, and 90°), the peak strength of shale mainly depends on the strength of the shale bedding plane, and thus, the peak strength is small.

(2) The global shear strain field of shale with prefabricated circular holes is closely related to the bedding dip angle. When the bedding angle is 0° and 90°, the global shear strain is small. When the bedding dip angle is between 0° and 90°, the global shear strain caused by the joint action of rock internal friction and bedding plane is large, and the global shear strain is the largest when the bedding dip angle is 30° and 45°.

(3) The failure mode around the circular hole of shale with a prefabricated circular hole is closely related to the bedding dip angle. When the bedding angle is 0°, 15°, 30°, and 45°, the failure mode around the circular hole is tension shear mixed failure; When the bedding angle is 60° and 75°, there is no damage around the circular hole. When the bedding angle is 90°, tensile failure occurs around the circular hole.

(4) The macroscopic crack failure mode of shale with prefabricated circular holes is closely related to the bedding angle. When the bedding angle is 0°, 15°, 30°, 45°, and 90°, the tensile failure runs through the circular holes are mainly produced. When the bedding angle is 60° and 75°, tensile failure away from the circular hole occurs along the weak surface of bedding. [37].

Data Availability

All data can be obtained from the corresponding author.

Conflicts of Interest

The authors declare that there are no conflicts of interest.

Acknowledgments

The authors thank the funding support of the Engineering Research Center of Geothermal Resources Development Technology and Equipment, Ministry of Education, Jilin University (No. 21013), Zhejiang Provincial Natural Science Foundation of China under Grant no. LQ21E040003, and Scientific Research Foundation of Shaoxing University (No. 13011001002/110).

References

[1] H. K. Verma, N. K. Samadhiya, M. Singh, R. K. Goel, and P. K. Singh, "Blast induced rock mass damage around tunnels," *Tunnelling and Underground Space Technology*, vol. 71, pp. 149–158, 2018.

[2] N. Innaurato, R. Mancini, and M. Cardu, "On the influence of rock mass quality on the quality of blasting work in tunnel driving," *Tunnelling and Underground Space Technology*, vol. 13, no. 1, pp. 81–89, 1998.

[3] V. M. S. R. Murthy and K. Dey, "Predicting overbreak from blast vibration monitoring in a lake tap tunnel–a success story," *Fragblast*, vol. 7, no. 3, pp. 149–166, 2003.

[4] H. K. Verma, V. V. R. Prasad, and R. K. Goel, "Investigations of rock mass damage induced by blasting in tunnelling," *Journal of Rock Mechanics and Tunnelling Technology*, vol. 22, no. 1, pp. 49–61, 2016.

[5] K. Dey and V. M. S. R. Murthy, "Determining blast damage envelope through vibration model and validation using seismic imaging," *Mining Technology*, vol. 120, no. 2, pp. 90–94, 2011.

[6] R. Holmberg, "Design of tunnel perimeter blasthole patterns to prevent rock damage," in *Proceedings of the IMM Tunnelling'79 Conference*, pp. 3–6, London, UK, 1979.

[7] C. Zhu, M. He, X. Zhang, Z. Tao, Q. Yin, and L. Li, "Nonlinear mechanical model of constant resistance and large deformation bolt and influence parameters analysis of constant resistance behavior," *Rock and Soil Mechanics*, vol. 42, no. 7, pp. 1911–1924, 2021.

[8] G. Shi, X. Yang, H. Yu, and C. Zhu, "Acoustic emission characteristics of creep fracture evolution in double-fracture fine sandstone under uniaxial compression," *Engineering Fracture Mechanics*, vol. 210, pp. 13–28, 2019.

[9] C. Zhu, M.-c. He, B. Jiang, X.-z. Qin, Q. Yin, and Y. Zhou, "Numerical investigation on the fatigue failure characteristics of water-bearing sandstone under cyclic loading," *Journal of Mountain Science*, vol. 18, no. 12, pp. 3348–3365, 2021.

[10] G. Li, Y. Hu, S.-m. Tian, M. weibin, and H.-l. Huang, "Analysis of deformation control mechanism of prestressed anchor on jointed soft rock in large cross-section tunnel," *Bulletin of Engineering Geology and the Environment*, vol. 80, no. 12, pp. 9089–9103, 2021.

[11] M. Gao, J. Xie, Y. Gao et al., "Mechanical behavior of coal under different mining rates: a case study from laboratory experiments to field testing," *International Journal of Mining Science and Technology*, vol. 31, no. 5, pp. 825–841, 2021.

[12] M. Gao, H. Hao, S. Xue et al., "Discing behavior and mechanism of cores extracted from Songke-2 well at depths below 4,500 m," *International Journal of Rock Mechanics and Mining Sciences*, vol. 149, Article ID 104976, 2022.

[13] C. Cao, W. Zhang, J. Chen, B. Shan, S. Song, and J. Zhan, "Quantitative estimation of debris flow source materials by integrating multi-source data: a case study," *Engineering Geology*, vol. 291, Article ID 106222, 2021.

[14] D. Chen, H. Chen, W. Zhang, J. Lou, and B. Shan, "An analytical solution of equivalent elastic modulus considering confining stress and its variables sensitivity analysis for fractured rock masses," *Journal of Rock Mechanics and Geotechnical Engineering*, vol. 2021, 2021.

[15] B. Ding, Z. Han, G. Zhang, X. Beng, and Y. Yang, "Flexural toppling mechanism and stability analysis of an anti-dip rock slope," *Rock Mechanics and Rock Engineering*, vol. 54, no. 8, pp. 3721–3735, 2021.

[16] Z. Dou, S. Tang, X. Zhang et al., "Influence of shear displacement on fluid flow and solute transport in a 3D rough fracture," *Lithosphere*, vol. 2021, Article ID 1569736, 2021.

[17] Z. Dou, Y. Liu, X. Zhang et al., "Influence of layer transition zone on rainfall-induced instability of multilayered slope," *Lithosphere*, vol. 2021, Article ID 2277284, 2021.

[18] R. H. C. Wong, P. Lin, and C. A. Tang, "Experimental and numerical study on splitting failure of brittle solids containing single pore under uniaxial compression," *Mechanics of Materials*, vol. 38, no. 1-2, pp. 142–159, 2006.

[19] D. Li, Q. Zhu, Z. Zhou, X. Li, and P. G. Ranjith, "Fracture analysis of marble specimens with a hole under uniaxial compression by digital image correlation," *Engineering Fracture Mechanics*, vol. 183, pp. 109–124, 2017.

[20] X. Fan, R. Chen, H. Lin, H. Lai, C. Zhang, and Q. Zhao, "Cracking and failure in rock specimen containing combined flaw and hole under uniaxial compression," *Advances in Civil Engineering*, vol. 2018, Article ID 9818250, 15 pages, 2018.

[21] H. Wang, A. Dyskin, E. Pasternak, P. Dight, and M. Sarmadivaleh, "Effect of the intermediate principal stress on 3-D crack growth," *Engineering Fracture Mechanics*, vol. 204, pp. 404–420, 2018.

[22] H. Wang, A. Dyskin, and E. Pasternak, "Comparative analysis of mechanisms of 3-D brittle crack growth in compression," *Engineering Fracture Mechanics*, vol. 220, Article ID 106656, 2019.

[23] H. Wang, A. Dyskin, E. Pasternak, P. Dight, and M. Sarmadivaleh, "Experimental and numerical study into 3D crack growth from a spherical pore in biaxial compression," *Rock Mechanics and Rock Engineering*, vol. 53, no. 1, pp. 77–102, 2020.

[24] G. Han, Q. Liang, R. Bao, and Y. Zhou, "Influence of Circular Hole Diameter on Deformation and Failure of Longmaxi Shale," *Geotechnical and Geological Engineering*, vol. 2022, pp. 1–9, 2022.

[25] Z. Li, S. Liu, W. Ren, J. Fang, Q. Zhu, and Z. Dun, "Multiscale laboratory study and numerical analysis of water-weakening effect on shale," *Advances in Materials Science and Engineering*, vol. 2020, Article ID 5263431, 14 pages, 2020.

[26] D. Charpentier, D. Tessier, and M. Cathelineau, "Shale microstructure evolution due to tunnel excavation after 100 years and impact of tectonic paleo-fracturing," *Case of Tournemire, France," Engineering Geology*, vol. 70, no. 1-2, pp. 55–69, 2003.

[27] M. Josh, L. Esteban, C. Delle Piane, J. Sarout, D. N. Dewhurst, and M. B. Clennell, "Laboratory characterisation of shale properties," *Journal of Petroleum Science and Engineering*, vol. 88-89, pp. 107–124, 2012.

[28] V. Ghiasi, H. Omar, J. Rostami et al., "Geotechnical and geological studies of NWCT tunnel in Iran focusing on the stabilization analysis and design of support: a case study," *Scientific Research and Essays*, vol. 6, no. 1, pp. 79–97, 2011.

[29] Z. Hou, C. Yang, Y. Guo et al., "Experimental study on anisotropic properties of Longmaxi formation shale under uniaxial compression," *Rock and Soil Mechanics*, vol. 36, no. 9, pp. 2541–2550, 2015.

[30] H. Niandou, J. F. Shao, J. P. Henry, and D. Fourmaintraux, "Laboratory investigation of the mechanical behaviour of Tournemire shale," *International Journal of Rock Mechanics and Mining Sciences*, vol. 34, no. 1, pp. 3–16, 1997.

[31] Y. Zhang, *Study on Anisotropy of Mechanical Properties of the Shale in West Hubei and East Chongqing*, Southwest University of Science and Technology, Mianyang, China, 2016.

[32] S. Yin, W. Ding, Y. Sun, X. Wang, M. Zhang, and N. Zhang, "Shale uniaxial compressive failure property and the affecting factors of UCS," *Earth Science Frontiers*, vol. 23, no. 2, pp. 75–95, 2016.

[33] B. Zhang, H. Ma, X. Tian, and C. Zhou, "Deep layered shale mechanical parameters anisotropy study," *Chinese Journal of Underground Space and Engineering*, vol. 16, no. S2, pp. 634–638, 2020.

[34] C. Zhao, C. Bao, H. Matsuda, C. Zhao, and J. Tian, "Application of digital image correlation method in experimental research on crack propagation of brittle rock," *Chinese Journal of Geotechnical Engineering*, vol. 37, no. 5, pp. 944–951, 2015.

[35] J. Blaber, B. Adair, and A. Antoniou, "Ncorr: open-source 2D digital image correlation matlab software," *Experimental Mechanics*, vol. 55, no. 6, pp. 1105–1122, 2015.

[36] B. He, L. Xie, F. Li, P. Zhao, and Y. Zhang, "Anisotropic mechanism and characteristics of deformation and failure of Longmaxi shale," *SCIENTIA SINICA Physica, Mechanica & Astronomica*, vol. 47, no. 11, Article ID 114611, 2017.

[37] J. Xie, *Experimental Investigation on Hydraulic Fracture Geometry of Perforated Well in Longmaxi Shale Gas Reservoir*, China University of Geosciences, Wuhan, China, 2019.